

論文 / 著書情報
Article / Book Information

題目(和文)	
Title(English)	High-fidelity Numerical Model for Compressible Multi-component Flow
著者(和文)	デン シ
Author(English)	Xi Deng
出典(和文)	学位:博士(理学), 学位授与機関:東京工業大学, 報告番号:甲第10938号, 授与年月日:2018年9月20日, 学位の種別:課程博士, 審査員:肖 鋒,奥野 喜裕,青木 尊之,末包 哲也,長崎 孝夫
Citation(English)	Degree:Doctor (Science), Conferring organization: Tokyo Institute of Technology, Report number:甲第10938号, Conferred date:2018/9/20, Degree Type:Course doctor, Examiner:,,,,,
学位種別(和文)	博士論文
Type(English)	Doctoral Thesis

TOKYO INSTITUTE OF TECHNOLOGY

DOCTORAL THESIS

**High-fidelity Numerical Model for
Compressible Multi-component Flow**

Author:

Xi DENG

Supervisor:

Professor Feng XIAO

*A thesis submitted in partial fulfilment of the requirements
for the degree of Doctor of Science*

Department of Energy Sciences

Interdisciplinary Graduate School of Science and Engineering

August 2018

Abstract

The development of accurate and robust numerical models for compressible multi-components flows has been one of the most active research areas in CFD (computational fluid dynamics) community for past decades, which has been constantly driven by the great demand of applications from a broad engineering. However, the complicated flow structures in compressible multi-components flows such as moving interfaces and reaction fronts pose great challenges to most of existing numerical methods. The inherent numerical dissipation errors in so-called high resolution methods may smear out fine flow structures, which even leads to wrong numerical solutions. Thus in this work, we have made following efforts to construct high-fidelity numerical methods.

1. We firstly propose the Boundary variation diminishing (BVD) algorithm which serves as a new guideline for reconstruction processes. The concept of this algorithm is to determine reconstruction function from several candidates thus to minimize numerical dissipation errors. Then, several effective implementation of BVD algorithm is introduced or designed. With these algorithm, new reconstruction schemes can be constructed under the BVD principle. The numerical tests show that the resultant scheme can achieve high order in smooth region but also solve sharp discontinuities. Thus the designed algorithms can effectively minimize numerical dissipation errors.

2. With the help of BVD algorithm, we propose two practical schemes which can solve problems involving discontinuities. We first design the MUSCL-THINC-BVD scheme, which significantly improves the accuracy of original MUSCL scheme. Despite of its algorithmic simplicity, it shows competitive performance compared with high order schemes. Then a novel limiting-free discontinuities capturing scheme is proposed. Different from long-lasting reconstruction processes which employ high order polynomials enforced with some carefully designed limiting projections to seek stable solutions around discontinuities, the current discretized scheme employs non-polynomial THINC

(Tangent of Hyperbola for INterface Capturing) functions with adaptive sharpness to solve both smooth and discontinuous solutions. Due to the essentially monotone and bounded properties of THINC function, difficulties to solve sharp discontinuous solutions and complexities associated with designing limiting projections can be prevented. Verified through numerical tests, the present method is able to capture both smooth and discontinuous solutions for reactive compressible gas dynamics with excellent solution quality competitive to other existing schemes.

3. The newly proposed schemes are applied to solve the five-equation model for interfacial two phase flows. The scheme is implemented to the volume fraction and other state variables under the same finite volume framework, which realizes the consistency among volume fraction and other physical variables. Moreover, this scheme can resolve discontinuous solutions with much less numerical dissipation in comparison with other existing methods, which enables to solve moving interfaces of compact thickness without additional “anti-diffusion” or “artificial compression” manipulation. Numerical results of benchmark tests show that the present method is able to capture the material interface as a well-defined sharp jump in volume fraction.

4. We extend our schemes to high order in the local high order reconstruction framework. We propose a new formulation for high-order multi-moment constrained finite volume (MCV) method. Two candidate polynomials for spatial reconstruction of third-order are built by adopting one additional constraint condition from the adjacent cells. A boundary gradient switching (BGS) algorithm based on the variation-minimization principle is devised to determine the spatial reconstruction from the two candidates, so as to remove the spurious oscillations around the discontinuities. The resulted non-oscillatory MCV3-BGS scheme is of fourth-order accuracy and completely free of case-dependent ad hoc parameters.

5. We have constructed a novel numerical model for Euler equations on 2D unstructured grids and 3D hybrid unstructured grids including tetrahedral, hexahedral, prismatic and

pyramidal elements. The model integrates the VPM (Volume integrated average and Point value based Multi-moment) spatial discretization scheme and the limiting projection with BVD manipulation. Distinguished from conventional finite volume method, both the volume-integrated average (VIA) and the point values (PV) at the cell vertices are memorized as prognostic variables and updated in time simultaneously. The resulting numerical model provides remarkably improved numerical accuracy and robustness with a moderate increase in algorithmic complexity and computational cost.

As verified through numerical tests, the proposed numerical method serves as a high fidelity tool to obtain accurate and robust numerical solutions for compressible multi-components flows, which are very challenging to other existing methods. Due to their algorithmic simplicity, it can be expected to be applied to wide engineering problems.

Acknowledgements

First of all, I will give my most sincere gratitude to my supervisor, Professor Feng Xiao, who spends lots of time and efforts on mentoring my research, advising my career and paying concerns on my future. It is my great fortune to be one of his students. Thanks to his selfless instruction and profound knowledge, I have learned a lot which is not only beneficial for my academic research but more importantly, will be helpful for my future life in the society. During five years, he is always the mentor who really cares about his student and guides them to a bright future. During five years, he is always willing to spare a lot of time from his busy schedule to discuss with us about research as well as how to behave in the society. He shares us with his rich experience and knowledge. His respectable enthusiasm about research inspires me a lot. During five years, he always puts the interests of his students in the first place. From the conversation with him, I could feel his care and expectation about us. His kindness and dedication will be kept in my mind and drive me go forward.

It is impossible for me to finish the work during Ph.D without the help and guidance from my senior Dr. Bin Xie. He gives me a lot of advices about CFD. At the same time, his preciseness about research, daily hardworking and creativity give me a very good example about how to be a successful young researcher. I always feel stressful when working with him because of his high efficiency. However, this stress greatly improves my way to do research. I also should give my thanks to Dr. Sun and Dr. Ikebata. They kindly helped me to solve several problems in my research. Also, I would like to thank my other colleagues, Mr. Jin, Mr. Inaba, and Mr. Shimizu. They make indispensable contributions for my research. Discussing with them is also very enjoyable.

Moreover, I am deeply thankful to my family for their love and sacrifices, especially to my mother who bears worries during my Ph.D study in a foreign country. They always support my choices and show great expectation about my future. It is their selfless love and sacrifices that brings courage to me.

In addition, my sincere thanks go to Prof. Suekane. As my sub-supervisor, he spent a lot of time to help me and paid kind concern about my daily life. I am also deeply indebted to Prof. Okuno. He devoted his time and efforts to support my study in ACEEES program. Thanks to him, I could finish ACEEES program smoothly. I am very grateful to Prof. Yokoi in Cardiff University. He gave me great help and support during my visit. I want to thank Prof. Shyue in National Taiwan University and Dr. Raphael in Univerite de Bordeaux. They gave me very precious advices and helped me to improve the quality of my work. I will also thank Prof. Aoki, Prof. Okuno and Prof. Nagasaki in advance for their time to be in my thesis supervisory committee.

Finally, I will express my gratitude to my friends and those who ever helped me. Because of you, my world becomes richer and brighter.

Contents

Abstract	i
Acknowledgements	iv
Contents	vi
List of Figures	vii
List of Tables	viii
Abbreviations	ix
1 Introduction	1
1.1 Background	1
1.2 Control Equations	3
1.2.1 Euler equations	3
1.2.2 Reacting Euler equations	4
1.2.3 Five equations model for compressible multiphase flow	5
1.3 Finite volume method for hyperbolic system	7
1.3.1 Finite volume method and finite volume wave propagation method	7
1.3.2 Reconstruction processes	10
1.3.3 Riemann solvers	12
1.4 Local high order reconstruction (LHR) method	19
1.4.1 Review of local high order reconstruction method	19
1.4.2 Limiting processes of LHR	21
1.5 Current issues for simulation of compressible multi-components flow	22
1.5.1 Numerical difficulties for detonation waves	22
1.5.2 Numerical difficulties for moving interface flows	25
1.6 Purposes of current research	29
1.7 Outline of the thesis	30
2 Boundary variation diminishing (BVD) principle	34
2.1 Boundary variation diminishing (BVD) algorithms	34

2.2	BVD admissible reconstruction function	39
2.2.1	Polynomial-based reconstruction functions	39
2.2.2	Tangent of Hyperbola for Interface Capturing (THINC) function	41
2.3	Numerical experiments	42
2.3.1	Convergence Test	43
2.3.2	Advection of one-dimensional complex waves	43
2.4	Summary	44
3	Practical BVD schemes for single phase and reacting Euler equations	47
3.1	Introduction	47
3.2	Formulation of MUSCL-THINC-BVD	48
3.3	Limiter-free discontinuity capturing schemes	50
3.3.1	Dissipation properties of THINC scheme	50
3.3.2	Formulations of adaptive THINC-BVD scheme	51
3.4	Solution procedures for Euler and reacting Euler equations	53
3.4.1	Control equations	53
3.4.2	Solution procedures with wave propagation method	55
3.5	Numerical experiments of MUSCL-THINC-BVD scheme	57
3.5.1	Euler equations	57
3.5.2	Euler reacting equations for stiff detonation	59
3.6	Numerical experiments of adaptive THINC-BVD scheme	74
3.6.1	1D Euler equations	75
3.6.2	1D Euler reacting equations for stiff detonation	81
3.6.3	2D Euler equations	84
3.6.4	2D Euler reacting equations for stiff detonation	89
3.7	Summary	91
4	Implementation of BVD schemes on compressible multiphase flows with moving interface	95
4.1	Introduction	95
4.2	Solution procedures for five equations model	100
4.2.1	Control equations	100
4.2.2	Solution procedures with wave propagation method	102
4.3	Numerical experiments for compressible multiphase flows	105
4.3.1	1D numerical tests	106
4.3.2	2D numerical tests	110
4.3.3	3D numerical tests	121
4.4	Summary	123
5	Multi-moment finite volume method with the boundary gradient switching (BGS) limiting on structured grids	126
5.1	Review of MCV method	126
5.2	Formulation of 3-point MCV scheme with slope constraint	128
5.3	A non-oscillatory MCV scheme with boundary gradient switching	133
5.4	Numerical experiments	136

5.4.1	1D linear advection equation	136
5.4.2	1D non-linear equation system	140
5.4.3	2D linear advection equation	147
5.4.4	2D Euler equations	149
5.5	Summary	154
6	A finite volume multi-moment method with boundary variation diminishing principle on hybrid unstructured grids	156
6.1	The computational grids and computational variables of VPM/MCV schemes	158
6.2	High resolution reconstruction on unstructured grids	160
6.3	Solution procedures for VIA and PV	163
6.3.1	Solution procedure for VIA	163
6.3.2	Solution procedure for PV	165
6.4	BVD algorithm on unstructured grids for limiting process	167
6.5	BVD algorithm on unstructured grids for dissipation reducing	169
6.6	Numerical experiments	171
6.6.1	Advection equation	172
6.6.2	2D Euler equations	182
6.6.3	2D reacting Euler equations	198
6.6.4	3D numerical experiments	201
6.7	Summary	208
7	Conclusions and future work	210
7.1	Major contributions of present study	211
7.2	Future work	213
	Bibliography	215

List of Figures

2.1	Numerical results of advection of complex waves with different algorithms.	45
3.1	Illustration of one possible situation corresponding to $ q_{i-1/2}^{L,MUSCL} - q_{i-1/2}^{R,THINC} + q_{i+1/2}^{L,THINC} - q_{i+1/2}^{R,MUSCL} $ when calculating $TBV_{i,min}^{THINC}$	49
3.2	Imaginary parts of modified wavenumber from THINC schemes with different β_s . A comparison with the TVD scheme is also included. The left one shows the whole resolvable wavenumber whereas the right one shows the zoomed region of the small wavenumber.	52
3.3	Sketch of the finite volume representation of data in three cells $\bar{\mathbf{q}}_i$. Reconstruction functions are denoted by $\tilde{\mathbf{q}}_i(x)$ and intercell values by $\mathbf{q}_{i-1/2}^L$ and $\mathbf{q}_{i-1/2}^R$. A Riemann solver is used to determine the fluctuation at cell interfaces.	56
3.4	Numerical results of Sod's problem for density field and pressure from MUSCL-THINC-BVD scheme.	58
3.5	Numerical results of Lax's problem for density field and pressure from MUSCL-THINC-BVD scheme.	58
3.6	Illustration of wrong produced detonation waves against true solution. Taken from [157].	60
3.7	Numerical experiments by refining mesh with WENO scheme. The numerical solutions produced by different mesh numbers are indicated in different colour.	61
3.8	Numerical results of the pressure field for the C-J detonation wave implemented with the Arrhenius law. Reference solutions are marked with black solid lines whereas numerical solutions are in red with symbols to provide a comparison between the WENO and MUSCL-THINC-BVD schemes.	62
3.9	As for Fig. 3.8 but for the temperature field.	62
3.10	As for Fig. 3.8 but for the density field.	63
3.11	As for Fig. 3.8 but for mass fraction.	63
3.12	As for Fig. 3.10 but with finer mesh.	63
3.13	Numerical results of pressure field for C-J detonation wave with the Heaviside model. Reference solutions are marked with black solid lines whereas numerical solutions are marked with red lines and symbols to provide a comparison between the WENO and MUSCL-THINC-BVD schemes.	64
3.14	As for Fig. 3.13 but for the temperature field.	65

3.15	As for Fig. 3.13 but for the density field.	65
3.16	As for Fig. 3.13 but for mass fraction.	65
3.17	Numerical results of pressure field for a strong detonation wave. Reference solutions are marked with black solid lines whereas numerical solutions are marked with red lines and symbols to provide a comparison between the WENO and MUSCL-THINC-BVD schemes.	66
3.18	As for Fig. 3.17 but for the temperature field.	67
3.19	As for Fig. 3.17 but for the density field.	67
3.20	As for Fig. 3.17 but for mass fraction.	67
3.21	Numerical results of the pressure field from the interaction between a detonation wave and an oscillatory profile problem. Reference solutions are marked with black solid lines whereas the numerical solutions are in red with symbols to provide a comparison between the WENO and MUSCL-THINC-BVD schemes.	68
3.22	As for Fig. 3.21 but for the temperature field.	69
3.23	As for Fig. 3.21 but for the density field.	69
3.24	As for Fig. 3.21 but for mass fraction.	69
3.25	Comparison of time cost between MUSCL-THINC-BVD and WENO schemes.	70
3.26	Numerical results for the propagating density wave test. L_1 errors and convergence rates from the mesh refinement computations by the original MUSCL scheme and the MUSCL-THINC-BVD scheme are plotted in the left panel, and the density profiles computed by different schemes on a 800-cell mesh are shown in the right panel.	71
3.27	Numerical solutions for multi-species detonation wave. Comparisons are made between the WENO scheme and proposed MUSCL-THINC-BVD scheme. Displayed are the pressure, density and mass fractions for each species.	72
3.28	Density field of the 2D detonation problem at $t = 0.3 \times 10^{-7}$. Comparisons are made between the reference solution, the WENO scheme with a coarse mesh, and the MUSCL-THINC-BVD with a coarse mesh. The profile at the left side is the reference result calculated using the WENO scheme with 2000×400 grid cells. The middle and right profiles are the results calculated using the WENO and MUSCL-THINC-BVD, schemes respectively, both with 400×80 grid cells.	74
3.29	As for Fig. 3.28 but at $t = 0.92 \times 10^{-7}$	74
3.30	As for Fig. 3.28 but at $t = 1.7 \times 10^{-7}$	74
3.31	Density field along the central line of x direction at $t = 1.7 \times 10^{-7}$. Reference solutions are marked with black solid lines whereas the numerical solutions are in red with symbols to provide a comparison between the WENO and MUSCL-THINC-BVD schemes.	75
3.32	Numerical results of Sod's problem for density field (top) and pressure (bottom) at $t = 0.25$ with 200 cells. Comparisons are made between the proposed scheme (left panels) and WENO scheme (right panels) and the exact solution (straight line).	78

3.33	Numerical results of Lax's problem for density field at time $t = 0.16$ with 200 cells. Comparisons are made between the proposed THINC-BVD scheme (left panel) and WENO scheme (right panel) against the exact solution (straight line).	79
3.34	Numerical results of two interacting blast waves problem for density field at $t = 0.038$ with 400 cells. Comparisons are made between the proposed scheme (left), WENO scheme (middle) and a discrete staggered compatible Lagrangian scheme (right).	80
3.35	Numerical results of Sedov blast wave problems. The solution of density field is presented on the left while pressure field on the right vs the exact solution (straight line).	81
3.36	Numerical results of density, temperature and mass fraction fields for C-J detonation wave with the Heaviside chemical reaction model. Reference solutions are represented by black solid lines. Comparisons are made between the WENO (right panels) and the proposed scheme (left panels).	83
3.37	Numerical results of density, temperature and mass fraction fields for C-J detonation wave with the Heaviside chemical reaction model for the interaction between a detonation wave and an oscillatory profile problem. Reference solutions are represented by black solid lines. Comparisons are made between the WENO (right panels) and the proposed scheme (left panels).	85
3.38	Density contour for Riemann problems 1, 2, 3, 4. Left: 5th order WENO scheme results. Right: Adaptive THINC-BVD scheme results.	88
3.39	CPU times recorded for Riemann problems #1, #2, #3, and #4 simulated by the TVD, WENO and BVD schemes. Comparisons are made amongst TVD, adaptive BVD and WENO schemes. Histograms (left axis): CPU time — Symbol-lines (right axis): ratio between the CPU times.	89
3.40	Density contours for double Mach reflection at time $t = 0.2$ with grid resolution $\Delta x = \Delta y = \frac{1}{100}$ (top panels) and $\Delta x = \Delta y = \frac{1}{200}$ (bottom panels). The figures are drawn with 30 density contours between 1.9 and 21.0.	90
3.41	Detonation problem — Density field at $t = 0.3 \times 10^{-7}$ (top panels) and $t = 1.7 \times 10^{-7}$ (bottom panels) — Left panels: Reference solution calculated by the 5th order WENO scheme with 2000×400 mesh cells — Middle panel: Solution obtained by 5th order WENO scheme with 400×80 mesh cells — Right panel: Solution obtained by the proposed BVD scheme with 400×80 mesh cells.	92
3.42	Detonation problem — Density field at $t = 1.7 \times 10^{-7}$ seen from a different angle compared to Fig. 3.41 — Left panels: Reference solution calculated by the 5th order WENO scheme with 2000×400 mesh cells — Middle panel: Solution obtained by 5th order WENO scheme with 400×80 mesh cells — Right panel: Solution obtained by the proposed BVD scheme with 400×80 mesh cells.	93

4.1	Numerical results for the passive advection test of a square liquid column at time $t = 10\text{ms}$. The solid line is the exact solution and the points show the computed solution with 200 mesh cells obtained using different methods. We denote the numerical result from MUSCL-THINC-BVD by MUSCL-BVD and that from [31] by WENO-JS. . . .	107
4.2	Numerical results for a two-phase (solid explosive-copper) impact problem at time $t = 85\mu\text{s}$. The solid line is the fine grid solution computed on a mesh of 5000 cells by MUSCL, and the points show the solutions with 200 meshes.	109
4.3	Comparisons of numerical results of shock/interface interaction problem between MUSCL-THINC-BVD and WENO schemes at $t=0.07$. . .	111
4.4	Numerical results for a planar Mach 1.22 shock wave in air interacting with a circular R22 gas bubble. Comparisons are made among MUSCL-THINC-BVD, MUSCL and WENO-JS schemes. Displayed are the Schlieren images of density variations at different instants. In each panel, the result of MUSCL-THINC-BVD (upper half) is plotted against the results of MUSCL or WENO-JS (lower half).	114
4.5	(continued)	115
4.6	The Schlieren-like images of density fields computed by the anti-diffusion interface sharpening technique[131] (the upper half in each panel) and the MUSCL-THINC-BVD scheme (the lower half in each panel) respectively with the same grid resolution (400 cells along the diameter of initial bubble).	116
4.7	Same as Fig.4.6, but with the upper half in each panel replaced by the results in [145] where a finer grid (1500 cells along the diameter of initial bubble) was used.	117
4.8	Schlieren images of density for the underwater explosion test at the instants $t = 0.95\text{ms}, 1.26\text{ms}, 1.58\text{ms}, 1.90\text{ms}$ (from top to bottom) computed by MUSCL, WENO-JS and MUSCL-THINC-BVD schemes respectively on a uniform grid of 600×600 cells.	118
4.9	Volume fraction contour at different instants for underwater explosion test using the MUSCL-THINC-BVD scheme on a uniform grid with 600×600 cells.	119
4.10	Distribution of density field along $x = 0$ cross-section for underwater explosion test at $t = 0.2\text{ms}$. The mesh size of the present computation is $h = 0.0067$. Comparisons are made with the published work [66, 129] where the cell size is $h = 0.005$	120
4.11	The material interface calculated by different schemes at $t = 3.16\text{ms}$ for underwater explosion test. Comparisons are made between MUSCL(a) and MUSCL-THINC-BVD(b) schemes.	120
4.12	Distribution of VOF function along $x = 0$ cross-section for underwater explosion test at $t = 2.55, 3.16\text{ms}$. Comparisons are made between MUSCL and MUSCL-THINC-BVD schemes.	121

4.13	Schlieren images of density fields for the Mach 6.0 shock-water interaction benchmark test at instants $t = 0.5, 0.75, 0.89, 1.1, 1.5,$ and 2.15 solved by the MUSCL-THINC-BVD scheme on a 2000×500 uniform grid.	122
4.14	Numerical results for 3D air-shock and helium-bubble interactions. Displayed are the color maps of density and pressure fields on the central cross-sections and the iso-surface of the volume fraction of 0.5 that represents the moving interface. From top to bottom are the numerical results at $136\mu s, 274\mu s$ and $346\mu s$ respectively.	124
4.15	Numerical results for 3D air-shock and helium-bubble interaction. Displayed are the experimental snapshots reported in [150] (left column) and the grayscale maps of density on the central plane in numerical results.	125
5.1	Stencils for spatial reconstruction.	133
5.2	Numerical results of 1D advection of a square wave by MCV3-4L scheme (left panel) and MCV3-4R (right panel) with 200 cells after one period.	138
5.3	Numerical result of 1D advection of a square wave by MCV3-BGS scheme with 200 cells after one period.	139
5.4	Numerical results of 1D advection of complex wave with 200 cells after one period.	140
5.5	Numerical results of Burgers' equation at $t=1$ with 100 cells.	142
5.6	Numerical result for density field of Sod's problem at $t = 0.25$ with 200 cells.	143
5.7	Numerical result for density field of Lax's problem at $t = 0.16$ with 200 cells.	144
5.8	Numerical result for density field of shock-turbulence interaction at $t = 1.8$ with 200 cells.	146
5.9	Numerical result for density field of two interacting blast waves at $t = 0.038$ with 400 cells.	147
5.10	Numerical result of 2D rotation of complex wave after one period with 100×100 cells. shown are initial profile (left panel) and numerical result (right panel).	149
5.11	Numerical result for pressure field of 2D explosion at $t = 0.25$ with 200×200 cells. Shown are bird's-eye view of pressure distribution (left panel) and cut-off profile along radial direction (right panel).	151
5.12	Same as Fig. 5.11, but for density field.	151
5.13	Numerical result for density field of the double Mach reflection at $t = 0.2$ with 120×384 cells.	152
5.14	Same as Fig. 5.13, but with 250×800 cells.	152
5.15	Enlarged view of vortex structures and instability along the slip lines of double Mach reflection at $t = 0.2$ with 120×384 cells (left panel) and 250×800 cells (right panel).	153
5.16	Density contours for the Mach 3 wind tunnel with a step at time of $t = 4$ on 160×480 cells. Thirty equally spaced contours are shown ranging from 0.1 to 6.4	153

5.17	Same as Fig.5.16, but with 320×960 cells.	154
6.1	The computational grid elements and related definitions. From left to right is triangular, quadrilateral, tetrahedral, hexahedral, prismatic and pyramidal element.	158
6.2	The two-dimensional moment arrangement on triangular(left) and quadrilateral(right) elements.	159
6.3	Solution for PV in 2D problems.	162
6.4	Solution for PV in 3D problems.	162
6.5	The bird's eye view of initial complex profile for the solid rotation test.	178
6.6	Same as Fig.6.5, but for the numerical results after one rotation on a grid of 57670 triangular elements with different reconstruction schemes, (a) MCV-MLP; (b) MCV-MLP-BVD.	178
6.7	The same as Fig.6.6 but on 25600 quadrilateral mesh	179
6.8	Cutaway cross-section views of different types unstructured grids for advection test.	179
6.9	(a) Initial profile plotted with the 0.5 isosurface. (b) The cross section of the hybrid 3D unstructured grids composed of 27000 hexahedrons, 5400 pyramids and 2545907 tetrahedrons.	181
6.10	Contour lines of the results after one revolution on the $x - z$ plane cutting through the center of the cubic cross. The computation is on 100×100 Cartesian grid. Displayed are the initial profile (a) , the result computed by the conventional finite volume method with MLP limiting scheme [34] (b) and the result computed by the proposed VPM-MLP-BVD scheme	182
6.11	The same as in Fig. 6.10 but on the hybrid unstructured grids as shown in Fig. 6.9.	182
6.12	The distribution of variable along the central line at $t = 0.5/\pi$ with cell sizes of $h = 1/80$	183
6.13	Computational grids for convergence test of Euler equations. From left to right: grid A, grid B, and grid C.	184
6.14	Numerical results of Sod problem. Bird view of density distribution (a), and the plot along the centerline(b).	186
6.15	The same as Fig.6.14 but with Lax problem	186
6.16	Numerical solutions calculated by the 3rd order WENO scheme [4] with a triangular element size of $1/160$ away from the corner but $1/320$ around the corner	188
6.17	Density contours for the Mach 3 wind tunnel with a forward step at time of $t = 4$ on a unstructured grid with triangular elements that have $1/80$ edge length along the lower domain boundary.	188
6.18	Same as Fig. 6.17, but with $1/160$ triangular grid elements.	189
6.19	Same as Fig. 6.17, but with $1/320$ triangular grid elements.	189
6.20	The bird's eye view of Fig. 6.19.	189
6.21	The cells marked by black color indicate the regions containing discontinuous solutions where the limiter comes into effect in the calculation of Fig.6.18.	190

6.22	Density contours of the double Mach reflection test at $t = 0.2$ on the grid of triangular elements of 1/120 resolutions.	190
6.23	Same as Fig. 6.22, but on the grid of 1/240 resolution.	190
6.24	Same as Fig. 6.22, but on the grid of 1/480 resolution.	191
6.25	Closed-up view around the double Mach stem for triangular grids of 1/120(a), 1/240(b) and 1/480(c) resolutions respectively.	192
6.26	Mach number contours for supersonic inlet flow in a steady state on 49816 triangular grid elements.	193
6.27	The images of density field of interaction of a shock wave with a wedge at different instants.	193
6.28	A comparison between the experimental result (a) and computational one (b) at $t=2.2$	194
6.29	The Mach number contours for supersonic bump flow at steady state on 158×78 quadrilateral elements (a), and the plot of the Mach number along the lower wall in comparison with the results from [215] (b).	195
6.30	Same as Fig. 6.29, but for transonic flow regime.	196
6.31	Same as Fig. 6.29, but for subsonic flow regime.	197
6.32	Bird's eye view of the density of the circular explosion test at $t = 0.00012$	198
6.33	Same as Fig.6.32, but for pressure.	198
6.34	Density field of numerical solution to the interaction between a shock wave and boundary layer at $t = 1.0$	199
6.35	Temperature fields of unstable oblique detonation waves with the MLP scheme on different grids resolution	200
6.36	The same as Fig.6.35 but with the high resolution scheme VPM-BVD	201
6.37	Temperature contours of the shock focusing problem with right-moving Mach 2.2 at different time	202
6.38	Temperature contours of the shock focusing problem with right-moving Mach 2.5 at different time	203
6.39	Numerical results for 3D explosion test on an unstructured grid of 1.1 million prismatic elements. Displayed are the 3D view of density field on two perpendicular cross-sections on the central $x - y$ plane (a) and the central $x - z$ plane.	204
6.40	The density distribution along the radius direction of the results computed separately on the prismatic grid and the hexahedral grid. We also include the result from published work [45] which uses denser hexahedral grid of 400^3	204
6.41	A view of the hybrid unstructured grid used for the computation of the shock-cone interaction test.	205
6.42	Density contour surfaces views from different angles. (a): front view where the refracted shock waves can be clearly seen, and (b): a zoomed side view where the vortex half ring shedded behind the half cone is well resolved.	206
6.43	Pressure contours over the upper wing surface for the transonic flow passing ONERA M6 wing.	206

6.44	Comparison of computed pressure coefficient with experimental data and the DG scheme at different semi-span locations denoted by the percentage of the distance from the root to the tip. The results calculated by proposed scheme are shown in green and red lines	207
6.45	Numerical results for the transonic flow past RAE 2822 wing and body. (a) Pressure contour on the upper surface of wings and body. (b) Pressure coefficients along upper and lower surfaces of the body.	207

List of Tables

2.1	Numerical errors and convergence rates of the 1D advection equation	43
3.1	Numerical errors and convergence rate for density propagation waves problem. Comparisons are made among different schemes.	76
4.1	Material quantities for copper ($k = 1$) and explosive ($k = 2$) in Cochran-Chan equation of state (4.22).	108
4.2	Comparison between WENO and MUSCL-THINC-BVD regarding to the elapse time for one dimensional tests	110
5.1	Numerical errors and convergence rates of the Euler equation for sinusoidal profile distribution	137
5.2	Numerical errors and convergence rates of the 1D inviscid Burgers' equation	141
5.3	Numerical errors and convergence rates of the 2D advection equation	148
6.1	The cutoff number \mathcal{S}_c of indicator function for different type of grid elements.	168
6.2	Numerical errors and convergence orders of the advection equation on quadrilateral and triangular grids.	174
6.3	Comparisons of L_1 error, order and computational cost estimation of different schemes for the advection equation on triangular grids	174
6.4	Numerical errors and convergence orders of the advection equation on quadrilateral and triangular grids.	174
6.5	Comparisons with WENO schemes about numerical errors and convergence rates of the advection equation on uniform triangular grids.	175
6.6	Element statistics of different types unstructured grids used for advection test.	175
6.7	Numerical accuracy and convergence rate study for advection test on hybrid unstructured grids.	179
6.8	Numerical errors and convergence rates of the inviscid Burgers' equation with the MCV-MLP-BVD scheme	184
6.9	Numerical errors and convergence rates of Euler equations on different grids	185

Abbreviations

CFD	Computation Fluid Dynamics
EOS	Equation of State
FVM	Finite Volume Method
FDM	Finite Difference Method
BVD	Boundary Variation Diminishing
LHR	Local High order Reconstruction
THINC	Tangent of Hyperbola for INterface Capturing
MUSCL	Monotone Upstream-centered Schemes for Conservation Law
DG	Discontinuous Galerkin
DOF	Degree of Freedom
SV	Spectral Volume
FR	Flux Reconstruction
PV	Point Value
CFL	Courant-Friedrich-Lewy
MMC-FR	Multi-moment Constrained Flux Reconstruction
CIP	Constrained Interpolation Profile
VIA	Volume-Integrated Average
TVD	Total Variation Diminishing
TV	Total Variation
TVB	Total Variation Bounded
WENO	Weighted Essentially Non-oscillatory

ENO	Essentially Non-oscillatory
HLL	Harten Lax vanLeer
HLLC	Harten Lax vanLeer Contact
SSP	Strong Stability Preserving
SSPRK	SSP Runge-Kutta
MLP	Multi-dimensional Limiting Process
VPM	Volume integrated average and Point value based Multi-moment
MCV	Multi-moment Constrained finite Volume
BGS	Boundary Gradient Switching

Chapter 1

Introduction

1.1 Background

The development of accurate and robust numerical models for compressible flows has been one of the most active research areas in CFD (computational fluid dynamics) community for past decades, which has been constantly driven by the great demand of applications from a broad engineering problems. Most of the real-case problems involve complex geometric configurations and complex flow structures including shock waves and vortices, such as those found in aeroacoustic and aerodynamics regarding the design of high-speed vehicles [1]. Over the past decades, tremendous efforts have been made to construct reliable numerical solvers with adequate accuracy for aerodynamic engineering.

The flow structures become more complicated when involving multi-components. For example, compressible multiphase fluid dynamics is one of active and challenging research areas of great importance in both theoretical studies and industrial applications. For example, shock/interface interactions are thought to be crucial to the instability and evolution of material interfaces that separate different fluids as observed in a wide spectrum of phenomena [95]. The material interfaces greatly complicate the physics

and make problems formidably difficult for analytical and experimental approaches in many cases, where numerical simulation turns out to be the most effective approach to provide quantitative information to elucidate the fundamental mechanisms behind the complex phenomena of multiphase flows.

Another important phenomenon in compressible multi-components flow is detonation waves. Detonation waves are supersonic combustion waves with strong leading shocks. Because of their potential for high propulsion efficiency in aeronautics and astronautics engineering, detonation engines have been attracting greater attention in recent years [151–154]. Three kinds of engines, namely, pulse-detonation, rotational-detonation, and oblique-detonation engines, are studied experimentally and numerically. In numerical research on detonation waves, the coupling of the shock and heat release reactions plays a vital role and needs to be simulated precisely.

One of main features in compressible multi-components flow which pose numerical difficulties is that flow structures usually contain discontinuities. For example, one of the main features of high speed compressible flows, which can be described by nonlinear hyperbolic conservation laws, is that discontinuous solution such as shock waves may appear in spite of smooth initial conditions. Other types of discontinuous structures, such as the contact discontinuities in convection-dominant flows and the material interfaces between different immiscible fluids, are also widely observed. These discontinuities play crucial roles in fluid dynamics, and have thus been extensively investigated [58, 95].

Having become a widely accepted mainstream methodology for compressible fluid dynamics which may involve shock waves and other discontinuities, finite volume methods (FVM) have got the overwhelming popularity in the related fields due to its rigorous numerical conservation. In addition to the conservativeness, other essential features that make a numerical solver appealing for real-case applications in engineering practice include at least, adaptivity and flexibility to complex geometric configurations, high-order

accuracy for both smooth and discontinuous solutions, robustness for all Mach numbers (or all speed) and computational efficiency. More importantly, any effort to investigate the fluid dynamics using numerical simulations, however, has to face challenges to obtain accurate and stable solutions around discontinuities. Thus to meet the demands mentioned above, it is necessary to construct a high-fidelity numerical model.

1.2 Control Equations

To describe compressible multi-components flow, control equations are constructed based on continuum assumption. Written in the form of Euler equations or extended Euler equation, the control equations used in the present paper are hyperbolic systems. The characteristics of hyperbolic system determine how to design numerical schemes.

1.2.1 Euler equations

The general form which describes the time-dependent inviscid compressible flow can be written in the following form

$$\frac{\partial \rho}{\partial t} + \nabla \cdot \mathbf{m} = 0, \quad (1.1)$$

$$\frac{\partial \mathbf{m}}{\partial t} + \nabla \cdot (\mathbf{m} \otimes \mathbf{u} + p) = 0, \quad (1.2)$$

$$\frac{\partial E}{\partial t} + \nabla \cdot (\mathbf{u}E + p\mathbf{u}) = 0, \quad (1.3)$$

where $\mathbf{m} = (m_x, m_y, m_z)$ is momentum per unit volume, $\mathbf{u} = \mathbf{m}/\rho = (u, v, w)$ the velocity, ρ the density and E the total energy per unit volume. The pressure of perfect gas is computed by the equation of state $p = (E - \rho \mathbf{u}^2/2)(\gamma - 1)$ where γ denotes the ratio of specific heats. The total enthalpy can be calculated by $H = (E + p)/\rho$.

1.2.2 Reacting Euler equations

The Euler equations, which describe the time-dependent flow of an inviscid compressible and reactive gas with only two chemical states in one space dimension, can be written in the form

$$\frac{\partial \mathbf{q}}{\partial t} + \frac{\partial f(\mathbf{q})}{\partial x} = \phi(\mathbf{q}), \quad (1.4)$$

where the vectors of physical variables \mathbf{q} , flux functions f , and source terms ϕ are

$$\begin{aligned} \mathbf{q} &= (\rho, \rho u, E, \rho\alpha)^T, \\ f &= (\rho u, \rho u u + p, E u + p u, \rho u \alpha)^T, \\ \phi &= (0, 0, 0, -K(T)\rho\alpha)^T, \end{aligned} \quad (1.5)$$

respectively. The dependent variables ρ , u , E and α are density, velocity component in the x direction, total energy, and mass fraction of unreacted gas, respectively. Also, p is the pressure, T the temperature, and K the chemical reaction rate. The pressure is given by

$$p = (\gamma - 1)\left(E - \frac{1}{2}\rho u^2 - q_0\rho\alpha\right), \quad (1.6)$$

where q_0 denotes the chemical heat release, and γ is the ratio of specific heats. The temperature is calculated using

$$T = \frac{p}{\rho}. \quad (1.7)$$

For the reactive Euler equations, the reaction rate is often modeled with Arrhenius kinetics [83] using the form

$$K(T) = K_0 e^{-\frac{T_{ign}}{T}}, \quad (1.8)$$

where K_0 is the reaction rate constant and T_{ign} is the ignition temperature. The reaction rate may also be replaced by Heaviside kinetics with

$$K(T) = -\frac{1}{\xi} H(T - T_{ign}), \quad (1.9)$$

where $H(x) = 1$ for $x \geq 0$, and $H(x) = 0$ for $x < 0$; ξ represents the reaction time. Generally, the aspects concerning stiffness become more severe with Heaviside kinetics.

1.2.3 Five equations model for compressible multiphase flow

To describe the compressible multiphase flow, several numerical model have been proposed. In the present work, the inviscid compressible two-component flows are formulated by the five-equation model developed in [114]. By assuming that the material interface is in equilibrium of mixed pressure and velocity, the five-equation model consists of two continuity equations for phasic mass, a momentum equation, an energy equation and an advection equation of volume fraction as follows

$$\begin{aligned}
\frac{\partial}{\partial t} (\alpha_1 \rho_1) + \nabla \cdot (\alpha_1 \rho_1 \mathbf{u}) &= 0, \\
\frac{\partial}{\partial t} (\alpha_2 \rho_2) + \nabla \cdot (\alpha_2 \rho_2 \mathbf{u}) &= 0, \\
\frac{\partial}{\partial t} (\rho \mathbf{u}) + \nabla \cdot (\rho \mathbf{u} \otimes \mathbf{u}) + \nabla p &= 0, \\
\frac{\partial E}{\partial t} + \nabla \cdot (E \mathbf{u} + p \mathbf{u}) &= 0, \\
\frac{\partial \alpha_1}{\partial t} + \mathbf{u} \cdot \nabla \alpha_1 &= 0,
\end{aligned} \tag{1.10}$$

where ρ_k and $\alpha_k \in [0, 1]$ denote in turn the k th phasic density and volume fraction for $k = 1, 2$, \mathbf{u} the vector of particle velocity, p the mixture pressure and E the total energy. When considering more than two-phases, the five-equation model can be extended by supplementing additional continuity equations and volume fraction advection equations for each new phase.

To close the system, the fluid of each phase is assumed to satisfy the Mie-Grüneisen equation of state,

$$p_k(\rho_k, e_k) = p_{\infty, k}(\rho_k) + \rho_k \Gamma_k(\rho_k) (e_k - e_{\infty, k}(\rho_k)), \tag{1.11}$$

where $\Gamma_k = (1/\rho_k)(\partial p_k/\partial e_k)|_{\rho_k}$ is the Grüneisen coefficient, and $p_{\infty,k}$, $e_{\infty,k}$ are the properly chosen states of the pressure and internal energy along some reference curves (e.g., along an isentrope or other empirically fitting curves) in order to match the experimental data of the examined material [134]. Usually, parameters Γ_k , $p_{\infty,k}$ and $e_{\infty,k}$ can be taken as functions only of the density. This equation of state can be employed to approximate a wide variety of materials including some gaseous or solid explosives and solid metals under high pressure.

The conservativeness constraints lead to the mixing formula for volume fraction, density and internal energy as follows,

$$\begin{aligned}\alpha_1 + \alpha_2 &= 1, \\ \alpha_1\rho_1 + \alpha_2\rho_2 &= \rho, \\ \alpha_1\rho_1e_1 + \alpha_2\rho_2e_2 &= \rho e.\end{aligned}\tag{1.12}$$

Derived in [113], the mixture Grüneisen coefficient, pressure p_{∞} and internal energy e_{∞} can be expressed as

$$\begin{aligned}\frac{\alpha_1}{\Gamma_1(\rho_1)} + \frac{\alpha_2}{\Gamma_2(\rho_2)} &= \frac{1}{\Gamma}, \\ \alpha_1\rho_1e_{\infty,1}(\rho_1) + \alpha_2\rho_2e_{\infty,2}(\rho_2) &= \rho e_{\infty}, \\ \alpha_1\frac{p_{\infty,1}(\rho_1)}{\Gamma_1(\rho_1)} + \alpha_2\frac{p_{\infty,2}(\rho_2)}{\Gamma_2(\rho_2)} &= \frac{p_{\infty}(\rho)}{\Gamma(\rho)},\end{aligned}\tag{1.13}$$

under the isobaric assumption. The mixture pressure is then calculated by

$$p = \left(\rho e - \sum_{k=1}^2 \alpha_k \rho_k e_{\infty,k}(\rho_k) + \sum_{k=1}^2 \alpha_k \frac{p_{\infty,k}(\rho_k)}{\Gamma_k(\rho_k)} \right) / \sum_{k=1}^2 \frac{\alpha_k}{\Gamma_k(\rho_k)}.\tag{1.14}$$

It should be noted that the mixing rules of Eq.(4.4) and Eq.(4.5) ensure that the mixed pressure is free of spurious oscillations across the material interfaces [107, 109, 111–113]. Following the five equations model under isobaric closure [114], the sound speed

of mixture could be calculated as the volumetric average of the phasic sound speeds as

$$c^2 = \alpha_1 c_1^2 + \alpha_2 c_2^2. \quad (1.15)$$

1.3 Finite volume method for hyperbolic system

Finite volume methods (FVM) have got the overwhelming popularity in the related fields due to its rigorous numerical conservation. Moreover, FVM can be applied to unstructured grid, which is not an easy work for methods such as finite difference method. Thus, in present work the high fidelity numerical solvers are developed in finite volume framework.

1.3.1 Finite volume method and finite volume wave propagation method

The 1D scalar conservation law in following form is used to introduce the finite volume method

$$\frac{\partial q}{\partial t} + \frac{\partial f(q)}{\partial x} = 0, \quad (1.16)$$

where $q(x, t)$ is the solution function and $f(q)$ is the flux function. We divide the computational domain into N non-overlapping cell elements, $\mathcal{I}_i : x \in [x_{i-1/2}, x_{i+1/2}]$, $i = 1, 2, \dots, N$, with a uniform grid spacing $\Delta x = x_{i+1/2} - x_{i-1/2}$. For a standard finite volume method, the volume-integrated average value $\bar{q}_i(t)$ in cell \mathcal{I}_i is defined as

$$\bar{q}_i(t) \approx \frac{1}{\Delta x} \int_{x_{i-1/2}}^{x_{i+1/2}} q(x, t) dx. \quad (1.17)$$

The semi-discrete version of Eq. (1.16) in the finite volume form can be expressed as a ordinary differential equations (ODEs)

$$\frac{\partial \bar{q}(t)}{\partial t} = -\frac{1}{\Delta x} (\tilde{f}_{i+1/2} - \tilde{f}_{i-1/2}), \quad (1.18)$$

where the numerical fluxes \tilde{f} at cell boundaries can be computed by a Riemann solver

$$\tilde{f}_{i+1/2} = f_{i+1/2}^{\text{Riemann}}(q_{i+1/2}^L, q_{i+1/2}^R) \quad (1.19)$$

if the reconstructed left-side value $q_{i+1/2}^L$ and right-side value $q_{i+1/2}^R$ at cell boundaries are provided. Essentially, the Riemann flux can be written in a canonical form as

$$f_{i+1/2}^{\text{Riemann}}(q_{i+1/2}^L, q_{i+1/2}^R) = \frac{1}{2} (f(q_{i+1/2}^L) + f(q_{i+1/2}^R)) - \frac{|a_{i+1/2}|}{2} (q_{i+1/2}^R - q_{i+1/2}^L), \quad (1.20)$$

where $a_{i+1/2}$ stands for the characteristic speed of the hyperbolic conservation law. The remaining main task is how to calculate $q_{i+1/2}^L$ and $q_{i+1/2}^R$ through the reconstruction process.

As one kind of finite volume method, finite volume wave propagation method is also popularly used. Compared to the classical finite-volume method, the model system which is a quasi-conservative system of equations can be approximated in a consistent and accurate manner with wave propagation method [132, 135, 136]. Denoting the spatial discretization operator for convection terms in (4.7) by $\mathcal{L}(\bar{q}(t))$ the semi-discrete version of the finite-volume formulation can also be expressed as a system of ordinary differential equations (ODEs)

$$\frac{\partial \bar{q}(t)}{\partial t} = \mathcal{L}(\bar{q}(t)). \quad (1.21)$$

In the wave-propagation method, the spatial discretization operator for the convection terms in a cell C_i is computed using

$$\mathcal{L}(\bar{q}_i(t)) = -\frac{1}{\Delta x} (\mathcal{A}^+ \Delta q_{i-1/2} + \mathcal{A}^- \Delta q_{i+1/2} + \mathcal{A} \Delta q_i), \quad (1.22)$$

where $\mathcal{A}^+ \Delta q_{i-1/2}$ and $\mathcal{A}^- \Delta q_{i+1/2}$, are the right- and left-moving fluctuations, respectively, which enter into the grid cell, and $\mathcal{A} \Delta q_i$ is the total fluctuation within C_i . We need to solve Riemann problems to determine these fluctuations. The right- and left-moving fluctuations can be calculated using

$$\mathcal{A}^\pm \Delta q_{i-1/2} = \sum_{k=1}^3 [s^k (q_{i-1/2}^L, q_{i-1/2}^R)]^\pm \mathcal{W}^k (q_{i-1/2}^L, q_{i-1/2}^R), \quad (1.23)$$

where moving speeds s^k and jumps \mathcal{W}^k ($k = 1, 2, 3$) of the three propagating discontinuities can be solved by Riemann solvers [72] given the reconstructed values $q_{i-1/2}^L$ and $q_{i-1/2}^R$, which are computed from the reconstruction functions $\tilde{q}_{i-1}(x)$ and $\tilde{q}_i(x)$ to the left and right of the cell edge $x_{i-1/2}$, respectively. As usual, the notations for the quantities s^\pm are set by $s^+ = \max(s, 0)$ and $s^- = \min(s, 0)$. Similarly, the total fluctuation can be determined using

$$\mathcal{A} \Delta q_i = \sum_{k=1}^3 [s^k (q_{i-1/2}^R, q_{i+1/2}^L)] \mathcal{W}^k (q_{i-1/2}^R, q_{i+1/2}^L). \quad (1.24)$$

Given the spatial discretization, time integration scheme can be used to solve ODE. For example, we can employ the three-stage third-order SSP (Strong Stability-Preserving) Runge-Kutta scheme [73]

$$\begin{aligned} \bar{q}^* &= \bar{q}^n + \Delta t \mathcal{L}(\bar{q}^n), \\ \bar{q}^{**} &= \frac{3}{4} \bar{q}^n + \frac{1}{4} \bar{q}^* + \frac{1}{4} \Delta t \mathcal{L}(\bar{q}^*), \\ \bar{q}^{n+1} &= \frac{1}{3} \bar{q}^n + \frac{2}{3} \bar{q}^* + \frac{2}{3} \Delta t \mathcal{L}(\bar{q}^{**}), \end{aligned} \quad (1.25)$$

to solve the time evolution ODEs, where \bar{q}^* and \bar{q}^{**} denote the intermediate values at the sub-steps.

1.3.2 Reconstruction processes

The procedure to calculate $q_{i+1/2}^L$ and $q_{i+1/2}^R$ is named as the reconstruction process. The modern finite volume method (FVM) for hyperbolic systems is developed based on Godunov scheme which assumes that (1) the flow variables within each computing elements are constant and (2) numerical fluxes are calculated from the solution of the Riemann problem. In original Godunov scheme, $q_{i+1/2}^L$ and $q_{i+1/2}^R$ is calculated with first order accuracy due to the assumption that flow variables within each computing elements are constant. The resultant scheme is usually called as first order upwind scheme. Although it is the most robust scheme, it suffers from excessive numerical dissipation. Thus extension to higher order scheme has been made over the decades.

However, to construct high order reconstruction scheme is not an easy work. Spatial reconstruction schemes using high-order-polynomial fashion interpolation functions have been extensively exploited in the past decades, see [49] for comprehensive and updated review on the developments in the fields. The polynomial-based high-order (PHO) reconstructions are highly demanded and show excellent performance in resolving numerical solutions which have relatively smooth variations in space, such as acoustic waves and vortices in compressible flow. However, when applied to strong discontinuities, the PHO reconstructions have to be projected to lower order or smoother polynomials (or more precisely rational functions in nonlinear schemes) to suppress numerical oscillations, which is called limiting projection. The limiting projection can be designed by following principles demanded from mathematical or physical perspectives and maximum-principle-satisfying. The PHO reconstructions with limiting projection might result in excessive numerical dissipation and tend to smear out the discontinuities

in numerical solution. Thus spatial reconstruction scheme using high order polynomial should be designed carefully to prevent numerical oscillations as well as reduce numerical dissipation.

For example, a large amount of work has been done to explore the possibilities of reconstruction schemes to pursue high accuracy with an essentially non-oscillatory behavior (ENO). TVD (Total Variation Diminishing) schemes, such as the MUSCL (Monotone Upstream-centered Schemes for Conservation Law) scheme, can resolve discontinuities without numerical oscillations by introducing slope or flux limiters. However, although TVD schemes can ensure the physical fields to be bounded and monotonic in the transition region, they typically suffer from excessive numerical dissipation.

To improve the general accuracy, high order WENO (Weighted Essentially Non-Oscillatory) schemes have been introduced in [2] and improved in [2] as well as many other works thereafter. Through assigning weights to different candidate stencils according to smoothness indicators, WENO schemes can substantially prevent numerical oscillations in the vicinity of discontinuity. However, it has been recognized in [60] that the original WENO scheme generates excessive numerical dissipation that tends to smear out contact discontinuities or jumps in variables across material interface. Since then numerous studies have been contributed to further improve the accuracy of WENO schemes. For example, a series of new smoothness indicators have been proposed in [50, 61–63] where contributions of the less smooth candidate stencils are optimized to reduce numerical dissipation. Other variants have also been devised to improve the performance of original WENO scheme. For example, in [64] numerical dissipation is reduced through employing central discretization. Combination of high order flux with a high order smooth indicator is designed to improve the accuracy around discontinuities in [65]. All these works conceptually follow the original WENO scheme and make use of polynomial interpolations.

Although the WENO-type schemes are proven to be a great success in computing

smooth solutions with the highest possible order of accuracy (in terms of convergence rate) while effectively suppressing numerical oscillations around discontinuous solutions, the intrinsic numerical dissipation still persists and pollutes the numerical solution in spite of the efforts aforementioned. Thus to construct a high-fidelity method, accurate and robust spatial reconstruction scheme is demanded. In present work, we will explore several possibilities to realize new accurate but robust spatial reconstruction schemes.

1.3.3 Riemann solvers

The modern finite volume method (FVM) for hyperbolic systems is developed based on Godunov scheme [12] which assumes that (1) the flow variables within each computing elements are constant and (2) numerical fluxes are calculated from the solution of the Riemann problem. Owing to its robustness and flexibility, Godunov approach has been further developed for decades, and is popularly applied to solve Euler equations for high speed compressible flows. One branch in the development is the construction of approximate Riemann solvers, or in another word, upwind fluxes. Different from the exact Riemann solver, the approximate algorithms are non-iterative and hence less expensive. Over the years, several upwind fluxes have been proposed, which can be generally categorized into flux vector splitting (FVS) and flux difference splitting (FDS) methods.

The FVS methods split flux vectors into upstream and downstream travelling informations. These methods are generally less complicated and better compatible with implicit methods. However, they are not effective in capturing the discontinuities represented by linear waves. Thus they are prone to intensively smear out contact surfaces and shear waves. Schemes such as the Steger-Warming and the FVS scheme of van Leer belong to this approach.

On the other hand, the FDS methods are constructed from approximate solution of local Riemann problem between two adjacent states. The FDS methods can be further

divided into two groups as complete or incomplete Riemann solvers. The complete solvers have the same wave structures as the exact Riemann solver. For Euler equations, the wave structures comprise a contact discontinuity and two nonlinear waves which corresponds to either a shock or a rarefaction wave. By virtue of comprising all wave components, the complete FDS methods are capable of capturing linear as well as nonlinear waves. This attractive quality makes complete Riemann solvers such as the Roe solver, the Osher solver and Harten, Lax and van Leer with Contact (HLLC) solver widely used. Incomplete Riemann solvers, however, employ coarser wave structures which do not include the contact discontinuity. Thus, they generally bring excessive dissipation across contact. The incomplete solvers include the HLL, the Harten Lax van Leer Einfeldt (HLLC) and the Rusanov solver.

Among these approximated Riemann solvers introduced above, HLLC method, which is less dissipative, is considered to be one of the most preferred FDS method because it can capture contact very accurately. Unfortunately, it may encounter a problem of numerical instability known as the carbuncle phenomenon. In fact, it has been known that Riemann solvers, which can resolve the contact and shear waves exactly, usually suffer from numerical instability in the vicinity of strong shock waves. On the other side, HLL, which is more dissipative due to its incomplete wave structures, is very robust. It has an entropy satisfaction property, exactly resolves isolated shock and preserves positivity although it is notorious that it cannot resolve contact discontinuities exactly. In present work, following Riemann solver will be used.

(I) Riemann solver1: SLAU

In comparison with its predecessor, i.e. AUSM schemes [206–208], SLAU reformulates flux function with Mach number being evaluated from a multi-dimensional fluid velocity which mitigates the anomalies caused by pure one-dimensional formulation particular for the case that shock is not aligned with the mesh. More importantly, it reduces the numerical dissipation in low Mach number regime and is free from reference

parameters, such as the cutoff Mach number, which makes it particularly suitable for constructing the all-speed solver in present work.

We recast the Euler equations of conservative form (1.1)-(1.3) into

$$Q \frac{\partial \mathbf{U}}{\partial t} + \nabla \cdot \mathcal{F}(\mathbf{U}) = 0 \quad (1.26)$$

where \mathbf{U} and $\mathcal{F}(\mathbf{U})$ represent the vectors of conservative variables and flux functions, i.e.

$$\mathbf{U} = [\rho, \mathbf{m}, E]^T, \quad (1.27)$$

$$\mathcal{F}(\mathbf{U}) = [\mathbf{m}, \mathbf{m} \otimes \mathbf{u} + p\mathbf{n}, \mathbf{u}(E + p)]^T. \quad (1.28)$$

Following the formulation of SLAU2[201], $\mathcal{F}(\mathbf{U})$ can be rewritten as

$$\mathcal{F}(\mathbf{U}) = \frac{m + |m|}{2} \Psi_L + \frac{m - |m|}{2} \Psi_R + \mathcal{P}\mathbf{N}, \quad (1.29)$$

with

$$\Psi = [1, u, v, H]^T, \quad \mathbf{N} = [1, n_x, n_y, 0]^T,$$

where subscripts L/R denote the left and right states of physical fields at the cell-interface and H stands for total enthalpy $H = (E + p)/\rho$. The mass flux m is

$$m = \frac{1}{2}\rho_L (V_L + |\bar{V}|^+) + \rho_R (V_R - |\bar{V}|^-) - \frac{\chi}{c}(p_R - p_L), \quad (1.30)$$

where $V = \mathbf{u} \cdot \mathbf{n}_{ij}$ stands for the velocity normal to cell boundary. Other quantities in Eq.(1.30) are computed as follows,

$$\begin{aligned} |\bar{V}|^+ &= (1 - g) |\bar{V}| + g |V_L|, \quad |\bar{V}|^- = (1 - g) |\bar{V}| + g |V_R|, \\ |\bar{V}| &= \frac{\rho_L |V_L| + \rho_R |V_R|}{\rho_L + \rho_R}, \quad \chi = \left(1 - \widehat{M}\right)^2, \quad \bar{c} = \frac{c_L + c_R}{2} \\ \widehat{M} &= \min \left(1.0, \frac{1}{\bar{c}} \sqrt{\frac{|\mathbf{u}_L|^2 + |\mathbf{u}_R|^2}{2}}\right), \quad M_{L/R} = V_{L/R} / \bar{c}, \\ g &= -\max[\min(M_L, 0), -1] \cdot \min[\max(M_R, 0), -1]. \end{aligned}$$

Similarly, the pressure flux \mathcal{P} is computed by

$$\mathcal{P} = \frac{p_L + p_R}{2} + \frac{f_p^+ - f_p^-}{2} (p_L - p_R) + \sqrt{\frac{|\mathbf{u}_L|^2 + |\mathbf{u}_R|^2}{2}} (f_p^+ + f_p^- - 1) \bar{\rho} \bar{c}, \quad (1.31)$$

with

$$f_p^\pm = \begin{cases} \frac{1}{2} (1 \pm \text{sign}(M)), & \text{if } |M| \geq 1 \\ \frac{1}{4} (M \pm 1)^2 (2 \mp M), & \text{otherwise} \end{cases}, \quad \bar{\rho} = \frac{\rho_L + \rho_R}{2}.$$

It is noted that there are no user-specified parameters involved throughout the formulation.

(II) Riemann solver2: Roe

The numerical fluxes across surface segment Γ_{ij} can be also expressed in the form of $\mathbf{F}_{ij}(\mathbf{U}) = \mathbf{A}\mathbf{U}_{ij}$ where $\mathbf{A} = \partial\mathbf{F}/\partial\mathbf{U}$ is the Jacobian matrix, which is computed by using the integrated average of conservative variables \mathbf{U} in the neighboring cell sharing the boundary Γ_{ij} .

Decomposing the Jacobian matrix into an eigensystem of $A = R\Lambda L$, where R/L denotes the matrix of right/left eigenvectors and Λ the corresponding eigenvalues, we

solve (6.13) by

$$\frac{\partial \bar{\mathbf{U}}_i}{\partial t} = - \sum_{j=1}^{j=J} (A (\mathbf{U}_{ij}^+ + \mathbf{U}_{ij}^-) + R |\Lambda| L (\mathbf{U}_{ij}^+ - \mathbf{U}_{ij}^-)) |\Gamma_{ij}| \quad (1.32)$$

where \mathbf{U}_{ij}^\pm denotes the integrated averages on left-side and right-side of boundary Γ_{ij} respectively. It is noteworthy that all the values in the eigensystem are computed by Roe-averaging approximation with two adjacent VIAs. The complete structure of eigensystem on unstructured grids has been detailed in [32].

For 2D structured grids, the eigensystem can be calculated as The Jacobian matrix \mathbf{A} corresponding to flux $\mathbf{F}(\mathbf{U})$ is defined by

$$\mathbf{A} = \begin{pmatrix} 0 & 1 & 0 & 0 \\ -u^2 + (\gamma - 1)\mathbf{V} & -(\gamma - 3)u & -(\gamma - 1)v & (\gamma - 1) \\ -uv & v & u & 0 \\ u(\mathbf{V}(\gamma - 1) - H) & H - u^2(\gamma - 1) & -(\gamma - 1)uv & \gamma u \end{pmatrix}, \quad (1.33)$$

where

$$\begin{aligned} \mathbf{V} &= \frac{1}{2}(u^2 + v^2), \\ H &= \frac{P + E}{\rho}. \end{aligned} \quad (1.34)$$

The eigenvalues of Jacobian matrix \mathbf{A} are

$$\lambda_1 = u - a, \quad \lambda_2 = u, \quad \lambda_3 = u, \quad \lambda_4 = u + a, \quad (1.35)$$

where a is the sound speed. For ideal gases EOS, the sound speed a and total enthalpy H can be calculated by

$$\begin{aligned} a &= \sqrt{\frac{\gamma P}{\rho}}, \\ H &= \frac{a^2}{\gamma - 1} + \mathbf{V}. \end{aligned} \quad (1.36)$$

The corresponding right eigenvectors are given by

$$\mathbf{R}^x = \begin{pmatrix} 1 & 0 & 1 & 1 \\ u - a & 0 & u & u + a \\ v & 1 & v & v \\ H - ua & v & \mathbf{V} & H + ua \end{pmatrix}, \quad (1.37)$$

where each column of the matrix \mathbf{R}^x is corresponding to each right eigenvector. And the left eigenvectors are given by

$$\mathbf{L}^x = \begin{pmatrix} \frac{1}{2}(\gamma - 1)\frac{\mathbf{V}}{a^2} + \frac{u}{2a} & -\frac{1}{2}\left(\frac{u(\gamma - 1)}{a^2} + \frac{1}{a}\right) & -\frac{v(\gamma - 1)}{2a^2} & \frac{(\gamma - 1)}{2a^2} \\ -v & 0 & 1 & 0 \\ 1 - (\gamma - 1)\frac{\mathbf{V}}{a^2} & (\gamma - 1)\frac{u}{a^2} & (\gamma - 1)\frac{v}{a^2} & -\frac{(\gamma - 1)}{a^2} \\ \frac{1}{2}(\gamma - 1)\frac{\mathbf{V}}{a^2} - \frac{u}{2a} & -\frac{1}{2}\left(\frac{u(\gamma - 1)}{a^2} - \frac{1}{a}\right) & -\frac{v(\gamma - 1)}{2a^2} & \frac{(\gamma - 1)}{2a^2} \end{pmatrix}, \quad (1.38)$$

where each row of the matrix \mathbf{L}^x is corresponding to each left eigenvector.

(III) Riemann solver3: HLL-type

By assuming a two wave system, the HLL Riemann solver calculates numerical fluxes as

$$\mathbf{F}_{i+\frac{1}{2}}^{hll} = \begin{cases} \mathbf{F}_{\mathbf{L}} & \text{if } 0 \leq S_L, \\ \mathbf{F}^{hll} & \text{if } S_L \leq 0 \leq S_R, \\ \mathbf{F}_{\mathbf{R}} & \text{if } 0 \geq S_R, \end{cases} \quad (1.39)$$

where S_L is the smallest wave speed and S_R is the largest wave speed. The subscripts \mathbf{L} and \mathbf{R} imply the left and right values at the cell interface. The wave speed can be estimated by different formulations. In the present work, we use the simple estimation

proposed according to [13]

$$S_L = \min(u_L - c_L, u_R - c_R), \quad S_R = \min(u_L + c_L, u_R + c_R), \quad (1.40)$$

where c_L and c_R are sound speed calculated at the cell interface. This estimation can be applied directly in problems with complex equation of state. The HLL Riemann solver assumes that between the slowest and fastest waves there is only a single constant intermediate state vector \mathbf{U}^{hll} calculated by

$$\mathbf{U}^{hll} = \frac{S_R \mathbf{U}_R - S_L \mathbf{U}_L + \mathbf{F}_L - \mathbf{F}_R}{S_R - S_L}, \quad (1.41)$$

Then the corresponding HLL numerical flux \mathbf{F}^{hll} can be found as

$$\mathbf{F}^{hll} = \frac{S_R \mathbf{F}_L - S_L \mathbf{F}_R + S_L S_R (\mathbf{U}_R - \mathbf{U}_L)}{S_R - S_L}. \quad (1.42)$$

The above HLL numerical flux can be also written as a central difference term with the numerical diffusion as

$$\mathbf{F}^{hll} = \frac{1}{2}(\mathbf{F}_L + \mathbf{F}_R) + \varepsilon, \quad (1.43)$$

(III) Riemann solver4: HLLC

Assuming three wave structure with wave speed estimate S_L, S^*, S_R the flux is given by

$$\mathbf{F}^{\text{HLLC}} = \begin{cases} \mathbf{F}_L, & 0 \leq S_L \\ \mathbf{F}_{*L} = \mathbf{F}_L + S_L(\hat{\mathbf{U}}_{*L} - \mathbf{U}_L), & S_L \leq 0 \leq S_* \\ \mathbf{F}_{*R} = \mathbf{F}_R + S_R(\mathbf{U}_{*R} - \mathbf{U}_R), & S_* \leq 0 \leq S_R \\ \mathbf{F}_R \end{cases} \quad (1.44)$$

where state $U_{\star L/R}$ can be calculated as following

$$U_{\star k} = \rho_k \left(\frac{S_k - u_k}{S_k - S_\star} \right) \begin{pmatrix} 1 \\ S_\star \\ v_k \\ w_k \\ \frac{E_k}{\rho_k} (S_\star - u_k) \left[S_\star + \frac{p_k}{\rho_k (S_k - u_k)} \right] \end{pmatrix} \quad (1.45)$$

where $k = L$ or $k = R$. The wave speed can be estimated by pressure-velocity estimation method .

1.4 Local high order reconstruction (LHR) method

Conventional finite volume method are facing with difficulties when going to higher than second order. One of issues is numerical oscillation mentioned before. Another is that it's not straightforward to increase order on unstructured grids. Constructing a spatial discretization higher than second order on unstructured grids is not a trivial task for conventional finite volume formulation where only the volume-integrated average (VIA) for each grid cell is the degree of freedom (DOF) available for reconstruction. As a result, any interpolation higher than second order requires a wide stencil which may not be uniquely determined[174, 187].

1.4.1 Review of local high order reconstruction method

To get around the difficulties of conventional FVM in generating high-order schemes on unstructured grids, another approach that makes use of local high-order reconstruction (LHR) has been explored as well. LHR type methods create high-order reconstruction within each cell by locally increasing degree of freedoms (DOFs) as new prognostic

variables. The local DOFs are connected through basis functions and thus have well-defined data structures. Being the representative approach of this sort, the discontinuous Galerkin (DG) method [188, 189], as well as other local high reconstruction (LHR) methods enjoys the local data regularity and more rapid (spectral) convergence as summarized in [190]. Flux reconstruction (FR) [17] or its extension to unstructured grids [18], known latter as lifting collocation penalty (LCP) and correction procedure via reconstruction (CPR), provides a more general framework that unifies nearly all existing nodal type LHR methods that leave the reconstructed field discontinuous across cell boundaries where the numerical fluxes are required as in the conventional finite volume formulation.

Falling between conventional FVM and aforementioned LHR-based methods, other numerical formulations have been also proposed in recent years, such as the multi-moment finite volume method (MM-FVM) [22, 191–196] and discontinuous Galerkin / finite volume (DG/FV) method [14, 15]. These methods make use of multiple DOFs for each grid cell as the computational variables, but allow the spatial reconstructions being carried out over the target cell and its immediate neighbors in a more flexible and efficient manner. As a practical variant of MM-FVM, we have recently devised the multi-moment constrained finite volume method with solution points at center and vertices (MCV-SPCV) [28] on hybrid unstructured grids of arbitrary elements, which realizes 3rd order accuracy within a compact stencil including only adjacent neighboring cells. In the MCV-SPCV formulation, both the point value at cell center (PVC) and point values at cell vertices (PVV) are treated as the computational variables updated at each time step. The PVC is updated by an evolution equation derived from the finite volume formulation of flux form that guarantees the conservation of the VIA, while the PVV is computed from a prognostic equation of differential form where the spatial derivative terms can be directly obtained from the MCV reconstructions

1.4.2 Limiting processes of LHR

Devising a limiting projection in the presence of discontinuous solutions for LHR schemes still remains a problem not fully resolved. Despite some existing strategies such as using weighted essentially non-oscillatory (WENO) scheme/limiter [19, 20] or adding artificial viscosity [21], efforts are still required to make the LHR methods to provide reliable solutions to discontinuities.

Belong to the LHR family, the high order MCV method also need careful-designed limiting processes. According to well-known Godunov barrier for linear schemes, any monotonic linear scheme can be of only first order. As a result, the high-order MCV schemes will produce the non-physical oscillations while simulating the compressible flows, even for those cases with the smooth initial conditions where discontinuity will appear due to the nonlinearity of the governing equations. Several strategies have been employed by the local high-order schemes to suppress the numerical oscillations in the vicinity of discontinuities in the existing literature. One of the popular strategies is non-linear limiting projection. Earlier studies such as in [5] for DG method and in [192] for MCV method use the total variation bounded (TVB) limiters, where the TVB criterion is needed to find the “troubled cells” by evaluating the smoothness of the solution. For the troubled cells, where discontinuous solutions are detected, the total variation diminishing (TVD) limiting procedure is applied. As the TVD limiting has second-order accuracy at most, it tends to introduce too much extra numerical dissipation and degrades the high-order accuracy of the original schemes. The higher order limited reconstructions, such as the essentially non-oscillatory (ENO) and weighted essentially non-oscillatory (WENO) [2] reconstructions, are applied in [5] for DG method and in [195] for MCV method. The WENO limiter effectively reduces the numerical dissipation errors around smooth region and can retain the high-order convergence. However, the current implementations of the WENO limiting in the high-order schemes with local reconstructions cannot make the full use of the local DOFs, and the solutions are

heavily dependent on the TVB criterion that determines the “troubled cells” in an ad hoc fashion. This is one of the key issues to be solved for developing numerical models for practical applications using local high-order schemes.

1.5 Current issues for simulation of compressible multi-components flow

1.5.1 Numerical difficulties for detonation waves

Standard shock-capturing schemes, which resolve discontinuous solutions without numerical oscillations by introducing extra dissipative errors, have achieved by far the greater success when dealing with non-reacting inviscid compressible flow (Euler equations). However, problems may arise when applying shock-capturing schemes to the reactive Euler equation system, which is a non-homogeneous system with source terms that account for the effects of reactions. When time scales of the chemical reactions are significantly shorter than the hydrodynamic time scales, numerical stiffness appears and introduces problems. To deal with such stiff hyperbolic systems, standard shock-capturing schemes need greater grid resolution, usually overwhelming the available computational resources. Insufficient grid resolution may produce an incorrect propagation speed of the discontinuities and non-physical spurious waves even with enough temporal resolution. Because of numerical dissipations around discontinuities in shock-capturing scheme, the chemical reaction may be triggered too early in an adjacent cell of the discontinuity if a numerically smeared-out temperature profile contains values above the ignition temperature. If the reaction is fast, early triggered chemical reactions shift the discontinuity and thereby produce non-physical spurious waves, as first reported in [155].

During the past two decades, spurious phenomena in simulating stiff hyperbolic system have been investigated in several studies [68, 69, 80, 81, 156, 157, 160]. Various strategies have been proposed to obtain the correct wave propagation speed. One main strategy is to reduce the numerical dissipation using a ghost fluid/level set and front tracking methods [156, 159, 160], or locally resolving the detonation wave with a large number of adaptively placed grid cells [158]. Another advanced strategy is to revise the reaction step by accepting the smeared-out discontinuous profile. A temperature extrapolation method, which constructs a first or second extrapolation from a few grid cells ahead of the shock to obtain the temperature was proposed in [161]. Nevertheless, finding the temperature in front of the wave is non-trivial, especially in higher spatial dimensions [160]. Instead of extrapolating temperature from the cells in front of shock, the method in which a projection is performed to make the ignition temperature random during reaction step was proposed in [80, 84, 162]. This method achieves success in both one- and two-dimensional tests, although the assumption of a priori stiff source term prevents its use for non-stiff problems. To deal with both types, a fractional-step algorithm termed the MinMax scheme was proposed in [81]. Based on two-valued variable reconstruction in each cell, appropriate maximum and minimum values of the unknown are believed to deal with the under-resolved calculations for stiff-source conditions, but only one-dimensional tests were conducted in the work. In recent work [68], the high-order shock-capturing WENO (Weighted Essentially Non-Oscillatory) scheme was used to update the convection step. During the reaction step, the transition diffused points produced by the convection step are first identified, and then the flow variables at these points are extrapolated by a reconstructed polynomial using the subcell resolution method. Although this method can capture the correct location, extra steps, for example, to solve the shock location, is unavoidable and more importantly, the detonation front remains diffuse as existing shock-capturing schemes, despite their high order, introduce excessive numerical diffusion errors around discontinuities.

As studied in [69], the degree of the discrepancy in the propagation speed of discontinuities is highly dependent on how shock-capturing schemes spread the discontinuities. The fundamental reason behind this spurious phenomenon is that shock-capturing schemes introduce excessive numerical dissipation errors around discontinuities.

Even to simulate non-stiff detonation phenomena, a mature numerical model should at least meet following two requirements: 1). ability to resolve complex solution structures involved in detonation waves with reasonable computational cost. 2. adaptive to complex geometries which are common in engineering industry. To overcome numerical dissipation which will diffuse complex solution structures, several works [164–166] apply high order Weighted Essentially Non-oscillation Schemes (WENO) and WENO to simulate detonation waves. To further improve the ability to resolve flow structures, Mapped WENO-Z scheme was proposed by [167], in which a tangent domain mapping is used to cluster grid points near the detonation front. In [168], WENO scheme was combined with Adaptive Mesh Refinement (AMR), so called AMR-WENO method, to simulate multi-dimensional detonation with high resolution. Although these works provide high quality solution to detonation simulation and serve as an effective tool to investigate detonation phenomena, they are far from engineering application where complex boundaries cannot be aligned with the grid lines of a regular grids. To deal with irregular boundaries but to keep Cartesian grids in interior cells, which is not a trivial work since additional errors from careless treatment about irregular boundaries will pollute results, several major efforts including inverse Lax-Wendroff (ILW) boundary treatment [169, 170] and cut-cell method [171] have been devised to simulate detonation with irregular boundaries.

Compared with these treatment about irregular boundaries, unstructured mesh has advantages such as easy mesh adaptation and highly flexibility to very complicated configurations [172, 173]. However, as stated in [173], the reason that unstructured grids is not popular in detonation simulation is that implementation of high order finite volume method (FVM) on unstructured grids requires a wide stencil which may not be

uniquely determined [174]. Thus generally speaking, high order FVMs based on unstructured grids are less efficient than those based on structured grids. In view of this, several works [175] extended discontinuous Galerkin (DG) methods, which create high-order reconstruction by locally increasing degrees of freedom (DOFs) as new prognostic variables, to detonation simulation. However, as far as the author know, the work that implements DG on unstructured for detonation simulation is few, of which reason may be that devising a limiting projection in the presence of discontinuous solutions for such scheme still remains as a problem not fully resolved.

1.5.2 Numerical difficulties for moving interface flows

In comparison to the computation of single phase flow, development of numerical methods for multiphase flow faces more challenging tasks. The major complexity comes from the moving interfaces between different fluids that usually associate with strong discontinuities, singular forces and phase changes in some cases. Given the numerical methods developed for multiphase incompressible flows with interfaces having been reaching a relatively mature stage, the numerical solvers for compressible interfacial multiphase flows are apparently insufficient. For incompressible multiphase flows with moving interfaces where the density and other physical properties, e.g. viscosity and thermal conductivity, are constant in each fluid, the one-fluid model [94] can be implemented in a straightforward manner with an assumption that the physical fields change monotonically across the interface region. Thus, provided with an indication function which identifies the moving interface, one can uniquely determine the physical property fields for the whole computational domain. Some indication functions, such as volume of fluid (VOF) function [96–98] and level set function [99–101], have been proposed and proved to be able to capture moving interfaces with compact thickness and geometrical faithfulness if solved by advanced numerical algorithms. However, substantial barrier exists when implementing the one-fluid model to compressible interfacial multiphase flows.

The new difficulties we face when applying the one-fluid model ¹ to compressible interfacial multiphase flows lie in two aspects:

- (I) Density and energy in compressible flow have to be solved along with the indication function, and special formulations are required to maintain the physical consistency which results in a balanced state among all variables for the interface cell where a well-defined interface falls in;
- (II) The numerical dissipation in the so-called high-resolution schemes designed for solving single phase compressible flows involving shock waves tends to smear out discontinuities including the material interfaces in numerical solutions, which is fatal to simulations of interfacial multiphase flows even if the schemes can produce acceptable results in single phase cases.

For issue (I) mentioned above, mixing or averaging models that consist of Euler or Navier-Stokes equations along with the equations of interface-indication functions have been derived and widely used as an efficient approximation to the state of the interface cell where two or more species co-exist. A simple single-fluid model was reported in [102, 103, 197] for interfacial multiphase compressible flows using either explicit time marching or semi-implicit pressure-projection solution procedure. The latter results in a unified formulation for solving both compressible and incompressible multiphase flows. As the primitive variables are solved in these models, the conservation properties are not guaranteed, and thus might not be suitable for high-Mach flows involving shock waves. Conservative formulations, which have been well-established for single phase compressible flows with shock waves, however may lead to spurious oscillations in pressure or other thermal fields [105, 106]. It was found that special treatments are required in transporting the material interface and mixing/averaging the state variables to find the mixed state of fluids in the interfacial cell that satisfies pressure balance across

¹More precisely, it should be called single-state model or single-equivalent-fluid (SEF) model[114]. We call such model SEF in the present paper.

material interface for multiple polytropic and stiff gases [107–111], van der Waals [112] and Mie-Grüneisen equations of state (EOS) [113]. A more general five-equation model [114] was developed for a wide range fluids. These models apply to multiphase compressible flows with either spread or sharp interfaces. See [115] for a recent review on the models of this sort. We make use of the five-equation model in the present work as the PDE (partial differential equation) set to develop our numerical method, which can be applied to other extended system as well.

Provided the SEF models with some desired properties, such as hyperbolicity, conservation and well-balanced mixing closure without spurious oscillations in thermal variables, we can in principle implement numerical methods for single phase compressible flow (e.g. the standard shock-capturing schemes) to solve these multiphase models. TVD (Total Variation Diminishing) schemes, such as the MUSCL (Monotone Upstream-centered Schemes for Conservation Law) scheme, can solve discontinuities without numerical oscillations, which is of paramount importance to ensure the physical fields to be bounded and monotonic in the transition region. However, TVD schemes suffer from excessive numerical dissipation, which brings the problem (II) listed above to us. The intrinsic numerical dissipation smears out the flow structures including the discontinuities in mass fraction or volume fraction which is used to represent the material interfaces. Consequently, material interfaces are continuously blurred and smeared out, which is not acceptable in many applications, especially for the simulations that need long-term computation. As a remedy, using higher order schemes, like WENO (Weighted Essentially Non-Oscillatory) scheme, to solve compressible multiphase flows is also found in the literature [116, 117], where numerical dissipation is largely reduced, and the moving interfaces, as well as other flow structures, can be resolved with significantly improved accuracy. However, implementing high order schemes might generate numerical oscillations for compressible multiphase flows with complex EOS as discussed in [116], where even though the reconstructions were carried out in terms of the characteristic variables to reduce numerical oscillation,

spurious disturbances are still observed when waves are reflected from the material interface. In a more recent work [118], an intermediate state was introduced at each cell edge in characteristic decomposition to suppress numerical oscillations and stabilize computation. Furthermore, high order monotonicity-preserving scheme [119] was used to ensure the bounded value for volume fraction. It is noted that numerical dissipation even reduced in WENO and other high-order schemes still remains in conventional Eulerian advection schemes, which might be problematic in long-term simulations. In general, the implementation of high order shock capturing schemes to interfacial compressible multiphase flows demands further investigations.

There are different numerical methods to identify and compute moving interfaces in compressible multiphase flows, such as [120–122] on moving meshes and [123–127] on fixed meshes. As aforementioned, the VOF-type methods that use the volume fraction or mass fraction as the identification function of moving interface have been popularly used as well, which are referred to as interface-capturing methods in our context. Interface-capturing methods resolve the interfaces on fixed Eulerian grids and use advection schemes to transport the volume/mass fraction functions. It is well known that conventional Eulerian advection schemes have intrinsic numerical dissipation and tend to smear out the jumps in volume fraction or mass fraction functions which are used to identify the material interfaces between different fluids. In order to keep the compact thickness of material interfaces during computation, special numerical techniques are needed to steepen the jumps in the volume or mass fraction fields. For example, in [66, 128, 129] the advection equation of the interface function is treated by artificial compression method. As a post-processing approach, anti-diffusion techniques have also been introduced in [130] and [131]. An alternative approach is to reconstruct the volume fraction under the finite volume framework by using special functions. The THINC (Tangent of Hyperbola for INterface Capturing) method, for example, uses the hyperbolic tangent function [56] to capture the jumps in volume fraction. By virtue of

the desirable characteristics of the hyperbolic tangent function in mimicking the jump-like profile of the volume fraction field, the sharp interface can be accurately captured in a simple and efficient way [118, 132]. However, when applying interface-sharpening methods to the SEF models of multiphase compressible flows, velocity and pressure oscillations may occur across the interface [66, 129, 131–133] due to the inconsistency between the physical variables and the volume fraction field with sharpened or compressed jumps. As stated in [66, 129], in contrast to incompressible flows where the densities of fluids are fixed, artificial interface-sharpening scheme cannot be applied alone to volume fraction function in compressible multiphase flows. Modifications to other physical variables have to be made to maintain the consistency among the sharpened volume fraction and other physical fields [66, 129, 131, 133]. In [132], a homogeneous reconstruction has been proposed where the reconstructed volume fraction is used to extrapolate the remaining conservative variables across the interface to ensure the mechanical consistency across the isolated material interfaces.

1.6 Purposes of current research

In this work, new high fidelity numerical methods for compressible multi-components flow will be proposed and validated through wide numerical tests. To achieve high fidelity, the proposed numerical methods should at least have following characteristics.

1. The new method should be able to solve both smooth and discontinuous solutions. Especially, the current research will propose several strategies to deal with discontinuous solutions which is a long-lasting issue for most existing numerical schemes.
2. The high fidelity will be realized by minimizing numerical dissipation errors which are main sources of smearing flow structures. Thus, we will propose new reconstruction principles with which the reconstruction scheme can be constructed to solve both smooth and discontinuous solutions accurately.

3. In order to increase the accuracy of schemes especially on unstructured grids, local high order reconstruction method will be explored. We will first design new limiting processes to suppress numerical oscillations introduced by high order interpolation. Then schemes will be extended to hybrid unstructured grids.
4. The new proposed schemes will be applied to simulate compressible multi-components flow. The high fidelity property will be validated through numerical tests. Especially, we want to solve the issues in stiff detonation waves and shock-interface interaction problems, which are very challenging for most existing methods.

1.7 Outline of the thesis

The remainder of the thesis is organized as follows. In Chapter 2, we firstly propose the boundary variation diminishing (BVD) algorithm which serves as a new guideline for reconstruction processes. The main idea of BVD algorithm is to minimize the numerical dissipation errors. Under this principle, several effective implementation of BVD algorithms have been designed and tested. With these implementation of BVD algorithm, a series of schemes can be formulated. We call the reconstruction processes under the BVD algorithm as the BVD admissible reconstruction processes. One example is to combine high order polynomial with non-polynomial function. Due to BVD algorithm which minimizes the numerical dissipation errors, high order polynomial should be preferred in smooth region while non-polynomial function will be applied in critical region. The successful implementation of BVD algorithm is validated in this chapter.

In Chapter 3, we present two practical schemes with BVD algorithm. One is called MUSCL-THINC-BVD scheme. Another is a novel limiting-free discontinuities capturing scheme. Different from long-lasting reconstruction processes which employ high order polynomials enforced with some carefully designed limiting projections to seek stable solutions around discontinuities, the current discretized scheme employs

non-polynomial THINC (Tangent of Hyperbola for INterface Capturing) functions with adaptive sharpness to solve both smooth and discontinuous solutions. Due to the essentially monotone and bounded properties of THINC function, difficulties to solve sharp discontinuous solutions and complexities associated with designing limiting projections can be prevented. Verified through numerical tests, the present method is able to capture both smooth and discontinuous solutions in Euler equations for compressible gas dynamics with excellent solution quality competitive to other existing schemes. More profoundly, it provides an accurate and reliable solver for a class of reactive compressible gas flows with stiff source terms, such as the gaseous detonation waves, which are quite challenging to other high-resolution schemes. The stiff C-J detonation benchmark test reveals that the adaptive THINC-BVD scheme can accurately capture the reacting front of the gaseous detonation, while the WENO scheme with the same grid resolution generates unacceptable results. Compared with other methods, which by accepting smeared-out discontinuities profiles require extra treatments, the current method obtains the correct but also sharp detonation front by fundamentally reducing numerical dissipation errors in shock-capturing schemes. Owing also to its algorithmic simplicity, the proposed method can become as a practical and promising numerical solver for compressible gas dynamics, particularly for simulations involving strong discontinuities and reacting fronts with stiff source term.

In Chapter 4, we apply the MUSCL-THINC-BVD scheme to solve the five-equation model for interfacial two phase flows. This scheme employs the traditional shock capturing MUSCL (Monotone Upstream-centered Schemes for Conservation Law) scheme as well as the interface sharpening THINC (Tangent of Hyperbola for INterface Capturing) scheme as two building-blocks of spatial reconstruction on the BVD principle that minimizes the variations (jumps) of the reconstructed variables at cell boundaries, and thus effectively reduces the dissipation error in numerical solutions. The MUSCL-THINC-BVD scheme is implemented to the volume fraction and other state variables under the same finite volume framework, which realizes the consistency among volume

fraction and other physical variables. Numerical results of benchmark tests show that the present method is able to capture the material interface as a well-defined sharp jump in volume fraction, and obtain numerical solutions of superior quality in comparison to other existing methods. The proposed scheme is a simple and effective method of practical significance for simulating compressible interfacial multiphase flows.

In Chapter 5, we extend our schemes to high order in the local high order reconstruction framework. We propose a new formulation for high-order multi-moment constrained finite volume (MCV) method. In the one-dimensional building-block scheme, three local Degrees of Freedom (DOFs) are equidistantly defined within a grid cell. Two candidate polynomials for spatial reconstruction of third-order are built by adopting one additional constraint condition from the adjacent cells, i.e. the DOF at middle point of left or right neighbour. A boundary gradient switching (BGS) algorithm based on the variation-minimization principle is devised to determine the spatial reconstruction from the two candidates, so as to remove the spurious oscillations around the discontinuities. The resulted non-oscillatory MCV3-BGS scheme is of fourth-order accuracy and completely free of case-dependent ad hoc parameters. The widely used benchmark tests of one- and two-dimensional scalar and Euler hyperbolic conservation laws are solved to verify the performance of the proposed scheme in this paper. The MCV3-BGS scheme is very promising for the practical applications due to its accuracy, non-oscillatory feature and algorithmic simplicity.

In Chapter 6, we will introduce a novel numerical model for Euler equations on 2D unstructured grids and 3D hybrid unstructured grids including tetrahedral, hexahedral, prismatic and pyramidal elements. The model integrates the VPM (Volume integrated average and Point value based Multi-moment) spatial discretization scheme, the limiting projection with BVD manipulation and the Roe Riemann solver for unstructured grids. Distinguished from conventional finite volume method, both the volume-integrated average (VIA) and the point values (PV) at the cell vertices are memorized as prognostic variables and updated in time simultaneously. The VIA is computed by a finite volume

formulation of flux form while the PV is point-wisely updated using the differential formulation, where the Roe solver is used to compute both conventional and differential Riemann problems. A special technique is introduced to the limiting projection that effectively suppresses both numerical oscillation and dissipation. The resulting numerical model provides remarkably improved numerical accuracy and robustness with a moderate increase in algorithmic complexity and computational cost, which makes it of practical significance for real-case applications. The numerical results of benchmark tests are presented to demonstrate the appealing solution quality of the present model in comparison with other existing methods.

In the last Chapter 7, we will make a conclusion from this work. A discussion about future work will also be given.

Chapter 2

Boundary variation diminishing (BVD) principle

2.1 Boundary variation diminishing (BVD) algorithms

As introduced in Chapter 1, the Riemann flux can be written in a canonical form as

$$f_{i+1/2}^{\text{Riemann}}(q_{i+1/2}^L, q_{i+1/2}^R) = \frac{1}{2} (f(q_{i+1/2}^L) + f(q_{i+1/2}^R)) - \frac{|a_{i+1/2}|}{2} (q_{i+1/2}^R - q_{i+1/2}^L), \quad (2.1)$$

where $a_{i+1/2}$ stands for the characteristic speed of the hyperbolic conservation law. The right hand side consists of two parts. The first part is a non-dissipative term with a central difference scheme. The second part is the numerical dissipation term which is one of the main sources of numerical errors. The purpose of the BVD algorithm is to minimize this numerical dissipation term. The remaining main task is how to calculate $q_{i+1/2}^L$ and $q_{i+1/2}^R$ through the reconstruction process.

Effective and perhaps the most popular reconstruction schemes are polynomial-based reconstruction schemes. The polynomial-based high-order (PHO) reconstructions are highly demanded and show excellent performance in resolving numerical solutions

which have relatively smooth variations in space, such as acoustic waves and vortices in compressible flow. However, when applied to strong discontinuities, the PHO reconstructions have to be projected to lower order or smoother polynomials (or more precisely rational functions in nonlinear schemes) to suppress numerical oscillations, which is called limiting projection. The limiting projection can be designed by following principles demanded from mathematical or physical perspectives, like the TVD, ENO/WENO and maximum-principle-satisfying. The PHO reconstructions with limiting projection might result in excessive numerical dissipation and tend to smear out the discontinuities in numerical solution. We denote the polynomial-based high-order (PHO) reconstructions in cell \mathcal{I}_i by $q_i^W(x)$, and the cell boundary values are thus computed by $q_i^W(x_{i-1/2})$ and $q_i^W(x_{i+1/2})$ respectively.

Being aware that the polynomials might not be the best choice in some circumstances for constructing the numerical solution, [53–55] suggested other non-polynomial functions with better monotonicity-preserving property, like piecewise hyperbolic and piecewise rational reconstructions, which over-perform the polynomial reconstructions in capturing discontinuities with monotone distributions and are able to provide oscillationless solutions even without limiting projections. However, extending this sort of methods to higher order seems to be not straightforward. Similarly, we denote the non-polynomial-based reconstructions in cell \mathcal{I}_i by $q_i^T(x)$, and the cell boundary values are thus computed by $q_i^T(x_{i-1/2})$ and $q_i^T(x_{i+1/2})$ respectively.

Given two reconstruction functions shown above, i.e. $q_i^W(x)$ and $q_i^T(x)$, we use the BVD principle to choose the final reconstruction so that $|q_{i+1/2}^R - q_{i+1/2}^L|$ is minimized, which then effectively reduces the numerical dissipation. In this work, we present several BVD algorithms that compare the reconstructed values across cell boundaries. It is noted that we are focusing on the simple and easy-to-use versions of BVD, which are called in turn BVD(I), BVD(II), BVD(III) and BVD(IV).

1. BVD(I) algorithm [36]

(i) Find $q_i^\xi(x)$ and $q_{i+1}^\eta(x)$ with ξ and η being either W or T , so that the boundary variation (BV)

$$BV(q)_{i+\frac{1}{2}} = |q_i^\xi(x_{i+\frac{1}{2}}) - q_{i+1}^\eta(x_{i+\frac{1}{2}})|, \quad (2.2)$$

is minimized;

(ii) In case that a different choice for cell \mathcal{I}_i is made when applying step i) to the neighboring interface $x_{i-\frac{1}{2}}$, that is, $q_i^{\xi'}(x)$ found to minimize

$$BV(q)_{i-\frac{1}{2}} = |q_{i-1}^{\xi'}(x_{i-\frac{1}{2}}) - q_i^{\eta'}(x_{i-\frac{1}{2}})|, \quad (2.3)$$

with ξ' and η' being either W or T , is different from $q_i^\xi(x)$ found to minimize (2.2), adopt the following criterion to uniquely determine the reconstruction function.

$$q_i(x) = \begin{cases} q_i^W(x), & \text{if } \left(q_i^\xi(x_{i+\frac{1}{2}}) - q_{i+1}^\eta(x_{i+\frac{1}{2}}) \right) \left(q_{i-1}^{\xi'}(x_{i-\frac{1}{2}}) - q_i^{\eta'}(x_{i-\frac{1}{2}}) \right) < 0, \\ q_i^T(x), & \text{otherwise.} \end{cases} \quad (2.4)$$

(iii) Compute the left-side value $q_{i+\frac{1}{2}}^L$ at $x_{i+\frac{1}{2}}$ and the right-side value $q_{i-\frac{1}{2}}^R$ at $x_{i-\frac{1}{2}}$ by

$$q_{i+\frac{1}{2}}^L = q_i(x_{i+\frac{1}{2}}) \quad \text{and} \quad q_{i-\frac{1}{2}}^R = q_i(x_{i-\frac{1}{2}}). \quad (2.5)$$

2. BVD(II) algorithm

(i) For each reconstruction $q_i^\xi(x)$ with ξ being either W or T , calculate the minimum

value of total boundary variation (TBV), $mTBV_i^\xi$, for all possible candidate reconstructions over the neighboring cells by

$$\begin{aligned}
mTBV_i^\xi = \min & \left(|q_{i-1}^W(x_{i-\frac{1}{2}}) - q_i^\xi(x_{i-\frac{1}{2}})| + |q_{i+1}^W(x_{i+\frac{1}{2}}) - q_i^\xi(x_{i+\frac{1}{2}})|, \right. \\
& |q_{i-1}^T(x_{i-\frac{1}{2}}) - q_i^\xi(x_{i-\frac{1}{2}})| + |q_{i+1}^T(x_{i+\frac{1}{2}}) - q_i^\xi(x_{i+\frac{1}{2}})|, \\
& |q_{i-1}^W(x_{i-\frac{1}{2}}) - q_i^\xi(x_{i-\frac{1}{2}})| + |q_{i+1}^T(x_{i+\frac{1}{2}}) - q_i^\xi(x_{i+\frac{1}{2}})|, \\
& \left. |q_{i-1}^T(x_{i-\frac{1}{2}}) - q_i^\xi(x_{i-\frac{1}{2}})| + |q_{i+1}^W(x_{i+\frac{1}{2}}) - q_i^\xi(x_{i+\frac{1}{2}})| \right). \tag{2.6}
\end{aligned}$$

(ii) Given the minimum TBVs for both $q_i^W(x)$ and $q_i^T(x)$, $mTBV_i^W$ and $mTBV_i^T$ computed from (2.6), choose the reconstruction function for cell \mathcal{I}_i by

$$q_i(x) = \begin{cases} q_i^T, & \text{if } mTBV_i^T < mTBV_i^W, \\ q_i^W & \text{otherwise} \end{cases}. \tag{2.7}$$

That is the non-polynomial-based reconstruction function will be employed in the targeted cell I_i if the minimum TBV value of non-polynomial-based reconstruction is smaller than that of high order polynomial interpolation.

(iii) Compute the left-side value $q_{i+\frac{1}{2}}^L$ at $x_{i+\frac{1}{2}}$ and the right-side value $q_{i-\frac{1}{2}}^R$ at $x_{i-\frac{1}{2}}$.

3. BVD(III) algorithm [29]

(i) Compute the TBV of the target cell I_i with the high order polynomial reconstruction by

$$TBV_i^{(W)} = \frac{\left(q_{i-1}^W(x_{i-\frac{1}{2}}) - q_i^W(x_{i-\frac{1}{2}}) \right)^4 + \left(q_{i+1}^W(x_{i+\frac{1}{2}}) - q_i^W(x_{i+\frac{1}{2}}) \right)^4}{(\bar{q}_i - \bar{q}_{i-1})^4 + (\bar{q}_i - \bar{q}_{i+1})^4 + \epsilon}, \tag{2.8}$$

where ϵ is a small positive of 10^{-16} for avoiding zero-division. (ii) Compute the smoothness indicator by

$$S = \frac{1 - TBV_i^{(W)}}{\max(TBV_i^{(W)}, \epsilon)}, \tag{2.9}$$

The cutoff number S_c is used as the threshold value so that the cell where $S < S_c$ is identified to contain a non-smooth solution. We set $S_c = 1 \times 10^6$ here.

(iii) For cell I_i where $S < S_c$, the reconstruction function is determined by blending $q_i(x)^T$ and $q_i(x)^W$ as follows

$$q_i(x) = \omega_i q_i(x)^T + (1 - \omega_i) q_i(x)^W, \quad (2.10)$$

where ω_i is a weight parameter. By assuming that the high order polynomial reconstruction is applied on neighbor cells, ω_i is obtained by minimizing

$$\tau_i = \left(q_{i-1}^W(x_{i-\frac{1}{2}}) - q_i(x_{i-\frac{1}{2}}) \right)^2 + \left(q_{i+1}^W(x_{i+\frac{1}{2}}) - q_i(x_{i+\frac{1}{2}}) \right)^2, \quad (2.11)$$

which leads to

$$\frac{\partial \tau_i}{\partial \omega_i} = 0. \quad (2.12)$$

As long as ω_i is determined, the reconstruction function $q_i(x)$ is computed from (2.10).

(iv) Compute the left-side value $q_{i+\frac{1}{2}}^L$ at $x_{i+\frac{1}{2}}$ and the right-side value $q_{i-\frac{1}{2}}^R$ at $x_{i-\frac{1}{2}}$.

4. BVD(IV) algorithm

(i) Compute the TBVs of the target cell I_i using high order polynomial and non-polynomial for I_i and its two neighboring cells respectively,

$$TBV_i^W = |q_{i-1}^W(x_{i-\frac{1}{2}}) - q_i^W(x_{i-\frac{1}{2}})| + |q_i^W(x_{i+\frac{1}{2}}) - q_{i+1}^W(x_{i+\frac{1}{2}})| \quad (2.13)$$

and

$$TBV_i^T = |q_{i-1}^T(x_{i-\frac{1}{2}}) - q_i^T(x_{i-\frac{1}{2}})| + |q_i^T(x_{i+\frac{1}{2}}) - q_{i+1}^T(x_{i+\frac{1}{2}})|. \quad (2.14)$$

(ii) Given TBVs for both $q_i^W(x)$ and $q_i^T(x)$, TBV_i^W and TBV_i^T , choose the reconstruction function for cell \mathcal{I}_i by

$$q_i(x) = \begin{cases} q_i^T & \text{if } TBV_i^T < TBV_i^W, \\ q_i^W & \text{otherwise} \end{cases}. \quad (2.15)$$

(iii) Compute the left-side value $q_{i+\frac{1}{2}}^L$ at $x_{i+\frac{1}{2}}$ and the right-side value $q_{i-\frac{1}{2}}^R$ at $x_{i-\frac{1}{2}}$.

It is noted that the current BVD algorithm only considers two candidate functions. However, it can be extended to more than two candidate function straightforwardly.

2.2 BVD admissible reconstruction function

Under the BVD algorithm, reconstruction function is chosen from several candidate functions. In order to solve both smooth and discontinuous solution, high order polynomial which is suitable for smooth region and non-polynomial function which has good performance in critical region are employed as two candidates in the present work. We will introduce these BVD admissible reconstruction function hereafter.

2.2.1 Polynomial-based reconstruction functions

As introduced in previous chapter, polynomial-based reconstruction functions include TVD, ENO, WENO schemes in the FVM framework and DG, FR and MCV in the LHR framework. An effective and perhaps the most popular reconstruction scheme is the WENO schemes in which high order but non-oscillatory interpolation is achieved by a combination of several lower degree polynomials.

To introduce WENO scheme, we start from fifth-order WENO scheme which is the representative one in WENO family. The basic idea of fifth-order WENO scheme is to

choose the most smooth function from the three candidate stencils. One large stencil S_3 can be divided in to three sub-stencils as S_0, S_1, S_2 . Then we can construct the solution functions by using the volume integral average value of each cell inside three sub stencils S_0, S_1, S_2 and approximate the cell boundary value at the $x_{i+\frac{1}{2}}$ with 3rd order accuracy. The solution function of each stencil can be recovered from the following conditions

$$\bar{q}_{i+j+k-2} = \frac{1}{\Delta x_{i+j+k-2}} \int_{x_{i+j+k-\frac{5}{2}}}^{x_{i+j+k-\frac{3}{2}}} q^{(j)}(x) dx, j = 0, 1, 2, k = 0, 1, 2, \quad (2.16)$$

where $\Delta x_{i+j+k-2}$ is the mesh size. For simplicity, we assume a uniform grid spacing, i.e. $\Delta x_{j-i} = x_{i+j+k-\frac{5}{2}} - x_{i+j+k-\frac{3}{2}} = \Delta x$. Thus the third order approximation of $q_{i+\frac{1}{2}}$ is given respectively from solution function $q^{(j)}(x), j = 0, 1, 2$ as

$$q_{i+\frac{1}{2}}^{(0)} = \frac{1}{3}\bar{q}_{i-2} - \frac{7}{6}\bar{q}_{i-1} + \frac{11}{6}\bar{q}_i, \quad (2.17a)$$

$$q_{i+\frac{1}{2}}^{(1)} = -\frac{1}{6}\bar{q}_{i-1} + \frac{5}{6}\bar{q}_i + \frac{1}{3}\bar{q}_{i+1}, \quad (2.17b)$$

$$q_{i+\frac{1}{2}}^{(2)} = \frac{1}{3}\bar{q}_i + \frac{5}{6}\bar{q}_{i+1} - \frac{1}{6}\bar{q}_{i+2}, \quad (2.17c)$$

where $q_{i+\frac{1}{2}}^{(j)}$ is the abbreviation of $q^{(j)}(x_{i+\frac{1}{2}})$. Similarly, we can construct a high order polynomial with large stencil S_3 , which can achieve the possible largest order, by

$$q_{i+\frac{1}{2}}^{(3)} = \frac{1}{30}\bar{q}_{i-2} - \frac{13}{60}\bar{q}_{i-1} + \frac{47}{60}\bar{q}_i + \frac{9}{20}\bar{q}_{i+1} - \frac{1}{20}\bar{q}_{i+2}. \quad (2.18)$$

On the other hand, the fifth order approximation can be written through a convex combination of the three third order approximation (2.17a),(2.17b) and (2.17c),namely

$$q_{i+\frac{1}{2}}^{(3)} = \gamma_0 q_{i+\frac{1}{2}}^{(0)} + \gamma_1 q_{i+\frac{1}{2}}^{(1)} + \gamma_2 q_{i+\frac{1}{2}}^{(2)}, \quad (2.19)$$

where $\{\gamma_0, \gamma_1, \gamma_2\} = \{\frac{1}{10}, \frac{3}{5}, \frac{3}{10}\}$. In order to eliminate the oscillation at the discontinuities, optimal linear weights $\gamma_0, \gamma_1, \gamma_2$ are replaced by non-linear weights $\omega_0, \omega_1, \omega_2$

according to the smoothness of polynomials.

For those stencils containing discontinuities, non-linear weights should be assigned with a small numbers. To achieve this, a measurement for smoothness in each sub-stencil, so-called smoothness indicator, is defined by

$$\beta_j = \sum_{l=1}^2 \int_{x_{i-\frac{1}{2}}}^{x_{i+\frac{1}{2}}} (\Delta x)^2 \left[\frac{\partial^l q^j(x)}{\partial x^l} \right]^2 dx, \quad j = 0, 1, 2. \quad (2.20)$$

Having the smoothness indicator, the weighted parameters are given by

$$\omega_j = \frac{\alpha_j}{\alpha_0 + \alpha_1 + \alpha_2}, \quad \alpha_j = \frac{\gamma_j}{(\epsilon + \beta_j)^2}, \quad j = 0, 1, 2. \quad (2.21)$$

where ϵ is a small number that is used to avoid the denominator equals to zero.

The original WENO schemes suffer from accuracy loss around critical region. Several efforts have been made hereafter to improve the accuracy of original WENO scheme. One of them, which we will use in the present work is called WENO-Z. The smoothness indicator for WENO-Z scheme is defined by

$$\beta_j = \left(\frac{\beta_j + \epsilon}{\beta_j + \epsilon + \tau_5} \right), \quad j = 0, 1, 2, \quad (2.22)$$

where ϵ equals to 10^{-40} and $\tau_5 = |\beta_2 - \beta_0|$. The new WENO weights ω_j can be then calculated by

$$\omega_j = \frac{\alpha_j}{\sum_{k=0}^2 \alpha_k}, \quad \alpha_k = \frac{\gamma_j}{\beta_j}, \quad j = 0, 1, 2. \quad (2.23)$$

2.2.2 Tangent of Hyperbola for Interface Capturing (THINC) function

Originally used as interface capturing schemes in multiphase flow, the THINC function [56, 57] is the non-polynomial reconstruction function we will employ with in the

present work. Being a Sigmoid-type function, the THINC reconstruction (hyperbolic tangent function) is a differentiable and monotone function that fits well a step-like discontinuity. The THINC reconstruction function is written as

$$q_i^T(x) = \bar{q}_{min} + \frac{\bar{q}_{max}}{2} \left(1 + \theta \tanh \left(\beta \left(\frac{x - x_{i-1/2}}{x_{i+1/2} - x_{i-1/2}} - \tilde{x}_i \right) \right) \right), \quad (2.24)$$

where $\bar{q}_{min} = \min(\bar{q}_{i-1}, \bar{q}_{i+1})$, $\bar{q}_{max} = \max(\bar{q}_{i-1}, \bar{q}_{i+1}) - \bar{q}_{min}$ and $\theta = \text{sgn}(\bar{q}_{i+1} - \bar{q}_{i-1})$. The jump thickness is controlled by parameter β . In our numerical tests shown later a constant value of $\beta = 1.8$ is used, or explicitly stated otherwise. The unknown \tilde{x}_i , which represents the location of the jump center, is computed from $\bar{q}_i = \frac{1}{\Delta x} \int_{x_{i-1/2}}^{x_{i+1/2}} q_i(x)^T dx$. Then the reconstructed values at cell boundaries by THINC function can be expressed by

$$\begin{aligned} q_i^T(x_{i+1/2}) &= \bar{q}_{min} + \frac{\bar{q}_{max}}{2} \left(1 + \theta \frac{\tanh(\beta) + A}{1 + A \tanh(\beta)} \right) \\ q_i^T(x_{i-1/2}) &= \bar{q}_{min} + \frac{\bar{q}_{max}}{2} (1 + \theta A) \end{aligned} \quad (2.25)$$

where $A = \frac{B/\cosh(\beta)-1}{\tanh(\beta)}$, $B = \exp(\theta \beta(2C-1))$ and $C = \frac{\bar{q}_i - \bar{q}_{min} + \epsilon}{\bar{q}_{max} + \epsilon}$ with $\epsilon = 10^{-20}$.

2.3 Numerical experiments

Given two reconstruction functions shown above, i.e. WENO-Z and THINC, we use the BVD principle to choose the final reconstruction so that $|q_{i+1/2}^R - q_{i+1/2}^L|$ is minimized, which then effectively reduces the numerical dissipation. Using WENO and THINC as the candidate reconstructions, the resulted schemes are called WENO-THINC-BVD(I) \sim (IV) methods.

TABLE 2.1: Numerical errors and convergence rates of the 1D advection equation

N	WENOZ		BVD(I)		BVD(II)		BVD(III)		BVD(IV)	
	L_1 error	L_1	L_1 error	L_1	L_1 error	L_1	L_1 error	L_1	L_1 error	L_1
20	2.14e-04		2.14e-04		2.14e-04		2.14e-04		2.14e-04	
40	6.40e-06	5.07	6.40e-06	5.07	6.40e-06	5.07	6.40e-06	5.07	6.40e-06	5.07
80	2.00e-07	5.00	2.00e-07	5.00	2.00e-07	5.00	2.00e-07	5.00	2.00e-07	5.00
160	6.32e-09	4.99	6.32e-09	4.99	6.32e-09	4.99	6.32e-09	4.99	6.32e-09	4.99
320	2.04e-10	4.95	2.04e-10	4.95	2.04e-10	4.95	2.04e-10	4.95	2.04e-10	4.95

2.3.1 Convergence Test

An initially smooth profile defined by $q(x) = \sin(\pi x)$, $x \in [-1, 1]$ is advected. The L_1 errors and convergence rates after one period by different BVD algorithms are summarized in Table. 2.1 under different grid resolutions. As shown by the results, the numerical errors of WENOZ-THINC-BVD are identical to that of original WENOZ, which proves that all BVD algorithm can retrieve the 5th-order WENO scheme for smooth solution.

2.3.2 Advection of one-dimensional complex waves

Proposed in [31], the test of propagation of a complex wave which includes both discontinuous and smooth solutions has been used widely to examine the performance of numerical schemes in solving profiles of different smoothness. The initial distribution of the advected field is set the same as [31]. The numerical result with the WENOZ scheme after one period of computation on a 200-cell mesh is plotted in Fig. 2.1(a). Although WENOZ has good performance for smooth region, the discontinuity has been diffused by nearly 8 cells. The smeared discontinuity will become worse for a long time computation.

The numerical results calculated by the WENOZ-THINC-BVD scheme of different BVD algorithms have been shown in Fig. 2.1(b)-(f). All of them can solve discontinuities sharply by nearly 4 cells, which is a significant improvement of present schemes

in comparison with those which only use high order polynomials in reconstructions. The result calculated by BVD(I) is presented in Fig. 2.1(b). Besides the discontinuous region, BVD(I) also changes the solution around some critical points compared with the original WENOZ scheme. For algorithm BVD(II) as shown in Fig. 2.1(c), the numerical result in the smooth regions look almost the same as the original one in Fig. 2.1(a), while the numerical dissipation around the discontinuities is remarkably reduced. As one of algorithms devised for unstructured grids, algorithm BVD(III) is capable of solving discontinuities sharply but pollutes smooth regions as shown in Fig. 2.1(d), which may be caused by the assumption that neighbor cells are always smooth. Considering that the discontinuity cannot be resolved by only one cell, BVD(IV) is devised by evaluating TBV with the interpolation function over a group of neighboring cells. Shown in Fig. 2.1(e), good results comparable to BVD(I) and BVD(II) can be obtained by BVD(IV) which is simple and can be directly implemented on unstructured grids. It is noteworthy that BVD(IV) can use even larger β values. In Fig. 2.1(f), we show the result with $\beta = 4.0$ which generates sharper discontinuities resolved by only 2 cells.

2.4 Summary

In this chapter, we have made following achievements.

First, a new guideline, called BVD algorithm, for reconstruction processes in finite volume framework is introduced. The concept of this algorithm is to determine reconstruction function from several candidates thus to minimize numerical dissipation errors.

Second, several effective implementation of BVD algorithm is introduced or designed. With these algorithm, new reconstruction schemes can be constructed under the BVD principle. For example, we employ high order polynomial WENO and non-polynomial THINC function as two candidates. The numerical tests show that the resultant scheme

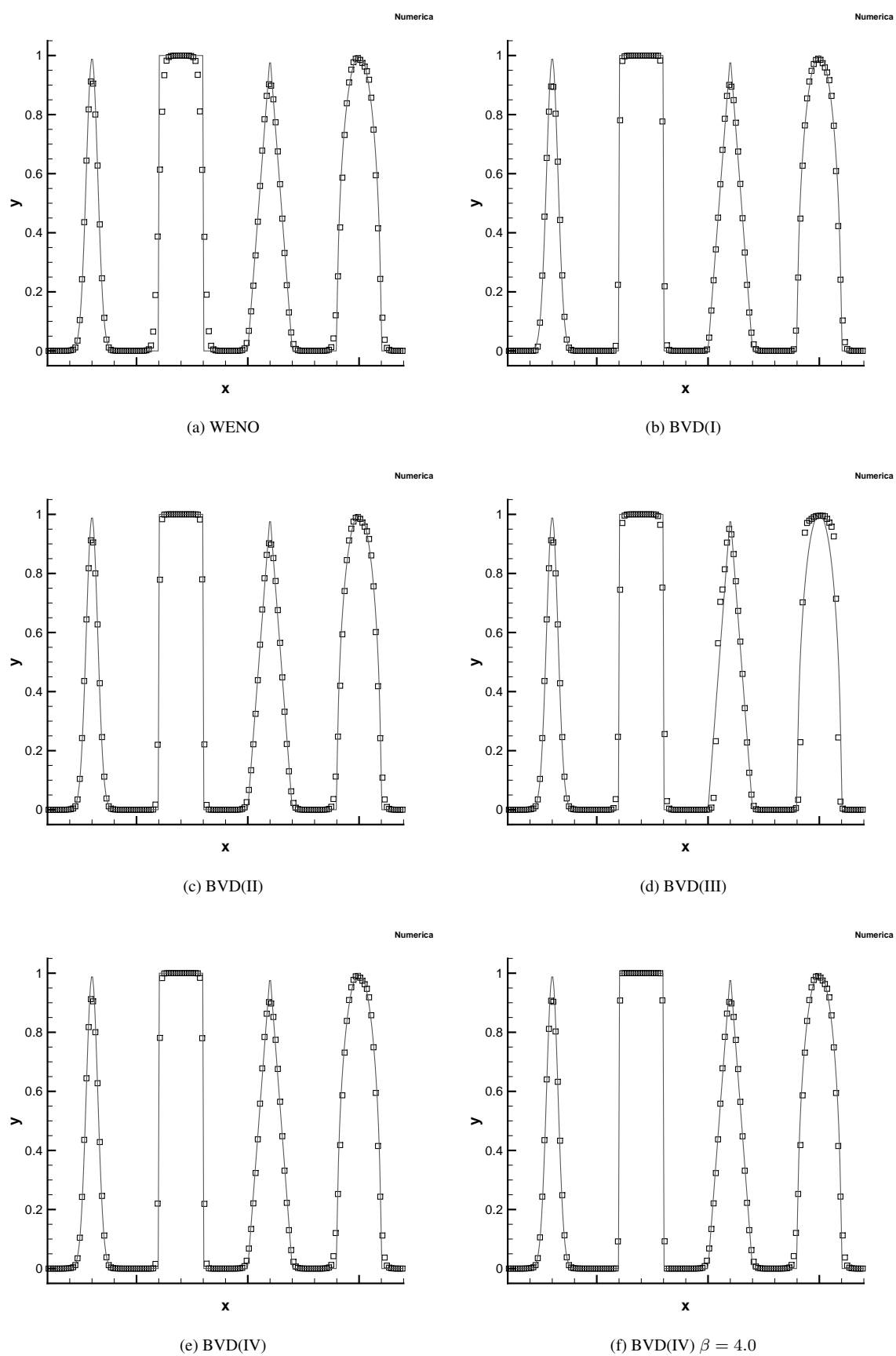


FIGURE 2.1: Numerical results of advection of complex waves with different algorithms.

can achieve high order in smooth region but also solve sharp discontinuities. Thus the designed algorithms can effectively minimize numerical dissipation errors. The results indicate that with BVD algorithm, newly designed schemes can outperform those only relying on high order polynomials.

In following chapters, we will employ the proposed BVD algorithm to design some simple but effective schemes to solve compressible multi-components flows.

Chapter 3

Practical BVD schemes for single phase and reacting Euler equations

3.1 Introduction

High order shock-capturing are facing with several issues such as numerical oscillations and excessive numerical diffusion when solving problems involving discontinuities.

For example, for the problems involving reactive fronts that associate with strong mass transfer and heat release, accurately resolving the reactive fronts as well-defined sharp discontinuities is crucial to get reliable numerical results. Any numerical error or deviation in the calculation of reactive fronts will trigger unphysical mass and heat transfers which, in turn, deviate the numerical results even further away from the correct solution. For example, unphysical phenomena, in which the positions of waves are predicted incorrectly, arise in simulation of stiff detonation waves as reported in [68, 69] where the conventional high-resolution schemes, like the WENO scheme, failed in reproducing correct numerical results to stiff detonation waves unless very high grid resolution is used. As discussed in [69], existing high-resolution schemes lack enough spatial accuracy to capture truly sharp discontinuities and resolve correct stiff detonation waves.

In this chapter, we will design practical BVD schemes which are not high order but have ability to solve the difficulties introduced by high order interpolation.

3.2 Formulation of MUSCL-THINC-BVD

In the present work, the MUSCL-THINC-BVD reconstruction scheme is designed to capture both smooth and non-smooth solutions. The BVD algorithm makes use of the MUSCL scheme and the THINC scheme [56] as the candidates for spatial reconstruction.

In the MUSCL scheme, a piecewise linear function is constructed from the volume-integrated average values \bar{q}_i , which reads

$$\tilde{q}_i(x)^{MUSCL} = \bar{q}_i + \sigma_i(x - x_i), \quad (3.1)$$

where $x \in [x_{i-1/2}, x_{i+1/2}]$ and σ_i is the slope defined at the cell center $x_i = \frac{1}{2}(x_{i-1/2} + x_{i+1/2})$. To prevent numerical oscillation, a slope limiter [136] is used to get numerical solutions satisfying the TVD property. The reconstructed values at cell boundaries from MUSCL reconstruction are denoted as $q_{i-1/2}^{R,MUSCL} = \tilde{q}_i(x_{i-1/2})^{MUSCL}$ and $q_{i+1/2}^{L,MUSCL} = \tilde{q}_i(x_{i+1/2})^{MUSCL}$. The MUSCL scheme, in spite of popular use in various numerical models, has excessive numerical dissipation and tends to smear out flow structures, which might be a fatal drawback in simulating interfacial multiphase flows.

The final reconstruction function is determined by the BVD algorithm introduced in the Chapter 2, which chooses the reconstruction function between $\tilde{q}_i(x)^{MUSCL}$ and $\tilde{q}_i(x)^{THINC}$ so that the variations of the reconstructed values at cell boundaries are minimized. BVD algorithm prefers the THINC reconstruction $\tilde{q}_i(x)^{THINC}$ within a cell where a discontinuity exists. It is sensible that the THINC reconstruction should only be employed when a discontinuity is detected. In practice, we make use of the following

conditions as an additional criterion to implement the THINC reconstruction

$$\delta < C < 1 - \delta \quad \text{and} \quad (\bar{q}_{i+1} - \bar{q}_i)(\bar{q}_i - \bar{q}_{i-1}) > 0, \quad (3.2)$$

where δ is a small positive.

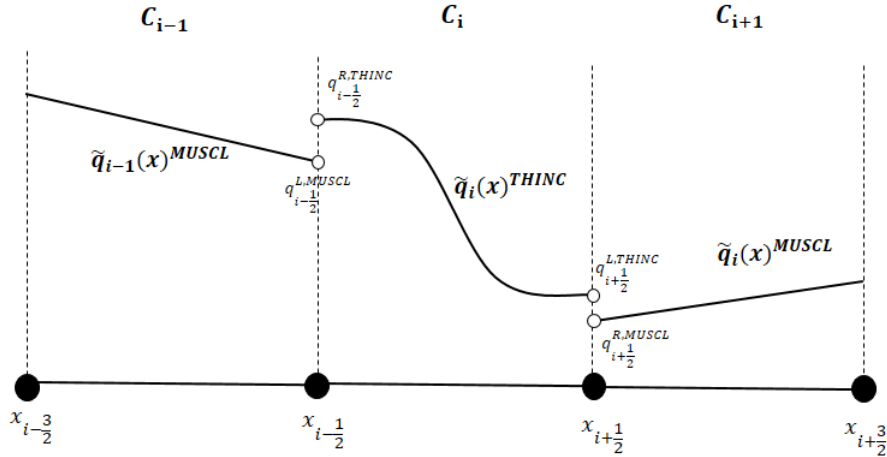


FIGURE 3.1: Illustration of one possible situation corresponding to $|q_{i-1/2}^{L,MUSCL} - q_{i-1/2}^{R,THINC}| + |q_{i+1/2}^{L,THINC} - q_{i+1/2}^{R,MUSCL}|$ when calculating $TBV_{i,min}^{THINC}$.

Hence, THINC reconstruction function will be employed in the targeted cell if the minimum TBV value of THINC is smaller than that of MUSCL. In Fig. 3.1, we illustrate one possible situation corresponding to $|q_{i-1/2}^{L,MUSCL} - q_{i-1/2}^{R,THINC}| + |q_{i+1/2}^{L,THINC} - q_{i+1/2}^{R,MUSCL}|$ when evaluating $TBV_{i,min}^{THINC}$. As stated in [36], the BVD algorithm will realize the polynomial interpolation for smooth solution while for discontinuous solution a step like function will be preferred. It is noted that the present BVD algorithm is slightly different from that in [36]. The present BVD algorithm minimizes the total BVs at two ends of the target cell. Our numerical tests show that the present BVD algorithm can effectively reduce numerical dissipations and prevent the flow structures from being smeared out as that in [36].

As shown in numerical tests in this paper, discontinuities including the detonation front

can be resolved by the MUSCL-THINC-BVD scheme with substantially reduced numerical dissipation in comparison with a standard 5th-order WENO scheme [2]. We remark that the MUSCL-THINC-BVD is essentially a shock capturing scheme, which can solve discontinuous solutions sharply without explicit special treatment in regard to the detonation front as with other methods.

3.3 Limiter-free discontinuity capturing schemes

3.3.1 Dissipation properties of THINC scheme

As aforementioned, the common practice to suppress spurious numerical oscillations associated with high order polynomial-based reconstruction schemes is to introduce certain amount of numerical dissipations by projecting high order polynomials to lower order or smoother ones, which, as a consequence, essentially prevents discontinuous solutions from being resolved sharply. Realizing that the polynomial-based reconstruction may not be the proper choice when the solution includes discontinuities, several authors [53–55] have proposed other non-polynomial functions with possible better monotonicity-preserving property. It has been shown that these non-polynomial functions have better performance in capturing discontinuities with monotone distributions and are able to provide oscillation-free solutions without relying on classical limiting projections. However, these schemes still have significant numerical dissipation.

In the present work, a new spatial reconstruction scheme is proposed. Without relying on high order polynomials, the reconstruction scheme employs THINC (Tangent of Hyperbola for INterface Capturing) functions [56, 57] with adaptive sharpness to solve both smooth and discontinuous solutions. Because THINC is a bounded and monotone function, the introduction of any extra limiting projection is no more mandatory.

As demonstrated in the previous chapter, adjusting the value of parameter β can modify the sharpness of the jump transition in the THINC reconstruction. In order to elucidate the effect of the sharpness parameter β on numerical dissipation of the THINC scheme, we applied the approximate dispersion relation (ADR) analysis described in [74] to the THINC scheme with different wavenumbers \mathbf{w} . The spectral properties of THINC schemes with different β are shown in Fig. 3.2, in which the numerical dissipation is quantified through the imaginary parts of the modified wavenumber. It can be seen that dissipation errors decrease as β increases from 1.0 to 1.3. However, it is observed that in a band of wavenumbers the THINC scheme with $\beta = 1.2$ or $\beta = 1.3$ produces values larger than zero, which implies that the THINC scheme with these β values may modulate the waves in this band. It is observed as the compressive or anti-diffusion effect in the numerical results. In order to compare with other popularly used schemes, we also show numerical dissipations of the TVD schemes with Minmod, Van Leer and Superbee limiters [75]. As shown in the right side of Fig. 3.2, the THINC scheme with $\beta_s = 1.1$ has much smaller numerical dissipation than TVD scheme with Minmod limiter, and has similar but slightly better performance than the Van Leer limiter. THINC with a larger slope parameter ($\beta_s = 1.3$) has the similar spectral property to the TVD method with Superbee limiter. They both show a positive imaginary part at low wavenumber band, which leads to the well-known squaring effect [74] on the solution profile. This squaring effect is preferred for discontinuous solutions.

The above analysis reveals that it is possible to design a reconstruction strategy for smooth and discontinuous solutions by adaptively choosing the sharpness parameter β . We present next such an algorithm using the BVD principle.

3.3.2 Formulations of adaptive THINC-BVD scheme

For each cell i , we prepare two THINC reconstruction functions with different values of slope parameter β . A THINC reconstruction function $\tilde{q}_i^s(x)$ with a small β_s is prepared

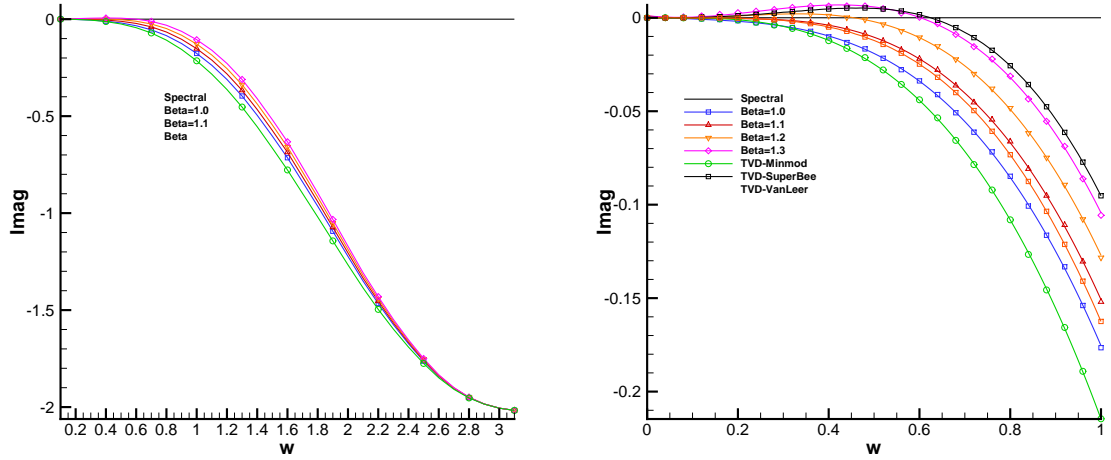


FIGURE 3.2: Imaginary parts of modified wavenumber from THINC schemes with different β_s . A comparison with the TVD scheme is also included. The left one shows the whole resolvable wavenumber whereas the right one shows the zoomed region of the small wavenumber.

to represent a smooth solution, which produces the reconstruction values $q_{i+1/2}^{L,s}$ and $q_{i-1/2}^{R,s}$. To capture discontinuities, another THINC reconstruction function $\tilde{q}_i^l(x)$ with a large β_l is employed as an alternative candidate for reconstruction. The values at cell boundaries $q_{i+1/2}^{L,l}$ and $q_{i-1/2}^{R,l}$ are then obtained from $\tilde{q}_i^l(x)$ accordingly.

The final reconstruction function is adaptively determined by BVD algorithm. Let us define the total boundary variations (TBV) for a target cell i as

$$TBV_i^p = |q_{i-1/2}^{L,p} - q_{i-1/2}^{R,p}| + |q_{i+1/2}^{L,p} - q_{i+1/2}^{R,p}|, \quad p = \{s, l\}. \quad (3.3)$$

Then the final reconstruction function is determined by

$$\tilde{q}_i^f(x) = \begin{cases} \tilde{q}_i^s(x) & \text{if } TBV_i^s < TBV_i^l, \\ \tilde{q}_i^l(x) & \text{otherwise} \end{cases}, \quad (3.4)$$

by which the reconstruction values at cell boundaries can be calculated. The resultant scheme is named adaptive THINC-BVD, which has the following characteristics:

- (I) Since THINC functions with adaptive sharpness are employed as the spatial discretization to deal with both smooth and discontinuous solutions, extra limiting process is not needed to prevent numerical oscillations;
- (II) Numerical dissipation is reduced by minimizing the total boundary variation for each cell. Different from the BVD algorithm in [36], the current procedure simplifies the algorithm significantly and thus can be extended to unstructured grids.

It is noted that some arbitrariness is left in choosing β_s and β_l . Based on the numerical dissipation analysis aforementioned, we use $\beta_s = 1.1$ to resolve the smooth solutions. A larger value can be chosen for β_l to represent a jump-like solution. In this paper $\beta_l = 2.0$ is used for all numerical tests. From our numerical experiments, a β_l valued from 1.6 to 2.2 produces good or acceptable results.

In spite of its simplicity, the adaptive THINC-BVD scheme can produce accurate results for both smooth and discontinuous solutions competitive to most existing high-resolution schemes. We present numerical verifications in the following section.

3.4 Solution procedures for Euler and reacting Euler equations

3.4.1 Control equations

The general form which describes the time-dependent inviscid compressible flow with and without reaction in one space dimension can be written in the following form

$$\frac{\partial \mathbf{q}}{\partial t} + \frac{\partial f(\mathbf{q})}{\partial x} = \phi(\mathbf{q}), \quad (3.5)$$

where the vectors of physical variables \mathbf{q} , flux functions f and source terms ϕ are

$$\mathbf{q} = (\rho, \rho u, E)^T, \quad f = (\rho u, \rho u u + p, E u + p u)^T, \quad \phi = (0, 0, 0)^T, \quad (3.6)$$

for Euler equations while

$$\mathbf{q} = (\rho, \rho u, E, \rho \alpha)^T, \quad f = (\rho u, \rho u u + p, E u + p u, \rho u \alpha)^T, \quad \phi = (0, 0, 0, -K(T)\rho \alpha)^T, \quad (3.7)$$

for reacting Euler equations with only two chemical states. The dependent variables ρ , u , E and α are the density, velocity component in x direction, total energy and mass fraction of unreacted gas, respectively. p is the pressure, T the temperature and K the chemical reaction rate. The pressure is obtained through an equation of state of the form

$$p = (\gamma - 1)\left(E - \frac{1}{2}\rho u^2 + \mathcal{R}\right), \quad (3.8)$$

where $\mathcal{R} = 0$ for Euler equation and $\mathcal{R} = -q_0\rho\alpha$ for reacting Euler equations which involves the heat release from chemical reaction processes, where q_0 denotes chemical heat release and γ is the ratio of specific heats. The temperature is calculated by

$$T = \frac{p}{\rho}. \quad (3.9)$$

For reactive Euler equations, the reaction rate can be modeled by Heaviside kinetics with

$$K(T) = -\frac{1}{\xi}H(T - T_{ign}), \quad (3.10)$$

where $H(x) = 1$ for $x \geq 0$, and $H(x) = 0$ for $x < 0$ and ξ represents the reaction time. Last, T_{ign} is the given ignition temperature. Generally, the stiffness issue becomes severe with such Heaviside kinetics.

3.4.2 Solution procedures with wave propagation method

Advection step

To solve the above model system, we choose the wave propagation method which is a more flexible framework to solve hyperbolic systems in comparison with the classical finite volume method [70, 135].

In the wave-propagation method, the spatial discretization operator for convection terms in cell C_i is computed by

$$\mathcal{L}(\bar{\mathbf{q}}_i(t)) = -\frac{1}{\Delta x} (\mathcal{A}^+ \Delta \mathbf{q}_{i-1/2} + \mathcal{A}^- \Delta \mathbf{q}_{i+1/2} + \mathcal{A} \Delta \mathbf{q}_i) \quad (3.11)$$

where $\mathcal{A}^+ \Delta \mathbf{q}_{i-1/2}$ and $\mathcal{A}^- \Delta \mathbf{q}_{i+1/2}$, are the right- and left-moving fluctuations, respectively, which enter into cell C_i , and $\mathcal{A} \Delta \mathbf{q}_i$ is the total fluctuation within C_i . At any interface between two cells C_{i-1} and C_i , discontinuous data is to be solved. A Riemann problem is then solved to determine these fluctuations. The right- and left-moving fluctuations can be calculated by

$$\mathcal{A}^\pm \Delta \mathbf{q}_{i-1/2} = \sum_{k=1}^3 [s^k (\mathbf{q}_{i-1/2}^L, \mathbf{q}_{i-1/2}^R)]^\pm \mathcal{W}^k (\mathbf{q}_{i-1/2}^L, \mathbf{q}_{i-1/2}^R), \quad (3.12)$$

where moving speeds s^k and the jumps \mathcal{W}^k ($k = 1, 2, 3$) of three propagating discontinuities can be solved by Riemann solvers [72] given the pointwise reconstructed values $\mathbf{q}_{i-1/2}^L$ and $\mathbf{q}_{i-1/2}^R$ which are computed from the reconstruction functions $\tilde{\mathbf{q}}_{i-1}(x)$ and $\tilde{\mathbf{q}}_i(x)$ to the left and right sides of cell edge $x_{i-1/2}$, respectively. The reconstruction process in finite volume method is illustrated in Fig. 3.3. In our simulations, the HLLC Riemann solver [72] is employed. Similarly, the total fluctuation can be determined by

$$\mathcal{A} \Delta \mathbf{q}_i = \sum_{k=1}^3 [s^k (\mathbf{q}_{i-1/2}^R, \mathbf{q}_{i+1/2}^L)]^\pm \mathcal{W}^k (\mathbf{q}_{i-1/2}^R, \mathbf{q}_{i+1/2}^L). \quad (3.13)$$

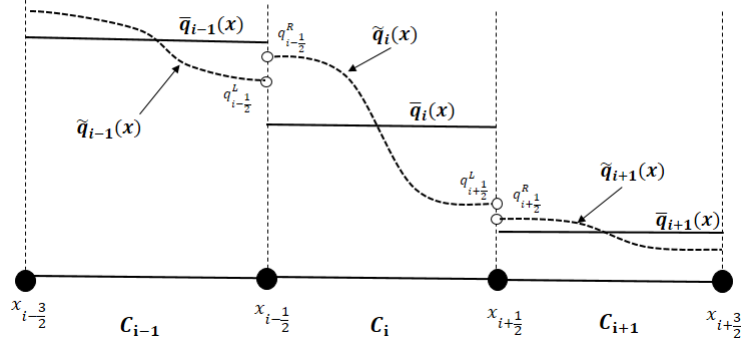


FIGURE 3.3: Sketch of the finite volume representation of data in three cells $\bar{\mathbf{q}}_i$. Reconstruction functions are denoted by $\tilde{\mathbf{q}}_i(x)$ and intercell values by $\mathbf{q}_{i-1/2}^L$ and $\mathbf{q}_{i-1/2}^R$. A Riemann solver is used to determine the fluctuation at cell interfaces.

Given the spatial discretization, the three-stage third-order SSP (Strong Stability-Preserving) Runge-Kutta scheme [73] is employed for time marching.

Reaction step

In the reaction step, the explicit Euler method is employed as follows;

$$\bar{\mathbf{q}}_C^{n+1} = \bar{\mathbf{q}}^n + \Delta t \mathcal{S}(\bar{\mathbf{q}}^n), \quad (3.14)$$

in which the $\bar{\mathbf{q}}_C^{n+1}$ is the updated value at reaction step and $\mathcal{S}(\bar{\mathbf{q}})$ is the reaction operator. The above reaction step over Δt is denoted by $R(\Delta t)$. To get the numerical solution at time step $n + 1$, a second order Strang-splitting scheme [161] is employed. The numerical solution at time step t_{n+1} is obtained by

$$\bar{\mathbf{q}}^{n+1} = A\left(\frac{\Delta t}{2}\right)R(\Delta t)A\left(\frac{\Delta t}{2}\right)\bar{\mathbf{q}}^n. \quad (3.15)$$

In our numerical examples, N_r sub-steps may be used in one reaction step. Thus the above equation is modified by

$$\bar{\mathbf{q}}^{n+1} = A\left(\frac{\Delta t}{2}\right)R\left(\frac{\Delta t}{N_r}\right)\dots R\left(\frac{\Delta t}{N_r}\right)A\left(\frac{\Delta t}{2}\right)\bar{\mathbf{q}}^n. \quad (3.16)$$

In our numerical tests, unless otherwise stated, we set $Nr = 1$. It should be noted that implicit time scheme has not been considered since it may introduce extra numerical dissipation.

3.5 Numerical experiments of MUSCL-THINC-BVD scheme

In this section, some comparative tests in one- and two- dimensions are conducted between the 5th order WENO scheme and the proposed MUSCL-THINC-BVD scheme. We have proposed a new scheme in FVM framework. Thus we choose 5th order WENO, which is a popular-used scheme in FVM, to compare with the new scheme.

3.5.1 Euler equations

Sod problems

The Sod problem is employed here to test the performance of schemes in capturing the shock front as well as the contact discontinuity. The initial distribution on computational domain $[0, 1]$ is specified as [76]

$$(\rho_0, u_0, p_0) = \begin{cases} (1, 0, 1) & 0 \leq x \leq 0.5 \\ (0.125, 0, 0.1) & \text{otherwise} \end{cases} . \quad (3.17)$$

These results represented in Fig. 3.4 show that the proposed scheme has good performance in capturing discontinuous solutions.

Lax's problem

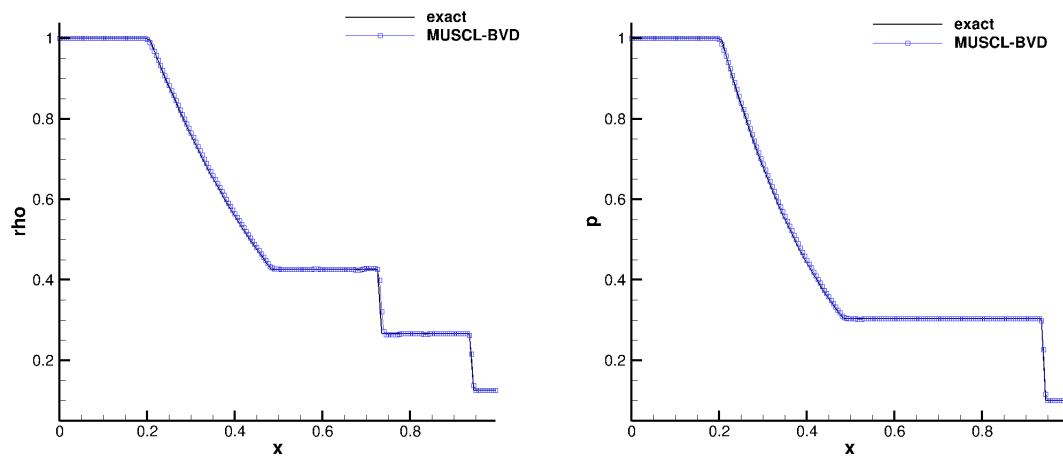


FIGURE 3.4: Numerical results of Sod's problem for density field and pressure from MUSCL-THINC-BVD scheme.

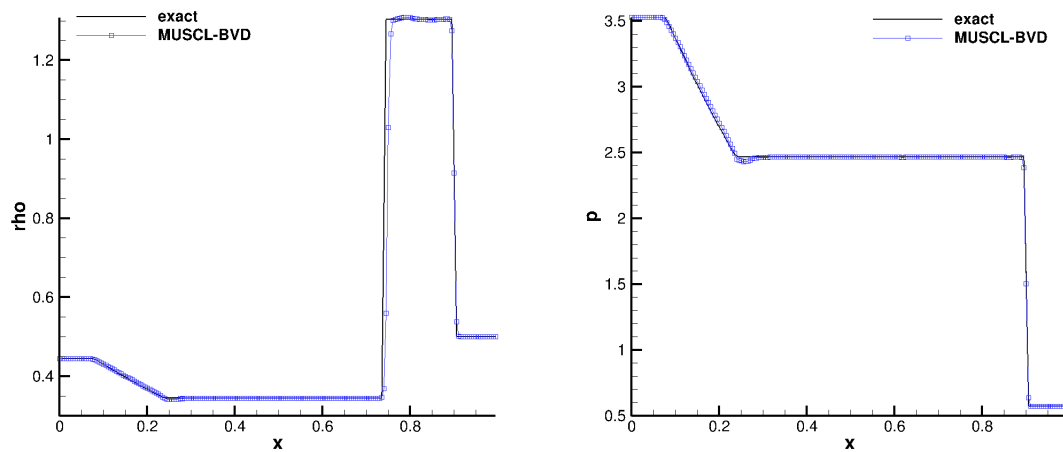


FIGURE 3.5: Numerical results of Lax's problem for density field and pressure from MUSCL-THINC-BVD scheme.

The Lax problem is employed here to check the ability of the proposed numerical scheme to capture relatively strong shock. The initial condition is given by

$$(\rho_0, u_0, p_0) = \begin{cases} (0.445, 0.698, 3.528) & 0 \leq x \leq 0.5 \\ (0.5, 0, 0.571) & \text{otherwise} \end{cases} . \quad (3.18)$$

With the same number of cells as in previous case, the computation lasts until time $t = 0.16$. From the result shown in Fig. 3.5, we can see that the contact discontinuous solution can be resolved sharply.

3.5.2 Euler reacting equations for stiff detonation

During the past two decades, spurious phenomena in simulating stiff hyperbolic system have been investigated in several studies [68, 69, 80, 81, 156, 157, 160]. Various strategies have been proposed to obtain the correct wave propagation speed. One main strategy is to reduce the numerical dissipation using a ghost fluid/level set and front tracking methods [156, 159, 160], or locally resolving the detonation wave with a large number of adaptively placed grid cells [158]. Another advanced strategy is to revise the reaction step by accepting the smeared-out discontinuous profile. A temperature extrapolation method, which constructs a first or second extrapolation from a few grid cells ahead of the shock to obtain the temperature was proposed in [161]. Nevertheless, finding the temperature in front of the wave is non-trivial, especially in higher spatial dimensions [160]. Instead of extrapolating temperature from the cells in front of shock, the method in which a projection is performed to make the ignition temperature random during reaction step was proposed in [80, 84, 162]. This method achieves success in both one- and two-dimensional tests, although the assumption of a priori stiff source term prevents its use for non-stiff problems. To deal with both types, a fractional-step algorithm termed the MinMax scheme was proposed in [81]. Based on two-valued variable reconstruction in each cell, appropriate maximum and minimum values of the unknown are believed to deal with the under-resolved calculations for stiff-source conditions, but only one-dimensional tests were conducted in the work. In recent work [68], the high-order shock-capturing WENO (Weighted Essentially Non-Oscillatory) scheme was used to update the convection step. During the reaction step, the transition diffused points produced by the convection step are first identified, and then the flow variables at these points are extrapolated by a reconstructed polynomial using the subcell resolution method. Although this method can capture the correct location, extra steps, for example, to solve the shock location, is unavoidable and more importantly, the detonation front remains diffuse as existing shock-capturing schemes, despite their high order, introduce excessive numerical diffusion errors around discontinuities.

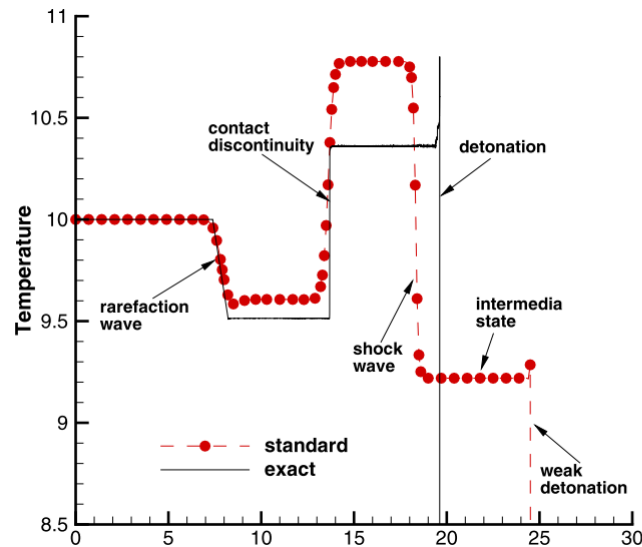


FIGURE 3.6: Illustration of wrong produced detonation waves against true solution. Taken from [157].

To explain the spurious phenomenon caused by low spatial resolution, the illustration of wrong produced detonation wave is presented in Fig. 3.6. There is a bifurcating wave pattern exists in the wrong solution: the strong detonation waves changes into a moving forward weak detonation wave, in which all the chemical energy is released, followed by a shock wave travelling more slowly. The small spikes produced by WENO are due to the weak detonation wave as shown in Fig. 3.6. It has been widely considered that with superfine grid resolution, shock capturing schemes even with lower order accuracy will produce correct detonation position. As shown in Fig. 3.7, by gradually refining mesh the numerical solution becomes closer to exact solution.

As studied in [69], the degree of the discrepancy in the propagation speed of discontinuities is highly dependent on how shock-capturing schemes spread the discontinuities. The fundamental reason behind this spurious phenomenon is that shock-capturing schemes introduce excessive numerical dissipation errors around discontinuities.

C-J detonation wave with Arrhenius law

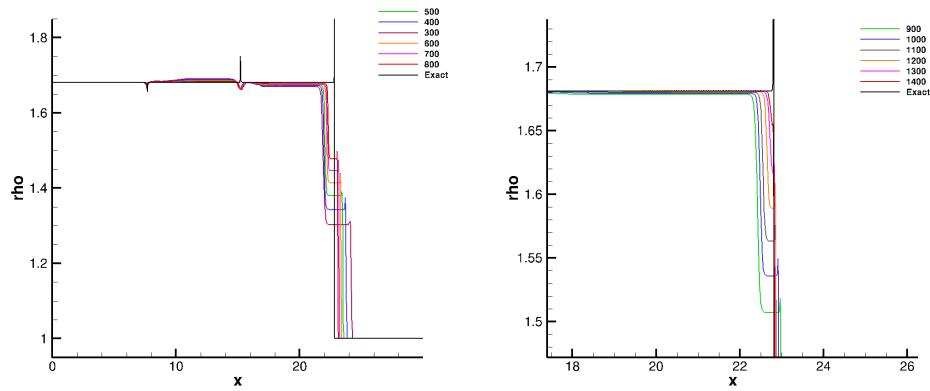


FIGURE 3.7: Numerical experiments by refining mesh with WENO scheme. The numerical solutions produced by different mesh numbers are indicated in different colour.

For the Chapman-Jouguet (C-J) model with an Arrhenius source term, the corresponding detonation wave is considered; see also [68, 80, 81]. Initially, the completely burnt gas is set on the left-hand side and the completely unburnt gas on the right. We set the ratio of the specific heats $\gamma = 1.4$, the heat release $q_0 = 25$ the ignition temperature $T_{ign} = 25$ and $K_0 = 16418$. Given any initial state $(\rho_0, u_0, p_0, 1.0)$ on the right side, the C-J initial state $(\rho_{CJ}, u_{CJ}, p_{CJ}, 0.0)$ on the left side can be obtained [82, 83]. The computation domain is $[0, 30]$ where the initial discontinuity is located at $x = 10$. In this simulation, we set $\rho_0 = 1.0$, $u_0 = 0.0$, and $p_0 = 1.0$. The computation evolves until $t = 1.8$. The computation was performed using the standard 5th-order WENO scheme and then the MUSCL-THINC-BVD scheme with $N = 300$ cells. For the former, CFL=0.05 whereas for the latter, CFL=0.1. The numerical results for pressure, temperature, density, and mass fraction are displayed in Fig. 3.8–3.11 in which the reference solution is calculated by the standard 5th-order WENO scheme with $N = 10000$ cells. From the results, the correct speed of the C-J detonation is found using the MUSCL-THINC-BVD scheme with larger CFL number whereas a spurious weak detonation appears ahead of the detonation wave using the WENO scheme. Despite its higher order, the WENO scheme introduces too many numerical diffusion errors around the discontinuities and hence generates spurious numerical solutions. A comparison of results for

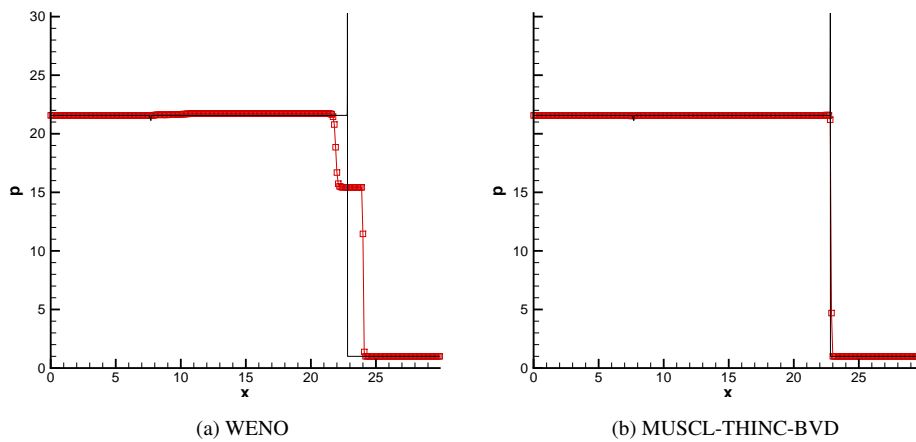


FIGURE 3.8: Numerical results of the pressure field for the C-J detonation wave implemented with the Arrhenius law. Reference solutions are marked with black solid lines whereas numerical solutions are in red with symbols to provide a comparison between the WENO and MUSCL-THINC-BVD schemes.

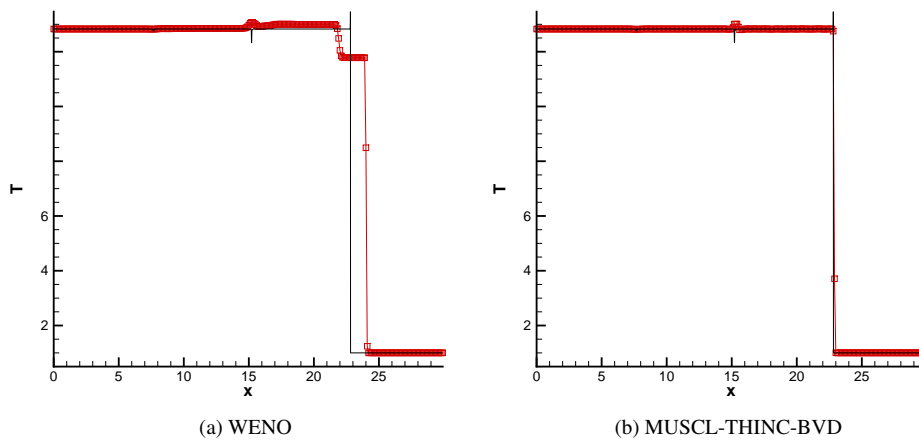


FIGURE 3.9: As for Fig. 3.8 but for the temperature field.

the density field from both schemes was also made with a finer grid of $N = 1500$ cells (Fig. 3.12). Note the combustion spike has been resolved by the MUSCL-THINC-BVD scheme as there is less diffusion around the critical regions.

C-J detonation wave with the Heaviside model

The C-J detonation, for which the chemical reaction is modeled by the Heaviside formulation, is considered in this example. As in [68, 80, 81], the parameter values are $\frac{1}{\xi} = 0.5825 \times 10^{10}$, $\gamma = 1.4$, $q_0 = 0.5196 \times 10^{10}$, and $T_{ign} = 0.1155 \times 10^{10}$. The completely burnt gas is set on the right side with the initial state as $\rho_0 = 1.201 \times 10^{-3}$,

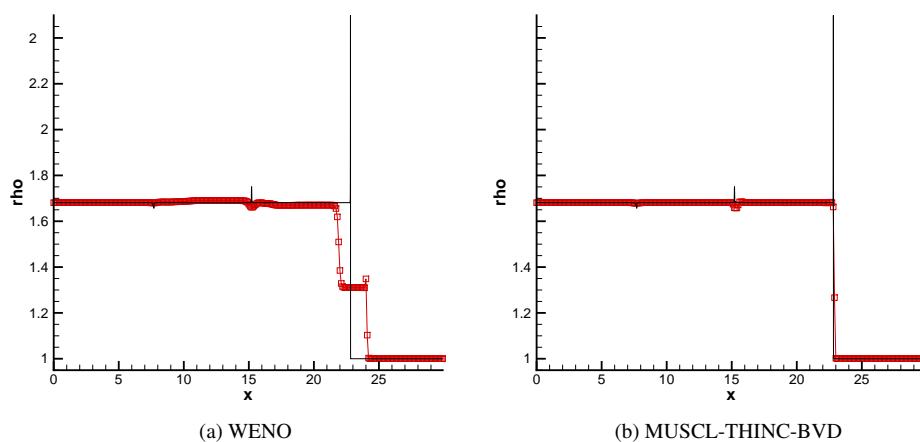


FIGURE 3.10: As for Fig. 3.8 but for the density field.

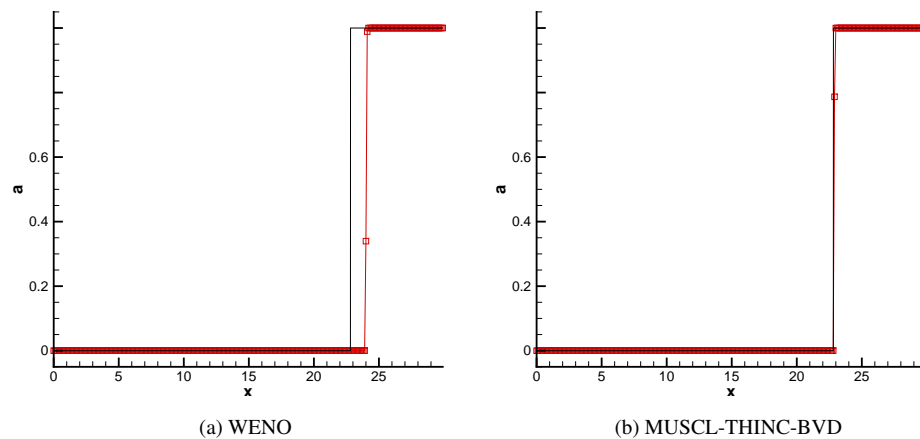


FIGURE 3.11: As for Fig. 3.8 but for mass fraction.

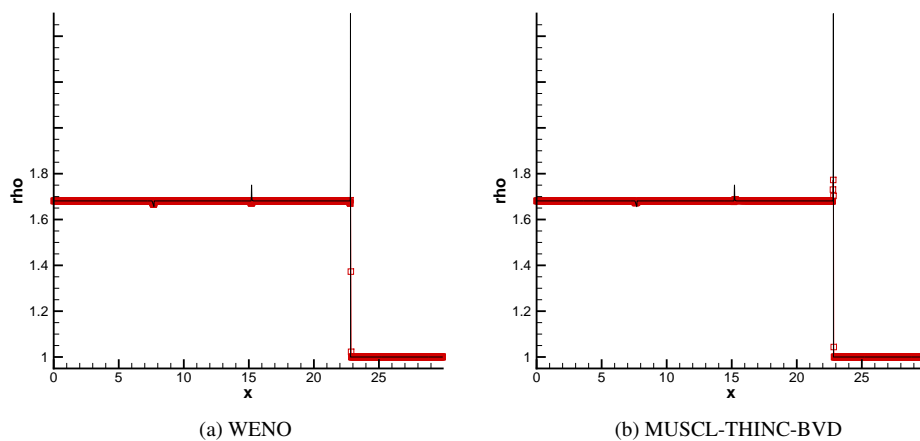


FIGURE 3.12: As for Fig. 3.10 but with finer mesh.

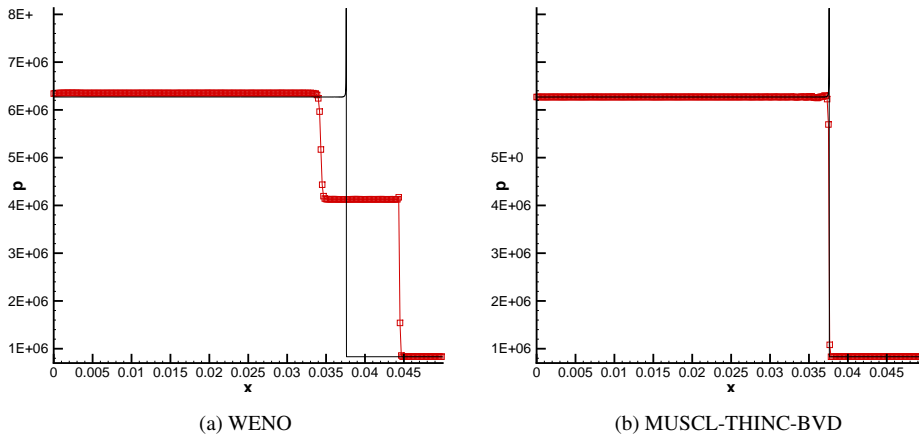


FIGURE 3.13: Numerical results of pressure field for C-J detonation wave with the Heaviside model. Reference solutions are marked with black solid lines whereas numerical solutions are marked with red lines and symbols to provide a comparison between the WENO and MUSCL-THINC-BVD schemes.

$u_0 = 0.0$, and $p_0 = 8.321 \times 10^5$. The completely unburnt gas is set on the left side where $(\rho_{CJ}, u_{CJ}, p_{CJ}, 0.0)$ are determined by the C-J detonation model. The computational domain is $[0, 0.05]$ where discontinuity is set at $x = 0.005$. The number of cells is $N = 300$. The computation is allowed to evolve until $t = 3 \times 10^{-7}$ with a reaction sub-step of $Nr = 10$. The exact position of the wave will be at $x = 0.03764$. We set CFL=0.01 for the WENO scheme and CFL=0.1 for the MUSCL-THINC-BVD scheme. The results of pressure, temperature, density, and mass fraction are plotted in Fig. 3.13–3.16. With a larger CFL number, the correct detonation speed is captured by MUSCL-THINC-BVD scheme. However, as reported in [68] wrong results are produced by the standard WENO scheme no matter how small the time step is as the stiffness problem is due to spatial rather than the temporal errors.

Strong detonation

With data taken from [80], the simulation of a strong detonation is considered here. All parameter settings are the same as for the previous example except for pressure at the left side, which is set larger than the value calculated by the C-J detonation model. Hence, for the initial state at the left side, we have $\rho_l = \rho_{CJ}$, $u_l = u_{CJ}$, and $p_l = 8.27 \times 10^6 > p_{CJ}$. Different from the profile of the C-J detonation, the solution consists of a

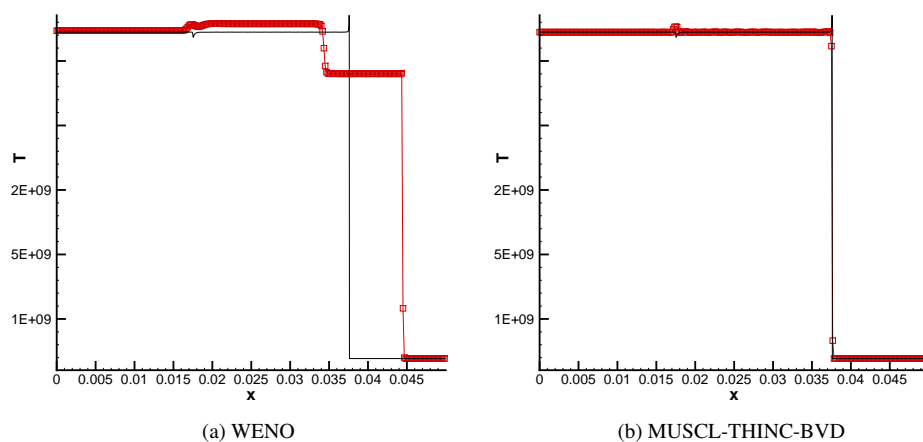


FIGURE 3.14: As for Fig. 3.13 but for the temperature field.

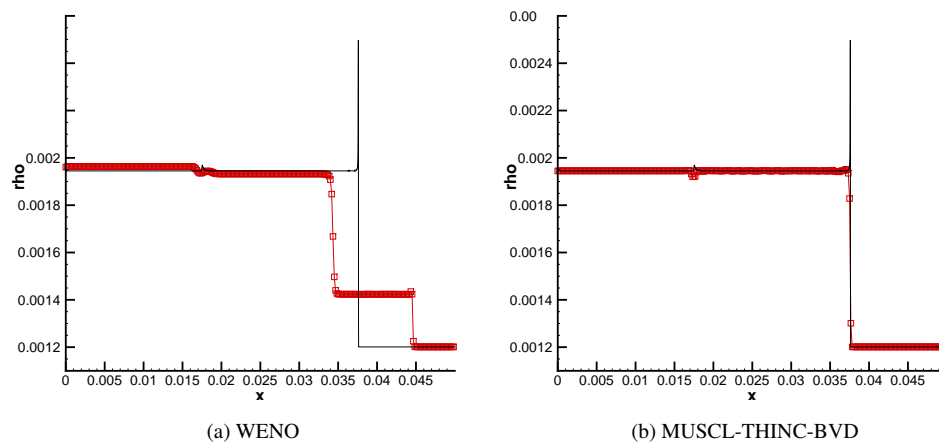


FIGURE 3.15: As for Fig. 3.13 but for the density field.

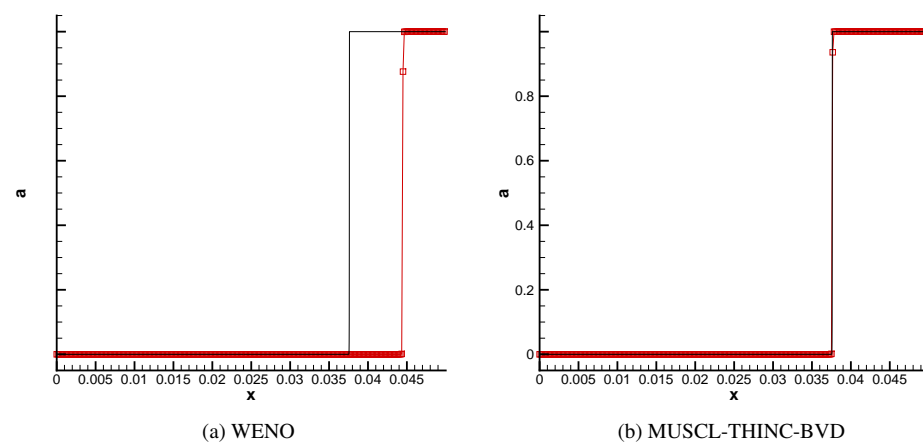


FIGURE 3.16: As for Fig. 3.13 but for mass fraction.

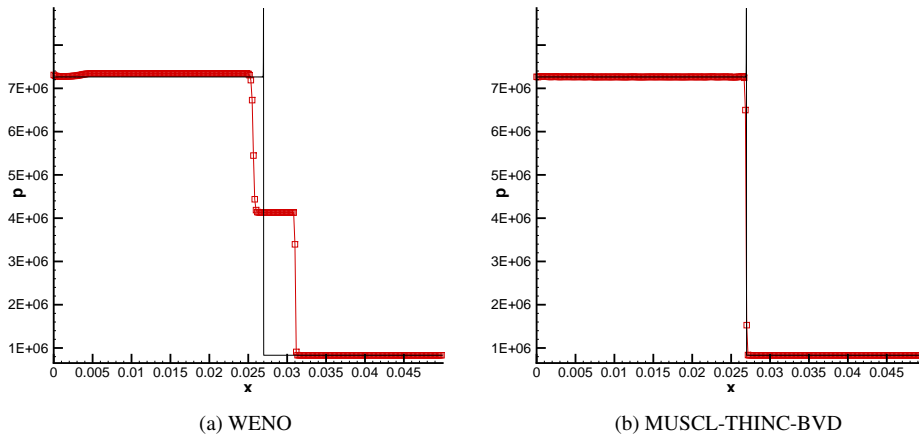


FIGURE 3.17: Numerical results of pressure field for a strong detonation wave. Reference solutions are marked with black solid lines whereas numerical solutions are marked with red lines and symbols to provide a comparison between the WENO and MUSCL-THINC-BVD schemes.

right-moving strong detonation wave, a right-moving discontinuity, and a left-moving rarefaction wave. The solutions are run for a duration $t = 2 \times 10^{-7}$ with CFL=0.02; the number of cells is $N = 300$. The distributions for pressure, density, temperature, and mass fraction field are shown in Fig. 3.17–3.20. Clearly, the WENO scheme produces a spurious weak detonation where the location of the detonation front is essentially incorrect. In contrast, MUSCL-THINC-BVD resolves the correct right-moving strong detonation wave. Moreover, in regard to the right-moving discontinuity, the MUSCL-THINC-BVD scheme requires only two cells for a solution whereas more than five points are required for the WENO scheme.

Interaction between a detonation wave and an oscillatory profile

The interaction between a detonation wave and an oscillatory profile was investigated to establish the behavior of the proposed scheme for different field distributions. The same problem has been simulated in [68, 84]. The parameters are taken as $\gamma = 1.2$, $q_0 = 50$, $\frac{1}{\xi} = 1000$ and $T_{ign} = 3$. The computational domain is set as $[0, 2\pi]$, which is

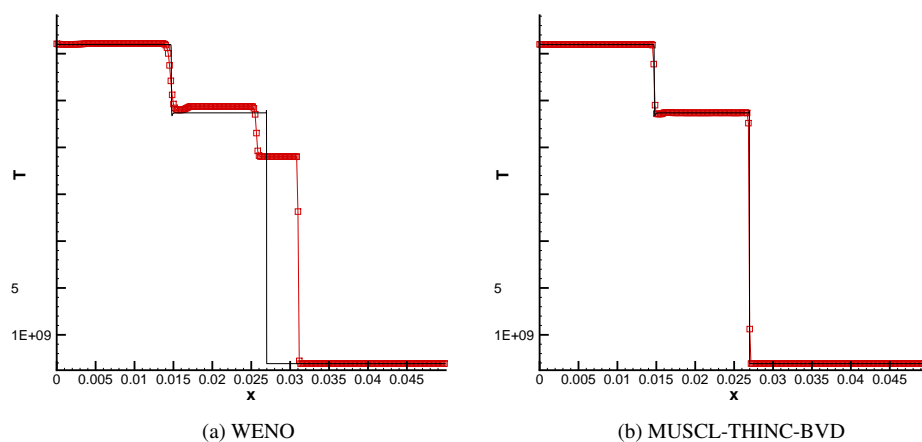


FIGURE 3.18: As for Fig. 3.17 but for the temperature field.

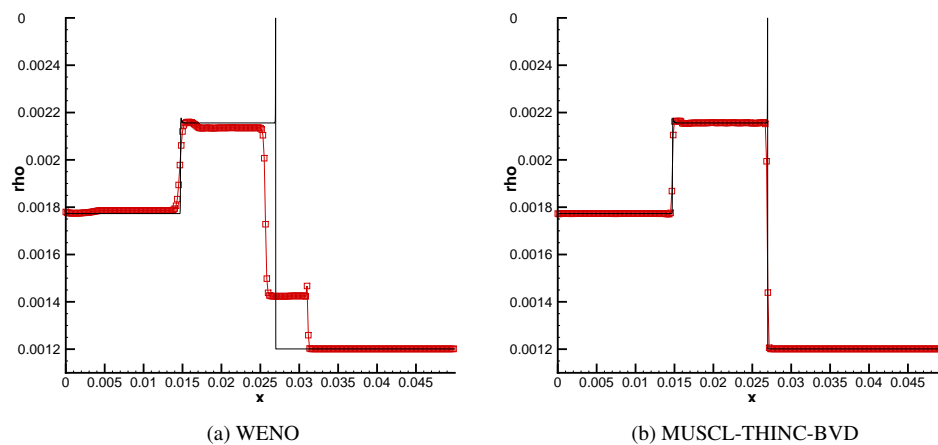


FIGURE 3.19: As for Fig. 3.17 but for the density field.

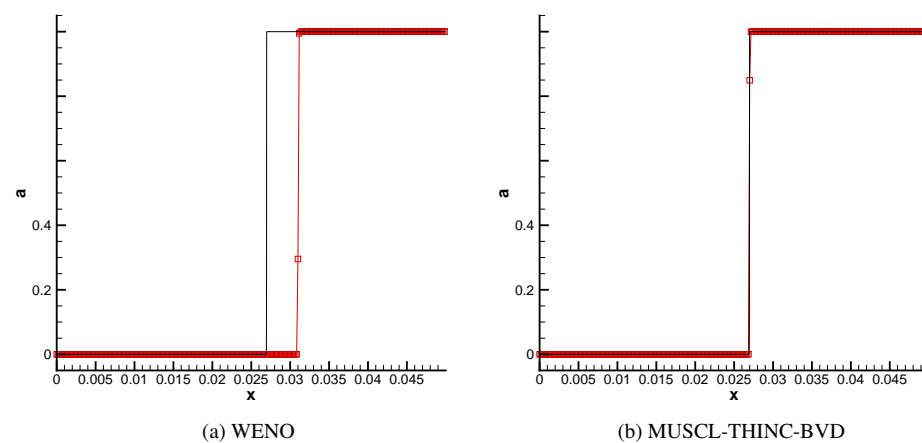


FIGURE 3.20: As for Fig. 3.17 but for mass fraction.

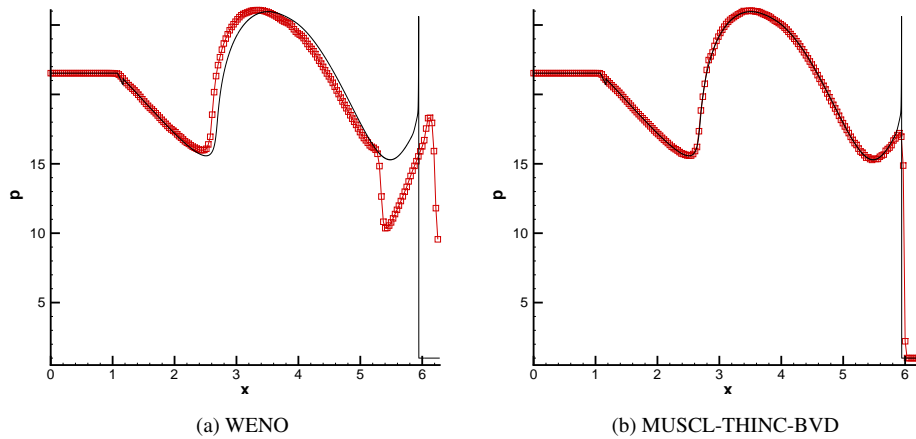


FIGURE 3.21: Numerical results of the pressure field from the interaction between a detonation wave and an oscillatory profile problem. Reference solutions are marked with black solid lines whereas the numerical solutions are in red with symbols to provide a comparison between the WENO and MUSCL-THINC-BVD schemes.

divided into $N = 200$ cells. The initial state is

$$(\rho, u, p, \alpha) = \begin{cases} (1.79463, 3.0151, 21.53134, 0.0) & x \leq \frac{\pi}{2} \\ (1.0 + 0.5 \sin 2x, 0.0, 1.0, 1.0) & \text{otherwise} \end{cases}. \quad (3.19)$$

The computation is run for $t = \frac{\pi}{5}$ with CFL=0.1. The numerical results for density, temperature, pressure, and mass fraction fields are plotted in Fig. 3.21–3.24. The MUSCL-THINC-BVD scheme still prevents the occurrence of spurious waves produced by the standard shock capturing WENO scheme, as well as resolves the complicated flow field produced by the interaction between detonation waves and oscillatory profiles.

At the end of this subsection, the CPU costs for each computational case shown above are summarized in Fig. 3.25. The computations were conducted with the same grid resolution and the same CFL number on a single CPU (Intel Core i7-4790, 3.60GHz). It can be seen that the time consumption of MUSCL-THINC-BVD is much less than the WENO due to the algorithmic simplicity of the proposed scheme.

Accuracy test for density propagation waves

In order to investigate the accuracy of the proposed scheme, propagating density wave is

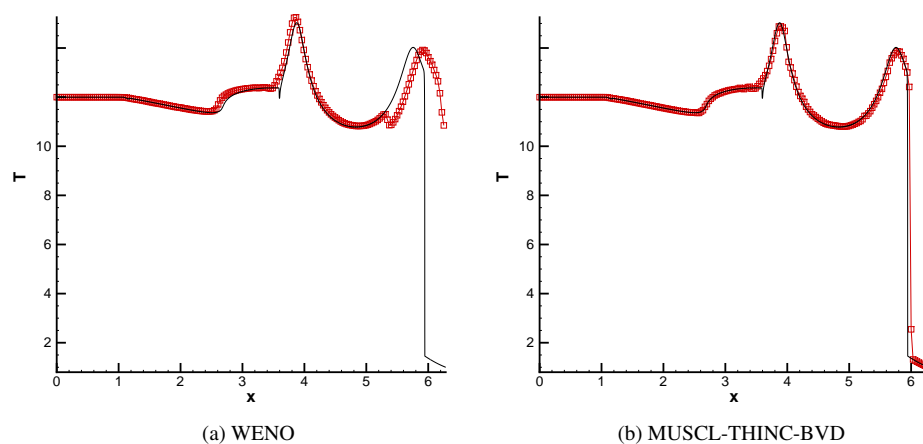


FIGURE 3.22: As for Fig. 3.21 but for the temperature field.

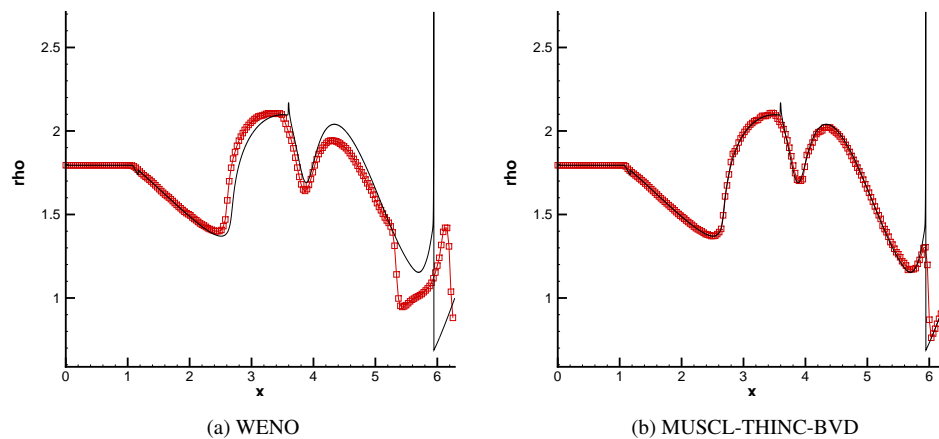


FIGURE 3.23: As for Fig. 3.21 but for the density field.

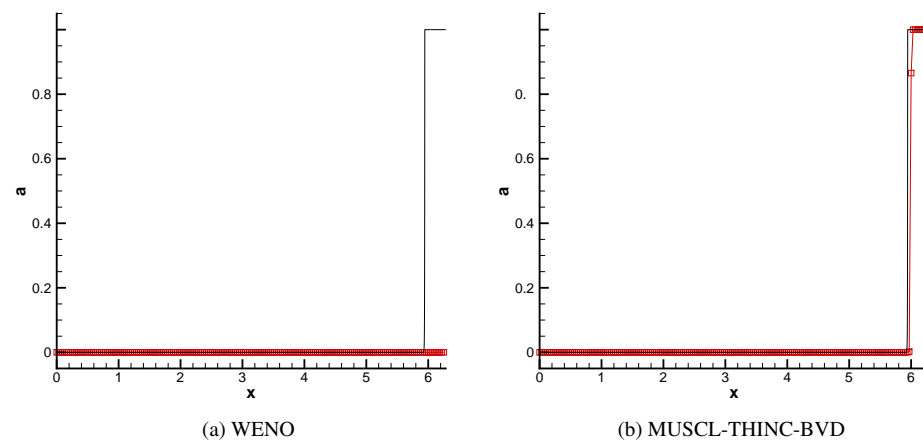


FIGURE 3.24: As for Fig. 3.21 but for mass fraction.

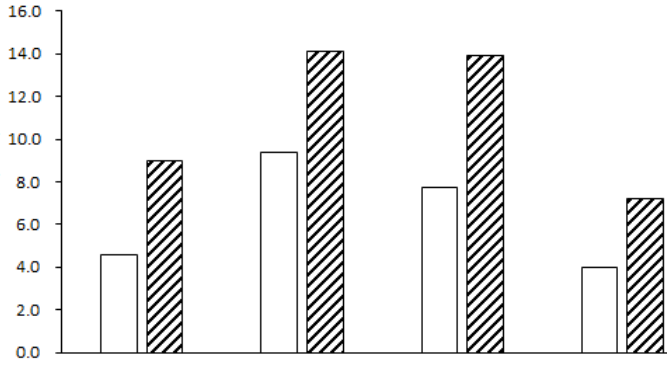


FIGURE 3.25: Comparison of time cost between MUSCL-THINC-BVD and WENO schemes.

studied in this test. The initial pressure and velocity field are set constant as $p_0 = 1.0$ and $u_0 = 1.0$, while an initial perturbation of density field is given by $\rho_0 = \sin(24.0\pi x) + 2.0$. The computation domain is $[-1, 1]$ where periodic boundary conditions applies to both left and right ends. The reaction effect is ignored in this test case. The L_1 errors and convergence rates of the numerical solutions of the MUSCL-THINC-BVD scheme on gradually refined meshes after one period at $t = 2.0$ with CFL=0.4 are shown in Fig. 3.26 in comparison with the original MUSCL scheme. It is seen from Fig. 3.26 (left) that the MUSCL-THINC-BVD scheme shows a similar convergence rate to the original MUSCL scheme, but substantially reduces the numerical errors for all mesh resolutions. For further comparison, we plot the density fields computed by different schemes with a $N = 800$ mesh. It is obvious that the MUSCL-THINC-BVD scheme is much superior to the original MUSCL scheme in resolving fine flow structures. It is noted that in the present work the minmod limiter, which is the most dissipative and of lowest accuracy among TVD schemes, is used in the BVD algorithm. This may degrade the convergence rate if THINC reconstruction is chosen. Nevertheless, through our numerical tests, uniform second order convergence rate can be achieved if more accurate TVD limiters such as van Leer are used. Moreover, as shown in [36] the BVD algorithm can realize higher convergence rate if a high order scheme, such as the WENO scheme therein, is used as a candidate reconstruction scheme in the BVD method.

Multi-species detonation wave with one reaction equation problems

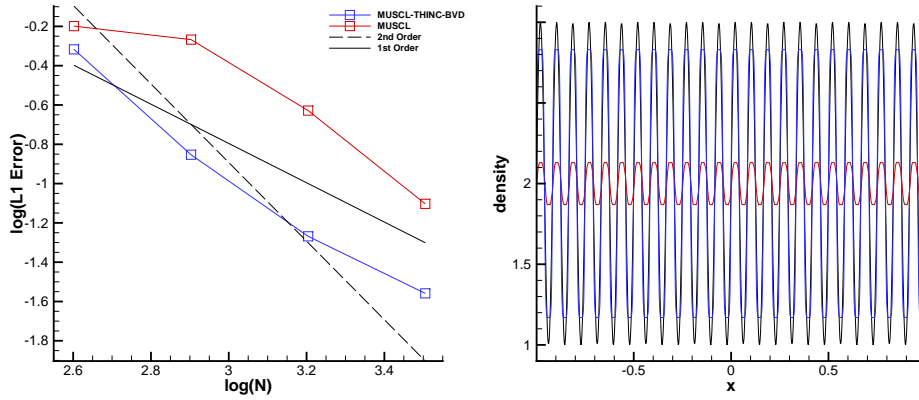


FIGURE 3.26: Numerical results for the propagating density wave test. L_1 errors and convergence rates from the mesh refinement computations by the original MUSCL scheme and the MUSCL-THINC-BVD scheme are plotted in the left panel, and the density profiles computed by different schemes on a 800-cell mesh are shown in the right panel.

As the MUSCL-THINC-BVD is a spatial reconstruction for finite volume formulation to solve general hyperbolic systems, extension to detonation waves involving multi-species is straightforward. In this test, we simulate the simple reaction $2\text{H}_2 + \text{O}_2 = 2\text{H}_2\text{O}$ as an example. The initial condition is set the same as [162, 163] where

$$(\rho, u, p, \alpha_{\text{H}_2}, \alpha_{\text{O}_2}, \alpha_{\text{H}_2\text{O}}) = \begin{cases} (2.0, 10.0, 40.0, 0.325, 0.0, 0.675) & x \leq 2.5 \\ (1.0, 0.0, 1.0, 0.4, 0.6, 0.0) & \text{otherwise} \end{cases}, \quad (3.20)$$

where α_{H_2} , α_{O_2} and $\alpha_{\text{H}_2\text{O}}$ are the mass fractions for hydrogen, oxygen and water respectively. This problem is solved on the interval $[0, 50]$ with the mesh number $N = 50$. The sub-step $N_r = 100$ is used in the reaction step. The exact solution consists of a detonation waves followed by a right-moving contact discontinuity and a shock. The numerical solutions of pressure and density fields at $t = 3$ with $\text{CFL}=0.1$ are presented in Fig. 3.27. It is obvious that the proposed MUSCL-THINC-BVD scheme is able to resolve the correct propagation speed of the detonation wave. However, the WENO scheme produces spurious waves as reported in [163].

2D stiff detonation problem

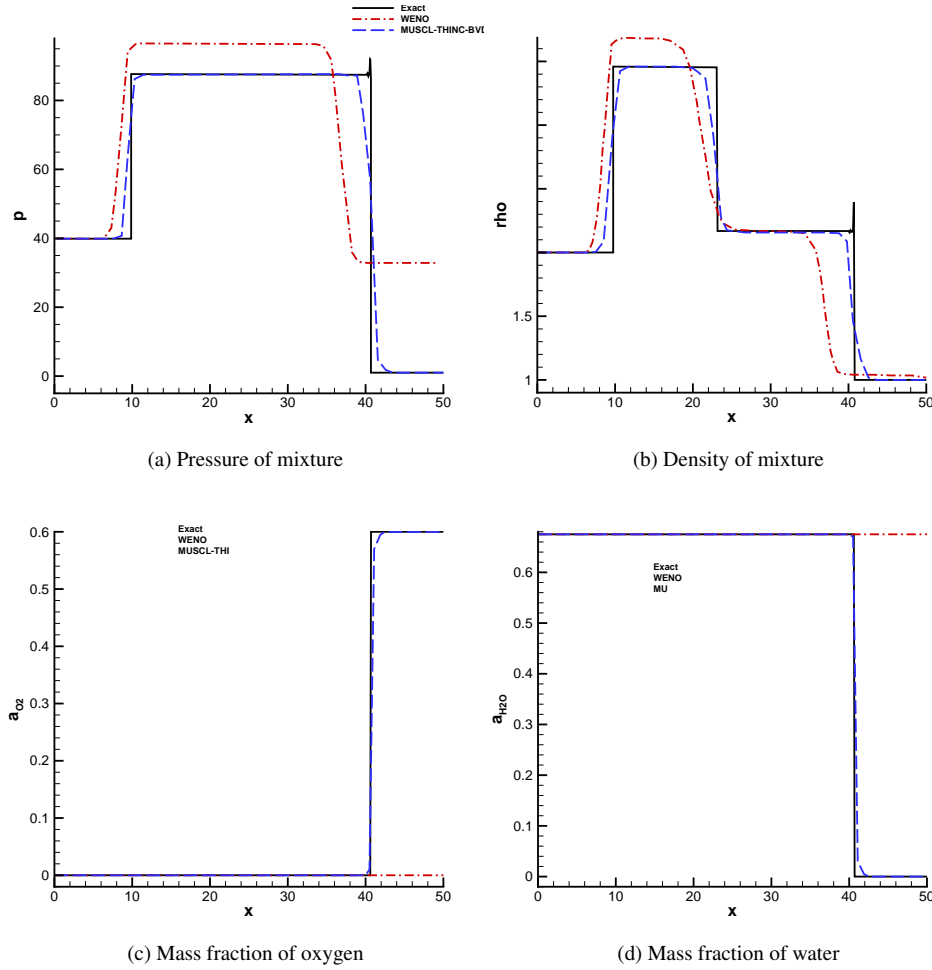


FIGURE 3.27: Numerical solutions for multi-species detonation wave. Comparisons are made between the WENO scheme and proposed MUSCL-THINC-BVD scheme. Displayed are the pressure, density and mass fractions for each species.

The two-dimensional detonation wave problem, which has also been investigated by the [68, 69, 80], is considered here. A two-dimensional shock tube is configured within a computational domain of $[0, 0.025] \times [0, 0.005]$. Reflective boundary conditions are imposed on the upper and lower boundaries, whereas the zero-gradient boundary condition is imposed on the left and right boundaries. The parameters q_0 , $\frac{1}{\xi}$ and T_{ign} in the Heaviside chemical reaction model are the same as in the one-dimensional case. The initial conditions are

$$(\rho, u, v, p, \alpha) = \begin{cases} (\rho_l, u_l, 0, p_l, 0) & \text{if } x \leq \psi(y) \\ (\rho_r, u_r, 0, p_r, 1) & \text{if } x > \psi(y), \end{cases} \quad (3.21)$$

where

$$\psi(y) = \begin{cases} 0.004 & \text{if } |y - 0.0025| \geq 0.001 \\ 0.005 - |y - 0.0025| & \text{if } |y - 0.0025| < 0.001. \end{cases} \quad (3.22)$$

The right states $(\rho_r, u_r, 0, p_r, 1)$ are the same as in Section 3.6.2 and $\rho_l = \rho_{CJ}$, $p_l = p_{CJ}$ whereas $u_l = 8.162 \times 10^4 > u_{CJ}$. As stated in [92], one important feature of this solution is that a cellular pattern forms after the triple points travel in the transverse direction and reflect back and forth between the upper and lower boundaries, which will produce more complex solution than the corresponding one dimensional case.

The CFL number is set to 0.1. To provide a better comparison, the reference solution is calculated using the standard 5th-order WENO scheme with 2000×400 grid cells. At the same time, a comparison is made between the MUSCL-THINC-BVD and WENO schemes with 400×80 cells. The density profiles at different times are presented in Fig. 3.28–3.30 in which the reference solutions are shown on the left side and the solutions with 400×80 grid cells obtained using WENO and MUSCL-THINC-BVD are shown in the center and right side, respectively. In Fig. 3.28, the reaction zone are smeared using the WENO scheme compared with that for the MUSCL-THINC-BVD scheme. Moreover, MUSCL-THINC-BVD resolves the two vortices formed behind the detonation front as also noted in [29] as the BVD algorithm can improve the resolution quality. In Figs. 3.29 and 3.30, spurious waves in front of the detonation are produced by the WENO scheme whereas the MUSCL-THINC-BVD scheme has produced a sharp detonation front on a coarse mesh. To further illustrate the performance of the proposed scheme, the density distribution along $y = 0.0025$ at $t = 1.7 \times 10^{-7}$ is plotted in Fig. 3.31. Again WENO scheme produces spurious waves in front of shock. However, the proposed MUSCL-THINC-BVD scheme can simulate stiff detonation waves with less numerical dissipation.

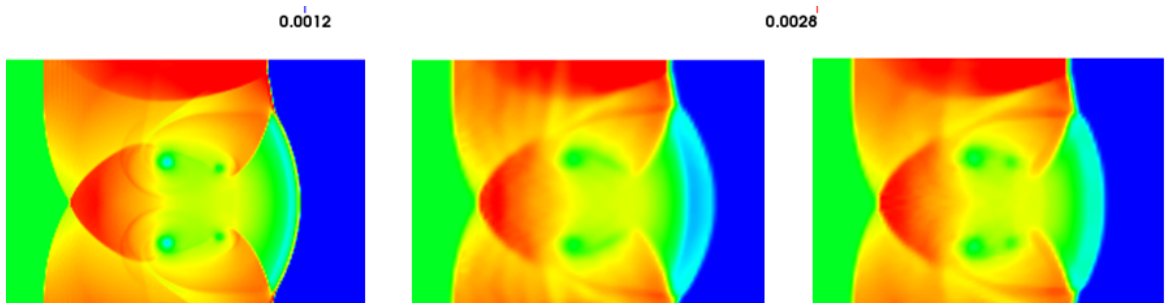


FIGURE 3.28: Density field of the 2D detonation problem at $t = 0.3 \times 10^{-7}$. Comparisons are made between the reference solution, the WENO scheme with a coarse mesh, and the MUSCL-THINC-BVD with a coarse mesh. The profile at the left side is the reference result calculated using the WENO scheme with 2000×400 grid cells. The middle and right profiles are the results calculated using the WENO and MUSCL-THINC-BVD, schemes respectively, both with 400×80 grid cells.

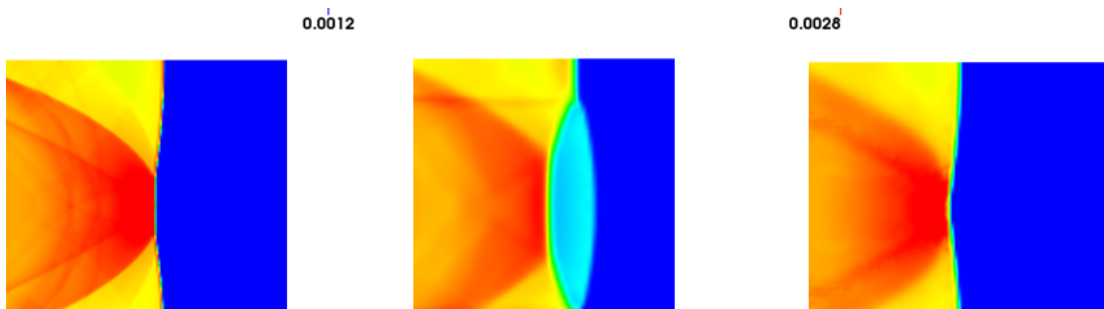


FIGURE 3.29: As for Fig. 3.28 but at $t = 0.92 \times 10^{-7}$.

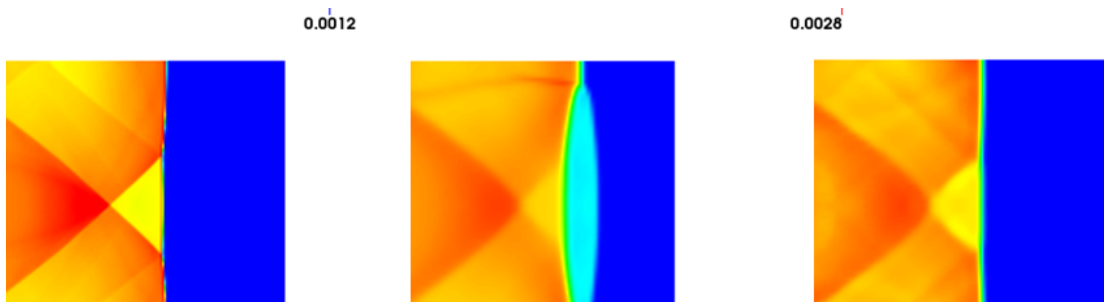


FIGURE 3.30: As for Fig. 3.28 but at $t = 1.7 \times 10^{-7}$.

3.6 Numerical experiments of adaptive THINC-BVD scheme

In this section, some comparative tests in one- and two- dimensions are conducted between the 5th order WENO scheme and the proposed adaptive BVD-THINC scheme. The reconstruction process is conducted in terms of primitive variables and the ratio of specific heats is set to $\gamma = 7/5$.

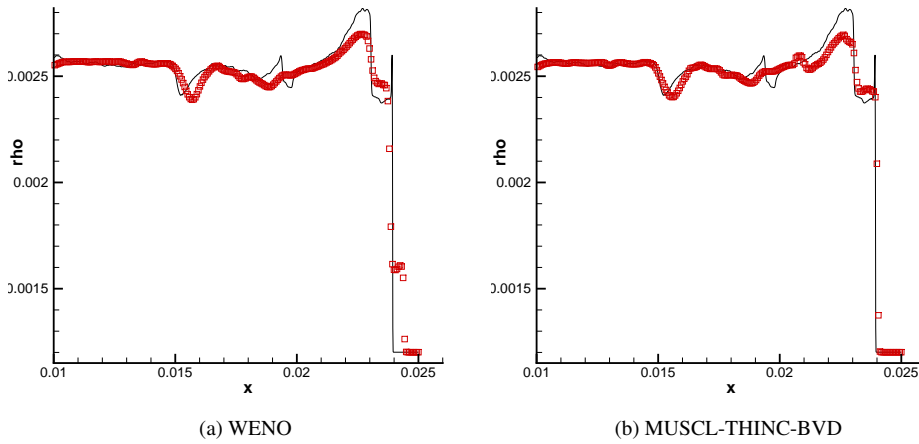


FIGURE 3.31: Density field along the central line of x direction at $t = 1.7 \times 10^{-7}$. Reference solutions are marked with black solid lines whereas the numerical solutions are in red with symbols to provide a comparison between the WENO and MUSCL-THINC-BVD schemes.

3.6.1 1D Euler equations

Accuracy test for density propagation waves

In order to investigate the accuracy of the proposed scheme, propagating density wave is studied in this test. The initial pressure and velocity field are set constant as $p_0 = 1.0$ and $u_0 = 1.0$, while an initial perturbation of the density field is given by $\rho_0 = \sin(\pi x) + 1.0$. The computation domain is $[-1, 1]$ and periodic boundary conditions are applied to both left and right ends. The L_1 , L_∞ errors and corresponding convergence rates are calculated on gradually refined meshes after one period at $t = 2.0$ with CFL=0.4. Comparisons are made amongst the proposed adaptive THINC-BVD, TVD schemes with different limiters and the 5th order accurate WENO scheme. We observe in Table. 3.1 that adaptive THINC-BVD scheme has much smaller errors in both L_1 and L_∞ norms compared to TVD schemes with Minmod, Van Leer or Superbee limiters. Moreover, the proposed scheme shows a uniform 2nd order convergence rate in L_1 for this test with smooth solution. The WENO scheme demonstrates higher-order accuracy and less numerical errors for the smooth solution. As showcased in [36], by using WENO or other high-order schemes as one of the candidates for reconstruction, the BVD algorithm can

TABLE 3.1: Numerical errors and convergence rate for density propagation waves problem. Comparisons are made among different schemes.

Schemes	Mesh	L_1 errors	L_1 order	L_∞ errors	L_∞ order
Minmod	40	4.547×10^{-2}		1.025×10^{-1}	
	80	1.337×10^{-2}	1.77	4.347×10^{-2}	1.23
	160	3.812×10^{-3}	1.81	1.795×10^{-2}	1.27
	320	1.031×10^{-3}	1.89	7.298×10^{-3}	1.30
Van Leer	40	2.101×10^{-2}		5.151×10^{-2}	
	80	5.568×10^{-3}	1.92	1.952×10^{-2}	1.40
	160	1.408×10^{-3}	1.98	7.302×10^{-3}	1.42
	320	3.423×10^{-4}	2.04	2.715×10^{-3}	1.43
Superbee	40	2.134×10^{-2}		6.087×10^{-2}	
	80	9.024×10^{-3}	1.24	3.443×10^{-2}	0.82
	160	2.642×10^{-3}	1.77	1.487×10^{-2}	1.21
	320	7.159×10^{-4}	1.88	6.651×10^{-3}	1.16
THINC-BVD	40	1.518×10^{-2}		4.721×10^{-2}	
	80	3.766×10^{-3}	2.01	1.821×10^{-2}	1.37
	160	8.969×10^{-4}	2.07	6.866×10^{-3}	1.41
	320	2.198×10^{-4}	2.03	2.545×10^{-3}	1.43
WENO	40	4.473×10^{-5}		8.799×10^{-5}	
	80	1.396×10^{-6}	5.00	2.822×10^{-6}	4.96
	160	4.361×10^{-8}	5.00	8.487×10^{-8}	5.06
	320	1.361×10^{-9}	5.00	2.544×10^{-9}	5.06

realize higher-order and more accurate numerical results for smooth solutions. Nevertheless, as shown in following numerical tests, adaptive THINC-BVD will outperform high order WENO schemes when solving problems involving discontinuities.

Sod's problem

As one of famous benchmark tests for shock-capturing schemes, the Sod problem is employed here to test the performance of schemes in capturing the shock front as well as the contact discontinuity. The initial distribution on computational domain $[0, 1]$ is specified as [76]

$$(\rho_0, u_0, p_0) = \begin{cases} (1, 0, 1) & 0 \leq x \leq 0.5 \\ (0.125, 0, 0.1) & \text{otherwise} \end{cases}. \quad (3.23)$$

The computation is carried out with 200 uniform cells and with time integrated up

to $t = 0.25$. The comparative numerical results calculated from WENO scheme and the proposed solver are shown in Fig. 3.32 for density and pressure fields respectively. From the results, it can be seen that standard 5th order WENO scheme can solve both the shock wave and contact discontinuity without numerical oscillations. However, just like other standard shock-capturing schemes, the WENO schemes present difficulties to sharply solve discontinuous linearly degenerate fields which correspond to contact discontinuities. However it can get satisfying results for the shock since shock waves have the compressive character. On the contrary, the proposed scheme can solve contact discontinuities on one or two cells only. Moreover, it reduces the numerical diffusion around shock as well. These results show that the proposed scheme has good performance in capturing discontinuous solutions for this only mildly difficult test.

Lax's problem

The Lax problem is employed here to check the ability of the proposed numerical scheme to capture relatively strong shock. The initial condition is given by

$$(\rho_0, u_0, p_0) = \begin{cases} (0.445, 0.698, 3.528) & 0 \leq x \leq 0.5 \\ (0.5, 0, 0.571) & \text{otherwise} \end{cases} . \quad (3.24)$$

With the same number of cells as in previous case, the computation lasts until time $t = 0.16$. From the result shown in Fig. 6.15, we can see that the contact discontinuous solution can be resolved sharply while a much diffused profile is produced by WENO scheme since around strong discontinuities WENO scheme, just like other high order polynomial-based reconstruction schemes, does sacrifice some accuracy preventing the occurrence of spurious numerical oscillations.

Collela-Woodward blastwaves

In Collela and Woodward introduced their famous blastwave involving multiple interactions of strong shocks and rarefaction waves. The initial distribution has uniform density of $\rho = 1$ and zero velocity. The domain $\Omega = [0, 1]$ is split into three parts

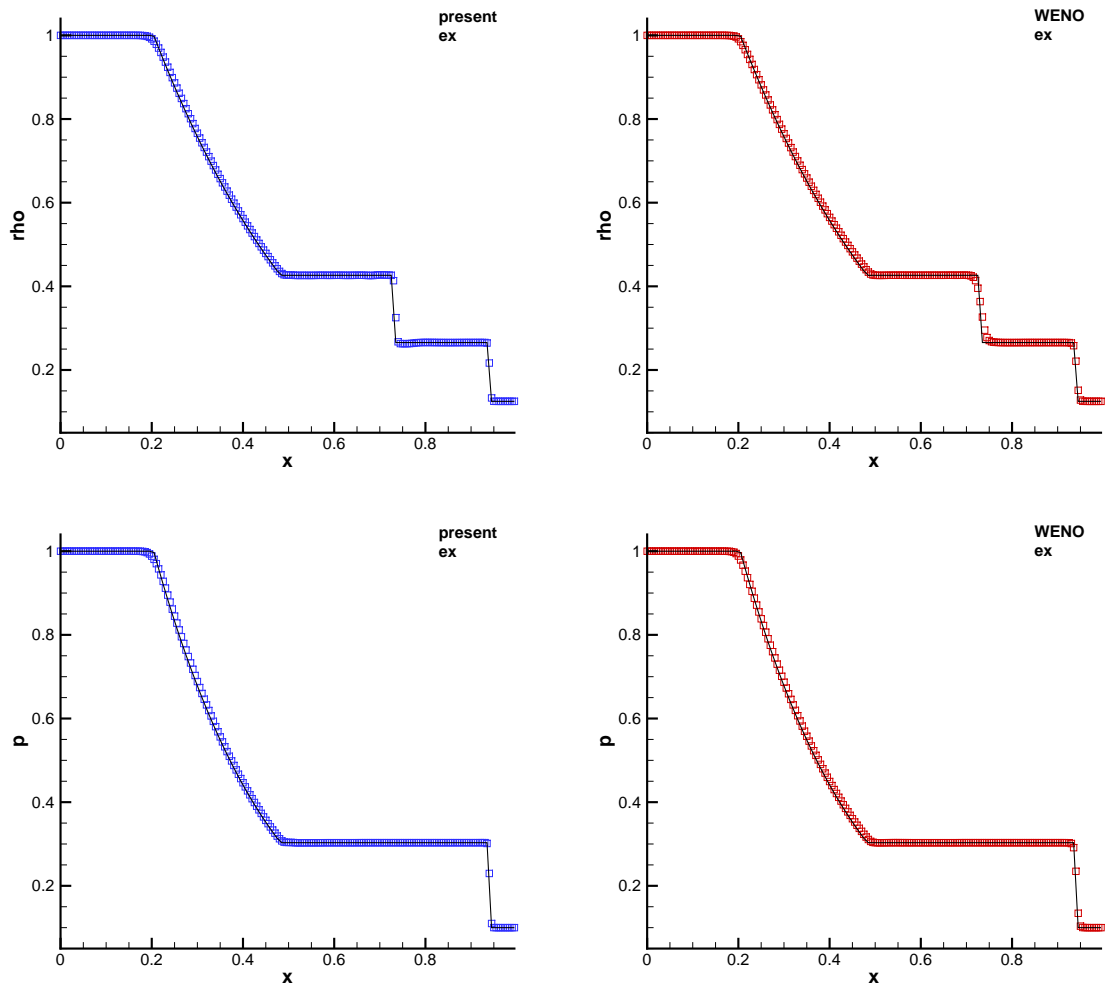


FIGURE 3.32: Numerical results of Sod's problem for density field (top) and pressure (bottom) at $t = 0.25$ with 200 cells. Comparisons are made between the proposed scheme (left panels) and WENO scheme (right panels) and the exact solution (straight line).

$\Omega_L = [0, 0.1]$, $\Omega_M = [0.1, 0.9]$ and $\Omega_C = [0.9, 1]$ for which the constant pressure values are $p_L = 1000$, $p_M = 0.01$ and $p_R = 100$. Reflective boundary conditions are imposed at the two ends of computational domain. Two blast waves are generated by the initial jumps and then evolve and violently interact. Classically 400 mesh cells are used in the literature for this test problem when high order schemes are tested. We depict the numerical density at time $t = 0.038$ in Fig. 3.34 against a reference solution obtained with WENO scheme with a very fine mesh. The solution produced by WENO scheme for 400 cells presents discontinuities, contact and shock which are smeared, especially the first contact discontinuity around $x \simeq 0.6$. On the contrary the proposed scheme

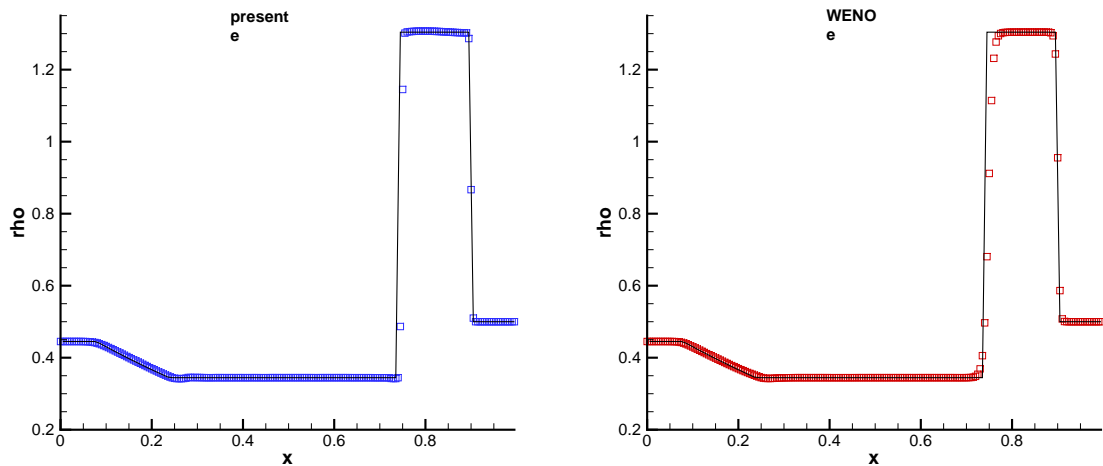


FIGURE 3.33: Numerical results of Lax's problem for density field at time $t = 0.16$ with 200 cells. Comparisons are made between the proposed THINC-BVD scheme (left panel) and WENO scheme (right panel) against the exact solution (straight line).

can capture this contact discontinuity with only three points, while polynomial based high order scheme may demand several tenths of cells. For comparison purposes we also provide the results obtained by a discrete staggered compatible Lagrangian scheme on the right panel of Fig. 3.34, see [77]. Such mesh moving (Lagrangian) numerical method preserves exactly the contact discontinuities because the mesh moves with the fluid velocity. Therefore this scheme is one of the most accurate tools to capture those contact discontinuities. It is seen that the proposed BVD scheme's results compare well with Lagrangian ones¹.

Sedov blast wave

We verify the robustness of the present scheme on Sedov blast wave which involves low density and low pressure. The initial condition is set as the same as [78, 79] in which (ρ_0, u_0, p_0) is $(1.0, 0.0, 10^{-12})$ everywhere except that the energy in the center cell is given by the constant $\frac{E_0}{\Delta x}$ with $E_0 = 3.2 \times 10^6$. Such high energy deposition generates strong left and right moving shocks, followed by exponential decay of density and pressure. Those exponential decays leads to almost near vacuum region in the

¹ Note that the Lagrangian results present an overshoot of three cells at about $x = 0.765$ of maximal value $\rho = 9.5$ which are omitted here because it does not alter our comments.

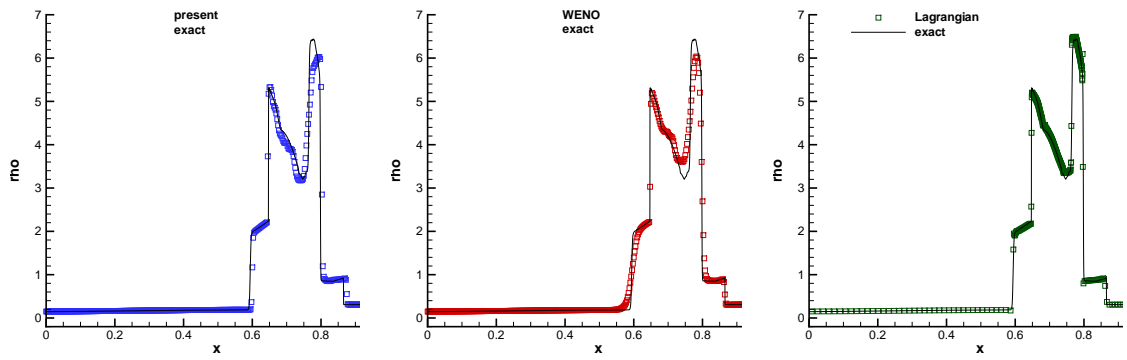


FIGURE 3.34: Numerical results of two interacting blast waves problem for density field at $t = 0.038$ with 400 cells. Comparisons are made between the proposed scheme (left), WENO scheme (middle) and a discrete staggered compatible Lagrangian scheme (right).

center of the domain. The mesh size is $\Delta x = \frac{1}{200}$ and the mesh is uniform. Since this problem involves near-vacuum condition, numerical oscillations given by the high order reconstruction schemes may break up the computation. Thus positivity-preserving techniques are usually demanded to preserve positivity of density. Without relying on high order polynomials as reconstruction function, the present scheme is able to solve this near-vacuum state without any extra positivity-preserving technique. The computational result is presented in the Fig. 3.35 where we plot the density and pressure vs the exact solution. Compared with the Fig. 5.1 in [78] the results of which are obtained by a positivity-preserving WENO scheme, the present scheme produces sharper solutions around the shocks without the need to add extra dissipation for the near-vacuum states.

3.6.2 1D Euler reacting equations for stiff detonation

C-J detonation wave with the Heaviside model

In this example, the C-J detonation for which the chemical reaction is modeled by a simple Heaviside function is considered. Likewise as in [68, 80, 81], the parameter values of the model are $\frac{1}{\xi} = 0.5825 \times 10^{10}$, $\gamma = 1.4$, $q_0 = 0.5196 \times 10^{10}$ and

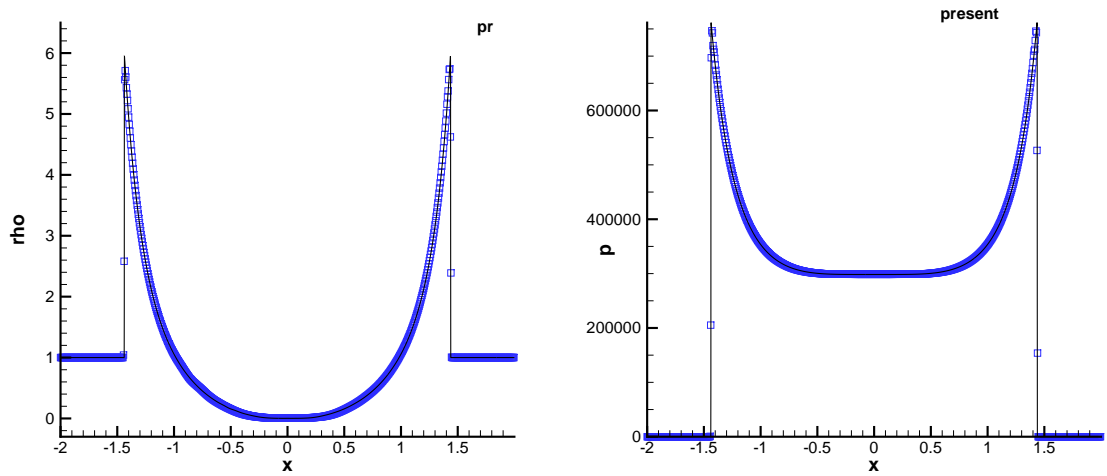


FIGURE 3.35: Numerical results of Sedov blast wave problems. The solution of density field is presented on the left while pressure field on the right vs the exact solution (straight line).

$T_{ign} = 0.1155 \times 10^{10}$. The computational domain is $[0, 0.05]$ and the initial discontinuity is set at $x = 0.005$. The totally burnt gas is set on the right side with the initial state: $\rho_0 = 1.201 \times 10^{-3}$, $u_0 = 0.0$ and $p_0 = 8.321 \times 10^5$. The totally unburnt gas is set on the left side where $(\rho_{CJ}, u_{CJ}, p_{CJ}, 0.0)$ are determined by the C-J detonation model [82, 83]. The computation is performed with uniform mesh of cell number $N = 300$ until final time $t = 3 \times 10^{-7}$. At this time the exact position of the burning wave is at $x = 0.03764$ and the states to the left and right are known. When dealing with such stiff hyperbolic system, standard shock-capturing schemes with insufficient grid resolution may produce incorrect propagation speed and non-physical spurious waves even with enough temporal resolution. Due to the presence of large numerical dissipation around the discontinuity for classical shock-capturing schemes, the chemical reaction may be triggered too early in the adjacent cell of an numerically smeared discontinuity for which the temperature profile contains the value above the ignition temperature. If the reaction is fast, the wrongly triggered chemical reaction does shift the discontinuity, and consequently produces non-physical reflected or refracted waves and a wrong chronometry for physical ones. To verify that our scheme can prevent the creation of non-physical spurious waves by virtue of its low numerical dissipation around discontinuity, we solve this problem by setting the CFL= 0.01 for the 5th order WENO scheme,

while we fix the CFL= 0.1 for the proposed scheme.

The results of density, temperature and mass fraction are plotted in Fig. 3.36 where the reference solution is calculated by the standard 5th order WENO scheme with $N = 10000$ cells. We observe that while the proposed approach can correctly capture the wave front, WENO presents the previously described drawbacks even with smaller CFL numbers. For WENO scheme, CFL= 0.1 number will make spurious phenomena more severe. In fact, as reported in [68] wrong results are produced by standard WENO schemes no matter how small the time step is since the stiffness problem is due to spatial rather than the temporal errors. It is noted that being the benchmark case to test numerical methods, the stiff detonation model used here presents more severe conditions than the physically realizable cases. Having verified with the stiff C-J detonation wave test, the proposed scheme also works well for non-stiff problems which have more physical significance.

Interaction between a detonation wave and an oscillatory profile

Interaction between a detonation wave and an oscillatory profile is considered in this section, see [68, 84]. The parameters of the model are $\gamma = 1.2$, $q_0 = 50$, $\frac{1}{\xi} = 1000$ and $T_{ign} = 3$. The computational domain is set as $[0, 2\pi]$ divided by $N = 200$ uniform cells. The initial state is

$$(\rho_0, u_0, p_0, \alpha_0) = \begin{cases} (1.79463, 3.0151, 21.53134, 0.0) & x \leq \frac{\pi}{2} \\ (1.0 + 0.5 \sin(2x), 0.0, 1.0, 1.0) & \text{otherwise} \end{cases}. \quad (3.25)$$

The simulation is run to final time $t = \frac{\pi}{5}$ with CFL= 0.1. The numerical results of density, temperature and mass fraction fields are plotted in Fig. 3.37. We observe that the proposed scheme can effectively prevent the occurrence of spurious waves which are produced by standard shock capturing WENO scheme. Also, the complicated flow field produced by the interaction between the detonation wave and the oscillatory profiles can be sharply resolved by the proposed scheme, while the effect of wrong wave

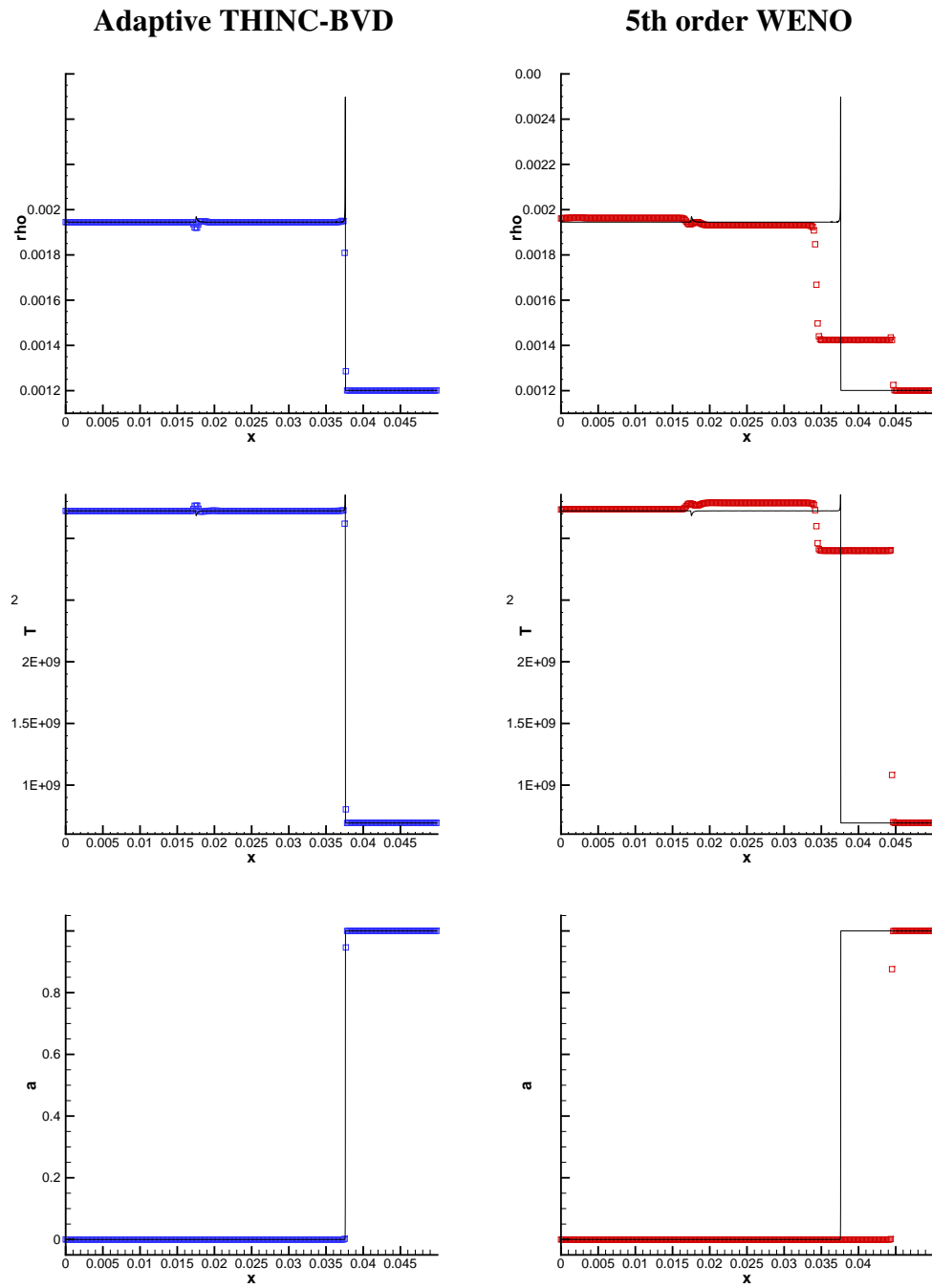


FIGURE 3.36: Numerical results of density, temperature and mass fraction fields for C-J detonation wave with the Heaviside chemical reaction model. Reference solutions are represented by black solid lines. Comparisons are made between the WENO (right panels) and the proposed scheme (left panels).

computation does dramatically pollute WENO results.

3.6.3 2D Euler equations

2D Riemann problems

A set of two-dimensional Riemann problems which have been proposed and extensively studied in [58, 85] is employed to verify that the behaviors of the proposed THINC-BVD scheme on Euler equations. This test is employed to prove that the extension of the THINC-BVD scheme to two dimensions can produce accurate, robust and non-oscillatory solutions. Involving different configurations based on an initial condition made of 2×2 constant states, the 2D Riemann problems are usually employed as benchmark tests to examine the behavior of new schemes. Note that most of the interfaces between those states are Kelvin-Helmholtz instable. As a consequence it has been reported by several works [67, 86–90] that the sharp capture of discontinuities along with the resolution of small-scale features generated by the Kelvin-Helmholtz instability does require fine enough grids or very high order schemes. The computational domain is set to $[-0.5, 0.5] \times [-0.5, 0.5]$, and four different configurations are studied in this work, the initial conditions of which are as follows,

Riemann problem #1:

$$(\rho_0, u_0, v_0, p_0) = \begin{cases} (2.0, 0.75, 0.5, 1.0) & x \leq 0.0, y \geq 0.0 \\ (1.0, -0.75, 0.5, 1.0) & x < 0.0, y < 0.0 \\ (1.0, 0.75, -0.5, 1.0) & x > 0.0, y > 0.0 \\ (3.0, -0.75, -0.5, 1.0) & x > 0.0, y < 0.0 \end{cases}. \quad (3.26)$$

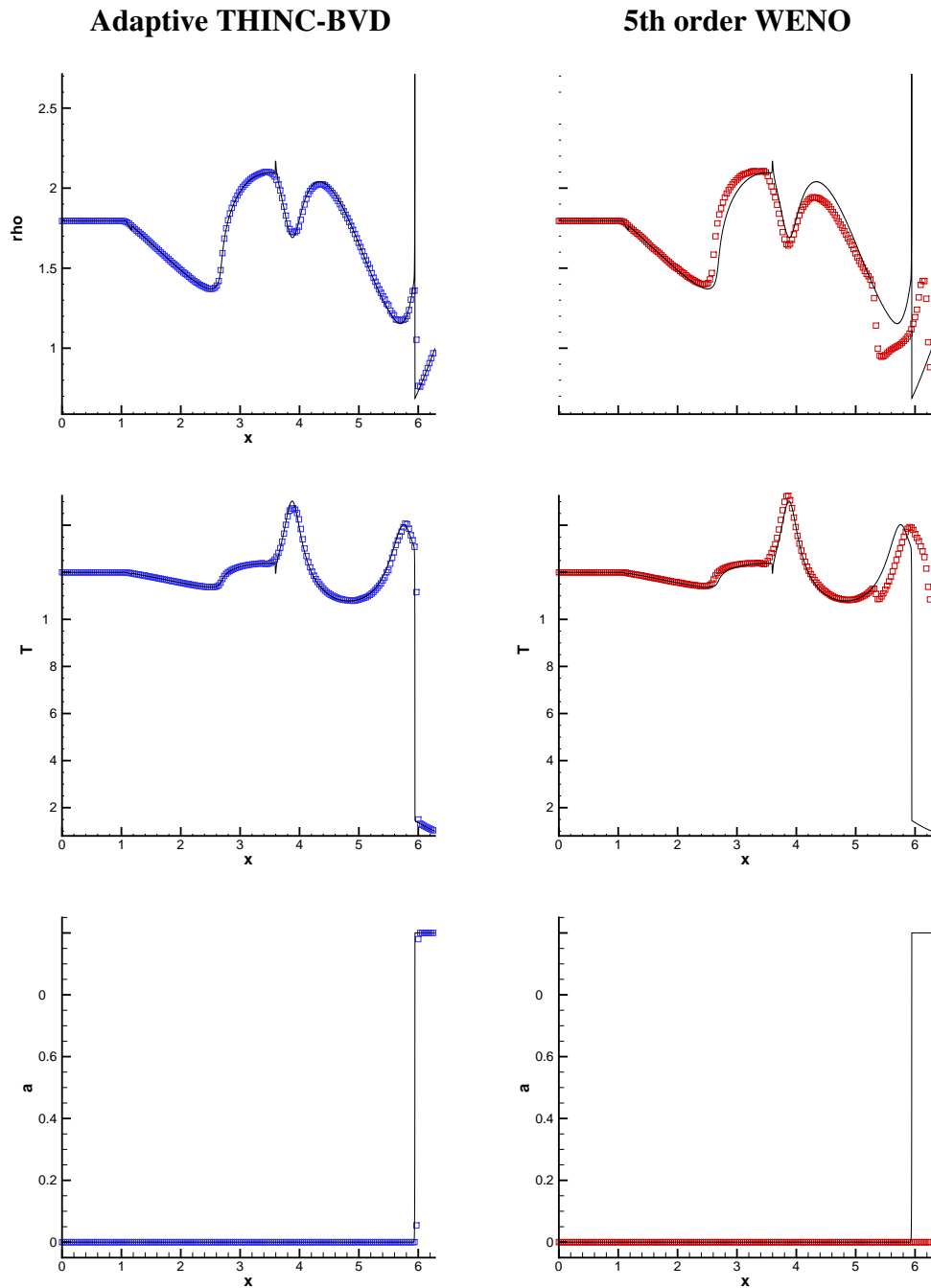


FIGURE 3.37: Numerical results of density, temperature and mass fraction fields for C-J detonation wave with the Heaviside chemical reaction model for the interaction between a detonation wave and an oscillatory profile problem. Reference solutions are represented by black solid lines. Comparisons are made between the WENO (right panels) and the proposed scheme (left panels).

Riemann problem #2:

$$(\rho_0, u_0, v_0, p_0) = \begin{cases} (2.0, -0.75, 0.5, 1.0) & x \leq 0.0, y \geq 0.0 \\ (1.0, 0.75, 0.5, 1.0) & x < 0.0, y < 0.0 \\ (1.0, -0.75, -0.5, 1.0) & x > 0.0, y > 0.0 \\ (3.0, 0.75, -0.5, 1.0) & x > 0.0, y < 0.0 \end{cases}. \quad (3.27)$$

Riemann problem #3:

$$(\rho_0, u_0, v_0, p_0) = \begin{cases} (0.5323, 1.206, 0.0, 0.3) & x \leq 0.3, y \geq 0.3 \\ (0.138, 1.206, 1.206, 0.029) & x < 0.3, y < 0.3 \\ (1.5, 0.0, 0.0, 1.5) & x > 0.3, y > 0.3 \\ (0.5323, 0.0, 1.206, 0.3) & x > 0.3, y < 0.3 \end{cases}. \quad (3.28)$$

Riemann problem #4:

$$(\rho_0, u_0, v_0, p_0) = \begin{cases} (0.5197, -0.6259, 0.1, 0.4) & x \leq 0.0, y \geq 0.0 \\ (0.8, 0.1, 0.1, 0.4) & x < 0.0, y < 0.0 \\ (1.0, 0.1, 0.1, 1.0) & x > 0.0, y > 0.0 \\ (0.5197, 0.1, -0.6259, 0.4) & x > 0.0, y < 0.0 \end{cases}. \quad (3.29)$$

A uniform grid made of 600×600 cells is employed in all calculation. The numerical results calculated by the proposed scheme and the WENO scheme are all presented in Fig. 3.38. The density variable contours are plotted with an identical color scale for both schemes. The reference results can be found in [90] where grid of 1200×1200 and six order WENO schemes are used to solve those 2D Riemann problems. From the results of Fig. 3.38 we can first observe that the two schemes produce comparable numerical solutions for the main flow structures. However the proposed scheme does capture sharper discontinuities than WENO scheme. Moreover the occurrence

and the number of small scale structures are more pronounced by THINC-BVD. Contrarily to the statement made in [67] that the number of vortices will depend on the order of the scheme and cell size, we show that a supposedly low-order scheme such as THINC-BVD can nonetheless significantly reduce the numerical viscosity around discontinuities, and, also, can produce more small-scale flow structures. In addition, the performance of proposed scheme is evaluated through the comparison of the CPU times of three methods: a second-order classical TVD scheme, the 5th order WENO and the current THINC-BVD scheme. All methods have been developed under the same framework by the same developer so that this comparison is rather fair.

In Fig 3.39 we gather the CPU times and the ratio between those CPU times. It can be seen that on average and consistently THINC-BVD is about 2 times more expensive than TVD, while WENO costs more than 5 times. As a consequence WENO is nearly 3 times slower than THINC-BVD. The results substantiate that the proposed THINC-BVD scheme improves the numerical accuracy at a very low computational cost leading to a genuine appealing computational efficiency.

Double Mach reflection

A Mach 10 hypersonic propagating planar shock reflected by 30° ramp is simulated in this test case. Although there exists no exact solution, this test has been adopted as a standard benchmark test to assess the ability of a numerical scheme to capture accurately both the strong reflected and refracted shocks as well as the small-scale structures in the re-circulation zone. The low dissipation of a numerical scheme can be visually estimated by the number vortex structures resulting from Kelvin-Helmholtz instabilities along the slip line in the re-circulation zone. The numerical schemes with large numerical viscosity tend to smear out these structures. The computational domain is $[0, 3.2] \times [0, 1]$. A right-moving Mach 10 shock is imposed with 60° angle relative to x -axis. At the right boundary of the computational domain, the boundary condition is given by setting all gradients to be zero. The solution is computed up to time $t = 0.2$ with two different grid resolutions, $\Delta x = \Delta y = \frac{1}{100}$ for the top panels of Fig. 3.40

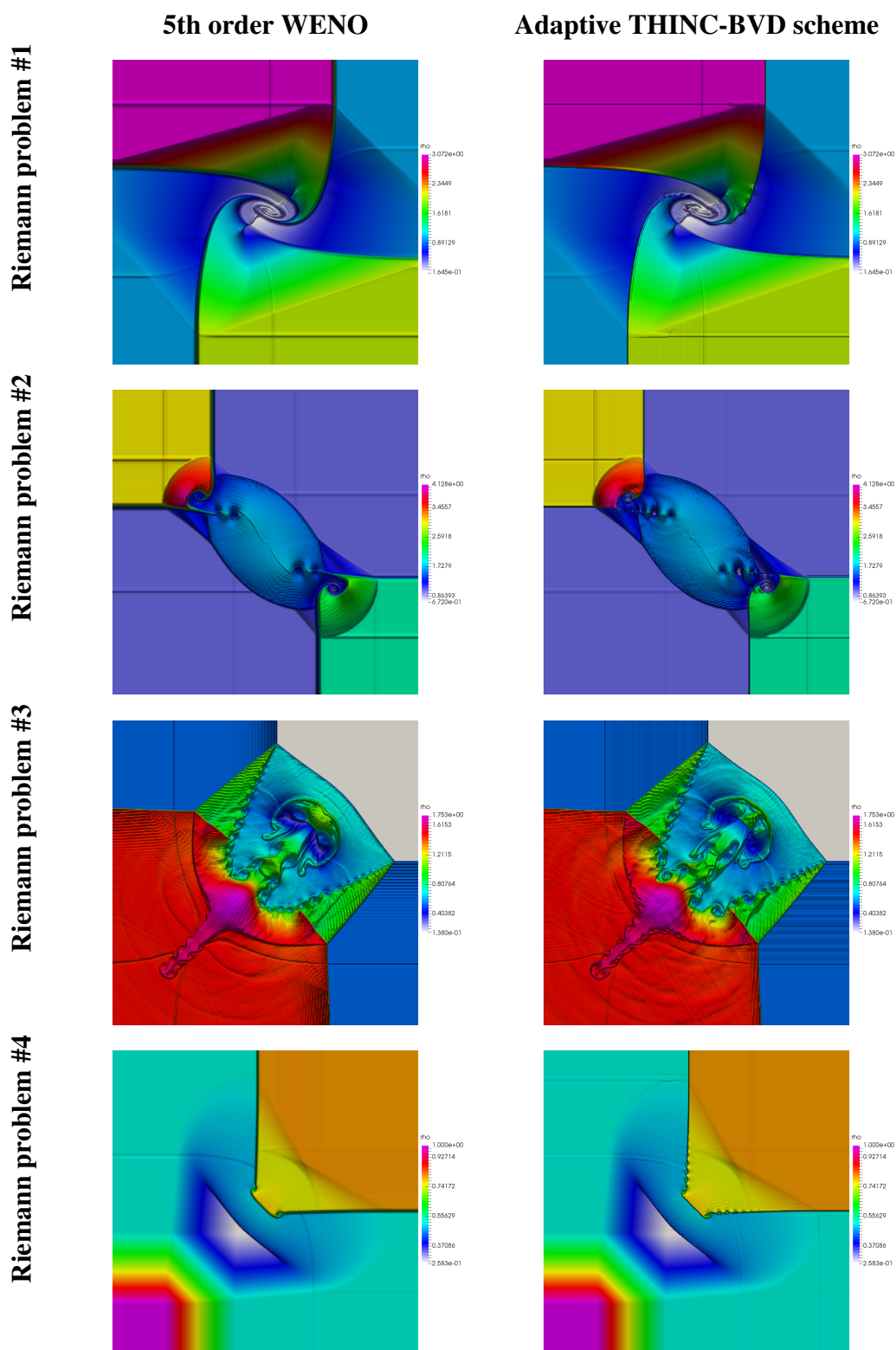


FIGURE 3.38: Density contour for Riemann problems 1, 2, 3, 4. Left: 5th order WENO scheme results. Right: Adaptive THINC-BVD scheme results.

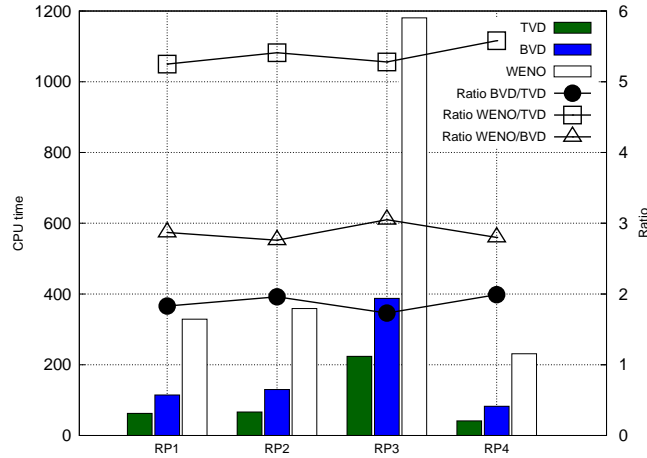


FIGURE 3.39: CPU times recorded for Riemann problems #1, #2, #3, and #4 simulated by the TVD, WENO and BVD schemes. Comparisons are made amongst TVD, adaptive BVD and WENO schemes. Histograms (left axis): CPU time — Symbol-lines (right axis): ratio between the CPU times.

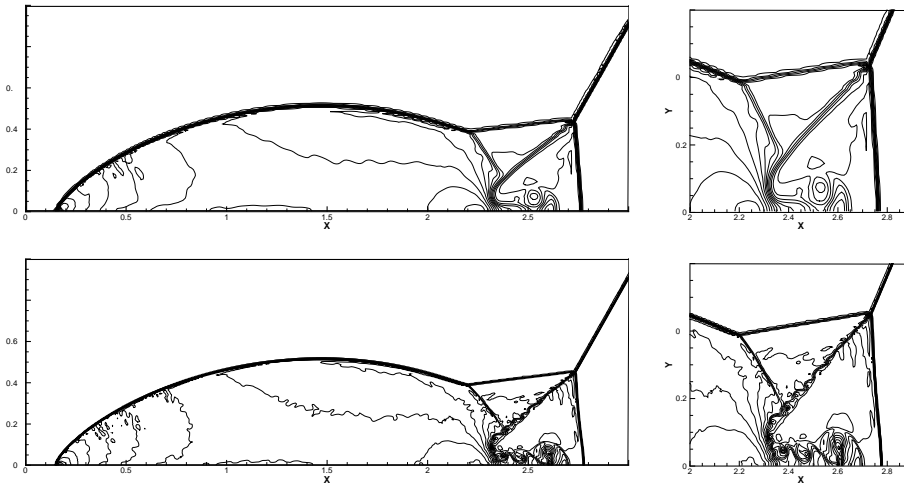


FIGURE 3.40: Density contours for double Mach reflection at time $t = 0.2$ with grid resolution $\Delta x = \Delta y = \frac{1}{100}$ (top panels) and $\Delta x = \Delta y = \frac{1}{200}$ (bottom panels). The figures are drawn with 30 density contours between 1.9 and 21.0.

and $\Delta x = \Delta y = \frac{1}{200}$ for the bottom ones. The results are in good agreement with those computed with high order schemes. For instance, compared with the Fig. 17 in [91] where the computation is conducted with several high order schemes with grid size $\Delta x = \Delta y = \frac{1}{240}$, the present scheme seems to resolve more vortices along the slip line. These results show that without relying on high order polynomial reconstructions, the proposed scheme can nonetheless reach high resolution capability (i.e. low dissipation), comparably with the state-of-the-art high order schemes.

3.6.4 2D Euler reacting equations for stiff detonation

Two dimensional detonation waves problem which was also investigated in [68, 69, 80] is considered here. A two-dimensional shock tube with $[0, 0.025] \times [0, 0.005]$ is set as computational domain. Reflective boundary conditions are prescribed to upper and lower boundaries, while zero-gradient boundary conditions are imposed to the left and the right boundaries. The parameters q_0 , $\frac{1}{\xi}$ and T_{ign} in Heaviside chemical reaction model are same as in Subsection 3.6.2. The initial conditions are

$$(\rho_0, u_0, v_0, p_0, \alpha) = \begin{cases} (\rho_l, u_l, 0, p_l, 0) & \text{if } x \leq \psi(y) \\ (\rho_r, u_r, 0, p_r, 1) & \text{if } x > \psi(y), \end{cases} \quad (3.30)$$

where

$$\psi(y) = \begin{cases} 0.004 & \text{if } |y - 0.0025| \geq 0.001 \\ 0.005 - |y - 0.0025| & \text{if } |y - 0.0025| < 0.001. \end{cases} \quad (3.31)$$

The right states $(\rho_r, u_r, 0, p_r, 1)$ are the same as in Subsection 3.6.2 and $\rho_l = \rho_{CJ}$, $p_l = p_{CJ}$ while $u_l = 8.162 \times 10^4 > u_{CJ}$. As stated in [92], one important feature of this solution is that a cellular pattern will form after the triple point has traveled in the transverse direction and hereafter reflected back and forth against the upper and lower boundaries.

Because there exists no known exact solution to this problem, we have simulated a fine solution obtained by the 5th order WENO scheme on 2000×400 mesh cells, see left-panels of Fig. 3.41-3.42. The numerical density is displayed on Fig. 3.41 for WENO (middle panels) and BVD (right panels) schemes at time $t = 0.3 \times 10^{-7}$ on top and $t = 1.7 \times 10^{-7}$ on bottom. A 3D elevation plot and a projected 2D plot are simultaneously presented where color and elevation represent the density. The same scale is used for all panels. From this figure we observe that the coarse grid WENO results present spurious oscillations which are not visible on THINC-BVD results and very less pronounced on the fine WENO solution. Moreover some of the finer structures seen

just after the up-front reaction front seem more accurately captured by THINC-BVD. More importantly we can see that the reaction front structure is incorrectly captured by WENO which smears excessively the wave front. On Fig. 3.42 we propose a different angle of visualization to emphasize this front structure. This numerical diffusion of the front has an important impact on the form of the resulting fine structures. BVD results seem to be less impacted by numerical dissipation and spurious phenomena than WENO for this test case.

3.7 Summary

For practical use, efficient spatial reconstruction schemes named MUSCL-THINC-BVD schemes and adaptive THINC-BVD are proposed in this work in the context of finite volume schemes to solve hyperbolic systems of PDEs. Instead of relying on high order polynomial reconstructions, the current scheme employs THINC (hyperbolic tangent shape) function with adaptive sharpness and a newly proposed BVD algorithm to reconstruct values at cell boundaries by reducing the total amount of dissipation. Through 1D and 2D benchmark tests, it is shown that the proposed scheme can capture more small-scale flow structures and, at the same time, prevent the occurrence of spurious waves which can pollute stiff detonation problems. The resolution around discontinuities is significantly improved by the proposed approach. Systematic comparisons against exact/reference solutions and 5th order WENO numerical solutions have been presented. Unlike most existing high order polynomial-based reconstruction schemes which may demand the development of complex limiting procedures to suppress those spurious numerical oscillations, THINC-BVD is formulated in a simple, efficient and easy-to-code form. This makes this scheme a promising alternative for simulation of flows involving discontinuity. Moreover the reconstruction procedures only demand a local neighborhood to the current cell which is harmless for parallel framework. Owing also to its algorithmic simplicity, the proposed method can become as a practical and promising

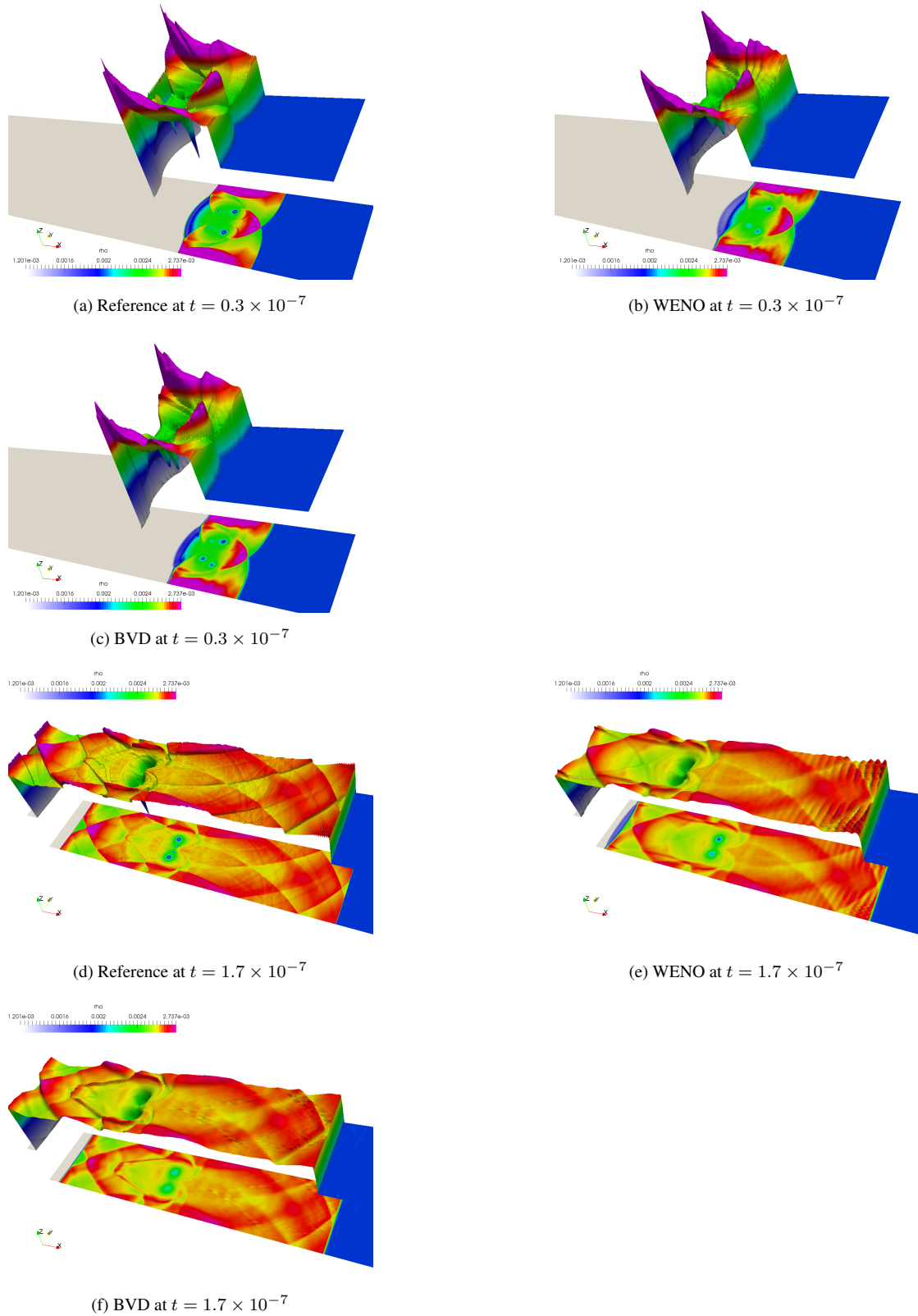


FIGURE 3.41: Detonation problem — Density field at $t = 0.3 \times 10^{-7}$ (top panels) and $t = 1.7 \times 10^{-7}$ (bottom panels) — Left panels: Reference solution calculated by the 5th order WENO scheme with 2000×400 mesh cells — Middle panel: Solution obtained by 5th order WENO scheme with 400×80 mesh cells — Right panel: Solution obtained by the proposed BVD scheme with 400×80 mesh cells.

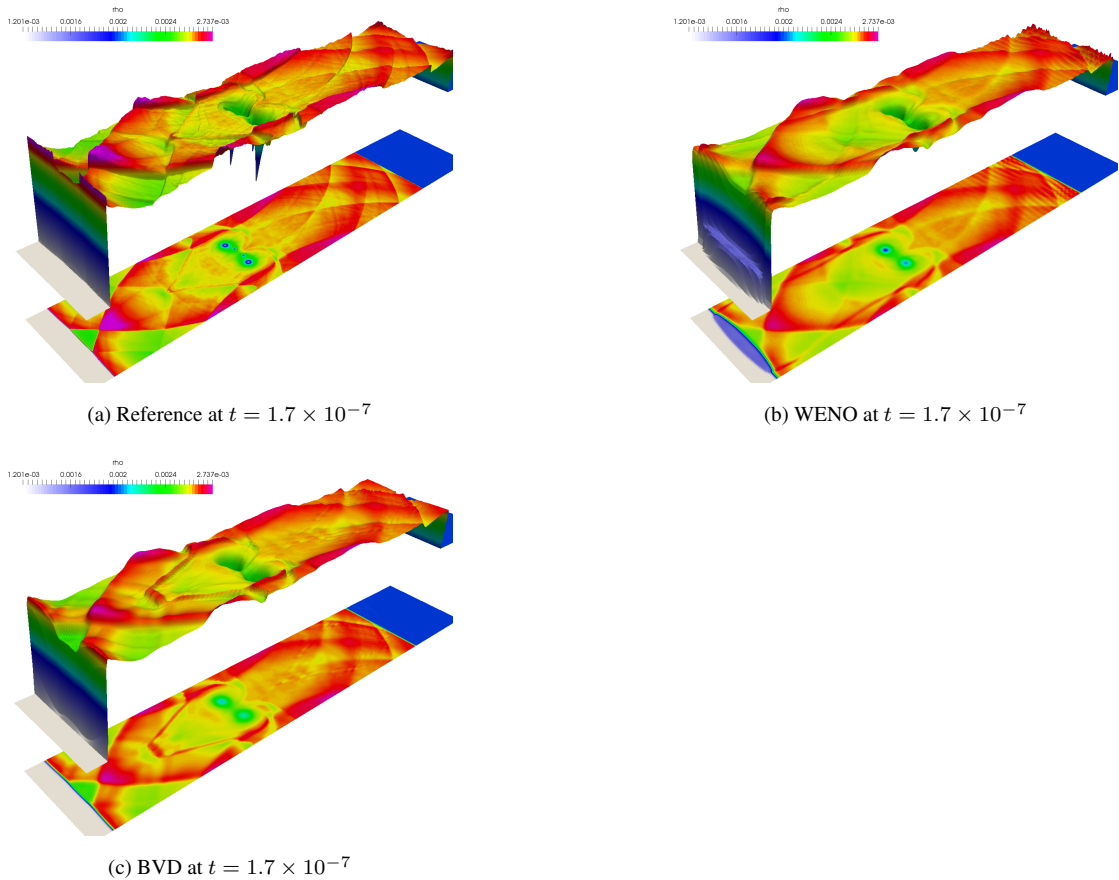


FIGURE 3.42: Detonation problem — Density field at $t = 1.7 \times 10^{-7}$ seen from a different angle compared to Fig. 3.41 — Left panels: Reference solution calculated by the 5th order WENO scheme with 2000×400 mesh cells — Middle panel: Solution obtained by 5th order WENO scheme with 400×80 mesh cells — Right panel: Solution obtained by the proposed BVD scheme with 400×80 mesh cells.

numerical solver for compressible gas dynamics, particularly for simulations involving strong discontinuities and reacting fronts with stiff source term.

We also apply them to solve stiff detonation problems. This method can significantly reduce numerical dissipation errors and thereby prevent false calculations of the propagation speeds of discontinuities or spurious waves, a common phenomenon when applying conventional shock-capturing schemes under insufficient grid resolution. We remark that the detonation propagation is a classical multi-scale process, for which the length scale covers $10^{-9} \sim 10^1$ m, and therefore an insufficient grid resolution is a non-trivial problem, especially in engineering research. Unlike several methods that by accepting the diffused discontinuities profiles reply on extra treatments, the current

method resolves the correct position of the detonation front by fundamentally reducing the numerical dissipation errors around discontinuities. Moreover, being a spatial reconstruction for finite volume formulation to solve general hyperbolic systems, the proposed scheme can be extended to solve multi-species problems straightforwardly.

Chapter 4

Implementation of BVD schemes on compressible multiphase flows with moving interface

4.1 Introduction

Compressible multiphase fluid dynamics is one of active and challenging research areas of great importance in both theoretical studies and industrial applications. For example, shock/interface interactions are thought to be crucial to the instability and evolution of material interfaces that separate different fluids as observed in a wide spectrum of phenomena [95]. The material interfaces greatly complicate the physics and make problems formidably difficult for analytical and experimental approaches in many cases, where numerical simulation turns out to be the most effective approach to provide quantitative information to elucidate the fundamental mechanisms behind the complex phenomena of multiphase flows.

In comparison to the computation of single phase flow, development of numerical methods for multiphase flow faces more challenging tasks. The major complexity comes

from the moving interfaces between different fluids that usually associate with strong discontinuities, singular forces and phase changes in some cases. Given the numerical methods developed for multiphase incompressible flows with interfaces having been reaching a relatively mature stage, the numerical solvers for compressible interfacial multiphase flows are apparently insufficient. For incompressible multiphase flows with moving interfaces where the density and other physical properties, e.g. viscosity and thermal conductivity, are constant in each fluid, the one-fluid model [94] can be implemented in a straightforward manner with an assumption that the physical fields change monotonically across the interface region. Thus, provided with an indication function which identifies the moving interface, one can uniquely determine the physical property fields for the whole computational domain. Some indication functions, such as volume of fluid (VOF) function [96–98] and level set function [99–101], have been proposed and proved to be able to capture moving interfaces with compact thickness and geometrical faithfulness if solved by advanced numerical algorithms. However, substantial barrier exists when implementing the one-fluid model to compressible interfacial multiphase flows.

The new difficulties we face when applying the one-fluid model to compressible interfacial multiphase flows lie in two aspects: Density and energy in compressible flow have to be solved along with the indication function, and special formulations are required to maintain the physical consistency which results in a balanced state among all variables for the interface cell where a well-defined interface falls in; The numerical dissipation in the so-called high-resolution schemes designed for solving single phase compressible flows involving shock waves tends to smear out discontinuities including the material interfaces in numerical solutions, which is fatal to simulations of interfacial multiphase flows even if the schemes can produce acceptable results in single phase cases.

For the first issue mentioned above, mixing or averaging models that consist of Euler or Navier-Stokes equations along with the equations of interface-indication functions have been derived and widely used as an efficient approximation to the state of the interface

cell where two or more species co-exist. A simple single-fluid model was reported in [102, 103, 197] for interfacial multiphase compressible flows using either explicit time marching or semi-implicit pressure-projection solution procedure. The latter results in a unified formulation for solving both compressible and incompressible multiphase flows. As the primitive variables are solved in these models, the conservation properties are not guaranteed, and thus might not be suitable for high-Mach flows involving shock waves. Conservative formulations, which have been well-established for single phase compressible flows with shock waves, however may lead to spurious oscillations in pressure or other thermal fields [105, 106]. It was found that special treatments are required in transporting the material interface and mixing/averaging the state variables to find the mixed state of fluids in the interfacial cell that satisfies pressure balance across material interface for multiple polytropic and stiff gases [107–111], van der Waals [112] and Mie-Grüneisen equations of state (EOS) [113]. A more general five-equation model [114] was developed for a wide range fluids. These models apply to multiphase compressible flows with either spread or sharp interfaces. See [115] for a recent review on the models of this sort. We make use of the five-equation model in the present work as the PDE (partial differential equation) set to develop our numerical method, which can be applied to other extended system as well.

Provided the SEF models with some desired properties, such as hyperbolicity, conservation and well-balanced mixing closure without spurious oscillations in thermal variables, we can in principle implement numerical methods for single phase compressible flow (e.g. the standard shock-capturing schemes) to solve these multiphase models. TVD schemes, such as the MUSCL scheme, can solve discontinuities without numerical oscillations, which is of paramount importance to ensure the physical fields to be bounded and monotonic in the transition region. However, TVD schemes suffer from excessive numerical dissipation, which brings the problem (II) listed above to us. The intrinsic numerical dissipation smears out the flow structures including the discontinuities in mass fraction or volume fraction which is used to represent the

material interfaces. Consequently, material interfaces are continuously blurred and smeared out, which is not acceptable in many applications, especially for the simulations that need long-term computation. As a remedy, using higher order schemes, like WENO (Weighted Essentially Non-Oscillatory) scheme, to solve compressible multiphase flows is also found in the literature [116, 117], where numerical dissipation is largely reduced, and the moving interfaces, as well as other flow structures, can be resolved with significantly improved accuracy. However, implementing high order schemes might generate numerical oscillations for compressible multiphase flows with complex EOS as discussed in [116], where even though the reconstructions were carried out in terms of the characteristic variables to reduce numerical oscillation, spurious disturbances are still observed when waves are reflected from the material interface. In a more recent work [118], an intermediate state was introduced at each cell edge in characteristic decomposition to suppress numerical oscillations and stabilize computation. Furthermore, high order monotonicity-preserving scheme [119] was used to ensure the bounded value for volume fraction. It is noted that numerical dissipation even reduced in WENO and other high-order schemes still remains in conventional Eulerian advection schemes, which might be problematic in long-term simulations. In general, the implementation of high order shock capturing schemes to interfacial compressible multiphase flows demands further investigations.

There are different numerical methods to identify and compute moving interfaces in compressible multiphase flows, such as [120–122] on moving meshes and [123–127] on fixed meshes. As aforementioned, the VOF-type methods that use the volume fraction or mass fraction as the identification function of moving interface have been popularly used as well, which are referred to as interface-capturing methods in our context. Interface-capturing methods resolve the interfaces on fixed Eulerian grids and use advection schemes to transport the volume/mass fraction functions. It is well known that conventional Eulerian advection schemes have intrinsic numerical dissipation and tend to smear out the jumps in volume fraction or mass fraction functions which are used

to identify the material interfaces between different fluids. In order to keep the compact thickness of material interfaces during computation, special numerical techniques are needed to steepen the jumps in the volume or mass fraction fields. For example, in [66, 128, 129] the advection equation of the interface function is treated by artificial compression method. As a post-processing approach, anti-diffusion techniques have also been introduced in [130] and [131]. An alternative approach is to reconstruct the volume fraction under the finite volume framework by using special functions. The THINC (Tangent of Hyperbola for INterface Capturing) method, for example, uses the hyperbolic tangent function [56] to capture the jumps in volume fraction. By virtue of the desirable characteristics of the hyperbolic tangent function in mimicking the jump-like profile of the volume fraction field, the sharp interface can be accurately captured in a simple and efficient way [118, 132]. However, when applying interface-sharpening methods to the SEF models of multiphase compressible flows, velocity and pressure oscillations may occur across the interface [66, 129, 131–133] due to the inconsistency between the physical variables and the volume fraction field with sharpened or compressed jumps. As stated in [66, 129], in contrast to incompressible flows where the densities of fluids are fixed, artificial interface-sharpening scheme cannot be applied alone to volume fraction function in compressible multiphase flows. Modifications to other physical variables have to be made to maintain the consistency among the sharpened volume fraction and other physical fields [66, 129, 131, 133]. In [132], a homogeneous reconstruction has been proposed where the reconstructed volume fraction is used to extrapolate the remaining conservative variables across the interface to ensure the mechanical consistency across the isolated material interfaces.

This work presents a novel methodology to resolve problem (II) addressed above. We apply MUSCL-THINC-BVD scheme introduced in the previous chapter to solve five equation models. More substantially, MUSCL-THINC-BVD scheme is applied to the volume fraction and other state variables simultaneously in a finite volume framework, so that the consistency can be realized among the physical variables and volume fraction

throughout the solution procedure. Hence the manipulations required in other existing methods to adjust the physical variables to be consistent with the volume fraction, are not needed in the present method. The numerical model is formulated under a standard finite volume framework with a Riemann solver in the wave propagation form [70]. The numerical tests verify the capability of the present method in capturing the material interface as a well-resolved sharp jump in volume fraction. The numerical results for a wide range of benchmark tests in one, two and three dimensions show superior solution quality competitive to other existing methods.

4.2 Solution procedures for five equations model

4.2.1 Control equations

the inviscid compressible two-component flows are formulated by the five-equation model developed in [114]. By assuming that the material interface is in equilibrium of mixed pressure and velocity, the five-equation model consists of two continuity equations for phasic mass, a momentum equation, an energy equation and an advection equation of volume fraction as follows

$$\begin{aligned}
 \frac{\partial}{\partial t} (\alpha_1 \rho_1) + \nabla \cdot (\alpha_1 \rho_1 \mathbf{u}) &= 0, \\
 \frac{\partial}{\partial t} (\alpha_2 \rho_2) + \nabla \cdot (\alpha_2 \rho_2 \mathbf{u}) &= 0, \\
 \frac{\partial}{\partial t} (\rho \mathbf{u}) + \nabla \cdot (\rho \mathbf{u} \otimes \mathbf{u}) + \nabla p &= 0, \\
 \frac{\partial E}{\partial t} + \nabla \cdot (E \mathbf{u} + p \mathbf{u}) &= 0, \\
 \frac{\partial \alpha_1}{\partial t} + \mathbf{u} \cdot \nabla \alpha_1 &= 0,
 \end{aligned} \tag{4.1}$$

where ρ_k and $\alpha_k \in [0, 1]$ denote in turn the k th phasic density and volume fraction for $k = 1, 2$, \mathbf{u} the vector of particle velocity, p the mixture pressure and E the total energy. When considering more than two-phases, the five-equation model can be extended by

supplementing additional continuity equations and volume fraction advection equations for each new phase.

To close the system, the fluid of each phase is assumed to satisfy the Mie-Grüneisen equation of state,

$$p_k(\rho_k, e_k) = p_{\infty,k}(\rho_k) + \rho_k \Gamma_k(\rho_k) (e_k - e_{\infty,k}(\rho_k)), \quad (4.2)$$

where $\Gamma_k = (1/\rho_k)(\partial p_k/\partial e_k)|_{\rho_k}$ is the Grüneisen coefficient, and $p_{\infty,k}$, $e_{\infty,k}$ are the properly chosen states of the pressure and internal energy along some reference curves (e.g., along an isentrope or other empirically fitting curves) in order to match the experimental data of the examined material [134]. Usually, parameters Γ_k , $p_{\infty,k}$ and $e_{\infty,k}$ can be taken as functions only of the density. This equation of state can be employed to approximate a wide variety of materials including some gaseous or solid explosives and solid metals under high pressure. For example, the Mie-Grüneisen EOS can be changed to stiffened gas EOS by setting different parameters.

The conservativeness constraints lead to the mixing formula for volume fraction, density and internal energy as follows,

$$\begin{aligned} \alpha_1 + \alpha_2 &= 1, \\ \alpha_1 \rho_1 + \alpha_2 \rho_2 &= \rho, \\ \alpha_1 \rho_1 e_1 + \alpha_2 \rho_2 e_2 &= \rho e. \end{aligned} \quad (4.3)$$

Derived in [113], the mixture Grüneisen coefficient, pressure p_{∞} and internal energy e_{∞} can be expressed as

$$\begin{aligned} \frac{\alpha_1}{\Gamma_1(\rho_1)} + \frac{\alpha_2}{\Gamma_2(\rho_2)} &= \frac{1}{\Gamma}, \\ \alpha_1 \rho_1 e_{\infty,1}(\rho_1) + \alpha_2 \rho_2 e_{\infty,2}(\rho_2) &= \rho e_{\infty}, \\ \alpha_1 \frac{p_{\infty,1}(\rho_1)}{\Gamma_1(\rho_1)} + \alpha_2 \frac{p_{\infty,2}(\rho_2)}{\Gamma_2(\rho_2)} &= \frac{p_{\infty}(\rho)}{\Gamma(\rho)}, \end{aligned} \quad (4.4)$$

under the isobaric assumption. The mixture pressure is then calculated by

$$p = \left(\rho e - \sum_{k=1}^2 \alpha_k \rho_k e_{\infty,k}(\rho_k) + \sum_{k=1}^2 \alpha_k \frac{p_{\infty,k}(\rho_k)}{\Gamma_k(\rho_k)} \right) / \sum_{k=1}^2 \frac{\alpha_k}{\Gamma_k(\rho_k)}. \quad (4.5)$$

It should be noted that the mixing rules of Eq.(4.4) and Eq.(4.5) ensure that the mixed pressure is free of spurious oscillations across the material interfaces [107, 109, 111–113]. Following the five equations model under isobaric closure [114], the sound speed of mixture could be calculated as the volumetric average of the phasic sound speeds as

$$c^2 = \alpha_1 c_1^2 + \alpha_2 c_2^2. \quad (4.6)$$

When sound speed is very different from different materials, the time step will be restricted with the local wave speed as well as local sound speed.

4.2.2 Solution procedures with wave propagation method

We rewrite the one dimensional quasi-conservative five-equation model (4.1) as

$$\frac{\partial \mathbf{q}}{\partial t} + \frac{\partial \mathbf{f}(\mathbf{q})}{\partial x} + \mathbf{B}(\mathbf{q}) \frac{\partial \mathbf{q}}{\partial x} = 0, \quad (4.7)$$

where the vectors of physical variables \mathbf{q} and flux functions \mathbf{f} are

$$\begin{aligned} \mathbf{q} &= (\alpha_1 \rho_1, \alpha_2 \rho_2, \rho u, E, \alpha_1)^T, \\ \mathbf{f} &= (\alpha_1 \rho_1 u, \alpha_2 \rho_2 u, \rho u u + p, E u + p u, 0)^T, \end{aligned} \quad (4.8)$$

respectively. The matrix \mathbf{B} is defined as

$$\mathbf{B} = \text{diag} (0, 0, 0, 0, u), \quad (4.9)$$

where u denotes the velocity component in x direction.

We divide the computational domain into N non-overlapping cell elements, $C_i : x \in [x_{i-1/2}, x_{i+1/2}]$, $i = 1, 2, \dots, N$, using a uniform grid with the spacing $\Delta x = x_{i+1/2} - x_{i-1/2}$. For a standard finite volume method, the volume-integrated average value $\bar{\mathbf{q}}_i(t)$ in cell C_i is defined as

$$\bar{\mathbf{q}}_i(t) \approx \frac{1}{\Delta x} \int_{x_{i-1/2}}^{x_{i+1/2}} \mathbf{q}(x, t) dx. \quad (4.10)$$

Denoting all the spatial discretization terms in (4.7) by $\mathcal{L}(\bar{\mathbf{q}}(t))$, the semi-discrete version of the finite volume formulation can be expressed as a system of ordinary differential equations (ODEs)

$$\frac{\partial \bar{\mathbf{q}}(t)}{\partial t} = \mathcal{L}(\bar{\mathbf{q}}(t)). \quad (4.11)$$

In the wave-propagation method, the spatial discretization for cell C_i is computed by

$$\mathcal{L}(\bar{\mathbf{q}}_i(t)) = -\frac{1}{\Delta x} (\mathcal{A}^+ \Delta \mathbf{q}_{i-1/2} + \mathcal{A}^- \Delta \mathbf{q}_{i+1/2} + \mathcal{A} \Delta \mathbf{q}_i) \quad (4.12)$$

where $\mathcal{A}^+ \Delta \mathbf{q}_{i-1/2}$ and $\mathcal{A}^- \Delta \mathbf{q}_{i+1/2}$ are the right- and left-moving fluctuations, respectively, and $\mathcal{A} \Delta \mathbf{q}_i$ is the total fluctuation within C_i . Riemann problems are solved to determine these fluctuations. The right- and left-moving fluctuations can be calculated by

$$\mathcal{A}^\pm \Delta \mathbf{q}_{i-1/2} = \sum_{k=1}^3 [s^k (\mathbf{q}_{i-1/2}^L, \mathbf{q}_{i-1/2}^R)]^\pm \mathcal{W}^k (\mathbf{q}_{i-1/2}^L, \mathbf{q}_{i-1/2}^R), \quad (4.13)$$

where moving speeds s^k and the jumps \mathcal{W}^k ($k = 1, 2, 3$) of three propagating discontinuities can be solved by the Riemann solver [72] with the reconstructed values $\mathbf{q}_{i-1/2}^L$ and $\mathbf{q}_{i-1/2}^R$ computed from the reconstruction functions $\tilde{\mathbf{q}}_{i-1}(x)$ and $\tilde{\mathbf{q}}_i(x)$ to the left and right sides of cell edge $x_{i-1/2}$, respectively. Similarly, the total fluctuation can be determined by

$$\mathcal{A} \Delta \mathbf{q}_i = \sum_{k=1}^3 [s^k (\mathbf{q}_{i-1/2}^R, \mathbf{q}_{i+1/2}^L)]^\pm \mathcal{W}^k (\mathbf{q}_{i-1/2}^R, \mathbf{q}_{i+1/2}^L). \quad (4.14)$$

We will describe with details about the reconstructions to get these values, $\mathbf{q}_{i-1/2}^L$ and $\mathbf{q}_{i-1/2}^R$, at cell boundaries in the next subsection as the core part of this paper.

In practice, given the reconstructed values $\mathbf{q}_{i-1/2}^L$ and $\mathbf{q}_{i-1/2}^R$, the minimum and maximum moving speeds $s^1(\mathbf{q}_{i-1/2}^L, \mathbf{q}_{i-1/2}^R)$ and $s^3(\mathbf{q}_{i-1/2}^L, \mathbf{q}_{i-1/2}^R)$ are computed as

$$\begin{aligned} s^1 &= \min\{u_{i-1/2}^L - c_{i-1/2}^L, u_{i-1/2}^R - c_{i-1/2}^R\}, \\ s^3 &= \max\{u_{i-1/2}^L + c_{i-1/2}^L, u_{i-1/2}^R + c_{i-1/2}^R\}, \end{aligned} \quad (4.15)$$

where $c_{i-1/2}^L$ and $c_{i-1/2}^R$ are the sound speeds calculated by reconstructed values $\mathbf{q}_{i-1/2}^L$ and $\mathbf{q}_{i-1/2}^R$ respectively. Then the speed of the middle wave is estimated by the HLLC Riemann solver [72] as

$$s^2 = \frac{p_{i-1/2}^R - p_{i-1/2}^L + \rho_{i-1/2}^L u_{i-1/2}^L (s^1 - u_{i-1/2}^L) - \rho_{i-1/2}^R u_{i-1/2}^R (s^3 - u_{i-1/2}^R)}{\rho_{i-1/2}^L (s^1 - u_{i-1/2}^L) - \rho_{i-1/2}^R (s^3 - u_{i-1/2}^R)}. \quad (4.16)$$

The left-side intermediate state variables $\mathbf{q}_{i-1/2}^{*L}$ is evaluated by

$$\mathbf{q}_{i-1/2}^{*L} = \frac{(\mathbf{u}_{i-1/2}^L - s^1)\mathbf{q}_{i-1/2}^L + (p_{i-1/2}^L \mathbf{n}_{i-1/2}^L - p_{i-1/2}^* \mathbf{n}_{i-1/2}^{*L})}{s^2 - s^1}, \quad (4.17)$$

where the vector $\mathbf{u}_{i-1/2}^L = (u_{i-1/2}^L, u_{i-1/2}^L, u_{i-1/2}^L, u_{i-1/2}^L, s^2)$, $\mathbf{n}_{i-1/2}^L = (0, 0, 1, u_{i-1/2}^L, 0)$, $\mathbf{n}_{i-1/2}^{*L} = (0, 0, 1, s^2, 0)$ and the intermediate pressure may be estimated as

$$p_{i-1/2}^* = \rho_{i-1/2}^L (u_{i-1/2}^L - s^1)(u_{i-1/2}^L - s^2) + p_{i-1/2}^L = \rho_{i-1/2}^R (u_{i-1/2}^R - s^1)(u_{i-1/2}^R - s^2) + p_{i-1/2}^R. \quad (4.18)$$

Analogously, the right-side intermediate state variables $\mathbf{q}_{i-1/2}^{*R}$ is

$$\mathbf{q}_{i-1/2}^{*R} = \frac{(\mathbf{u}_{i-1/2}^R - s^3)\mathbf{q}_{i-1/2}^R + (p_{i-1/2}^R \mathbf{n}_{i-1/2}^R - p_{i-1/2}^* \mathbf{n}_{i-1/2}^{*R})}{s^2 - s^3}. \quad (4.19)$$

Then we calculate the jumps $\mathcal{W}^k(\mathbf{q}_{i-1/2}^L, \mathbf{q}_{i-1/2}^R)$ as

$$\begin{aligned}\mathcal{W}^1 &= \mathbf{q}_{i-1/2}^{*L} - \mathbf{q}_{i-1/2}^L, \\ \mathcal{W}^2 &= \mathbf{q}_{i-1/2}^{*R} - \mathbf{q}_{i-1/2}^{*L}, \\ \mathcal{W}^3 &= \mathbf{q}_{i-1/2}^R - \mathbf{q}_{i-1/2}^{*R}.\end{aligned}\tag{4.20}$$

For the non-conservative term, the jump for the volume fraction is simply zero for both \mathcal{W}^1 , \mathcal{W}^3 and $\alpha_1^R - \alpha_1^L$ for \mathcal{W}^2 from above equations. Given the spatial discretization, we employ the three-stage third-order SSP (Strong Stability-Preserving) Runge-Kutta scheme [73]

$$\begin{aligned}\bar{\mathbf{q}}^* &= \bar{\mathbf{q}}^n + \Delta t \mathcal{L}(\bar{\mathbf{q}}^n), \\ \bar{\mathbf{q}}^{**} &= \frac{3}{4}\bar{\mathbf{q}}^n + \frac{1}{4}\bar{\mathbf{q}}^* + \frac{1}{4}\Delta t \mathcal{L}(\bar{\mathbf{q}}^*), \\ \bar{\mathbf{q}}^{n+1} &= \frac{1}{3}\bar{\mathbf{q}}^n + \frac{2}{3}\bar{\mathbf{q}}^* + \frac{2}{3}\Delta t \mathcal{L}(\bar{\mathbf{q}}^{**}),\end{aligned}\tag{4.21}$$

to solve the time evolution ODEs, where $\bar{\mathbf{q}}^*$ and $\bar{\mathbf{q}}^{**}$ denote the intermediate values at the sub-steps. For temporal integration, we have also tested the Euler first-order explicit and second order Runge-Kutta schemes, which produce stable numerical results as the third order SSP Runge-Kutta does. It is observed that the results from first and second-order temporal schemes are slightly diffusive.

4.3 Numerical experiments for compressible multiphase flows

Numerical tests in one-, two- and three- dimensions are presented in this section to verify the proposed MUSCL-THINC-BVD scheme in comparison with the WENO scheme. Here we use the WENO scheme which is one of representative high order shock-capturing schemes. We denote it as WENO-JS in our tests. As addressed in [116], the WENO reconstruction should be implemented for characteristic fields in order to reduce the numerical oscillations, which is not an easy task for complex equations

of state [118]. Whereas, it is found that the MUSCL-THINC-BVD scheme can prevent numerical oscillations even it is implemented to the primitive variables.

The one dimensional tests were conducted on a workstation with a single CPU (Intel(R) Xeon(R) CPU E5-2687W, 3.10GHZ), while two and three dimensional computations were accelerated with a NVIDIA GTX980ti GPU (graphics processing unit) card.

4.3.1 1D numerical tests

Passive advection of a square liquid column

To evaluate the ability of the proposed scheme to capture interface as well as to maintain the equilibrium of velocity and pressure fields, a simple interface-only problem in one dimension is considered in this test. The problem consists of a square liquid column in gas transported with a uniform velocity $u = u_0 = 10^2$ m/s under equilibrium pressure $p = p_0 = 10^5$ Pa in a tube of one meter. For initial condition, liquid is set in the region of $x \in [0.4, 0.6]$ m and gas is filled elsewhere. We set initially the volume fraction of liquid $\alpha_1 = 1 - \epsilon$ for the liquid region and $\alpha_1 = \epsilon$ in the gas region, and the volume fraction of gas is then $\alpha_2 = 1 - \alpha_1$. The small positive ϵ is set 10^{-8} in numerical tests in this paper. The densities for the liquid and gas phases are $\rho_1 = 10^3$ kg/m³ and $\rho_2 = 1$ kg/m³, respectively.

To model the thermodynamic behavior of liquid and gas, we use the EOS of the stiffened gas where the material-dependent parameters in (4.2) are

$$\Gamma_k = \gamma_k - 1, \quad p_{\infty,k} = \gamma_k \mathcal{B}_k \quad \text{and} \quad e_{\infty,k} = 0,$$

with the constants being $\gamma_1 = 4.4$, $\mathcal{B}_1 = 6 \times 10^8$ Pa for the liquid and $\gamma_2 = 1.4$, $\mathcal{B}_2 = 0$ for the gas respectively.

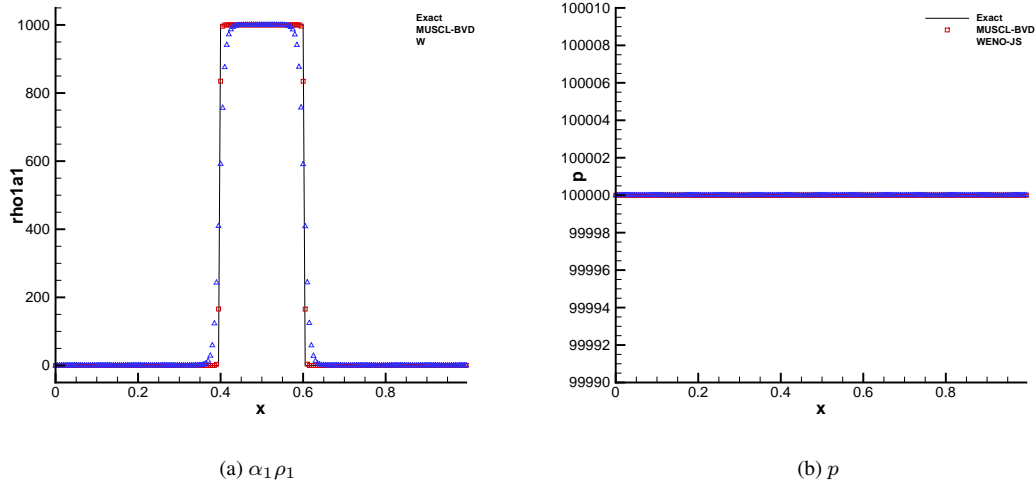


FIGURE 4.1: Numerical results for the passive advection test of a square liquid column at time $t = 10\text{ms}$. The solid line is the exact solution and the points show the computed solution with 200 mesh cells obtained using different methods. We denote the numerical result from MUSCL-THINC-BVD by MUSCL-BVD and that from [31] by WENO-JS.

The computations using WENO-JS and MUSCL-THINC-BVD are carried out separately. Periodic boundary condition is used on the left and right boundaries during the computations. Figure 4.1 shows numerical results of partial density and pressure fields at time $t = 10\text{ms}$ using a 200-cell mesh with $CFL = 0.5$. It is obvious that MUSCL-THINC-BVD can solve the sharp interface within only two cells while the WENO scheme, in spite of high-order accuracy, excessively diffuses the interface due to the intrinsic numerical dissipation around discontinuities as other conventional shock capturing schemes. Meanwhile, MUSCL-THINC-BVD can retain the correct pressure equilibrium and particle velocity without spurious oscillations across the interfaces. Any extra procedure is not conducted to sharpen the interface, which is used in other existing works to keep the steepness of the jump in volume fraction field to identify the interface. The MUSCL-THINC-BVD reconstruction is implemented to other state variables, which remains the thermo-dynamical consistency among the physical fields.

Two-material impact problem

Following [113, 140], the two-phase impact benchmark problem is computed. At the

TABLE 4.1: Material quantities for copper ($k = 1$) and explosive ($k = 2$) in Cochran-Chan equation of state (4.22).

k	$\rho_{0k}(\text{kg/m}^3)$	$\mathcal{B}_{1k}(\text{GPa})$	$\mathcal{B}_{2k}(\text{GPa})$	\mathcal{E}_{1k}	\mathcal{E}_{2k}	γ_k	C_{vk}
1	8900	145.67	147.75	2.99	1.99	3	393J/kg·K
2	1840	12.87	13.42	4.1	3.1	1.93	1087J/kg·K

beginning, there is a right-moving copper (phase 1) plate with the speed $u_1 = 1500$ m/s interacting with a solid explosive (phase 2) at rest on the right of the plate under the uniform atmospheric condition which has pressure $p_0 = 10^5$ Pa and temperature $T_0 = 300\text{K}$ throughout the domain. The material properties of the copper and (solid) explosive are modeled by the Cochran-Chan equation of state where in (4.2) we set the same Γ_k as in the stiffened gas case, but with $p_{\infty,k}$, $e_{\infty,k}$ defined by

$$\begin{aligned}
 p_{\infty,k}(\rho_k) &= \mathcal{B}_{1k} \left(\frac{\rho_{0k}}{\rho_k} \right)^{-\mathcal{E}_{1k}} - \mathcal{B}_{2k} \left(\frac{\rho_{0k}}{\rho_k} \right)^{-\mathcal{E}_{2k}}, \\
 e_{\infty,k}(\rho_k) &= \frac{-\mathcal{B}_{1k}}{\rho_{0k}(1-\mathcal{E}_{1k})} \left[\left(\frac{\rho_{0k}}{\rho_k} \right)^{1-\mathcal{E}_{1k}} - 1 \right] + \frac{\mathcal{B}_{2k}}{\rho_{0k}(1-\mathcal{E}_{2k})} \left[\left(\frac{\rho_{0k}}{\rho_k} \right)^{1-\mathcal{E}_{2k}} - 1 \right] - C_{vk}T_0.
 \end{aligned} \tag{4.22}$$

Here γ_k , \mathcal{B}_{1k} , \mathcal{B}_{2k} , \mathcal{E}_{1k} , \mathcal{E}_{2k} , C_{vk} , and ρ_{0k} are material-dependent quantities, see Table 4.1 for a typical set of values for copper and explosive considered.

The solution of this test is characterized by a left-moving shock wave to the copper, a right-moving shock waves to the inert explosive, and a material interface lying in between that separates these two different materials. We solved this problem with a 200-cell grid and $CFL = 0.5$ up to $t = 85\mu\text{s}$. Figure 4.2 shows the results for the partial densities, velocity, and the copper volume fraction of both WENO and MUSCL-THINC-BVD for comparison. Again, MUSCL-THINC-BVD can keep sharp interface without spurious numerical oscillations in velocity fields. It should be noted that due to complicated EOS, characteristic decomposition is conducted as in [118] when implementing the WENO scheme. In previous work [132], there is a slight overshoot on the partial density $\alpha_1\rho_1$ on the left of the interface when using THINC method for the

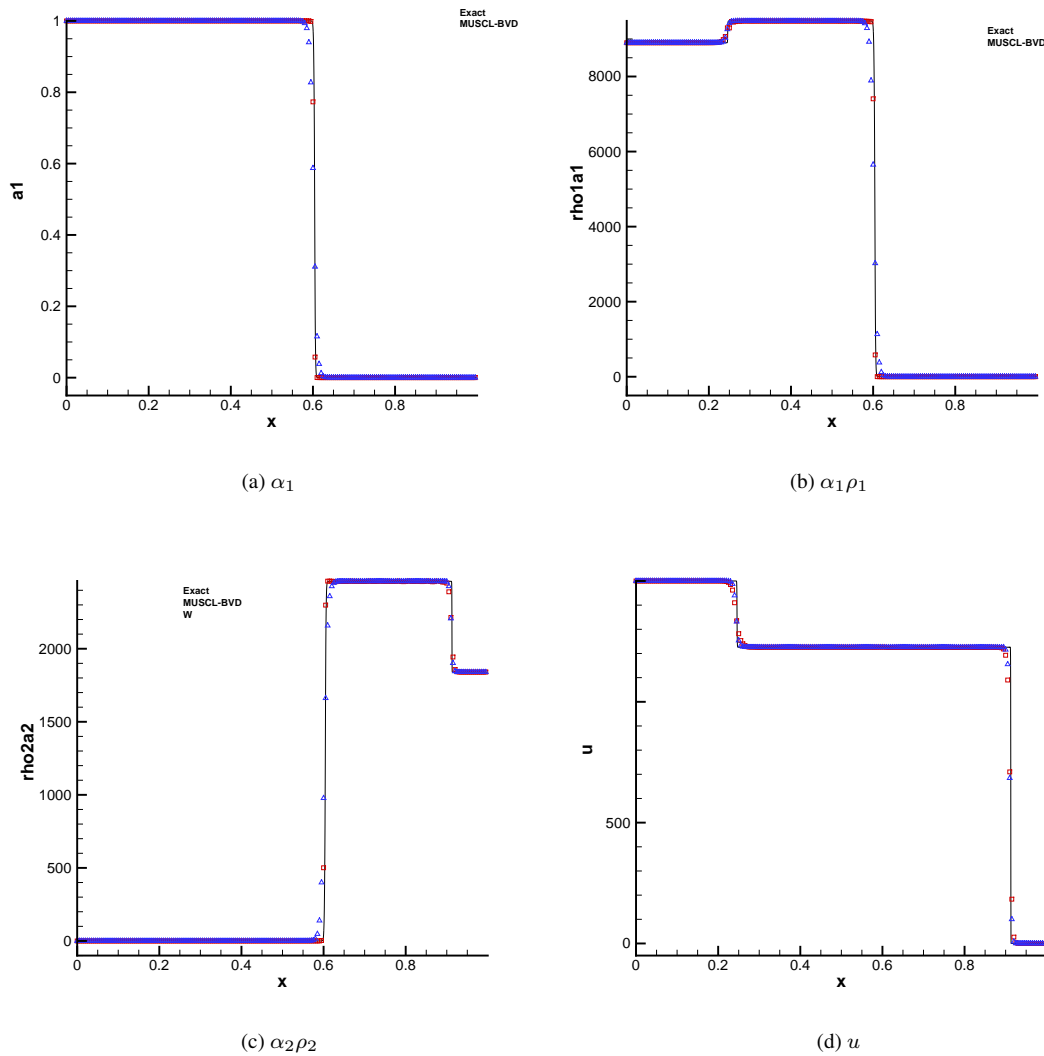


FIGURE 4.2: Numerical results for a two-phase (solid explosive-copper) impact problem at time $t = 85\mu\text{s}$. The solid line is the fine grid solution computed on a mesh of 5000 cells by MUSCL, and the points show the solutions with 200 meshes.

volume fraction. This oscillation is not observed in present study due to the consistency in MUSCL-THINC-BVD reconstructions for physical fields.

Shock interface interaction problem

The interaction between a strong shock wave in helium and an air/helium interface has been studied. Typically, such problem is very challenging for some interface tracking methods. For example, the schemes which are not conservative on discrete level may miscalculate the position and speed of the waves resulted from the interaction [141].

TABLE 4.2: Comparison between WENO and MUSCL-THINC-BVD regarding to the elapse time for one dimensional tests

	Test 1	Test 2	Test 3
WENO-JS	9.90s	3.02s	8.90s
MUSCL-THINC-BVD	4.23s	1.74s	3.72s

The initial conditions are the same as [116], where a Mach 8.96 shock wave is generated and traveling in helium toward a material interface with air which is moving toward the shock wave simultaneously. The detail initial configuration is given by

$$(\alpha_1 \rho_1, \alpha_2 \rho_2, u_0, p_0, \alpha_1) = \begin{cases} (0.386, 0, 26.59, 100, 1) & \text{for } -1 \leq x < -0.8 \\ (0.1, 0, -0.5, 1, 1) & \text{for } -0.8 \leq x < -0.2 \\ (0, 1, -0.5, 1, 0) & \text{for } -0.2 \leq x < 1 \end{cases} . \quad (4.23)$$

The calculation domain is $[-1, 1]$ which is divided by 200 uniform mesh cells. The solutions at $t=0.07$ were computed with the CFL number of 0.1. The comparisons of numerical results between MUSCL-THINC-BVD and WENO schemes are presented in Figure 4.3. The results from MUSCL-THINC-BVD show much superior solution quality in resolving material interface without obvious numerical oscillations, while some oscillations are observed in the pressure and velocity fields in the results of WENO scheme in the region of the reflected shock wave even although efforts have been made to implement reconstructions to the characteristic variables as also reported in [116].

In order to evaluate the computational efficiency of the MUSCL-THINC-BVD method, we also compare the computational cost in Table 4.2 for the 1D numerical tests shown above. Without decomposing state variables into characteristic fields, the computation cost of MUSCL-THINC-BVD is thus about half of the WENO scheme.

4.3.2 2D numerical tests

Two dimensional shock-bubble interactions

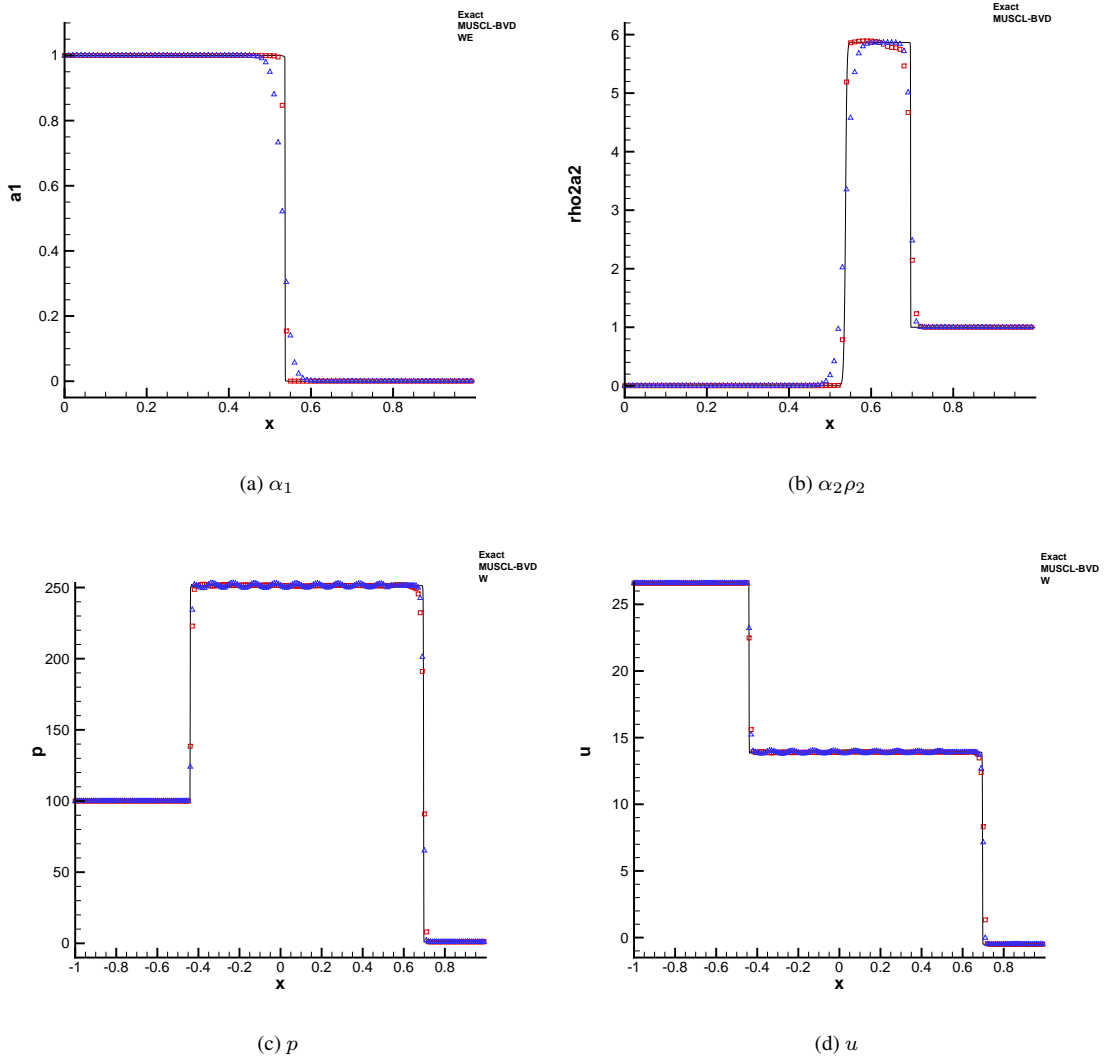


FIGURE 4.3: Comparisons of numerical results of shock/interface interaction problem between MUSCL-THINC-BVD and WENO schemes at $t=0.07$.

In this widely used benchmark test [130, 131, 142–145], we investigate the interactions between a shock wave of Mach 1.22 in air and a cylindrical bubble of refrigerant-22 (R22) gas. The experimental results can be referred in [146]. A planar rightward-moving Mach 1.22 shock wave in air impacts a stationary R22 gas bubble with radius $r_0 = 25\text{mm}$. In this numerical test, both air and R22 are modeled as perfect gases. Inside the R22 gas bubble, the state variables are

$$(\rho_1, \rho_2, u, v, p, \alpha_1) = (3.863 \text{ kg/m}^3, 1.225 \text{ kg/m}^3, 0, 0, 1.01325 \times 10^5 \text{ Pa}, 1 - \varepsilon),$$

while outside the bubble the corresponding parameters are

$$(\rho_1, \rho_2, u, v, p, \alpha_1) = (3.863 \text{ kg/m}^3, 1.225 \text{ kg/m}^3, 0, 0, 1.01325 \times 10^5 \text{ Pa}, \varepsilon)$$

in the pre-shock region and

$$(\rho_1, \rho_2, u, v, p, \alpha_1) = (3.863 \text{ kg/m}^3, 1.686 \text{ kg/m}^3, 113.5 \text{ m/s}, 0, 1.59 \times 10^5 \text{ Pa}, \varepsilon)$$

in the post-shock region respectively, where $\varepsilon = 10^{-8}$. The mesh size is $\Delta x = \Delta y = \frac{1}{8}$ mm which corresponds to a grid-resolution of 400 cells across the bubble diameter. Zero-gradient boundary conditions are imposed at the left and right boundaries while symmetric boundaries are imposed at the top and bottom boundaries. Schlieren-type images of density gradient, $|\nabla\rho|$, at different time instants are presented in Figs.4.4-4.5, in which comparisons are made among WENO, MUSCL and MUSCL-THINC-BVD schemes. The MUSCL-THINC-BVD scheme maintains much better the compact thickness of the material interfaces and gives large-scale flow structures similar to the results computed from the WENO scheme. Moreover, MUSCL-THINC-BVD scheme is able to reproduce finer flow structures due to largely reduced numerical dissipation. As one of the important features of the flow field, the instability develops along the interface, which then rolls up and produces small filaments as shown in Figure 4.4. These fine structures tend to be smeared out by numerical schemes with large numerical dissipation [131] unless high-resolution computational meshes are used. Not only the well-resolved material interface, we can also observe that the reflected shock waves and transmitted shock waves can be captured more clearly by MUSCL-THINC-BVD scheme in comparison with the original MUSCL schemes and competitive to the 5th-order WENO shock-capturing scheme. The resolution quality has been improved remarkably by MUSCL-THINC-BVD scheme to reproduce the complex flow features which are easily diffused out by conventional shock capturing schemes.

We compared our numerical results with the published works in literature which were

computed on same or finer grids. In Fig. 4.6, we plot our results on a coarse mesh where the initial diameter is resolved by 400 cells against the results computed by the anti-diffusion interface sharpening technique [131] on the same grid resolution. We further made comparisons in Fig. 4.7 with the multi-scale sharp interface simulation on a finer grid [145] where 1150 cells are used for the initial bubble diameter. It can be observed that similar small-scale structures have been re-produced by the MUSCI-THINC-BVD scheme with coarser grid resolution.

It should be noted that the Euler equations used to create the numerical results do not include the physical viscosity and surface tension. In the absence of physical viscosity, the solution of Euler equations does not converge, and the vortices will be continuously enforced when refined grid resolution is used [147]. So, it is hard to distinguish the physically-true structures and those due to the numerical schemes. The significance of the schemes with reduced numerical dissipation lies in the real-case applications where the physical dissipation (due to molecular or turbulent mixing) plays an important role. With reduced numerical dissipation, the true flow structures can be more faithfully reproduced under the effects of the physical dissipations.

Underwater explosion

We consider the underwater explosion problem which has been used in [66, 129, 130, 143, 148]. This test case involves complicated interactions of an air cavity generated from an initial high pressure region with a planar water-air interface lying above it. The computational domain is $[-2, 2] \times [-1.5, 2.5]$ m². The cylindrical air cavity of 0.24 m in diameter is initially centered at $(0, -0.3)$ with high pressure 10^9 Pa and high density 1250 kg/m³. The planar water-air interface is in equilibrium under standard atmospheric condition at $y = 0$. The thermodynamic behavior of water and air is modeled by the stiffened gas with the same equation of state as in Section 4.3.1. The transparent boundary condition is imposed for the top, left and right boundaries, while

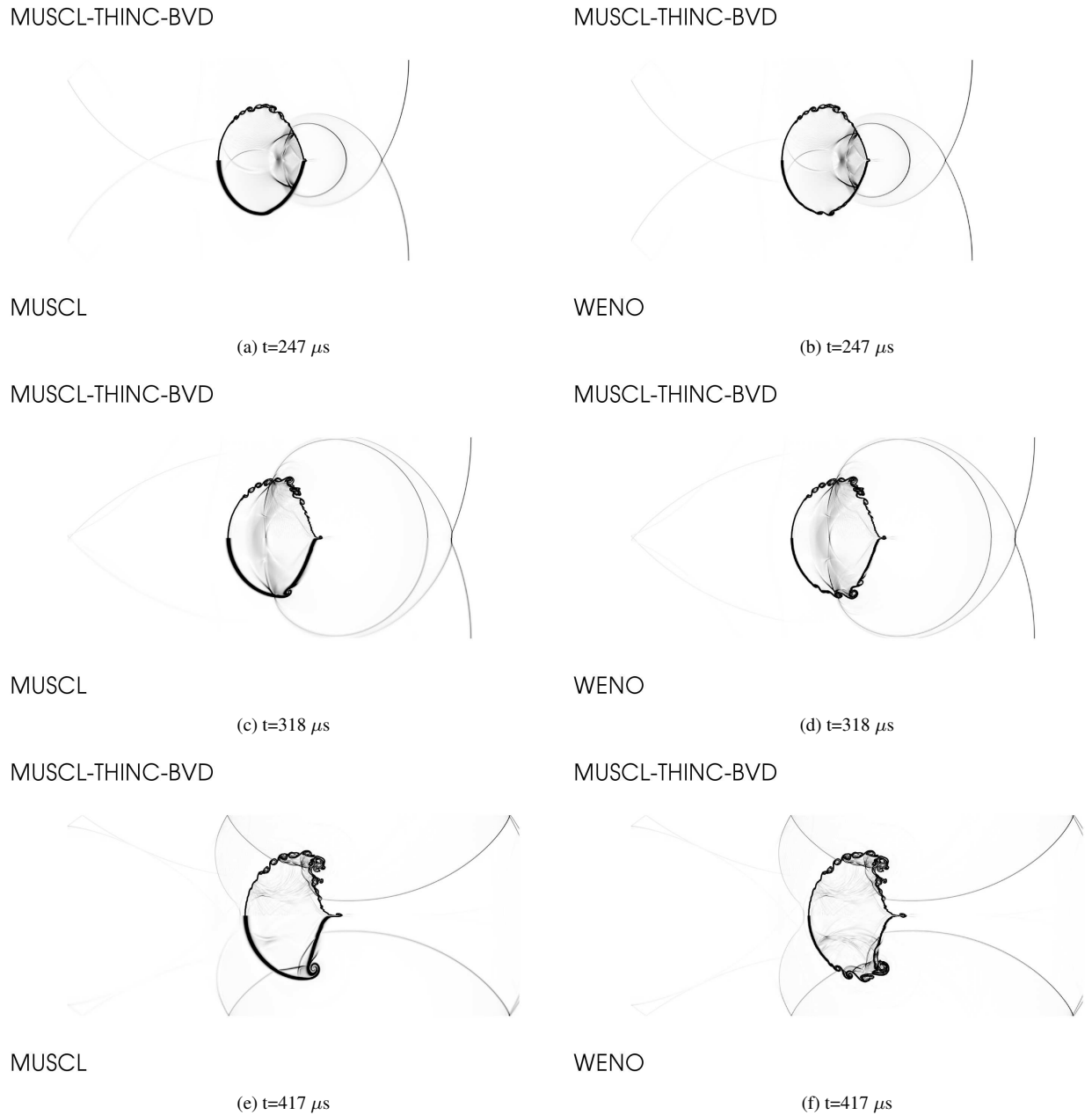


FIGURE 4.4: Numerical results for a planar Mach 1.22 shock wave in air interacting with a circular R22 gas bubble. Comparisons are made among MUSCL-THINC-BVD, MUSCL and WENO-JS schemes. Displayed are the Schlieren images of density variations at different instants. In each panel, the result of MUSCL-THINC-BVD (upper half) is plotted against the results of MUSCL or WENO-JS (lower half).

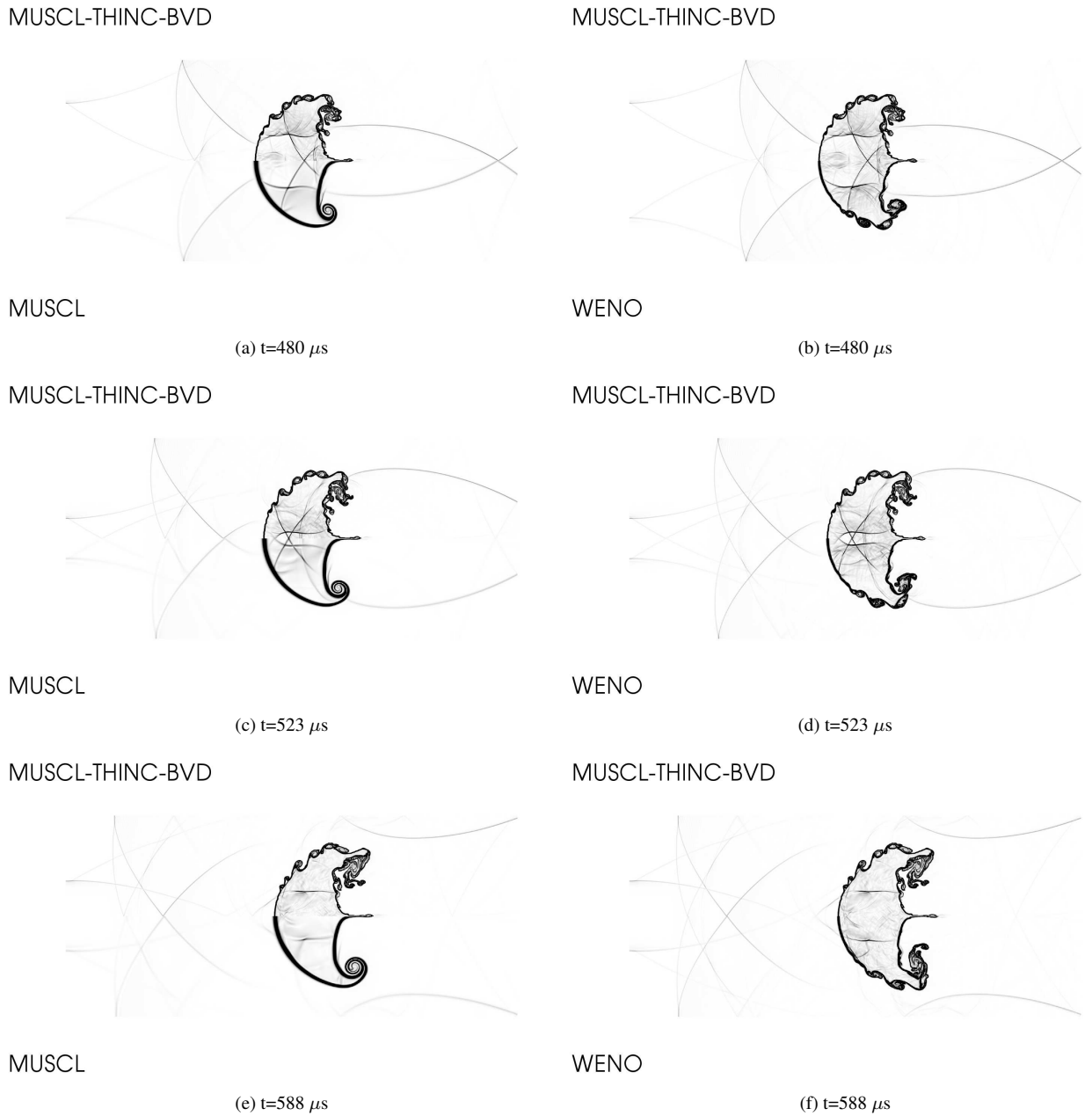


FIGURE 4.5: (continued)

for the bottom boundary the reflection condition is implemented. We conducted the simulation on a coarse uniform mesh with 600×600 by different schemes.

In Fig. 4.8, the numerical Schlieren diagrams for the mixture density computed from different schemes at several instants are displayed. The conventional shock-capturing schemes (both MUSCL and the 5th-order WENO) are not able to prevent the water-air

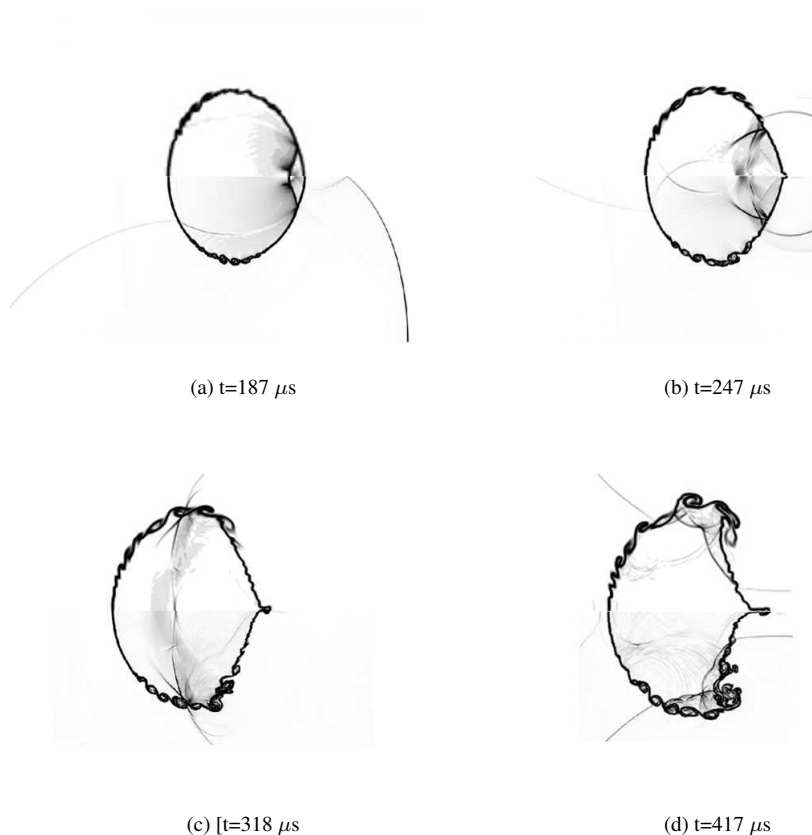


FIGURE 4.6: The Schlieren-like images of density fields computed by the anti-diffusion interface sharpening technique[131] (the upper half in each panel) and the MUSCL-THINC-BVD scheme (the lower half in each panel) respectively with the same grid resolution (400 cells along the diameter of initial bubble).

interfaces from smearing out, while MUSCL-THINC-BVD scheme can capture the interface sharply throughout the computation. Moreover, compared with original MUSCL scheme, flow structures including transmitted and reflected waves are much better resolved by MUSCL-THINC-BVD scheme, which produces competitive results with high order WENO schemes.

In Fig. 4.9, the volume fraction contour is presented. The initial circular underwater bubble evolves into an oval-like shape, which is in agreement with previous works [129, 143, 148]. It is observed that the material interfaces are sharply resolved so that the thin water bridge between the expanding bubble and the ambient air remains even in the later stage of the process, which is quite challenging for other existing methods. For example, the interface sharpening technique reported in [66] fails in resolving this thin

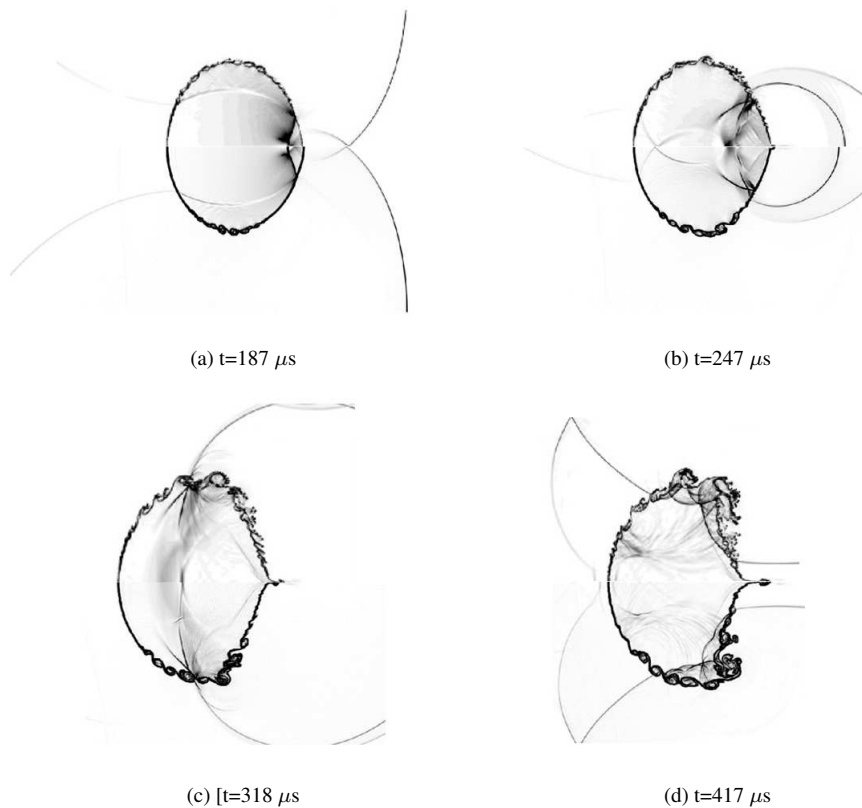


FIGURE 4.7: Same as Fig.4.6, but with the upper half in each panel replaced by the results in [145] where a finer grid (1500 cells along the diameter of initial bubble) was used.

bridge with the same grid resolution. As a quantitative comparison, we plot density profile along $x = 0$ cross-section in Fig. 4.10 against the results in [66, 129] that use finer grid resolution. With a coarser grid, the present results are in good agreement with those in the existing works.

To further illustrate the superiority of the proposed scheme in resolving the material interface, the computation is conducted to a larger time of $t = 3.16\text{ms}$, which has never been reported in the existing literatures. The material interfaces calculated by different schemes and the distributions of VOF function along $x = 0$ cross section are presented in Fig. 4.11-4.12. The MUSCL-THINC-BVD method keeps the compact thickness of the transition layer of the interface, while the MUSCL method smears out the interface over a wider band of mesh cells. For this long-time simulation, the intrinsic numerical dissipation of the conventional Eulerian high-resolution schemes for

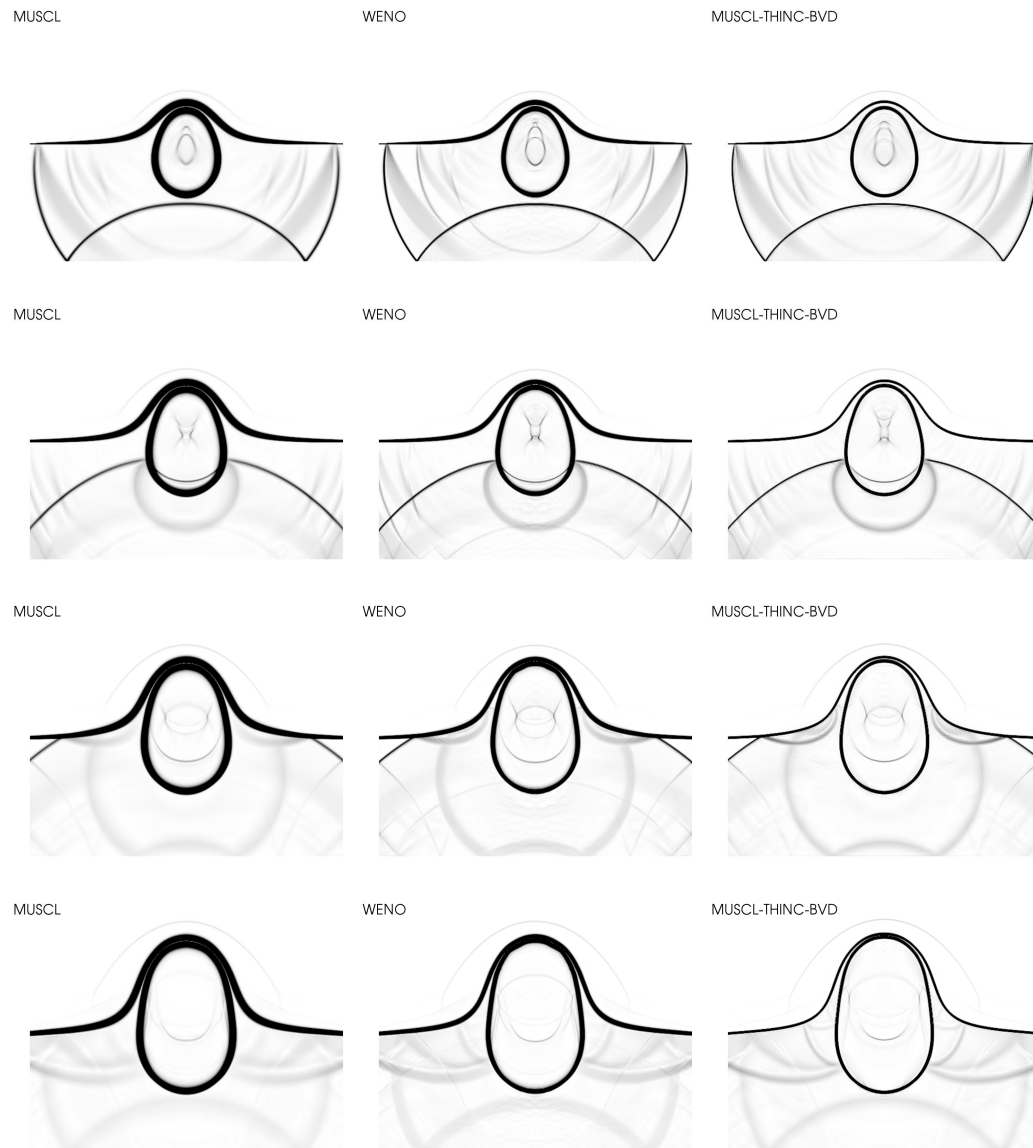


FIGURE 4.8: Schlieren images of density for the underwater explosion test at the instants $t = 0.95ms, 1.26ms, 1.58ms, 1.90ms$ (from top to bottom) computed by MUSCL, WENO-JS and MUSCL-THINC-BVD schemes respectively on a uniform grid of 600×600 cells.

compressible flows diffuses the material interface to an unacceptable extent. However, the resolution of material interface has been substantially improved by the MUSCL-THINC-BVD method.

Interaction of Mach 6 shock in air with a water column

This test was suggested in [66] to simulate the interaction of a Mach 6 shock in air with a water column, which has been also used in other works as a benchmark to examine

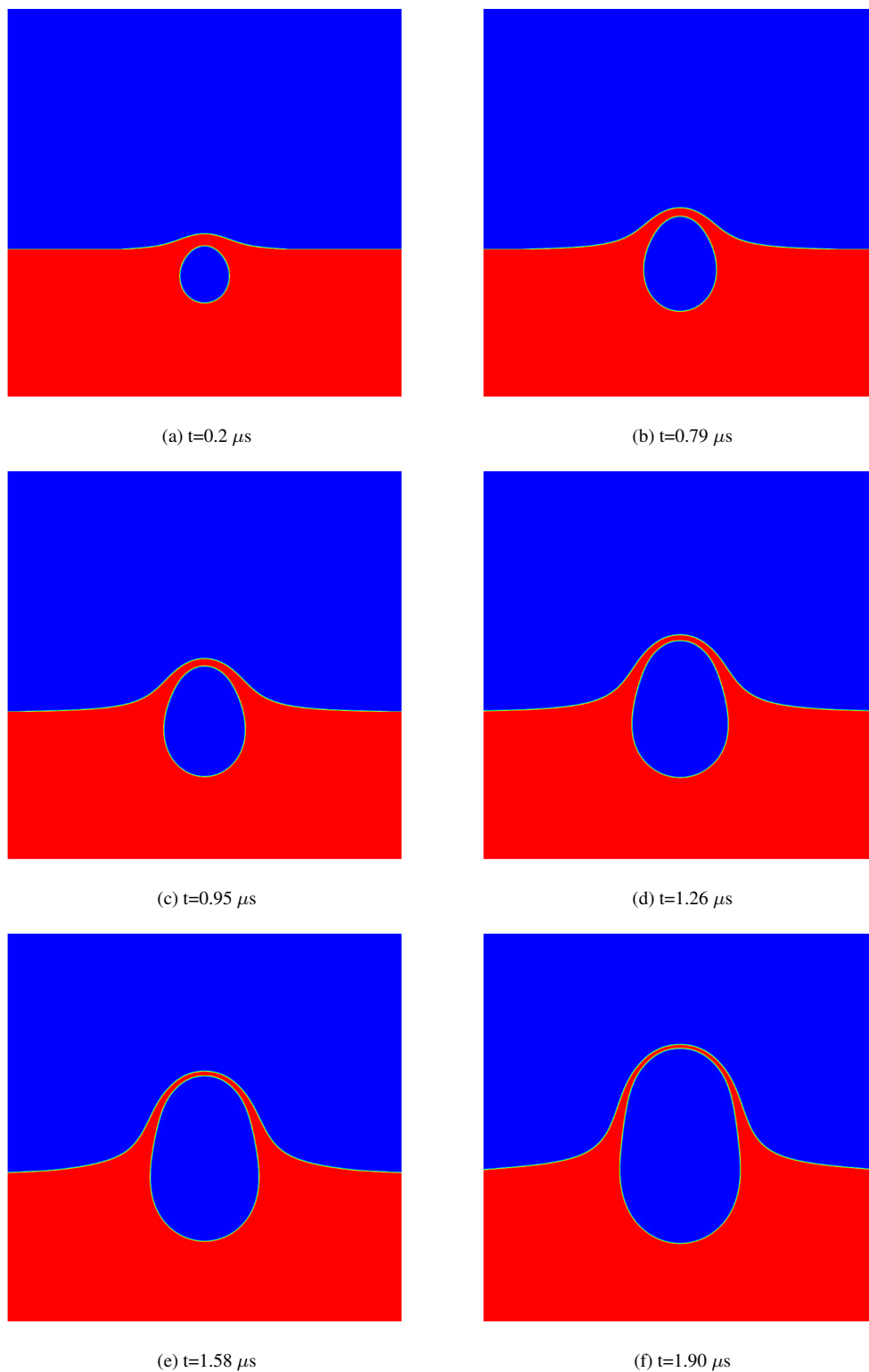


FIGURE 4.9: Volume fraction contour at different instants for underwater explosion test using the MUSCL-THINC-BVD scheme on a uniform grid with 600×600 cells.

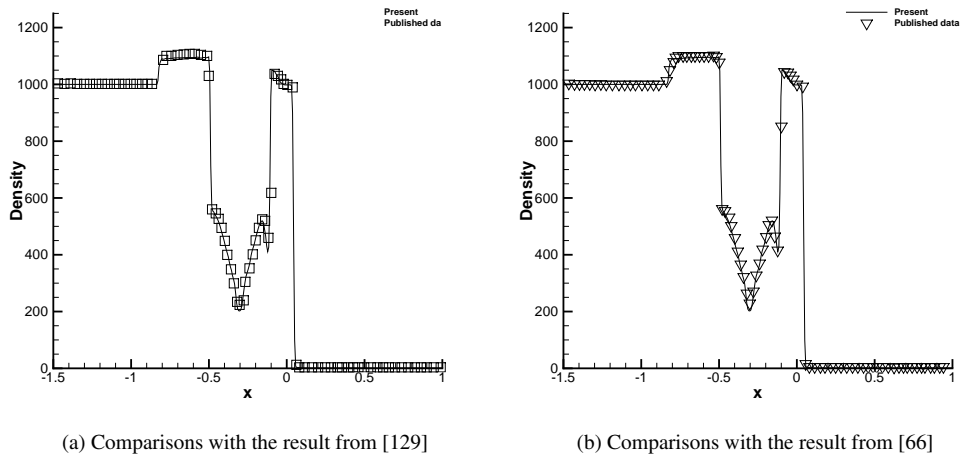


FIGURE 4.10: Distribution of density field along $x = 0$ cross-section for underwater explosion test at $t = 0.2$ ms. The mesh size of the present computation is $h = 0.0067$. Comparisons are made with the published work [66, 129] where the cell size is $h = 0.005$.

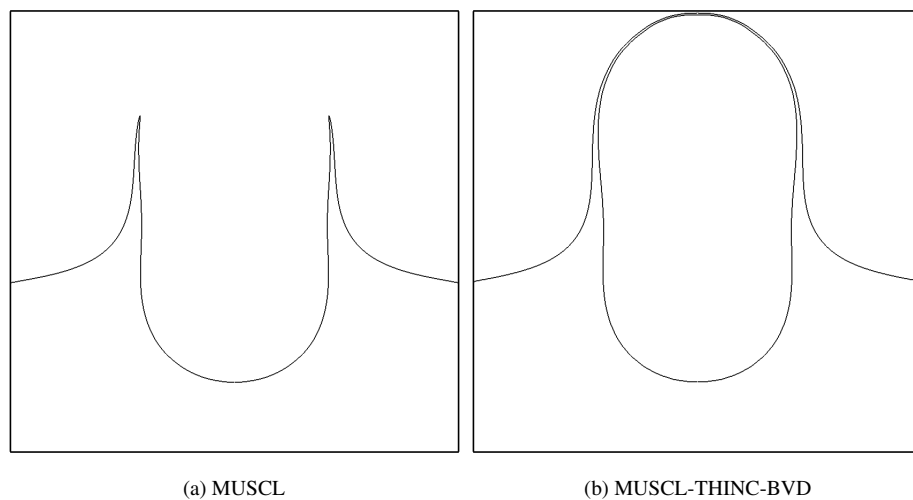


FIGURE 4.11: The material interface calculated by different schemes at $t = 3.16$ ms for underwater explosion test. Comparisons are made between MUSCL(a) and MUSCL-THINC-BVD(b) schemes.

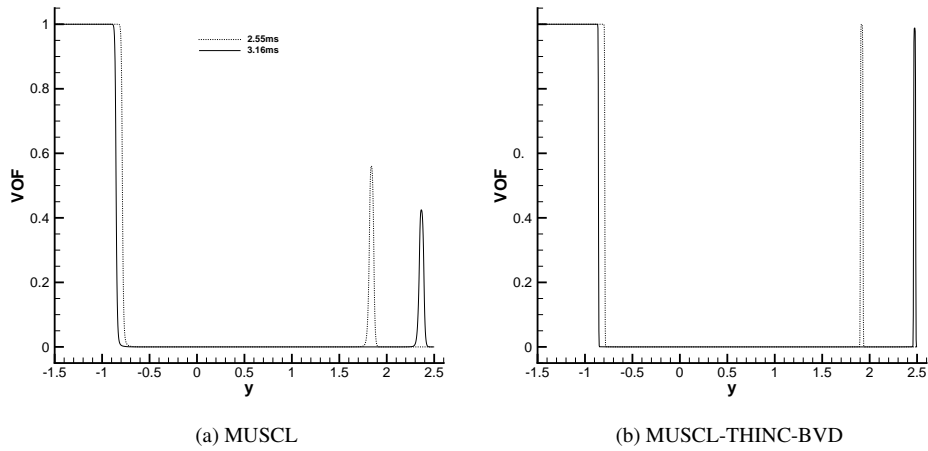


FIGURE 4.12: Distribution of VOF function along $x = 0$ cross-section for underwater explosion test at $t = 2.55, 3.16$ ms. Comparisons are made between MUSCL and MUSCL-THINC-BVD schemes.

numerical models for multiphase compressible flows [148, 149]. The computational domain for this problem is $[0, 8] \times [-1, 1]$ discretized by a 2000×500 uniform grid. Initially, a right moving Mach 6.0 plane shock is set at $x = 1.0$. A water column with the diameter 1.124 is centered at $(2, 0)$. Reflection boundaries are imposed for the top and bottom boundaries while transparent boundary conditions are set for the left and right boundaries. The Schlieren diagrams of density at different instants of the numerical solution computed by MUSCL-TINC-BVD scheme are shown in Fig. 4.13. Compared with Fig. 11 in [66] where fifth-order WENO scheme was applied with artificial compression technique for moving interface, the proposed scheme in present work not only captures the sharp material interface but also resolves more delicate flow structures on the same computational grid.

4.3.3 3D numerical tests

Extending the present numerical method to three dimensions is straightforward. Our 3D code has been generated with the CUDA (Compute Unified Device Architecture) toolkit, which can be executed on hardwares with GPU accelerators. We verified the 3D code by solving the air shock and helium bubble interaction benchmark test. A Mach

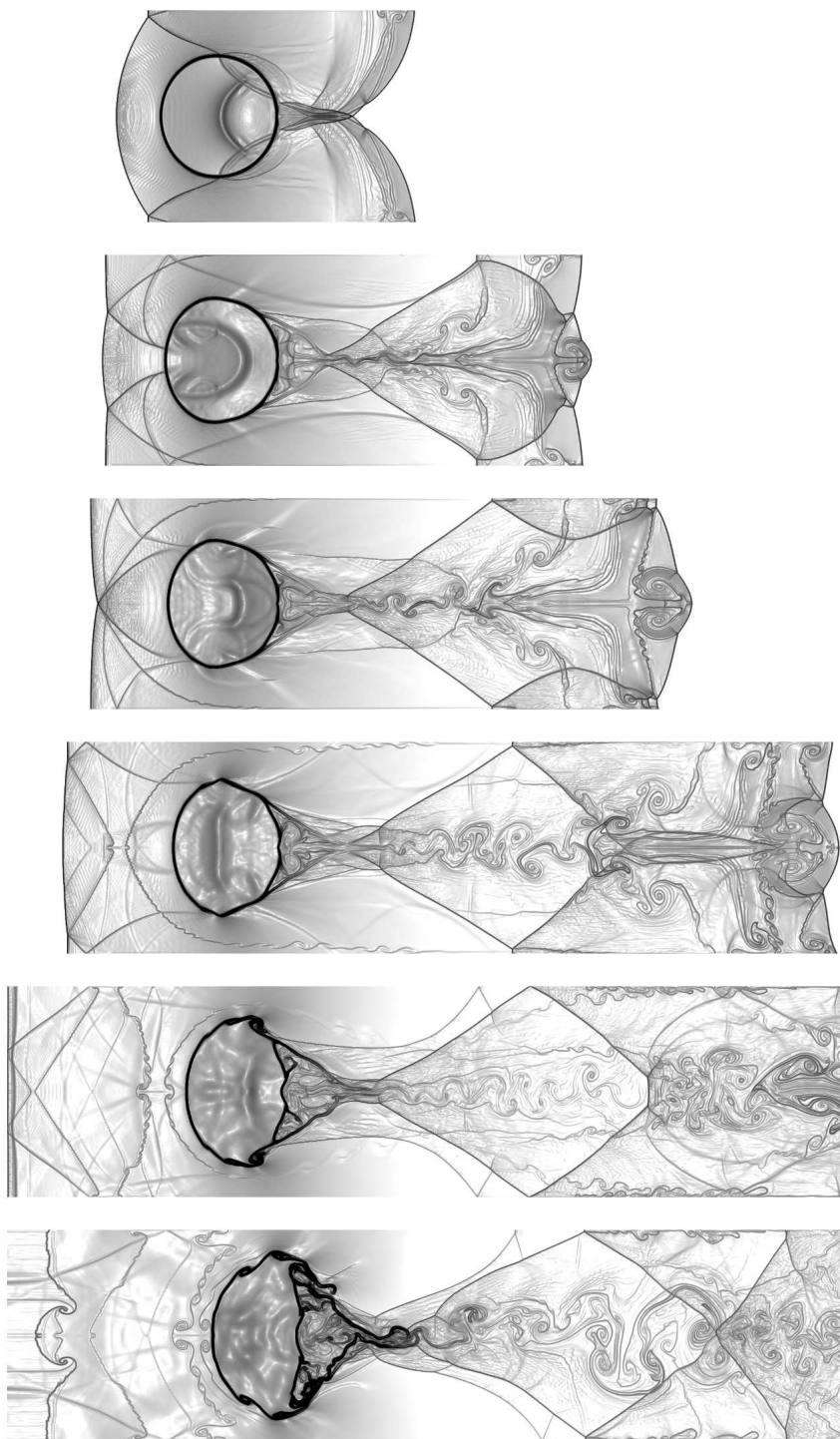


FIGURE 4.13: Schlieren images of density fields for the Mach 6.0 shock-water interaction benchmark test at instants $t = 0.5, 0.75, 0.89, 1.1, 1.5,$ and 2.15 solved by the MUSCL-THINC-BVD scheme on a 2000×500 uniform grid.

1.5 shock wave in the air interacts with a helium bubble. Same as the experimental conditions in [150], the density for the air is 1.29kg/m^3 and 0.167kg/m^3 for the helium bubble. The computational domain is 0.305m long, 0.08m wide and 0.08m high. The bubble radius is 0.02m. The domain is divided by a Cartesian grid of uniform cell, $\Delta x = \Delta y = \Delta z = \frac{1}{2200}$. We plot the surface of the deformed helium bubble, as well as the density and pressure fields on the central cross sections in Fig. 4.14. The plane shock impacts the helium bubble and deforms it axis-symmetrically into a twin-donut shape associated with complicated flow structures. The moving interfaces that separate air and helium are well resolved without numerical smearing. The comparisons with the experimental observations reported in [150] are shown in Fig. 4.15. Even though the density difference across the interfaces is relatively smaller in this test case, the bubble shapes, as well as the density disturbances at different instants, are reproduced by MUSCL-THINC-BVD scheme with adequate accuracy.

4.4 Summary

We implement MUSCL-THINC-BVD scheme to simulate compressible multiphase flows by solving the five-equation model. This scheme can resolve discontinuous solutions with much less numerical dissipation in comparison with other existing methods, which enables to solve moving interfaces of compact thickness without additional “anti-diffusion” or “artificial compression” manipulation. The MUSCL-THINC-BVD scheme is applied to volume fraction function and other physical variables as a normal finite volume scheme, and the consistency among different physical fields can be realized without any post adjustment.

The present method has been verified with widely used benchmark tests in comparison with other existing methods. Numerical results of the tests show a remarkable improvement in solution quality. Compared with the high-order shock-capturing schemes, the

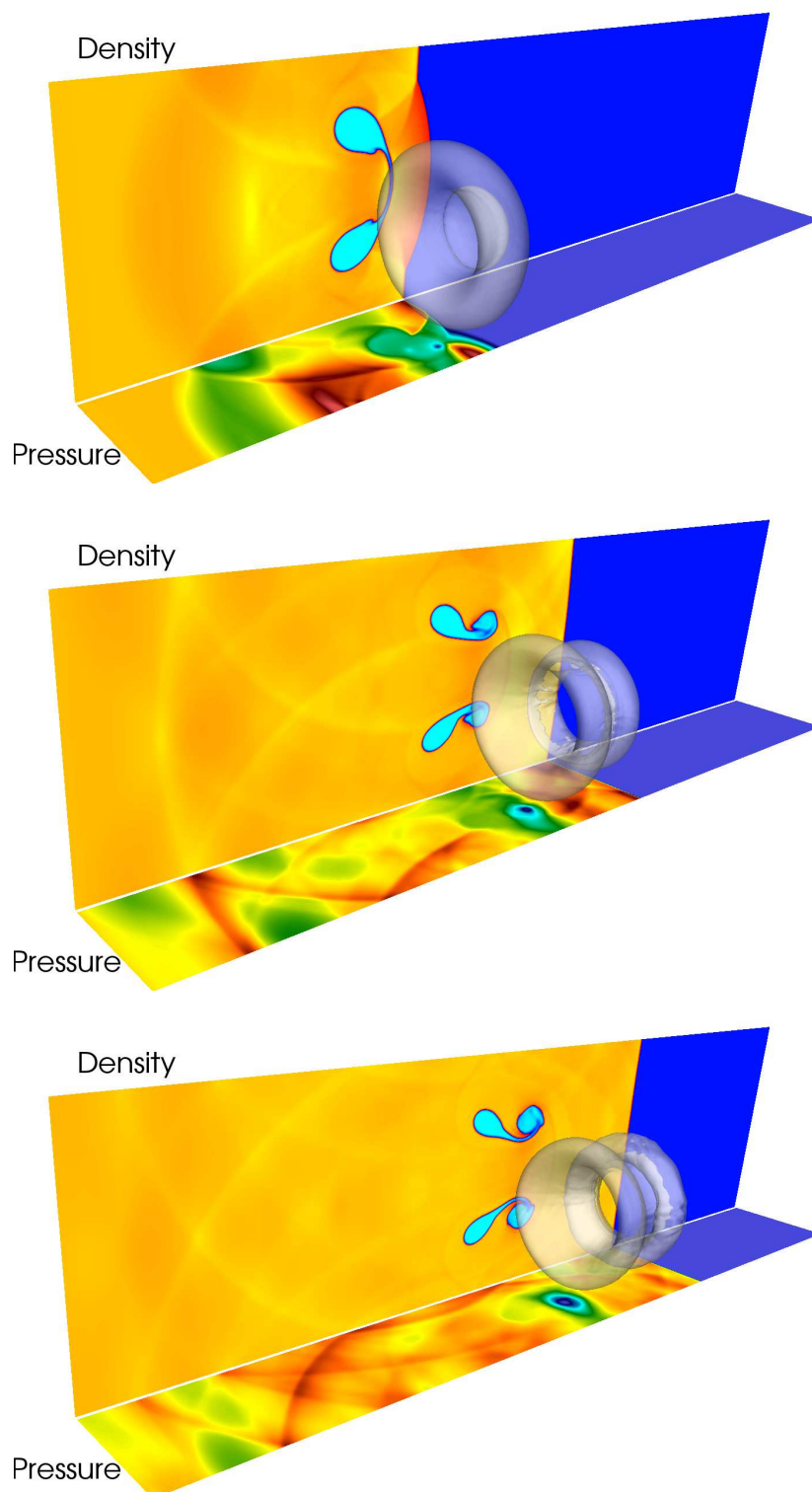


FIGURE 4.14: Numerical results for 3D air-shock and helium-bubble interactions. Displayed are the color maps of density and pressure fields on the central cross-sections and the iso-surface of the volume fraction of 0.5 that represents the moving interface. From top to bottom are the numerical results at $136\mu s$, $274\mu s$ and $346\mu s$ respectively.

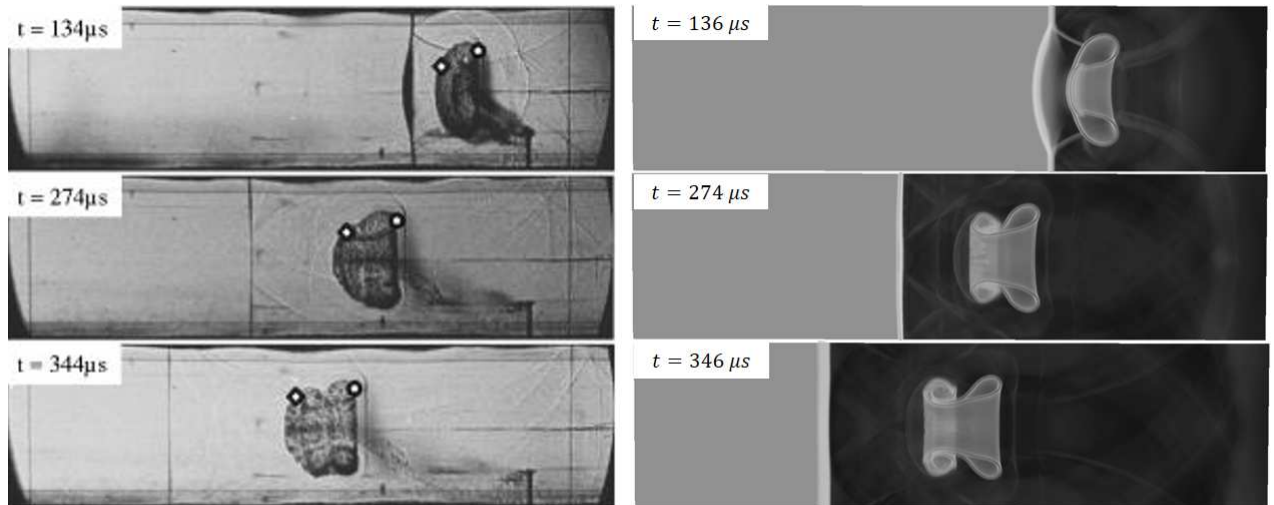


FIGURE 4.15: Numerical results for 3D air-shock and helium-bubble interaction. Displayed are the experimental snapshots reported in [150] (left column) and the grayscale maps of density on the central plane in numerical results.

new method shows competitive or superior numerical results but with less computational cost. This work provides an effective and practical approach to simulate compressible interfacial multiphase flows.

Chapter 5

Multi-moment finite volume method with the boundary gradient switching (BGS) limiting on structured grids

5.1 Review of MCV method

It is well known that the FVM has benefits such as it is algorithmically easy to design limiting processes to capture discontinuities. However, to increase order for FVM involves large stencil size. To overcome it, in this chapter we introduce MCV method which has compact stencils. It should be noted that to simulate problems involving strong discontinuities, FVM is better while to achieve high order and solve smooth flow region, MCV will be the better choice.

As one of high-order schemes with local reconstructions, multi-moment constrained finite volume (MCV) method [192] has been applied in both incompressible [22] and compressible flows[195]. The MCV scheme is appealing to the practical applications due to its flexibility to grid structures and the proper balance between the accuracy and the complexity of numerical schemes. Same as other local high-order schemes such as

discontinuous Galerkin (DG) method, the spectral volume (SV) method, the spectral difference (SD) method and the constrained interpolation profile (CIP) method, MCV schemes employ more than one local degrees of freedom (DOFs) within a local cell for a high-order spatial reconstruction. In MCV method, the point-wise values defined at solution points are adopted as DOFs and its spatial discretization formulations are derived by introducing the constraint conditions in terms of multi moments, including the point value (PV), the volume-integrated average (VIA) and the derivatives of the different orders of the physical fields.

According to well-known Godunov barrier for linear schemes, any monotonic linear scheme can be of only first order. As a result, the high-order MCV schemes will produce the non-physical oscillations while simulating the compressible flows, even for those cases with the smooth initial conditions where discontinuity will appear due to the nonlinearity of the governing equations. Several strategies have been employed by the local high-order schemes to suppress the numerical oscillations in the vicinity of discontinuities in the existing literature. One of the popular strategies is nonlinear limiting projection. Earlier studies such as in [5] for DG method and in [195] for MCV method use the total variation bounded (TVB) limiters, where the TVB criterion is needed to find the “troubled cells” by evaluating the smoothness of the solution. For the troubled cells, where discontinuous solutions are detected, the total variation diminishing (TVD) limiting procedure is applied. As the TVD limiting has second-order accuracy at most, it tends to introduce too much extra numerical dissipation and degrades the high-order accuracy of the original schemes. The higher order limited reconstructions, such as the essentially non-oscillatory (ENO) and weighted essentially non-oscillatory (WENO) reconstructions, are applied in for DG method and in [195] for MCV method. The WENO limiter effectively reduces the numerical dissipation errors around smooth region and can retain the high-order convergence. However, the current implementations of the WENO limiting in the high-order schemes with local reconstructions cannot make the full use of the local DOFs, and the solutions are heavily dependent on the

TVB criterion that determines the “troubled cells” in an ad hoc fashion. This is one of the key issues to be solved for developing numerical models for practical applications using local high-order schemes.

In this study, a new formulation for non-oscillatory three-point MCV scheme of fourth-order accuracy is proposed. Different from Hermite interpolation polynomial used in [195], where the first-order derivative at the cell center was employed to adjust numerical properties of the scheme, two cubic Lagrangian interpolation polynomials, which are constructed by using the DOFs in adjacent cells, are employed as candidates for spatial reconstruction. These two candidates are chosen through a new proposed boundary gradient switching (BGS) algorithm based on the underlying idea of the ENO method to remove the non-physical oscillations near the discontinuity. Since two candidate polynomials give the fourth-order accuracy, the proposed scheme is also expected to have the same convergence rate as verified by the numerical tests in this paper. The proposed scheme is implemented without any user-specifying ad hoc parameter. Furthermore, the stencil required by this new scheme still remains compact (within three cells), same as our previous study.

5.2 Formulation of 3-point MCV scheme with slope constraint

We consider the following hyperbolic system in one dimension,

$$\frac{\partial \mathbf{q}}{\partial t} + \frac{\partial \mathbf{f}(\mathbf{q})}{\partial x} = 0, \quad (5.1)$$

where \mathbf{q} is the vector of the dependent variables, and $\mathbf{f}(\mathbf{q})$ the vector of the flux functions.

The computational domain is divided into I non-overlapping cells, e.g. $\mathcal{C}_i = [x_{i-\frac{1}{2}}, x_{i+\frac{1}{2}}]$ ($i = 1, 2, \dots, I$). Within the computational cell \mathcal{C}_i , the local DOFs are defined as the point-wise values q_{ik} ($k = 1, 2, \dots, K$) at solution points x_{ik} , which are updated using the governing equations of differential-form as

$$\frac{\partial \mathbf{q}_{ik}}{\partial t} = - \left(\frac{\partial \mathbf{f}(\mathbf{q})}{\partial x} \right)_{ik}. \quad (5.2)$$

Using the framework of MCV method, the constraint conditions in terms of different kinds of moments are adopted to derive the discretization formulation of the right-hand side term in (5.2).

Here we briefly describe the numerical formulation for three-point MCV (MCV3) scheme, which is the basic framework for this study.

Within cell \mathcal{C}_i , three local DOFs are defined as the pointwise values as \mathbf{q}_{i1} , \mathbf{q}_{i2} and \mathbf{q}_{i3} at equidistantly arranged solution points $x_{i1} = x_{i-\frac{1}{2}}$, $x_{i2} = x_i$ and $x_{i3} = x_{i+\frac{1}{2}}$, where $x_i = (x_{i-\frac{1}{2}} + x_{i+\frac{1}{2}})/2$ is the center of cell \mathcal{C}_i .

Two kinds of moments are adopted to provide the constraint conditions for spatial discretization of the DOFs.

- **Point Values (PV)**

At the cell interface, e.g., $x = x_{i-\frac{1}{2}}$ PV moment is specified as

$$\overline{P} \mathbf{q}_{i-\frac{1}{2}}(t) = \mathbf{q} \left(x_{i-\frac{1}{2}}, t \right). \quad (5.3)$$

- **Volume-Integrated Average (VIA)**

Over the cell \mathcal{C}_i , VIA moment is specified as

$$\overline{V} \mathbf{q}_i(t) = \frac{1}{\Delta x} \int_{x_{i-\frac{1}{2}}}^{x_{i+\frac{1}{2}}} \mathbf{q}(x, t) dx. \quad (5.4)$$

The multi-moment constraint conditions are related with the local DOFs as

$$\begin{cases} \overline{P}\mathbf{q}_{i-\frac{1}{2}} = \mathbf{Q}_i\left(x_{i-\frac{1}{2}}\right) = \mathbf{q}_{i1}, \\ \overline{P}\mathbf{q}_{i+\frac{1}{2}} = \mathbf{Q}_i\left(x_{i+\frac{1}{2}}\right) = \mathbf{q}_{i3}, \\ \overline{V}\mathbf{q}_i = \int_{x_{i-\frac{1}{2}}}^{x_{i+\frac{1}{2}}} \mathbf{Q}_i(x) dx = \frac{1}{6}(\mathbf{q}_{i1} + 4\mathbf{q}_{i2} + \mathbf{q}_{i3}), \end{cases} \quad (5.5)$$

where $\mathbf{Q}_i(x)$ is a Lagrangian interpolation polynomial for physical field $\mathbf{q}(x)$ within cell \mathcal{C}_i , having the form of

$$\mathbf{Q}_i(x) = \sum_{k=1}^3 \mathbf{q}_{ik} \phi_{ik}(x), \quad (5.6)$$

with Lagrangian basis function $\phi_{ik}(x)$ written as

$$\phi_{ik}(x) = \prod_{l=1, l \neq k}^3 \frac{x - x_{il}}{x_{ik} - x_{il}}. \quad (5.7)$$

The different moments are updated by different formulations in our multi-moment schemes.

- PV moment is updated by differential-form governing equations as

$$\frac{\partial \overline{P}\mathbf{q}_{i-\frac{1}{2}}}{\partial t} \approx -\hat{\mathbf{f}}_{xi-\frac{1}{2}}. \quad (5.8)$$

The derivative of flux function in (5.8) is evaluated by solving a derivative Riemann problem as

$$\hat{\mathbf{f}}_{xi-\frac{1}{2}} = \text{dRiemann}\left(\hat{\mathbf{f}}_{xi-\frac{1}{2}}^-, \hat{\mathbf{f}}_{xi-\frac{1}{2}}^+\right), \quad (5.9)$$

where

$$\begin{cases} \hat{\mathbf{f}}_{xi-\frac{1}{2}}^- = \mathbf{A}_{i-\frac{1}{2}} \left(\frac{\partial \mathbf{Q}_{i-1}(x)}{\partial x} \right)_{i-\frac{1}{2}}, \\ \hat{\mathbf{f}}_{xi-\frac{1}{2}}^+ = \mathbf{A}_{i-\frac{1}{2}} \left(\frac{\partial \mathbf{Q}_i(x)}{\partial x} \right)_{i-\frac{1}{2}}, \end{cases} \quad (5.10)$$

with $\mathbf{A}_{i-\frac{1}{2}}$ being the Jacobian matrix at cell interface $x = x_{i-\frac{1}{2}}$.

- VIA moment is updated by a flux-form formulation assuring the conservation of the proposed scheme as

$$\frac{\partial \overline{\mathbf{q}}_i}{\partial t} \approx -\frac{1}{\Delta x_i} \left(\hat{\mathbf{f}}_{i+\frac{1}{2}} - \hat{\mathbf{f}}_{i-\frac{1}{2}} \right), \quad (5.11)$$

where $\Delta x_i = x_{i+\frac{1}{2}} - x_{i-\frac{1}{2}}$ and the numerical flux at cell interfaces are computed directly from the DOFs readily available there as the computational variables, i.e.

$$\hat{\mathbf{f}}_{i-\frac{1}{2}} = \mathbf{f}(\mathbf{q}_{i1}) \text{ and } \hat{\mathbf{f}}_{i+\frac{1}{2}} = \mathbf{f}(\mathbf{q}_{i3}).$$

Using the constraint relation (5.5), the spatial discretization of DOFs within cell \mathcal{C}_i are then determined from (5.8) and (5.11) as

$$\begin{cases} \frac{\partial q_{i1}}{\partial t} &= -\hat{\mathbf{f}}_{xi-\frac{1}{2}}, \\ \frac{\partial q_{i2}}{\partial t} &= -\frac{3}{2\Delta x_i} \left(\hat{\mathbf{f}}_{i+\frac{1}{2}} - \hat{\mathbf{f}}_{i-\frac{1}{2}} \right) + \frac{1}{4} \left(\hat{\mathbf{f}}_{xi-\frac{1}{2}} + \hat{\mathbf{f}}_{xi+\frac{1}{2}} \right), \\ \frac{\partial q_{i3}}{\partial t} &= -\hat{\mathbf{f}}_{xi+\frac{1}{2}}. \end{cases} \quad (5.12)$$

With spatial discretization given in (5.12), the semi-discrete equations are then solved using the explicit Runge-Kutta method. It is noted that as the values at the cell interfaces are shared by the two neighboring cells, either the first or the third equation needs to be solved with the second equation in (5.12).

The MCV scheme can be straightforwardly extended to multi-dimensions for structured grids. The one-dimensional formulation given above can be applied in multi-dimensional problems by sweeping the different directions respectively. The numerical procedure is described in detail in.

A three-point MCV scheme with TVD slope limiter was introduced in [195], which is also adopted in this study as an auxiliary spatial reconstruction profile in the present numerical formulation for a new high-order non-oscillatory MCV scheme.

Based on the basic idea proposed in [197], an additional constraint condition, i.e. the slope at the cell center, is introduced when building the spatial reconstruction of the dependent variable. Within cell \mathcal{C}_i , a cubic polynomial $\mathbf{Q}_i^{TVD}(x)$ is built using following conditions as

$$\begin{cases} \mathbf{Q}_i^{TVD}(x_{i1}) = \mathbf{q}_{i1}, \\ \mathbf{Q}_i^{TVD}(x_{i2}) = \mathbf{q}_{i2}, \\ \mathbf{Q}_i^{TVD}(x_{i3}) = \mathbf{q}_{i3}, \\ \mathbf{Q}_{x_i}^{TVD}(x_{i2}) = \mathbf{d}_i, \end{cases} \quad (5.13)$$

where \mathbf{q}_{i1} , \mathbf{q}_{i2} and \mathbf{q}_{i3} are the known local DOFs and \mathbf{d}_i is a parameter which can be used to adjust the numerical properties of the resulted scheme. By “TVD”, we mean that the slope \mathbf{d}_i is approximated by a TVD slope limiter as shown next.

The condition on the slope at the cell center plays a key role in the resulting scheme, which can be obtained by different algorithms to design the schemes with desired numerical properties [197].

To avoid the non-physical oscillations around the discontinuities, a minmod TVD slope limiter can be adopted as

$$\mathbf{d}_i = \text{minmod}(\mathbf{d}_l, \mathbf{d}_c, \mathbf{d}_r), \quad (5.14)$$

where

$$\begin{aligned} \mathbf{d}_l &= 2.0 \frac{\mathbf{q}_{i2} - \mathbf{q}_{i-1,2}}{\Delta x}, & \mathbf{d}_r &= 2.0 \frac{\mathbf{q}_{i+1,2} - \mathbf{q}_{i,2}}{\Delta x}, \\ \mathbf{d}_c &= \frac{-\frac{4}{3}\mathbf{q}_{i1} + \frac{1}{6}\mathbf{q}_{i-1,2} + \frac{4}{3}\mathbf{q}_{i3} - \frac{1}{6}\mathbf{q}_{i+1,2}}{\Delta x}, \end{aligned} \quad (5.15)$$

and

$$\text{minmod}(a, b, c) = \begin{cases} s \times \min(|a|, |b|, |c|) & \text{if } s = \text{sign}(a) = \text{sign}(b) = \text{sign}(c), \\ 0 & \text{otherwise.} \end{cases} \quad (5.16)$$

With spatial reconstruction $\mathbf{Q}_i^{TVD}(x)$ for the physical fields, the resulting scheme is non-oscillatory but at most of second-order accuracy even in the smooth areas. It should

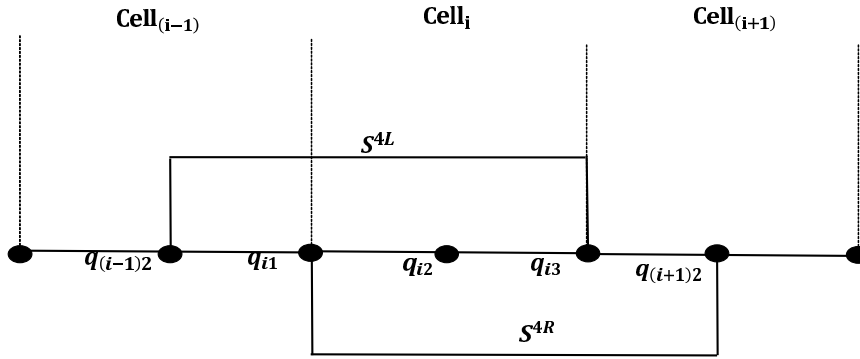


FIGURE 5.1: Stencils for spatial reconstruction.

be notified that by replacing $Q_{i-1}(x)$ and $Q_i(x)$ with $Q_{i-1}^{TVD}(x)$ and $Q_i^{TVD}(x)$ in (5.10) the derivatives of the flux and thus the numerical solution will change, while the evolution equations to update the DOFs remain the same in form as (5.12). Hereafter, we denote the corresponding scheme as MCV3-TVD scheme. The numerical formulations of MCV3-TVD is completely same as MCV3 scheme shown above, except that the polynomial $Q_i^{TVD}(x)$ is used in (5.10) instead of Lagrangian polynomial $Q_i(x)$ through (5.6).

Different from the limiting procedure adopting in the original MCV scheme, DOFs defined at the cell interface are always shared by the two neighboring cells in the current study. As a result, the computation become more efficient regarding to both memory requirement and CPU cost as discussed in [196].

5.3 A non-oscillatory MCV scheme with boundary gradient switching

In this subsection, we further develop a non-oscillatory scheme using the MCV framework, which doesn't lose the original accuracy in smooth areas.

Following the work in [196], the cubic interpolation polynomial of dependent variable can be obtained by adopting the DOFs in left and right cells directly, instead of using

the slope at cell center as an additional condition. As shown in Fig. 5.1, two stencils can be used for the reconstruction in cell \mathcal{C}_i , i.e. \mathcal{S}^{4L} including the pointwise values at x_{i-1} , $x_{i-\frac{1}{2}}$, x_i and $x_{i+\frac{1}{2}}$ and \mathcal{S}^{4R} including the pointwise values at $x_{i-\frac{1}{2}}$, x_i , $x_{i+\frac{1}{2}}$ and x_{i+1} .

Using stencil \mathcal{S}^{4L} , a cubic polynomial Q_i^{4L} in cell \mathcal{C}_i is built with the conditions as

$$\begin{cases} Q_i^{4L}(x_{i-1}) = q_{i-1,2}, \\ Q_i^{4L}(x_{i-\frac{1}{2}}) = q_{i1}, \\ Q_i^{4L}(x_i) = q_{i2}, \\ Q_i^{4L}(x_{i+\frac{1}{2}}) = q_{i3}. \end{cases} \quad (5.17)$$

Similarly, another cubic polynomial Q_i^{4R} is obtained by using stencil \mathcal{S}^{4R} as

$$\begin{cases} Q_i^{4R}(x_{i-\frac{1}{2}}) = q_{i1}, \\ Q_i^{4R}(x_i) = q_{i2}, \\ Q_i^{4R}(x_{i+\frac{1}{2}}) = q_{i3}, \\ Q_i^{4R}(x_{i+1}) = q_{i+1,2}. \end{cases} \quad (5.18)$$

Analogous to the MCV3-TVD scheme, substituting the spatial reconstruction $Q_i(x)$ in subsection ?? with Q_i^{4L} or Q_i^{4R} , and using the evolution equations (5.12) to update the DOFs, we get other two new schemes of fourth-order accuracy. We denote the scheme using $Q_i^{4L}(x)$ for reconstruction as MCV3-4L and one with $Q_i^{4R}(x)$ as MCV3-4R, hereafter. However, without any limiting both MCV3-4L and MCV3-4R schemes will generate spurious numerical oscillations around the discontinuities, which even leads to the blow-up of computations when solving problems with shock waves.

In this study, we propose a boundary gradient switching (BGS) algorithm considering the variation-minimization principle, which adopts the basic idea in ENO method and is used to choose the smoother spatial reconstruction profile between Q_i^{4L} and Q_i^{4R}

in comparison with \mathbf{Q}_i^{TVD} . This scheme is referred to as MCV3-BGS scheme, which effectively suppresses non-physical oscillations in numerical solutions while realizing high-order accuracy in smooth region. The numerical formulation given in (5.10) is then recast into

$$\begin{cases} \hat{\mathbf{f}}_{xi-\frac{1}{2}}^- = \mathbf{A}_{i-\frac{1}{2}} \text{BGS} \left[\left(\frac{\partial \mathbf{Q}_{i-1}(x)}{\partial x} \right)_{i-\frac{1}{2}} \right], \\ \hat{\mathbf{f}}_{xi-\frac{1}{2}}^+ = \mathbf{A}_{i-\frac{1}{2}} \text{BGS} \left[\left(\frac{\partial \mathbf{Q}_i(x)}{\partial x} \right)_{i-\frac{1}{2}} \right], \end{cases} \quad (5.19)$$

with $\text{BGS} \left[\left(\frac{\partial \mathbf{Q}_i(x)}{\partial x} \right)_{i-\frac{1}{2}} \right]$ being calculated by

$$\text{BGS} \left[\left(\frac{\partial \mathbf{Q}_i(x)}{\partial x} \right)_{i-\frac{1}{2}} \right] = \begin{cases} \text{dmin}(\mathbf{d}_1, \mathbf{d}_2) & \text{if } \text{sign}(\mathbf{d}_1) = \text{sign}(\mathbf{d}_2) = \text{sign}(\mathbf{d}_3), \\ \mathbf{d}_1 & \text{only if } \text{sign}(\mathbf{d}_1) = \text{sign}(\mathbf{d}_3), \\ \mathbf{d}_2 & \text{only if } \text{sign}(\mathbf{d}_2) = \text{sign}(\mathbf{d}_3), \\ \text{absmin}(\mathbf{d}_1, \mathbf{d}_2) & \text{otherwise,} \end{cases} \quad (5.20)$$

where

$$\begin{cases} \mathbf{d}_1 = \left(\frac{\partial \mathbf{Q}_i^{4L}(x)}{\partial x} \right)_{i-\frac{1}{2}}, \\ \mathbf{d}_2 = \left(\frac{\partial \mathbf{Q}_i^{4R}(x)}{\partial x} \right)_{i-\frac{1}{2}}, \\ \mathbf{d}_3 = \left(\frac{\partial \mathbf{Q}_i^{TVD}(x)}{\partial x} \right)_{i-\frac{1}{2}}, \end{cases} \quad (5.21)$$

and dmin is the variation diminishing function, absmin is the absolute minimum function defined by

$$\text{dmin}(\mathbf{d}_1, \mathbf{d}_2) = \begin{cases} \mathbf{d}_1 & \text{if } |\mathbf{d}_1 - \mathbf{d}_3| < |\mathbf{d}_2 - \mathbf{d}_3|, \\ \mathbf{d}_2 & \text{otherwise,} \end{cases} \quad (5.22)$$

$$\text{absmin}(\mathbf{d}_1, \mathbf{d}_2) = \begin{cases} \mathbf{d}_1 & \text{if } |\mathbf{d}_1| < |\mathbf{d}_2|, \\ \mathbf{d}_2 & \text{otherwise.} \end{cases} \quad (5.23)$$

With this BGS algorithm, the smoother approximation of derivative of flux function is

adopted during computations to remove the non-physical oscillations as shown in the benchmark tests in the next section. Meanwhile, the BGS processing doesn't degrade the accuracy of the proposed scheme since both MCV3-4L and MCV3-4R schemes are fourth-order accurate.

5.4 Numerical experiments

In this section, we verify the proposed MCV3-BGS scheme by simulating the widely-used benchmark tests of one- and two-dimensional hyperbolic conservation laws. The SSP Runge-Kutta method (SSPRK(5,4)) is adopted in this study for time marching and the maximal allowable CFL number for computational stability is about 0.6.

5.4.1 1D linear advection equation

The one-dimensional advection equation with a constant speed is simulated. The governing equation is specified by $\mathbf{q} = \phi$ and $\mathbf{f}(\mathbf{q}) = \phi$ in (5.1) where ϕ is the advected field.

Advection of one-dimensional sine wave

This test is carried out on gradually refined grids to evaluate the convergence rate of the proposed scheme. The initial smooth distribution is given by

$$\phi(x, 0) = \sin(\pi x), \quad x \in [-1, 1]. \quad (5.24)$$

The normalized error l_1 and l_∞ are defined as

$$l_1 = \sum_{i=1}^I \frac{|\phi_i^e - \phi_i^n|}{I}, \quad \text{and} \quad l_\infty = \max_{1 \leq i \leq I} |\phi_i^e - \phi_i^n|, \quad (5.25)$$

TABLE 5.1: Numerical errors and convergence rates of the Euler equation for sinusoidal profile distribution

	Grids	l_1 error	l_1 order	l_∞ error	l_∞ order
MCV3-4L	20	1.0441e-04	–	1.6298e-04	–
	40	6.5192e-06	4.00	1.0261e-05	3.99
	80	4.0899e-07	3.99	6.4196E-07	4.00
	160	2.5576e-08	4.00	4.0291e-08	3.99
	320	1.5990e-09	4.00	2.6706e-09	3.92
MCV3-4R	20	2.0007e-04	–	3.1091e-03	–
	40	1.3362e-05	3.90	2.0974e-04	3.89
	80	8.5350e-07	3.97	1.3405e-06	3.97
	160	5.3712e-08	3.99	8.4555e-08	3.99
	320	3.3652e-09	4.00	5.4692e-09	3.95
MCV3-BGS	20	1.7824e-04	–	5.5121e-04	–
	40	1.6697e-05	3.42	6.8212e-05	3.01
	80	1.1200e-06	3.80	6.0404e-06	3.50
	160	7.8740e-08	3.93	6.1734e-07	3.29
	320	4.9661e-09	3.99	5.2868e-08	3.55

where ϕ^e and ϕ^n stand for exact and numerical solutions respectively.

We ran the computation for one period (at $t = 2.0$) and summarize the numerical errors and the convergence rates for MCV3-4L, MCV3-4R and MCV-BGS in Table 5.1. Compared with MCV3-4L and MCV3-4R schemes, the BGS algorithm does not make significant differences in convergence rate regarding to l_1 error for this test with smooth solution. MCV3-BGS scheme achieves the fourth-order accuracy regarding to l_1 as expected.

Advection of one-dimensional square wave

In this test, the propagation of a square wave is simulated to check the ability of the proposed scheme to capture discontinuous solutions. The initial profile is

$$\phi(x, 0) = \begin{cases} 1 & \text{if } |x| \leq 0.4, \\ 0 & \text{otherwise.} \end{cases} \quad (5.26)$$

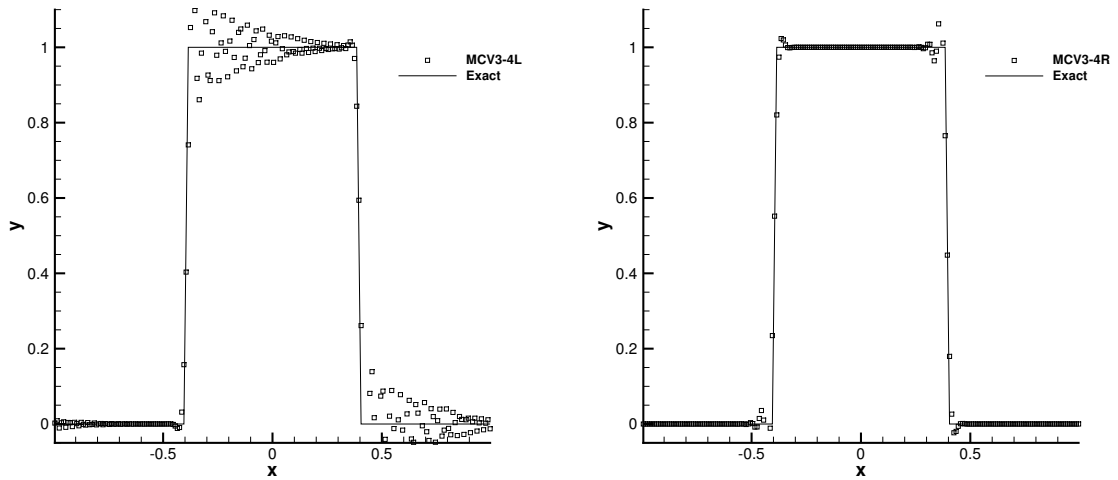


FIGURE 5.2: Numerical results of 1D advection of a square wave by MCV3-4L scheme (left panel) and MCV3-4R (right panel) with 200 cells after one period.

Numerical experiment was carried out on the uniform grid with 200 cells. The numerical results using MCV3-4L and MCV3-4R are depicted in Fig. 5.2. The non-physical oscillations are obviously found in both results. Considering the ability of dealing with the discontinuity, MCV3-4R scheme performs better than MCV3-4L scheme though it gives smaller absolute errors for a smooth profile in the above case. It is noted that this observation is only for the case of positive advection velocity. For negative advection velocity, a formulation needs to be constructed using new stencils symmetrical respect to the cell boundary in line with the upwinding spirit.

The numerical result by MCV3-BGS scheme is shown in Fig. 5.3. The BGS algorithm always tends to choose the smoother spatial reconstruction between MCV3-4L and MCV3-4R schemes and the non-physical oscillations are effectively removed. Meanwhile, the numerical diffusion is controlled to a minimized extent, as the jumps are well resolved by MCV3-BGS scheme with a more compact thickness in comparison with other existing schemes.

Advection of one-dimensional complex wave

To examine the performance of the proposed scheme in solving profiles of different smoothness, we further simulated the propagation of a complex wave [2], which includes both discontinuous and smooth solutions. The initial distribution of the advected

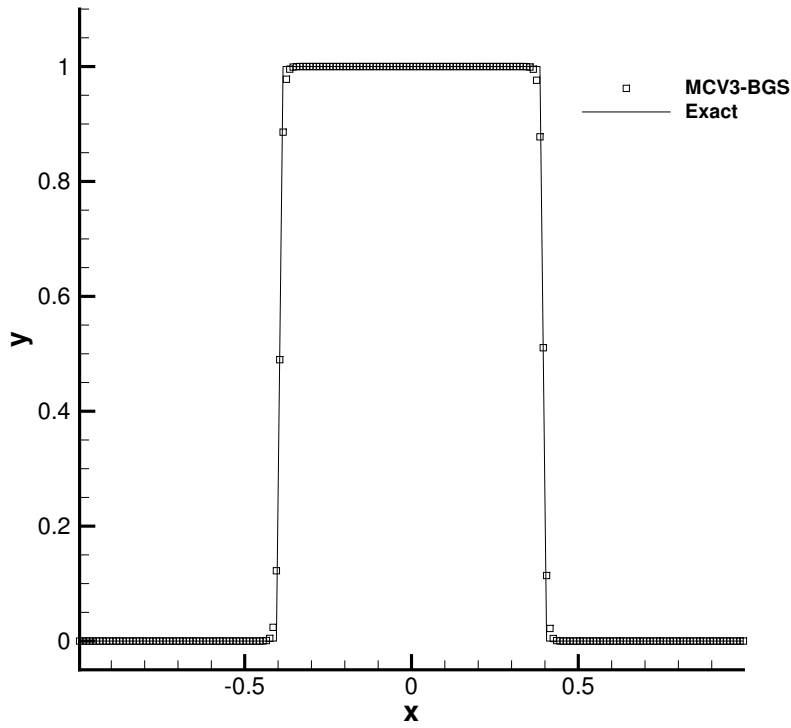


FIGURE 5.3: Numerical result of 1D advection of a square wave by MCV3-BGS scheme with 200 cells after one period.

field is

$$\phi(x, 0) = \begin{cases} \frac{1}{6} [G(x, \beta, z - \delta) + G(x, \beta, z + \delta) + 4G(x, \beta, z)] & \text{if } |x + 0.7| \leq 0.1, \\ 1 & \text{if } |x + 0.3| \leq 0.1, \\ 1 - |10(x - 0.1)| & \text{if } |x - 0.1| \leq 0.1, \\ \frac{1}{6} [F(x, \alpha, a - \delta) + F(x, \alpha, a + \delta) + 4F(x, \alpha, a)] & \text{if } |x - 0.5| \leq 0.1, \\ 0 & \text{otherwise,} \end{cases} \quad (5.27)$$

where functions F and G are defined as

$$G(x, \beta, z) = \exp[-\beta(x - z)^2], \quad F(x, \alpha, a) = \sqrt{\max[1 - \alpha^2(x - a)^2, 0]}, \quad (5.28)$$

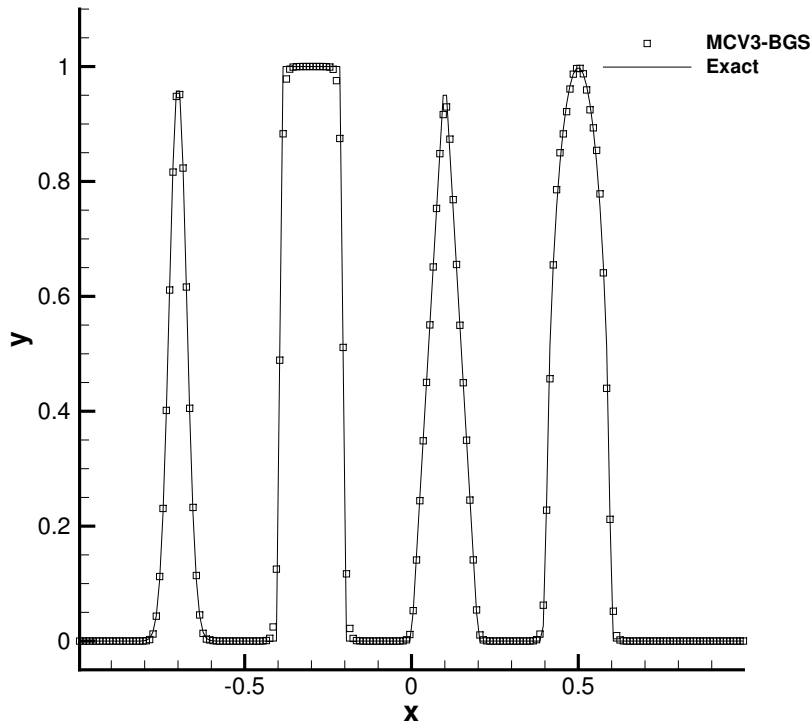


FIGURE 5.4: Numerical results of 1D advection of complex wave with 200 cells after one period.

and the coefficients are

$$a = 0.5, z = 0.7, \delta = 0.005, \alpha = 10.0, \beta = \log_2(36\delta^2). \quad (5.29)$$

The numerical result after one period of computation on a 200-cell mesh is plotted in Fig.5.4. It shows that the discontinuities are sharply represented without visible oscillations, while the smooth extremes are well preserved due to the high-order accuracy of the proposed scheme.

5.4.2 1D non-linear equation system

Accuracy test of 1D inviscid Burgers' equation

TABLE 5.2: Numerical errors and convergence rates of the 1D inviscid Burgers' equation

Grid	l_1 error	l_1 order	l_∞ error	l_∞ order
40	6.7402e-05	-	1.5536e-03	-
80	5.3180e-06	3.66	1.8428e-04	3.08
160	3.8335e-07	3.79	1.8069e-05	3.35
320	2.5456e-08	3.91	1.6796e-06	3.43
640	1.7071e-09	3.88	1.5114e-07	3.47

To test the convergence rate of proposed scheme on non-linear equations, we solve inviscid Burgers' equation with initial condition $u(x, 0) = 0.5 + \sin(\pi x)$. The exact solution profile will remain smooth until $t = 1.0/\pi$ before producing a moving shock and a rarefaction wave. The computation is evolved to $t = 0.5/\pi$ to calculate the l_1 and l_∞ errors which have been summered in Table 5.2. We can see that the proposed MCV3-BGS scheme converges nearly with a 4th-order accuracy regarding to l_1 order for this nonlinear test.

Shock capturing test of 1D inviscid Burgers' equation

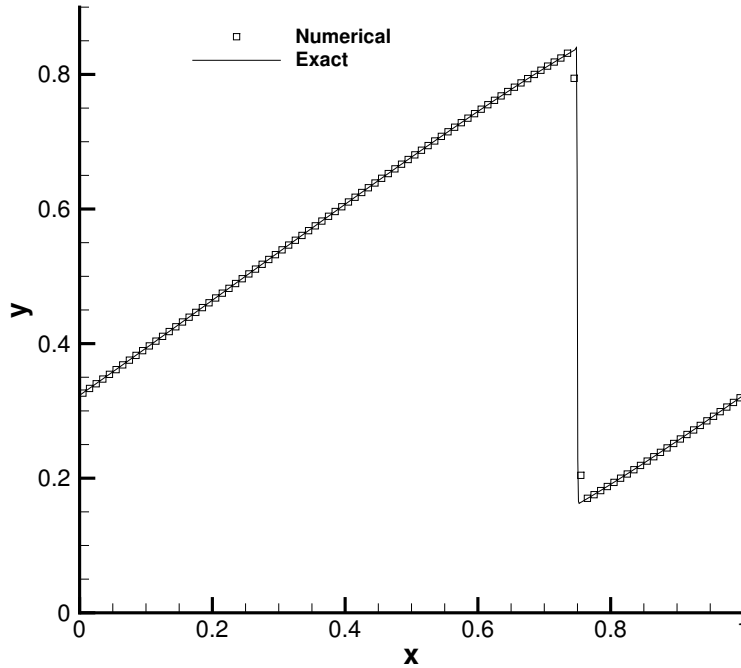
We solve the above equation with a smooth initial condition as

$$u(x, 0) = 0.5 + 0.4 \cos(2\pi x). \quad (5.30)$$

The time step is set as $\Delta t = 0.2\Delta x$ in this test. The result calculated on a uniform grid with 100 cells at $t = 1$ is given in Fig. 5.5.

Shock can be observed in the numerical result. With the BGS algorithm, the shock wave is well resolved (within two cells) without visible non-physical oscillation. The numerical result verified the performance of the proposed scheme in solving the non-linear problem.

One-dimensional Euler equations

FIGURE 5.5: Numerical results of Burgers' equation at $t=1$ with 100 cells.

The one-dimensional Euler equations are specified as

$$\mathbf{q} = [\rho, \rho u, E]^T, \quad \mathbf{f}(\mathbf{q}) = [\rho u, \rho u^2 + p, u(E + p)]^T, \quad (5.31)$$

where ρ is the density, u the velocity, p the pressure and E the total energy. The equation of state of ideal gas is $E = \frac{p}{\gamma-1} + \frac{1}{2}\rho u^2$ with $\gamma = 1.4$.

The Jacobian matrix \mathbf{A} is calculated following [195] as

$$\mathbf{A}_{i-\frac{1}{2}} = \frac{1}{2}(\bar{\mathbf{A}}_{i-\frac{1}{2}} + \tilde{\mathbf{A}}_{i-\frac{1}{2}}), \quad (5.32)$$

where $\bar{\mathbf{A}}_{i-\frac{1}{2}}$ is the Roe-averaged Jacobian matrix computed from the VIA moments of dependent variables in cells \mathcal{C}_{i-1} and \mathcal{C}_i and $\tilde{\mathbf{A}}_{i-\frac{1}{2}}$ is obtained directly from the point values of the physical variables at the cell interface.

For Euler equations, the BGS operation is applied to the characteristic variables and the

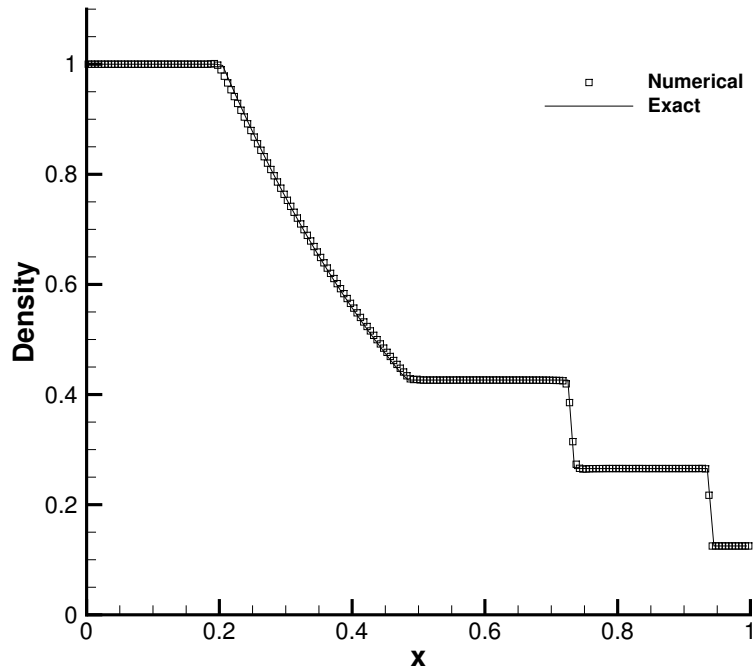


FIGURE 5.6: Numerical result for density field of Sod's problem at $t = 0.25$ with 200 cells.

solution procedure can be referred to [195]. As the same as [64], the time step in the test cases for one-dimensional Euler equations is simply set to be $\Delta t = 0.1\Delta x$ unless a special statement is made.

Sod's problem

For this problem, the initial distribution is specified as [76]

$$(\rho_0, u_0, p_0) = \begin{cases} (1, 0, 1) & \text{if } 0 \leq x \leq 0.5, \\ (0.125, 0, 0.1) & \text{otherwise.} \end{cases} \quad (5.33)$$

The computation is carried out with 200 uniform cells and the model is integrated up to $t = 0.25$. The numerical result is presented in Fig. 5.6. The current method shows better results in comparison with most existing methods.

Lax's problem

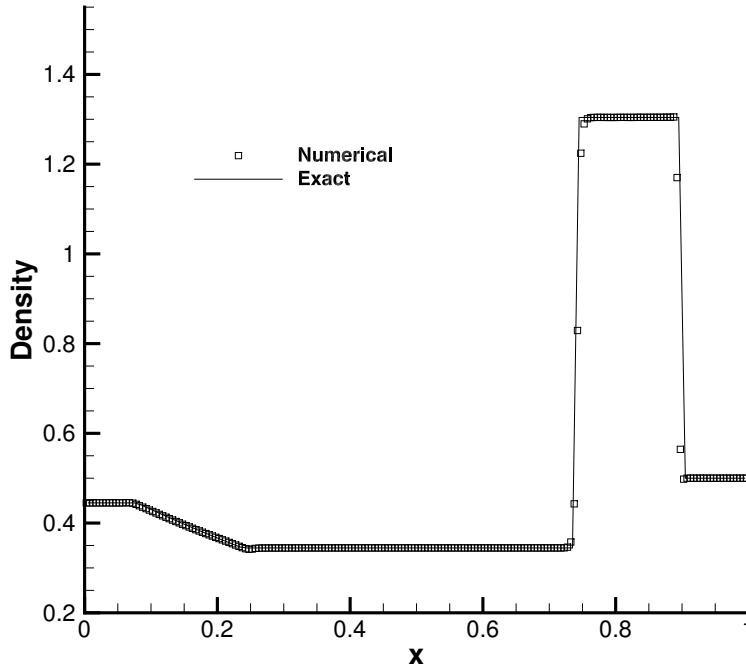


FIGURE 5.7: Numerical result for density field of Lax's problem at $t = 0.16$ with 200 cells.

As one of benchmark test for shock tube problem, Lax problem is used to check the ability of the numerical schemes to capture relatively strong shock [2]. The initial profile is

$$(\rho_0, u_0, p_0) = \begin{cases} (0.445, 0.698, 3.528) & \text{if } 0 \leq x \leq 0.5, \\ (0.5, 0, 0.571) & \text{otherwise.} \end{cases} \quad (5.34)$$

With the same number of cells as in the previous case, the numerical results at $t = 0.16$ are shown in Fig. 5.7. We can see that MCV3-BGS scheme can effectively suppress the oscillations near the shock and accurately resolve both contact discontinuity and expansion wave due to the less numerical diffusion.

Shock-turbulence interaction

As in [2], interactions between a shock wave and wavy perturbations are simulated with the following initial condition

$$(\rho_0, u_0, p_0) = \begin{cases} (3.857148, 2.629369, 10.333333) & \text{if } 0 \leq x \leq 1, \\ (1 + 0.2 \sin(5x - 5), 0, 1) & \text{otherwise.} \end{cases} \quad (5.35)$$

In this case, the shock moves towards the right and then interacts with a wave chain in density. Both shock and complex smooth structures exist in the solution. So, the numerical scheme is required to be not only capable of capturing the shock but also accurate enough to resolve the complex flow in smooth region with minimized numerical dissipation. The numerical results of MCV3-BGS with 200 mesh cells at $t = 1.8$ are shown in Fig. 5.8. The reference solution plotted by the solid line is computed by the classical fifth-order WENO scheme [2] with 2000 mesh cells. It can be seen from the numerical results that the present scheme can reproduce the shocks without spurious oscillations and accurately capture density perturbations.

Two interacting blast waves

We also computed two interacting blast waves suggested in [42]. Multiple interactions of strong shocks and rarefaction waves are included in this test problem. The initial distribution has uniform density of $\rho = 1$ and velocity of zero. The difference exists in the distribution of pressure as

$$p_0 = \begin{cases} 1000 & \text{if } 0 \leq x \leq 0.1, \\ 0.01 & \text{if } 0.1 < x \leq 0.9, \\ 100 & \text{otherwise.} \end{cases} \quad (5.36)$$

Reflective boundary conditions are imposed at the two ends of computational domain. Two blast waves are generated by the initial jumps and interact each other violently.

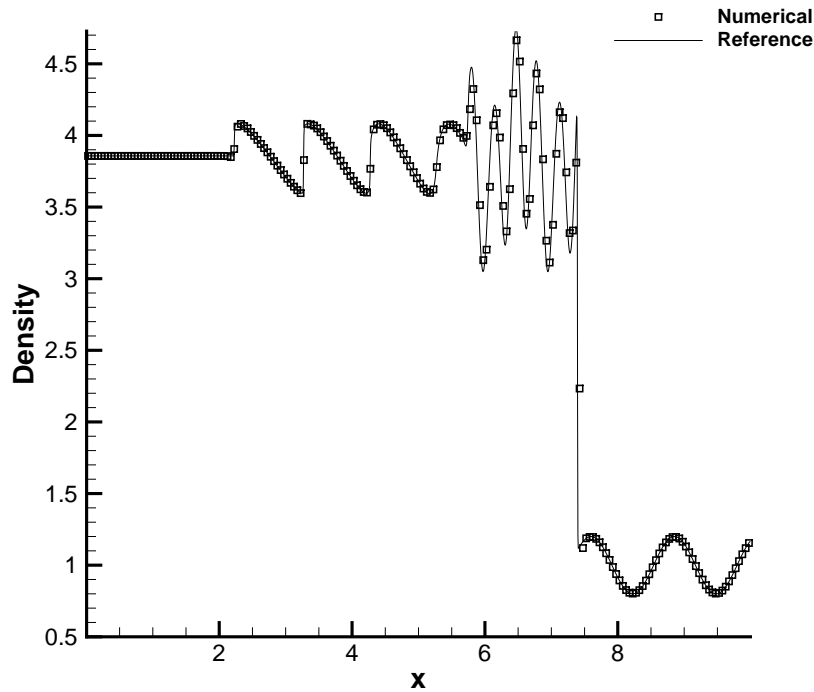


FIGURE 5.8: Numerical result for density field of shock-turbulence interaction at $t = 1.8$ with 200 cells.

Strong shocks, contact discontinuities and expansion fans are generated and cause further interactions. The number of the mesh cells of 400 is used in this test. Here we set $\Delta t = 0.02\Delta x$ due to strong shock.

We depict the numerical solution of density at $t = 0.038$ in Fig. 5.9, where the reference solution is computed by the classical fifth-order WENO scheme [2] with 2000 mesh cells.

Again, the numerical results of MCV3-BGS scheme are among the best ever reported in the literature.

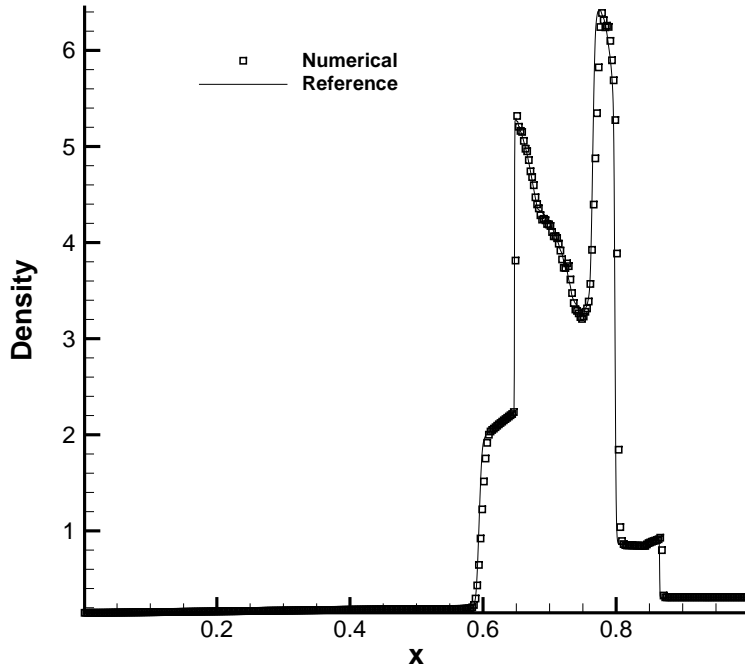


FIGURE 5.9: Numerical result for density field of two interacting blast waves at $t = 0.038$ with 400 cells.

5.4.3 2D linear advection equation

The two-dimensional hyperbolic system is written in Cartesian grid as

$$\frac{\partial \mathbf{q}}{\partial t} + \frac{\partial \mathbf{e}(\mathbf{q})}{\partial x} + \frac{\partial \mathbf{f}(\mathbf{q})}{\partial y} = 0, \quad (5.37)$$

where \mathbf{q} is the vector of dependent variables, $\mathbf{e}(\mathbf{q})$ and $\mathbf{f}(\mathbf{q})$ the vectors of flux functions in x - and y -directions, respectively.

The two-dimensional linear advection equation is specified by $\mathbf{q} = \phi$, $\mathbf{e}(\mathbf{q}) = u\phi$ and $\mathbf{f}(\mathbf{q}) = v\phi$ in (5.37) where (u, v) is the velocity vector.

Advection of two-dimensional sine wave

The convergence rate of the proposed scheme are checked in this two-dimensional advection case by running a smooth sine wave on gradually refined grids. The initial

TABLE 5.3: Numerical errors and convergence rates of the 2D advection equation

Grid	l_1 error	l_1 order	l_∞ error	l_∞ order
10	3.9644e-03	-	9.4769e-03	-
20	4.6692e-04	3.08	1.2102e-03	2.97
40	3.6717e-05	3.67	1.1372e-04	3.41
80	2.6815e-06	3.78	1.0026e-05	3.50
160	1.7166e-07	3.97	8.6287e-07	3.54

condition is given in computational domain $[-1, 1] \times [-1, 1]$ as

$$\phi(x, y, 0) = \sin[\pi(x + y)]. \quad (5.38)$$

The uniform velocity is set as $(u, v) = (1, 1)$. The normalized error l_1 at $t = 2$ are shown in Table 5.3.

The numerical results verify the expected convergence rate of 4th-order regarding to l_1 of the proposed MCV-BGS scheme in two-dimensional case as well.

Rotation of two-dimensional complex wave

We extend the one-dimensional Jiang and Shu's problem [2] to two-dimensional case with a rotational velocity field defined by $(u, v) = (-2\pi x, 2\pi y)$. The computational domain is $[-1, 1] \times [-1, 1]$. The initial distribution is defined by

$$u(x, y, 0) = \begin{cases} \frac{1}{6}[G(r_1 + \delta, \beta) + G(r_1 - \delta, \beta) + 4G(r_1, \beta)] & \text{if } r_1 \leq 0.2, \\ 1 & \text{if } |x| \leq 0.2, -0.7 \leq y \leq -0.3, \\ 1 - 5r_2 & \text{if } r_2 \leq 0.2, \\ \frac{1}{6}[F(r_3 + \delta, \alpha) + F(r_3 - \delta, \alpha) + 4F(r_3, \alpha)] & \text{if } |r_3| \leq 0.2, \\ 0 & \text{otherwise,} \end{cases} \quad (5.39)$$

where

$$r_1 = \sqrt{(x + 0.6)^2 + y^2}, \quad r_2 = \sqrt{(x - 0.6)^2 + y^2}, \quad r_3 = \sqrt{x^2 + (y - 0.6)^2}, \quad (5.40)$$

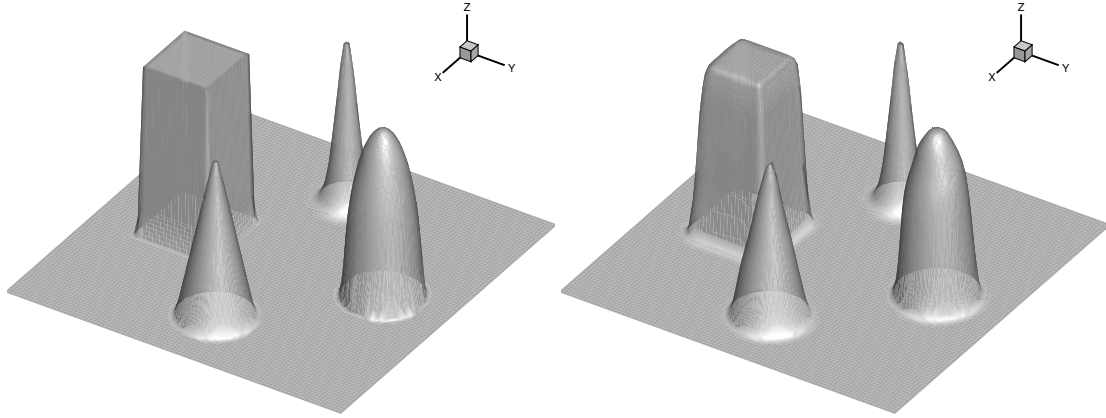


FIGURE 5.10: Numerical result of 2D rotation of complex wave after one period with 100×100 cells. shown are initial profile (left panel) and numerical result (right panel).

$G(r, \beta) = \exp(-\beta r^2)$, $F(r, \alpha) = \sqrt{\max(1 - \alpha^2 r^2, 0)}$ and the coefficients are set to be $\delta = 0.01$, $\alpha = 5$ and $\beta = \log_2(36\delta^2)$.

The model runs up to $t = 1$ (after one period) with 100×100 uniform cells. The initial profile and numerical result are shown in Fig. 5.10. There are no visible oscillation around the discontinuities and all structures including the smooth extremes are adequately resolved compared with the initial condition. Furthermore, we didn't find the noticeable deformation of the distribution of the advected field in this two-dimensional case.

5.4.4 2D Euler equations

In (5.37), two-dimensional Euler equations have the form of

$$\begin{cases} \mathbf{q} = [\rho, \rho u, \rho v, E]^T, \\ \mathbf{e}(\mathbf{q}) = [\rho u, \rho u^2 + p, \rho u v, u(E + p)]^T, \\ \mathbf{f}(\mathbf{q}) = [\rho v, \rho u v, \rho v^2 + p, v(E + p)]^T, \end{cases} \quad (5.41)$$

where u and v are velocity components in x - and y -directions. Due to the regularity of the mesh, we can implement the one-dimensional formulation to each directions directly. The expressions of Jacobian matrices $\mathbf{A} = (\partial \mathbf{e} / \partial \mathbf{q})$ for x direction and $\mathbf{B} =$

$(\partial \mathbf{f} / \partial \mathbf{q})$ for y direction can be found in text books. In practice, \mathbf{A} are calculated along the line segments as the equation (5.32) in which Jacobian matrix \mathbf{A} are an arithmetic average between $\bar{\mathbf{A}}$ and $\tilde{\mathbf{A}}$, where $\bar{\mathbf{A}}$ is the Roe-averaged Jacobian matrix computed from the VIA values of two neighboring cells along line segments while $\tilde{\mathbf{A}}$ is obtained directly from the point values. The same applies to matrix \mathbf{B} .

Two-dimensional explosion An axi-symmetric two dimensional explosion problem as described in [72] is simulated. As the initial condition, a region inside a circle of radius $R = 0.4$ is set with high pressure and density as

$$(\rho_0, u_0, v_0, p_0) = \begin{cases} (1.0, 0.0, 0.0, 1.0) & \text{if } r \leq R, \\ (0.125, 0.0, 0.0, 0.1) & \text{otherwise,} \end{cases} \quad (5.42)$$

where $r = \sqrt{x^2 + y^2}$ is distance to the center of the computational domain.

As time goes on, the fluid inside the circle will spread out and form a moving shock, a contact discontinuity and a rarefaction wave of cylindrical symmetry. The MCV-BGS model runs up to $t = 0.25$ on a grid with 200×200 uniform cells. The bird's-eye view of pressure distribution and the cut-off profile along radial direction are shown in Fig. 5.11. The corresponding numerical results of density are presented in Fig. 5.12.

It is observed from our numerical results that the MCV3-BGS scheme can accurately resolve the shock wave, contact discontinuity and rarefaction fan with adequate resolution. The symmetry of numerical solutions remain perfect, which demonstrates the less grid-dependency and high geometrical fidelity of the proposed scheme.

Double Mach reflection

A propagating planar shock, at $Ma = 10$ in hypersonic regime, reflected by 30° ramp is simulated in this case. It is well known that it is difficult for a numerical scheme to well resolve the very strong discontinuities and the rich small-scale structures developing with time at the same time [42]. The computational domain is $[0, 4] \times [0, 1]$. A

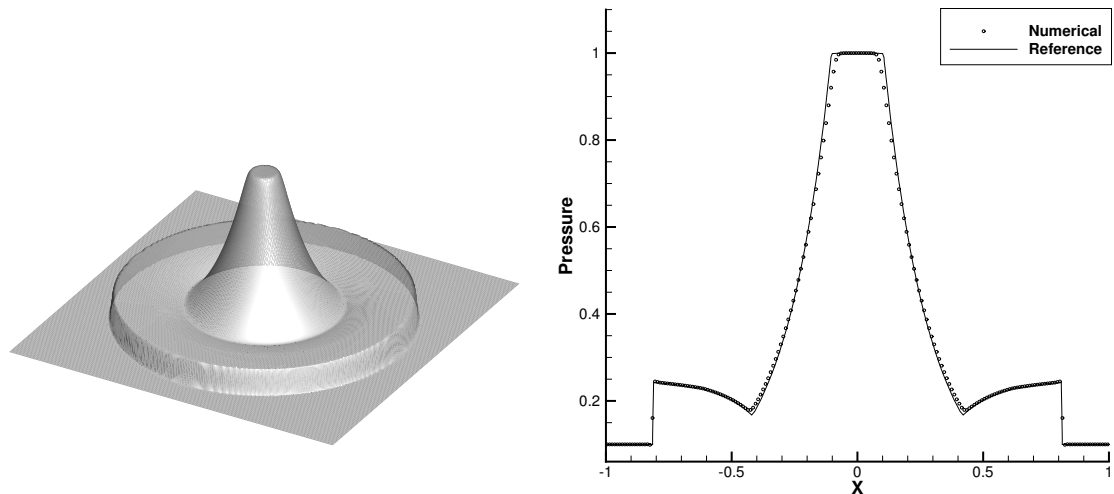


FIGURE 5.11: Numerical result for pressure field of 2D explosion at $t = 0.25$ with 200×200 cells. Shown are bird's-eye view of pressure distribution (left panel) and cut-off profile along radial direction (right panel).

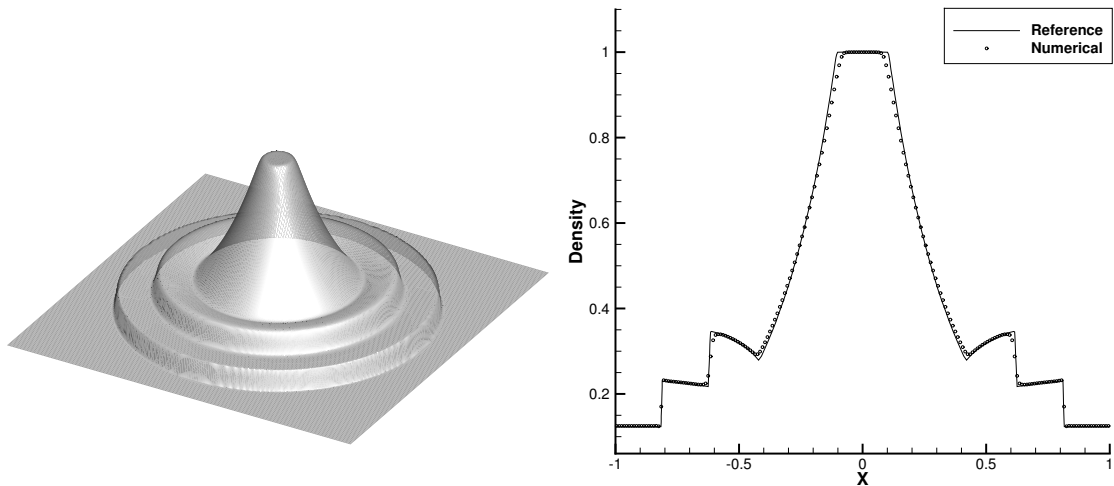


FIGURE 5.12: Same as Fig. 5.11, but for density field.

right-moving Mach 10 shock is imposed with 60° angle relative to x -axis. At the right boundary of the computational domain, the boundary condition is given by setting all gradients to be zero.

Two grid with different resolution are adopted to calculate this test. The contour plots of the numerical results of the density field at $t = 0.2$ are illustrated in Fig. 5.13 on coarse grid and Fig. 5.14 on fine one. The enlarged view of the vortex structures and instability along the slip lines are shown in Fig. 5.15. Both the strong discontinuities and the vortex structures are well resolved in the current results by MCV3-BGS scheme,

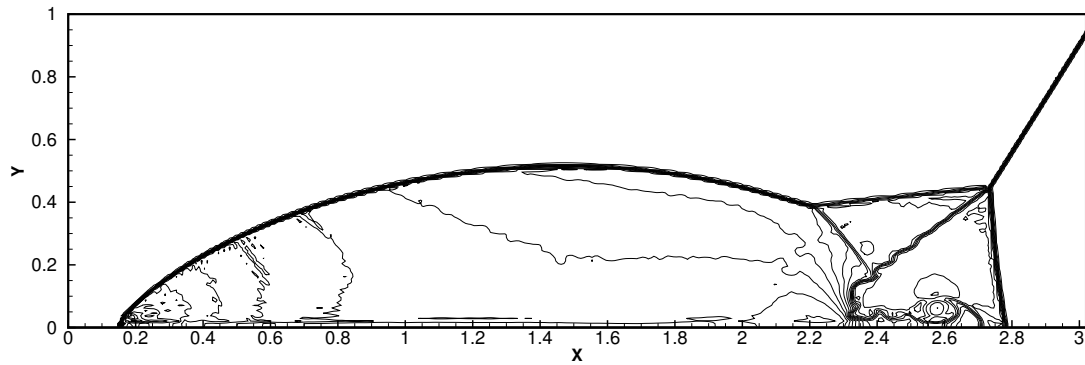


FIGURE 5.13: Numerical result for density field of the double Mach reflection at $t = 0.2$ with 120×384 cells.

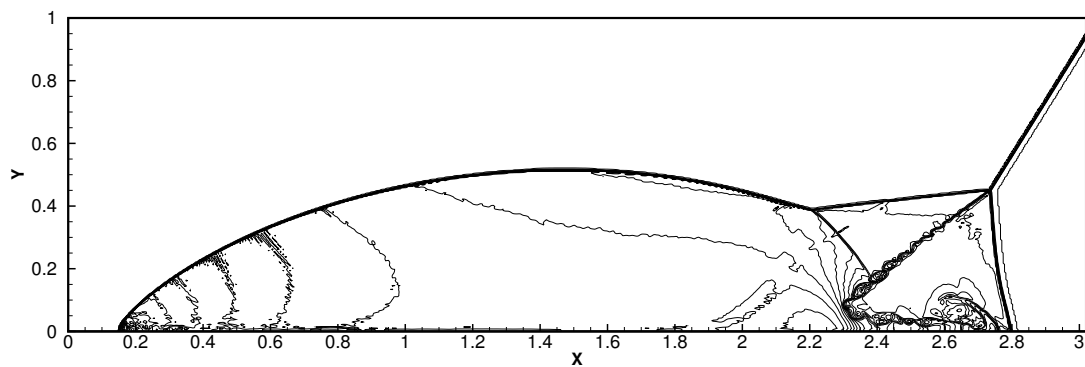


FIGURE 5.14: Same as Fig. 5.13, but with 250×800 cells.

which shows the well-controlled numerical dissipation in MCV3-BGS scheme.

A Mach 3 wind tunnel with a step

Mach 3 wind tunnel with a step is one of popular bench-mark tests for verification of high-resolution schemes [42]. In this case, an uniform Mach 3 flow is blown into a wind tunnel of $[0, 3] \times [0, 1]$ with a step of 0.2 unit high located at 0.6 unit away from the left end of the tunnel. The inflow and outflow conditions are prescribed on left and right side boundaries and the rest are imposed with reflective condition. The numerical test is conducted under different grid resolution. As shown in Figs.5.16 and 5.17, the contour profiles regarding to density field at $t = 4.0$ are depicted on grids of 160 and 320 respectively. It is seen that the shock waves and strong discontinuities are adequately resolved with numerical oscillation effectively eliminated. Meanwhile, the numerical dissipation is also suppressed so that the vortical structures of acoustic

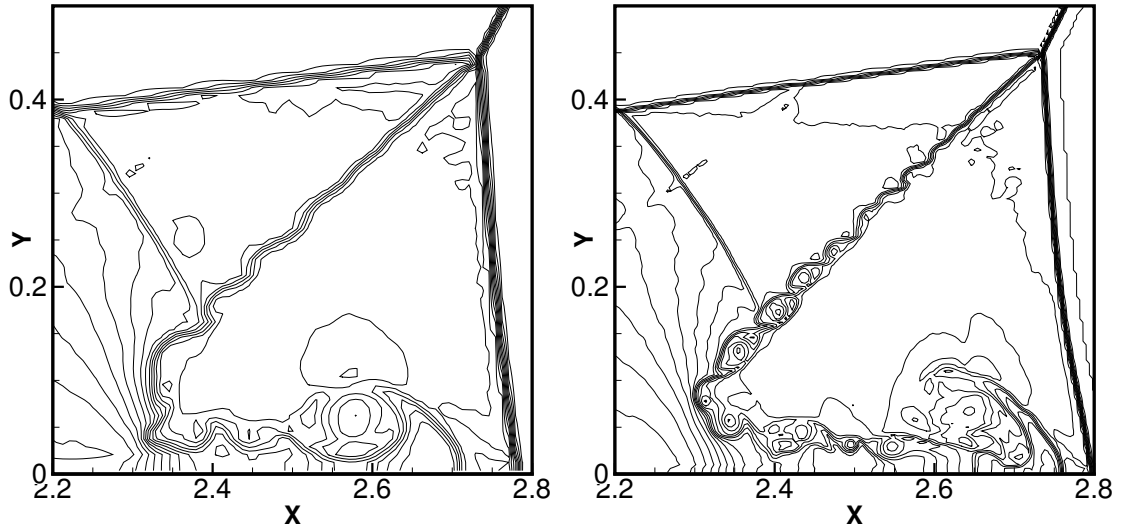


FIGURE 5.15: Enlarged view of vortex structures and instability along the slip lines of double Mach reflection at $t = 0.2$ with 120×384 cells (left panel) and 250×800 cells (right panel).

waves are sufficiently captured. The proposed method can resolve the vortex structures better with fewer mesh cells in comparison with the original WENO scheme and the new variants.

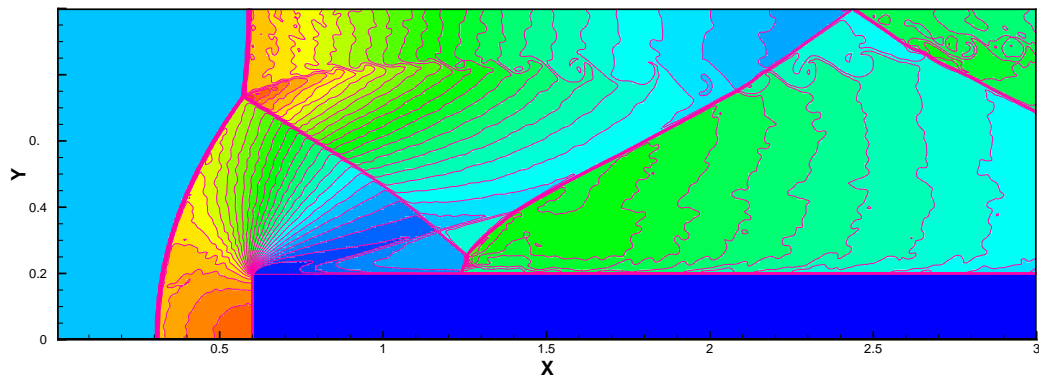
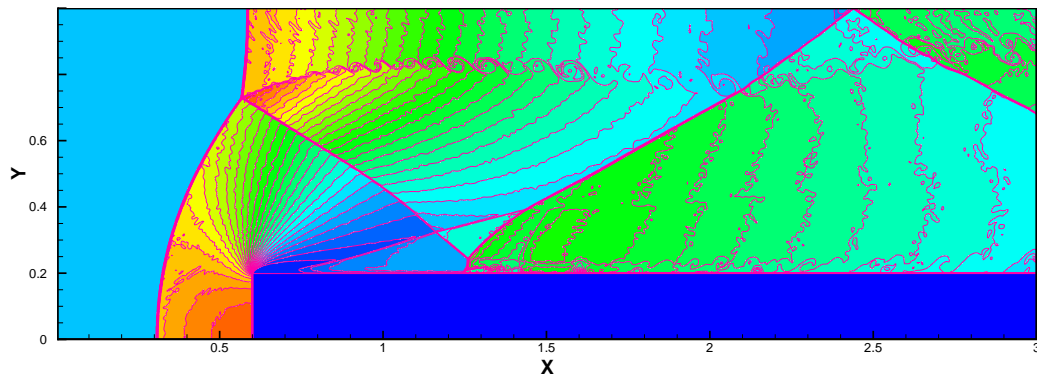


FIGURE 5.16: Density contours for the Mach 3 wind tunnel with a step at time of $t = 4$ on 160×480 cells. Thirty equally spaced contours are shown ranging from 0.1 to 6.4

FIGURE 5.17: Same as Fig.5.16, but with 320×960 cells.

5.5 Summary

In this chapter, we have proposed a new formulation for 3-point MCV scheme. Two fourth-order schemes, i.e. MCV3-4L and MCV3-4R, are derived by employing the additional DOFs defined at the center of left and right neighboring cells. A new BGS algorithm, underlying the ENO concept, has been proposed to design a non-oscillatory multi-moment scheme without degrading the fourth-order accuracy. The basic idea of the BGS algorithm is to choose a spatial reconstruction between MCV3-4L and MCV3-4R schemes, which minimizes the difference in the derivatives of flux functions between the high-order profile and the reconstruction with a slope limiter. This algorithm is easy to implement and free of and case-dependent ad hoc parameter. Thus, it is very proposing for practical applications.

Compared to other existing methods, the present scheme has at least following advantages.

1. Without any limiting process using either slope limiters or flux limiters, the proposed scheme doesn't suffer from loss of accuracy since a high-order reconstruction, either MCV3-4L or MCV3-4R is effectively adopted.

2. MCV3-BGS scheme does not need the priori detector, such as the TVB criterion, to peak up the "troubled cells". With effective oscillation-suppressing mechanism and well-controlled numerical dissipation, MCV3-BGS scheme resolves both smooth and discontinuous solutions.
3. Using the sub-grid DOFs, the spatial stencil used by MCV3-BGS is limited within three neighboring cells, which is very compact and suited for the grids with complex structures.

The performance of the proposed scheme is verified by the widely used benchmark tests for both scalar and Euler equations. The numerical results reveal that MCV3-BGS scheme is a high-fidelity scheme with local high order reconstruction that resolves both smooth and non-smooth solutions with appealing accuracy the robustness.

Chapter 6

A finite volume multi-moment method with boundary variation diminishing principle on hybrid unstructured grids

Previous chapters have introduced the work on structured grids. However, most of the real-case problems involve complex geometric configurations and complex flow structures including shock waves and vortices, such as those found in aeroacoustic and aerodynamics regarding the design of high-speed vehicles [1]. In such practical applications, numerical models should be preferably least (i) applicable to hybrid unstructured grids, (ii) adequately robust and accurate with good properties in suppressing both numerical oscillations and in limiting dissipation and (iii) algorithmically simple and computationally efficient. However, to achieve above properties is more difficult for unstructured grids. For example, as for increasing order, schemes based on structured grids only need to add cells in dimension-by-dimension fashion, which is in contrast to schemes on unstructured grids. For unstructured grids, one need to construct multi-dimensional interpolation function, which brings larger stencil size.

Owing to the intrinsic conservativeness and flexibility for unstructured grids, the finite volume method (FVM) has been widely accepted as the mainstream paradigm for compressible flow simulations. However, engineering practice shows that in many cases the conventional 2nd-order FVM that uses only volume-integrated average (VIA) as the computational variable for each grid cell has excessive numerical dissipation which tends to smear out vortices and other flow structures. Therefore, extensions of FVM to higher order formulations on unstructured have been proposed by using multi-dimensional interpolations with limiting projections over wide stencils [2–6]. A reconstruction for unstructured grids within the spirit of compact schemes has also been reported in [7, 8]. As a matter of fact, any FVM scheme higher than second-order brings significant complexity, especially for 3D hybrid meshes.

Owing to the intrinsic conservativeness and flexibility for unstructured grids, the finite volume method (FVM) has been widely accepted as the mainstream paradigm for compressible flow simulations. However, engineering practice shows that in many cases the conventional 2nd-order FVM that uses only volume-integrated average (VIA) as the computational variable for each grid cell has excessive numerical dissipation which tends to smear out vortices and other flow structures. Therefore, extensions of FVM to higher order formulations on unstructured have been proposed by using multi-dimensional interpolations with limiting projections over wide stencils [2–6]. A reconstruction for unstructured grids within the spirit of compact schemes has also been reported in [7, 8]. As a matter of fact, any FVM scheme higher than second-order brings significant complexity, especially for 3D hybrid meshes.

We have recently developed a novel numerical formulation for unstructured grids as another better trade-off between solution quality and computational cost. The formulation, so-called VPM (Volume integrated average and Point value based Multi-moment) method [22–24], uses both VIA and point values (PVs) as computational variables and makes piecewise reconstructions with the DOFs of VIAs and PVs collected from the target cell and its immediate neighbors. Being the computational variables, the VIA is

updated by a finite volume scheme of flux form which ensures rigorous numerical conservativeness, while PV is computed point-wisely by solving the governing equations in differential form ¹. More recently, multi-moment constrained finite volume method with solution points at center and vertices (MCV-SPCV)[28] was developed by replacing the VIA with the PV at the mass center of each cell as alternative computational variable, which can be viewed as another version of the multi-moment finite volume method (MM-FVM).

Thus, in this work we present a fully three-dimensional numerical solver for Euler equations on hybrid unstructured grids as a further and substantial step toward the numerical model for real-case applications by employing VPM/MCV and boundary variation diminishing (BVD) algorithm.

6.1 The computational grids and computational variables of VPM/MCV schemes

We consider in this work the general unstructured grids which may include hybrid elements Ω_i ($i = 1, 2, \dots, I$) of different shapes, such as triangular and quadrilateral elements for 2D, and tetrahedral, hexahedral, prismatic and pyramidal elements for 3D as shown in Fig. 6.1.

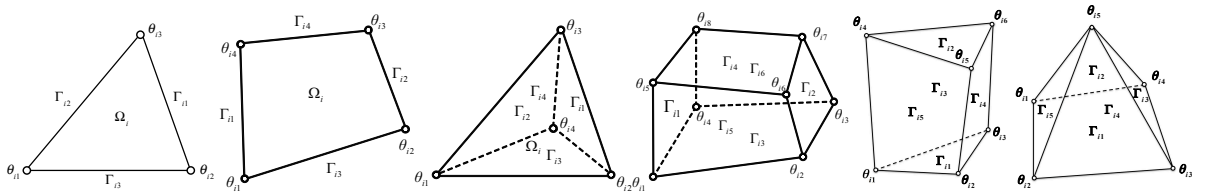


FIGURE 6.1: The computational grid elements and related definitions. From left to right is triangular, quadrilateral, tetrahedral, hexahedral, prismatic and pyramidal element.

¹The idea to update the cell-boundary value as another predicted variable in addition to the VIA in the conventional FVM was found in scheme V of [25], and explored further independently in [26] and [198] latter.

We denote the vertices and boundary segments by $\theta_{ik}(k = 1, \dots, K)$ and $\Gamma_{ij}(j = 1, \dots, J)$ where K and J stand for the total number of the vertices and edges\surfaces for each cell Ω_i . We define the location of vertices θ_{ik} , middle points θ_{ij} of Γ_{ij} and mass center θ_{ic} of Ω_i by (x_{ik}, y_{ik}, z_{ik}) , (x_{ij}, y_{ij}, z_{ij}) and (x_{ic}, y_{ic}, z_{ic}) respectively. The outward normal unit vector is denoted by $\mathbf{n}_{ij} = (n_{xij}, n_{yij}, n_{zij})$ directed from left(Ω^+) to right(Ω^-) side of Γ_{ij} , and the magnitude of boundary area Γ_{ij} by $|\Gamma_{ij}|$ and the volume of Ω_i by $|\Omega_i|$. We also use symbol Ω_{ij} to denote the surrounding cells adjacent to the target cell Ω_i with the common boundary segment Γ_{ij} . The global and local indices are stored separately and related by using a connection table.

Computational variables for MCV method

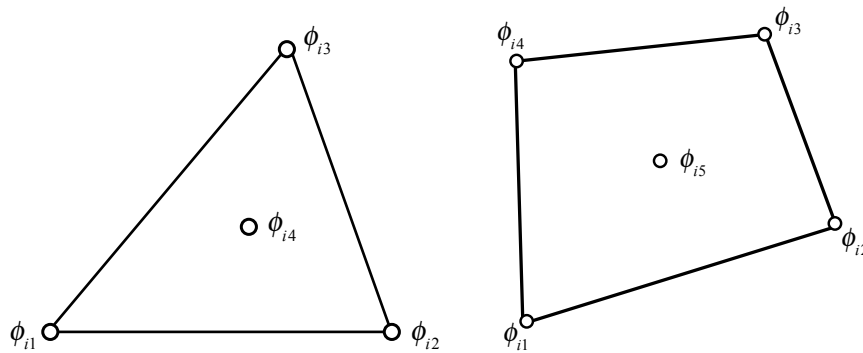


FIGURE 6.2: The two-dimensional moment arrangement on triangular(left) and quadrilateral(right) elements.

In the present MCV model, we define point values (PVs) at vertices and barycenter of cell Ω_i for physical variable ϕ as shown in Fig. 6.2,

$$\phi_{ik}(t) \equiv \phi(x_{ik}, y_{ik}, t), \quad k = 1, 2, \dots, K; \tag{6.1}$$

$$\phi_{i(K+1)}(t) \equiv \phi(x_{ic}, y_{ic}, t). \tag{6.2}$$

As shown above, the DOFs for MCV method include both cell volume integrated average (VIA) value and point values (PV), which is different from conventional FVM which includes only VIA as DOFS.

Computational variables for VPM method

Similar to the concept of the multi-moment finite volume method, we define the VIA and PVs at the vertices of cell Ω_i as

$$\begin{aligned}\bar{\phi}_i(t) &\equiv \frac{1}{|\Omega_i|} \int_{\Omega_i} \phi(x, y, z, t) d\Omega, \\ \phi_{ik}(t) &\equiv \phi(x_{ik}, y_{ik}, z_{ik}, t), \quad k = 1, \dots, K\end{aligned}\tag{6.3}$$

where ϕ stands for the generic transported variable per unit volume.

6.2 High resolution reconstruction on unstructured grids

For the sake of algorithmic simplicity on unstructured grids, we transform grid element Ω_i on physical coordinate $\mathbf{x} = (x, y)$ to the standard element on local coordinate system $\boldsymbol{\xi} = (\xi, \eta)$ by defining the basis functions N_{ik} . The N_{ik} is uniquely related to the element type, and formulation of transformation is given as

$$\mathbf{x} = \sum_{k=1}^K (\boldsymbol{\xi}_k N_{ik}), \quad \mathbf{x} \in \Omega_i,\tag{6.4}$$

where K indicates the total number of cell vertices and $K = 3$ for triangular elements, and $K = 4$ for quadrilateral elements.

Besides ϕ_{ik} and $\phi_{i(K+1)}$ as the computational variables in each cell, we add the derivatives of the physical field at cell center $\theta_{ic}(x_{ic}, y_{ic})$, i.e. $(\phi_{\xi ic}, \phi_{\eta ic})$ and $(\phi_{\xi^2 ic}, \phi_{\eta^2 ic})$, as other conditions to build high-order reconstructions. These derivative terms are computed by least-square method from the computational variables, ϕ_{ik} and $\phi_{i(K+1)}$ in the neighboring cells.

The piecewise reconstruction polynomial is then written as

$$\Phi_i(\phi; \xi, \eta) = \sum_{k=1}^{k=K+1} \psi_{ik} \phi_{ik} + A_1(\psi_{\xi} \phi_{\xi ic} + \psi_{\eta} \phi_{\eta ic}) + A_2(\psi_{\xi^2} \phi_{\xi^2 ic} + \psi_{\eta^2} \phi_{\eta^2 ic}),\tag{6.5}$$

or for 3D cases as

$$\begin{aligned} \Phi_i = & \sum_{k=1}^{k=K} \psi_{ik} \phi_{ik} + \bar{\psi} \bar{\phi}_i + A_1 (\psi_\xi \phi_{\xi ic} + \psi_\eta \phi_{\eta ic}) \\ & + B_1 \psi_\zeta \phi_{\zeta ic} + A_2 (\psi_{\xi^2} \phi_{\xi^2 ic} + \psi_{\eta^2} \phi_{\eta^2 ic}) + B_2 \psi_{\zeta^2} \phi_{\zeta^2 ic}, \end{aligned} \quad (6.6)$$

where ψ are the basis functions for the corresponding degrees of freedom (DOFs) as either point values and derivatives. The parameters A_1, A_2 are used to switch the reconstruction functions between triangular elements ($A_1 = 1, A_2 = 0$) and quadrilateral elements ($A_1 = 1, A_2 = 1$). From Eq.(6.5), we can derive cell averages by

$$\bar{\phi}_i = \frac{1}{|\Omega_i|} \int_{\Omega} \Phi_i(\phi; \xi, \eta) d\Omega \quad (6.7)$$

which results in a constraint relating $\phi_{i(K+1)}$ and ϕ_{ik} on triangular and quadrilateral elements respectively as

$$\bar{\phi}_i = \frac{1}{12} (\phi_{i1} + \phi_{i2} + \phi_{i3} + 9\phi_{i4}), \quad (6.8)$$

$$\bar{\phi}_i = \frac{1}{12} (\phi_{i1} + \phi_{i2} + \phi_{i3} + \phi_{i4} + 8\phi_{i5}). \quad (6.9)$$

The interested readers may consult [28] for the details of the basis functions as well as the MCV reconstructions.

For PV on vertices θ_{ik} , we compute the derivatives of variables \mathbf{U}_{ik} in the local coordinate $\boldsymbol{\xi}$ from $\Phi_{ikl}(\mathbf{U}, \boldsymbol{\xi})$ ($l = 1, 2, \dots, L$) constructed on the surrounding cells and transform them to global coordinate $\frac{\partial \mathbf{U}_{ikl}}{\partial \mathbf{x}} = \left(\frac{\partial \mathbf{U}_{ikl}}{\partial x}, \frac{\partial \mathbf{U}_{ikl}}{\partial y}, \frac{\partial \mathbf{U}_{ikl}}{\partial z} \right)$ by Eqn. (6.10), i.e.

$$\frac{\partial \mathbf{U}_{ikl}}{\partial \mathbf{x}} = \mathcal{M}^{\boldsymbol{\xi} \rightarrow \mathbf{x}} \left(\frac{\partial \Phi_{ikl}(\mathbf{U}, \boldsymbol{\xi})}{\partial \boldsymbol{\xi}} \right). \quad (6.10)$$

We approximate the upwinding-biased derivatives by,

$$\frac{\partial \mathbf{U}_{ik}^\pm}{\partial \tau} = \sum_{l=1}^L \omega_{ikl}^{\tau^\pm} \frac{\partial \mathbf{U}_{ikl}}{\partial \tau}, \quad \tau = x, y \text{ or } z \quad (6.11)$$

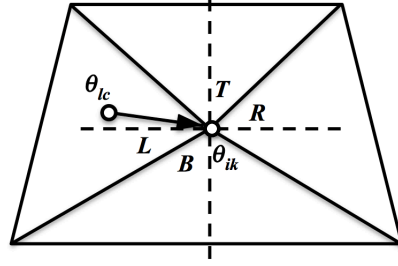


FIGURE 6.3: Solution for PV in 2D problems.

where $\omega_{ikl}^{\tau\pm}$ are the selective weights for derivatives on left and right sides of θ_{ik} along each directions, which are computed by

$$\omega_{ikl}^{\tau\pm} = \frac{\max\left(0, \mathbf{n}^{\tau\pm} \cdot \overrightarrow{\theta_{lc}\theta_{ik}}\right)}{\sum_{l=1}^L \max\left(0, \mathbf{n}^{\tau\pm} \cdot \overrightarrow{\theta_{lc}\theta_{ik}}\right)} \quad (6.12)$$

where $\overrightarrow{\theta_{lc}\theta_{ik}}$ denotes the vector from the mass center θ_{iklc} to vertex θ_{ik} as Fig. 6.3 for 2D cases and Fig. 6.4 for 3D problems, and $\mathbf{n}^{\tau\pm}$ the unit normal vectors, $\mathbf{n}^{x\pm}(\pm 1, 0, 0)$, $\mathbf{n}^{y\pm}(0, \pm 1, 0)$ and $\mathbf{n}^{z\pm}(0, 0, \pm 1)$ indicating directions of x , y and z respectively. Once derivatives are determined, PVs can be updated by Riemann solvers straightforwardly.

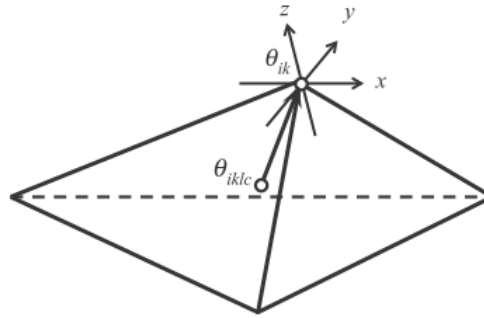


FIGURE 6.4: Solution for PV in 3D problems.

6.3 Solution procedures for VIA and PV

6.3.1 Solution procedure for VIA

In VPM/MCV method, the VIA is updated by finite volume method. For example, in present work we solve for VIA by the integral form of conservative equation of (1.1)-(1.3) which can be cast as follows

$$\frac{\partial}{\partial t} \int_{\Omega_i} \mathbf{U} d\Omega + \int_{\Gamma_{ij}} \mathbf{F}_{ij}(\mathbf{U}) d\Gamma = 0, \quad (6.13)$$

where \mathbf{U} represents the vector of conservative variables, and $\mathbf{F}(\mathbf{U})$ the numerical fluxes across cell boundaries, i.e.

$$\mathbf{U} = [\rho, \rho u, \rho v, \rho w, E]^T, \quad (6.14)$$

$$\mathbf{F}(\mathbf{U}) = [\rho v_n, \rho u v_n + p n_x, \rho v v_n + p n_y, \rho w v_n + p n_z, (E + p) v_n]^T \quad (6.15)$$

where $v_n = \mathbf{u} \cdot \mathbf{n}_{ij}$ stands for the transport velocity at interface. The numerical fluxes across surface segment Γ_{ij} can be also expressed in the form of $\mathbf{F}_{ij}(\mathbf{U}) = \mathbf{A} \mathbf{U}_{ij}$ where $\mathbf{A} = \partial \mathbf{F} / \partial \mathbf{U}$ is the Jacobian matrix, which is computed by using the integrated average of conservative variables \mathbf{U} in the neighboring cell sharing the boundary Γ_{ij} .

Decomposing the Jacobian matrix into an eigensystem of $A = R \Lambda L$, where R/L denotes the matrix of right/left eigenvectors and Λ the corresponding eigenvalues, we solve (6.13) by

$$\frac{\partial \bar{\mathbf{U}}_i}{\partial t} = - \sum_{j=1}^{j=J} (A (\mathbf{U}_{ij}^+ + \mathbf{U}_{ij}^-) + R |A| L (\mathbf{U}_{ij}^+ - \mathbf{U}_{ij}^-)) |\Gamma_{ij}| \quad (6.16)$$

where \mathbf{U}_{ij}^\pm denotes the integrated averages on left-side and right-side of boundary Γ_{ij} respectively. It is noteworthy that all the values in the eigensystem are computed by

Roe-averaging approximation with two adjacent VIAs. The complete structure of eigen-system on unstructured grids has been detailed in [32].

Another way to update VIA is to apply HLLC Riemann solver. Again, in order to deal with unstructured grids, the HLLC is formulated as

$$\frac{1}{|\Omega_i|} \oint_{\partial\Omega_i} \mathbf{F}_n(\mathbf{U}) d\Gamma = -\frac{1}{|\Omega_i|} \sum_{j=1}^J \mathbf{K}_{ij} \quad (6.17)$$

The numerical flux \mathbf{K}_{ij} can be calculated using HLLC Riemann solver as following equations

$$\mathbf{K}_{ij} = \mathbf{F}_{n,ij}(\mathbf{U}^-, \mathbf{U}^+) |\Gamma_{ij}| \quad (6.18)$$

where flux tensor function $\mathbf{F}_{n,ij}$ stands for the Riemann solver projected in normal direction. And \mathbf{U}^- , \mathbf{U}^+ are the left and right state of boundary value at cell interface. Using the concept of the rotational invariance, $\mathbf{F}_{n,j}$ is replaced by

$$\mathbf{F}_{n,ij} = \mathbf{T}^{-1} \mathbf{F}(\mathbf{T}_{ij} \mathbf{U}) \quad (6.19)$$

where \mathbf{T}_{ij} is the rotation matrix for face Γ_{ij} . Thus the expression of numerical flux \mathbf{K}_{ij} is rewritten as

$$\mathbf{K}_{ij} = \mathbf{T}^{-1} \mathbf{F}(\hat{\mathbf{U}}_L, \hat{\mathbf{U}}_R) \quad (6.20)$$

where $\hat{\mathbf{U}}_L, \hat{\mathbf{U}}_R$ is the rotated conserved variable and

$$\hat{\mathbf{U}}_L = \mathbf{T}_{ij} \mathbf{U}^-, \quad \hat{\mathbf{U}}_R = \mathbf{T}_{ij} \mathbf{U}^+. \quad (6.21)$$

Thus the flux function can be computed from the augmented one-dimensional Riemann problem

$$\frac{\partial \hat{\mathbf{U}}}{\partial t} + \frac{\partial \hat{\mathbf{F}}}{\partial s} = 0, \quad \hat{\mathbf{F}} = \mathbf{F}(\hat{\mathbf{U}}), \quad \hat{\mathbf{U}}(s, 0) = \begin{cases} \hat{\mathbf{U}}_L, & s < 0, \\ \hat{\mathbf{U}}_R, & s > 0. \end{cases} \quad (6.22)$$

Assuming three wave structure with wave speed estimate S_L, S^*, S_R the flux is given by

$$\hat{\mathbf{F}}^{\text{HLLC}} = \begin{cases} \hat{\mathbf{F}}_L, & 0 \leq S_L \\ \hat{\mathbf{F}}_{*L} = \hat{\mathbf{F}}_L + S_L(\hat{\mathbf{U}}_{*L} - \hat{\mathbf{U}}_L), & S_L \leq 0 \leq S_* \\ \hat{\mathbf{F}}_{*R} = \hat{\mathbf{F}}_R + S_R(\hat{\mathbf{U}}_{*R} - \hat{\mathbf{U}}_R), & S_* \leq 0 \leq S_R \\ \hat{\mathbf{F}}_R \end{cases} \quad (6.23)$$

where state $\hat{\mathbf{U}}_{*L/R}$ can be calculated as following

$$\hat{\mathbf{U}}_{*k} = \rho_k \left(\frac{S_k - u_k}{S_k - S_*} \right) \begin{pmatrix} 1 \\ S_* \\ v_k \\ w_k \\ \frac{E_k}{\rho_k} (S_* - u_k) \left[S_* + \frac{p_k}{\rho_k (S_k - u_k)} \right] \end{pmatrix} \quad (6.24)$$

where $k = L$ or $k = R$. The wave speed can be estimated by pressure-velocity estimation method.

6.3.2 Solution procedure for PV

The PV of (1.1)-(1.3) is computed point-wisely by the differential form of Euler equations,

$$\frac{\partial \mathbf{U}_{ik}}{\partial t} + \frac{\partial \mathbf{F}(\mathbf{U})_{ik}}{\partial x} + \frac{\partial \mathbf{G}(\mathbf{U})_{ik}}{\partial y} + \frac{\partial \mathbf{H}(\mathbf{U})_{ik}}{\partial z} = 0, \quad (6.25)$$

where \mathbf{U}_{ik} denotes the conservative variables on vertex θ_{ik} , and $\mathbf{F}(\mathbf{U})_{ik}$, $\mathbf{G}(\mathbf{U})_{ik}$, $\mathbf{H}(\mathbf{U})_{ik}$ the numerical fluxes regarding x , y , z directions respectively, i.e.

$$\mathbf{U}_{ik} = [\rho, \rho u, \rho v, E]_{ik}^T, \quad (6.26)$$

$$\mathbf{F}(\mathbf{U})_{ik} = [\rho u, \rho u^2 + p, \rho uv, \rho uw, u(E + p)]_{ik}^T, \quad (6.27)$$

$$\mathbf{G}(\mathbf{U})_{ik} = [\rho v, \rho uv, \rho v^2 + p, \rho vw, v(E + p)]_{ik}^T, \quad (6.28)$$

$$\mathbf{H}(\mathbf{U})_{ik} = [\rho w, \rho uw, \rho vw, \rho w^2 + p, w(E + p)]_{ik}^T. \quad (6.29)$$

Given Jacobian matrices $\mathbf{A} = \partial \mathbf{F}(\mathbf{U})_{ik} / \partial \mathbf{U}_{ik}$, $\mathbf{B} = \partial \mathbf{G}(\mathbf{U})_{ik} / \partial \mathbf{U}_{ik}$ and $\mathbf{C} = \partial \mathbf{H}(\mathbf{U})_{ik} / \partial \mathbf{U}_{ik}$, we rewrite (6.25) into

$$\frac{\partial \mathbf{U}_{ik}}{\partial t} + \mathbf{A} \frac{\partial \mathbf{U}_{ik}}{\partial x} + \mathbf{B} \frac{\partial \mathbf{U}_{ik}}{\partial y} + \mathbf{C} \frac{\partial \mathbf{U}_{ik}}{\partial z} = 0. \quad (6.30)$$

For hyperbolic systems, Jacobian matrices can be diagonalized as $\mathbf{A} = R_A \Lambda_A L_A$, $\mathbf{B} = R_B \Lambda_B L_B$ and $\mathbf{C} = R_C \Lambda_C L_C$, where L/R and Λ are the corresponding left-/right eigenvectors and the diagonal matrix of eigenvalues respectively. In practice, the matrices are computed with the Roe-averaged values from the surrounding VIAs on unstructured grids. Considering VIAs on cells Ω_{ikl} ($l = 1, 2, \dots, L$) sharing vertex θ_{ik} , we evaluate PVs of $\tilde{\phi}_{ik}$, standing for \tilde{u}_{ik} , \tilde{v}_{ik} , \tilde{w}_{ik} and \tilde{H}_{ik} , by

$$\tilde{\phi}_{ik} = \frac{\sum_{l=1}^{l=L} \sqrt{\bar{\rho}_{ikl}} \cdot \bar{\phi}_{ikl}}{\sum_{l=1}^{l=L} \sqrt{\bar{\rho}_{ikl}}}, \quad (6.31)$$

and compute sound speed \tilde{a}_{ik} by

$$\tilde{a}_{ik} = \left((\gamma - 1) \left(\tilde{H}_{ik} - \frac{1}{2} (\tilde{u}_{ik}^2 + \tilde{v}_{ik}^2 + \tilde{w}_{ik}^2) \right) \right). \quad (6.32)$$

We solve (6.30) point-wisely by Roe's Riemann solver in terms of the discontinuous derivatives of dependent variables,

$$\begin{aligned} \frac{\partial \mathbf{U}_{ik}}{\partial t} = & -\frac{1}{2} \left(\tilde{A} \left(\frac{\partial \mathbf{U}_{ik}^+}{\partial x} + \frac{\partial \mathbf{U}_{ik}^-}{\partial x} \right) + \tilde{R}_A \left| \tilde{\Lambda}_A \right| \tilde{L}_A \left(\frac{\partial \mathbf{U}_{ik}^+}{\partial x} - \frac{\partial \mathbf{U}_{ik}^-}{\partial x} \right) \right) \\ & -\frac{1}{2} \left(\tilde{B} \left(\frac{\partial \mathbf{U}_{ik}^+}{\partial y} + \frac{\partial \mathbf{U}_{ik}^-}{\partial y} \right) + \tilde{R}_B \left| \tilde{\Lambda}_B \right| \tilde{L}_B \left(\frac{\partial \mathbf{U}_{ik}^+}{\partial y} - \frac{\partial \mathbf{U}_{ik}^-}{\partial y} \right) \right), \quad (6.33) \\ & -\frac{1}{2} \left(\tilde{C} \left(\frac{\partial \mathbf{U}_{ik}^+}{\partial z} + \frac{\partial \mathbf{U}_{ik}^-}{\partial z} \right) + \tilde{R}_C \left| \tilde{\Lambda}_C \right| \tilde{L}_C \left(\frac{\partial \mathbf{U}_{ik}^+}{\partial z} - \frac{\partial \mathbf{U}_{ik}^-}{\partial z} \right) \right), \end{aligned}$$

where $\left(\frac{\partial \mathbf{U}_{ik}^+}{\partial x}, \frac{\partial \mathbf{U}_{ik}^-}{\partial x} \right)$, $\left(\frac{\partial \mathbf{U}_{ik}^+}{\partial y}, \frac{\partial \mathbf{U}_{ik}^-}{\partial y} \right)$ and $\left(\frac{\partial \mathbf{U}_{ik}^+}{\partial z}, \frac{\partial \mathbf{U}_{ik}^-}{\partial z} \right)$ denote the derivatives of variables \mathbf{U}_{ik} on left-side and right-side of point θ_{ik} regarding x, y, z direction respectively.

6.4 BVD algorithm on unstructured grids for limiting process

Solution monotonicity is enforced by replacing the high-order reconstruction by a limited linear polynomial

$$\phi(x, y, z) = \bar{\phi}_i + \omega (\phi_{xic} (x - x_{ic}) + \phi_{yic} (y - y_{ic}) + \phi_{zic} (z - z_{ic})) \quad (6.34)$$

where $(\phi_{xic}, \phi_{yic}, \phi_{zic})$ is the first-order derivative at mass center θ_{ic} , which are computed from the constrained conditions

$$\begin{aligned} \frac{1}{|\Omega_{i(j)}|} \int_{\Omega_{i(j)}} \phi(x, y, z) d\Omega &= \bar{\phi}_{i(j)}, \quad (j = 1, 2, \dots, J), \\ \phi(x_{ik}, y_{ik}, z_{ik}) &= \phi_{ik}, \quad (k = 1, 2, \dots, K), \end{aligned} \quad (6.35)$$

where subscript $i(j)$ includes the index of the target cell Ω_i as well as its all surrounding cells Ω_{ij} . The derivatives are computed by the least-square method. The limiter function $\omega \in [0, 1]$ is determined by the multi-dimensional limiting process (MLP) [34] scheme. We use the MLP-u2 limiter in the present work.

TABLE 6.1: The cutoff number \mathcal{S}_c of indicator function for different type of grid elements.

elements	triangular	quadrilateral	tetrahedral	hexahedral	prismatic	pyramidal
\mathcal{S}_c	5×10^4	5×10^5	2×10^5	5×10^5	1×10^6	1×10^5

To gain accuracy without loss of efficiency, the limiting projection (6.34) is applied only to the cells where discontinuous solutions are detected by the smoothness indicator, which is originated from [35] and redesigned in [29] by the BVD concept. As a measurement of the smoothness, the total boundary variation $TBV(\Phi)_i$ for the target cell is defined as follows

$$TBV(\Phi)_i = 1 - \frac{\sum_{j=1}^{j=J} \left(\frac{1}{|\Gamma_{ij}|} \int_{\Gamma_{ij}} \Phi_i(\xi, \eta, \zeta) d\Gamma - \frac{1}{|\Gamma_{ij}|} \int_{\Gamma_{ij}} \Phi_{ij}(\xi, \eta, \zeta) d\Gamma \right)^4}{\sum_{j=1}^{j=J} (\bar{\phi}_i - \bar{\phi}_{ij})^4}, \quad (6.36)$$

which indicates the differences of the reconstructed functions across the cell boundaries.

Then the smoothness indicator is defined by

$$\mathcal{S} = \frac{TBV(\Phi)_i}{\max((1 - TBV(\Phi)_i), \epsilon)}, \quad (6.37)$$

where $\epsilon = 10^{-8}$ is a small value used in present model to avoid zero-division.

The reconstruction is switched from the high-order polynomial (6.5) to the linear function (6.34) when $\mathcal{S} < \mathcal{S}_c$ holds. The cutoff number \mathcal{S}_c varies for different grid elements and is determined via numerical experiments. We give the recommended values for \mathcal{S}_c in Table 6.1 which are used in the numerical tests throughout this paper. As shown by numerical results, this limiting projection can effectively prevent the solution of VIA from unphysical oscillations.

As we don't require PV to be necessarily conservative, the overshoots/undershoots of PV can be simply removed by

$$\begin{aligned} \phi_{ik} &= \min(\phi_{ik}, \max(\bar{\phi}_{ikl})), \\ \phi_{ik} &= \max(\phi_{ik}, \min(\bar{\phi}_{ikl})), \end{aligned} \quad (6.38)$$

where $\max(\bar{\phi}_{ikl}) / \min(\bar{\phi}_{ikl})$ indicate the maximum/minimum VIAs ($\bar{\phi}_{ikl}$) on the surrounding cells sharing vertex θ_{ik} . We refer to the above limited reconstruction as the VPM/MCV-MLP reconstruction.

6.5 BVD algorithm on unstructured grids for dissipation reducing

To suppress excessive numerical dissipation introduced by limiting projection treatment, we implement the BVD algorithm [36]. From the observation that the numerical dissipation in Riemann solver (6.16) is proportional to the variation of the reconstructed fields across cell boundaries, the numerical dissipation can be effectively reduced if the spatial reconstructions can minimize the boundary variations.

As verified in [36], it is readily to reduce the boundary variation of smooth solution by using higher order polynomial, the limited VPM-MLP scheme in this study. For discontinuous solution, the THINC(tangent of hyperbola interface capturing) is preferable since its jump-like distribution can approximate the discontinuity inside the cell with high fidelity thus effectively reduces the variation of boundary reconstruction values. Then the unstructured version of BVD scheme[29] is applied cell-wisely to adaptively determine the optimum reconstruction by integrating VPM and THINC scheme via a weight function. The main solution procedure of BVD reconstruction is summarized as follows.

1. Prepare the limited VPM-MLP reconstruction polynomial $\Phi_i^{(1)}(\xi, \eta, \zeta)$ and the unstructured multi-dimensional THINC reconstruction as

$$\Phi_i^{(2)}(\xi, \eta, \zeta) = \phi_{\min} + \frac{\phi_{\max} - \phi_{\min}}{2} \left(1 + \tanh \left(\beta \left(\mathcal{P}_i(\xi, \eta, \zeta) + \hat{d}_i \right) \right) \right), \quad (6.39)$$

where ϕ_{\min} and ϕ_{\max} are the minimum and maximum values of VIAs in all adjacent cells sharing vertex θ_{ik} . The $\mathcal{P}_i(\xi, \eta, \zeta) + \hat{d}_i = 0$ is the equation of interface in local coordinate which is formed with either linear or quadratic polynomial and determined from surrounding VIA and PV by least-square method. The parameter $\beta = 3$ is used in this paper to control the jump sharpness. For more details of the THINC reconstructions, refer to [37, 38].

2. Evaluate smoothness respectively for $\Phi_i^{(1)}(\xi, \eta, \zeta)$ and $\Phi_i^{(2)}(\xi, \eta, \zeta)$ by Eqn. (6.36), yielding

$$TBV(\Phi)_i^{(1)} = \frac{\sum_{j=1}^{j=J} \left(\frac{1}{|\Gamma_{ij}|} \int_{\Gamma_{ij}} \Phi_i^{(1)}(\xi, \eta, \zeta) d\Gamma - \frac{1}{|\Gamma_{ij}|} \int_{\Gamma_{ij}} \Phi_{ij}^{(1)}(\xi, \eta, \zeta) d\Gamma \right)^4}{\sum_{j=1}^{j=J} (\bar{\phi}_i - \bar{\phi}_{ij})^4} \quad (6.40)$$

$$TBV(\Phi)_i^{(2)} = \frac{\sum_{j=1}^{j=J} \left(\frac{1}{|\Gamma_{ij}|} \int_{\Gamma_{ij}} \Phi_i^{(2)}(\xi, \eta, \zeta) d\Gamma - \frac{1}{|\Gamma_{ij}|} \int_{\Gamma_{ij}} \Phi_{ij}^{(1)}(\xi, \eta, \zeta) d\Gamma \right)^4}{\sum_{j=1}^{j=J} (\bar{\phi}_i - \bar{\phi}_{ij})^4} \quad (6.41)$$

Although there is an arbitrariness in determining reconstruction between $\Phi_i^{(1)}$ and $\Phi_i^{(2)}$, simplification is made based on the assumption that solution in neighboring cells is smooth and approximated by $\Phi_i^{(1)}$ straightforwardly. As discussed in [36], for the cell where a discontinuous solution exists the reconstruction with $TBV(\Phi)_i^{(2)}$ generates a smaller jump compared to a polynomial-based reconstruction. So, we identify the discontinuity when $TBV(\Phi)_i^{(2)} < TBV(\Phi)_i^{(1)}$, and proceed to the next step. Otherwise, if $TBV(\Phi)_i^{(2)} > TBV(\Phi)_i^{(1)}$, we choose $\Phi_i^{(1)}(\xi, \eta, \zeta)$ without advancing to the next step.

3. Re-formulate the reconstruction function on the target cell by $\Phi_i^{(3)}(\xi, \eta, \zeta) = \varpi_i \Phi_i^{(2)}(\xi, \eta, \zeta) + (1 - \varpi_i) \Phi_i^{(1)}(\xi, \eta, \zeta)$ where $\varpi_i \in [0, 1]$ is the weighting function blending $\Phi_i^{(1)}(\xi, \eta, \zeta)$ and $\Phi_i^{(2)}(\xi, \eta, \zeta)$, which is found by minimizing the total jump on the cell boundary according to the the BVD algorithm,

$$\epsilon_i = \sum_{j=1}^J |\Gamma_{ij}|^2 \left(\left(\varpi_i \left(\bar{\Phi}_i^{(2)} \right)_{\Gamma_{ij}} + (1 - \varpi_i) \left(\bar{\Phi}_i^{(1)} \right)_{\Gamma_{ij}} \right) - \left(\bar{\Phi}_{ij}^{(1)} \right)_{\Gamma_{ij}} \right)^2, \quad (6.42)$$

where the integrated averages over cell boundaries are computed by

$$\left(\overline{\Phi}_i^{(1)}\right)_{\Gamma_{ij}} = \frac{1}{|\Gamma_{ij}|} \int_{\Gamma_{ij}} \Phi_i^{(1)}(\xi, \eta, \zeta) d\Gamma, \quad (6.43)$$

$$\left(\overline{\Phi}_i^{(2)}\right)_{\Gamma_{ij}} = \frac{1}{|\Gamma_{ij}|} \int_{\Gamma_{ij}} \Phi_i^{(2)}(\xi, \eta, \zeta) d\Gamma. \quad (6.44)$$

Consequently, the weight function ϖ_i can be determined from

$$\frac{\partial \epsilon_i}{\partial \varpi_i} = 0,$$

which yields

$$\varpi_i = \frac{\sum_{j=1}^J |\Gamma_{ij}|^2 \left(\left(\overline{\Phi}_i^{(2)}\right)_{\Gamma_{ij}} - \left(\overline{\Phi}_i^{(1)}\right)_{\Gamma_{ij}} \right) \left(\left(\overline{\Phi}_{ij}^{(1)}\right)_{\Gamma_{ij}} - \left(\overline{\Phi}_i^{(1)}\right)_{\Gamma_{ij}} \right)}{\sum_{j=1}^J |\Gamma_{ij}|^2 \left(\left(\overline{\Phi}_i^{(2)}\right)_{\Gamma_{ij}} - \left(\overline{\Phi}_i^{(1)}\right)_{\Gamma_{ij}} \right)^2}.$$

With ϖ_i determined, we make use of $\Phi_i^{(3)}(x, y, z)$ for reconstruction in target cell Ω_i . It is noted that the BVD algorithm for reducing numerical dissipation is used only for cells containing discontinuities identified by the criterion $\mathcal{S} < \mathcal{S}_c$. We refer to the VPM/MCV-MLP reconstruction with the implementation of BVD algorithm as VPM/MCV-MLP-BVD reconstruction.

6.6 Numerical experiments

In this section, we verify the accuracy, robustness and computational efficiency of the presented model with some widely used benchmark tests. In order to quantify the numerical accuracy, we define numerical errors in L_1 and L_∞ norms as follows,

$$E(L_1) = \frac{\sum_{i=1}^{N_e} (|\phi_{ni} - \phi_{ei}| |\Omega_i|)}{\sum_{i=1}^{N_e} (|\phi_{ei}| |\Omega_i|)}, \quad E(L_\infty) = \frac{\max |\phi_{ni} - \phi_{ei}|}{\max |\phi_{ei}|}. \quad (6.45)$$

where ϕ_{ni} and ϕ_{ei} denote numerical and exact solutions respectively.

6.6.1 Advection equation

Accuracy test for 2D

To evaluate the numerical accuracy and convergence rate of proposed MCV-MLP-BVD reconstruction, we computed the linear advection transport of a sine function on two unstructured grids of quadrilateral and triangular elements with gradually refined resolutions. The initial profile is given by

$$\phi_0(x, y) = \sin 2\pi(x + y) \quad (6.46)$$

on domain of $[0, 1] \times [0, 1]$ with periodic boundary conditions in both x and y directions.

The advection is carried out by a constant and uniform velocity specified with $u = 1.0$, $v = 1.0$. Numerical experiments were conducted until time $t = 1$ with time step adjusted by CFL number 0.2 throughout all computations. We tabulated numerical errors and convergence rates of the original MCV reconstruction and the MCV-MLP-BVD reconstruction in Table 6.2. It is observed that the MCV-MLP-BVD scheme can ensure exactly 3th order accuracy on both grids. Also, there is no difference in both L_1 and L_∞ error with and without BVD technique, which illustrates the MCV-MLP-BVD scheme can effectively identify the solution smoothness and realize the highest possible numerical accuracy of the MCV reconstruction.

To quantify the computational cost in comparison with the conventional FVM, we run the same test using FVM with the superbee-TVD scheme [209] on triangular grids of different resolutions. All calculations were conducted on a single core of Intel(R) Xeon(R) CPU E5-2687W (3.10 GHZ). We give the elapse time for different schemes in Table 6.3 with numerical errors and convergence rates. It is observed that the time of MCV-MLP-BVD is about 1.2 times of the original MCV scheme. It is also shown that

the MCV and MCV-MLP-BVD schemes require much less DOFs and computational cost in comparison with conventional FVM scheme to reach the same accuracy level. For example, the L_1 error of MCV-MLP-BVD with 849 cell numbers is almost the same as that of FVM with 14412 cells. This advantage becomes more significant as the grid resolution is refined due to the superior convergence property of the MCV and MCV-MLP-BVD schemes.

To show that the MCV-MLP-BVD scheme can also work with larger CFL number, we conduct the same accuracy test with CFL number 0.9 on triangular mesh. We compared the numerical results with CFL number 0.2 against those with CFL number 0.9 in Table.6.4 which shows that 3rd order convergence rate regarding to L_1 error can be achieved with large CFL number.

TABLE 6.2: Numerical errors and convergence orders of the advection equation on quadrilateral and triangular grids.

Grid	Cell	MCV			MCV-MLP-BVD			
		L_1 error	order	L_∞ error	order	L_1 error	L_∞ error	order
Quadrilateral	100	1.358×10^{-1}		1.295×10^{-1}		1.358×10^{-1}		1.295×10^{-1}
	400	1.703×10^{-2}	3.00	1.683×10^{-2}	2.94	1.703×10^{-2}	3.00	1.683×10^{-2}
	1600	2.115×10^{-3}	3.01	2.108×10^{-3}	3.00	2.115×10^{-3}	3.01	2.108×10^{-3}
	6400	2.636×10^{-4}	3.00	2.634×10^{-4}	3.00	2.636×10^{-4}	3.00	2.634×10^{-4}
	25600	3.303×10^{-5}	3.00	3.302×10^{-5}	3.00	3.303×10^{-5}	3.00	3.302×10^{-5}
Triangular	226	9.292×10^{-2}		9.452×10^{-2}		9.292×10^{-2}		9.452×10^{-2}
	894	1.177×10^{-2}	3.00	1.194×10^{-2}	3.01	1.177×10^{-2}	3.00	1.194×10^{-2}
	3588	1.445×10^{-3}	3.02	1.467×10^{-3}	3.02	1.445×10^{-3}	3.02	1.467×10^{-3}
	14412	1.783×10^{-4}	3.01	1.841×10^{-4}	2.99	1.783×10^{-4}	3.01	1.841×10^{-4}
	57518	2.244×10^{-5}	3.00	2.492×10^{-5}	2.89	2.244×10^{-5}	3.00	2.492×10^{-5}

TABLE 6.3: Comparisons of L_1 error, order and computational cost estimation of different schemes for the advection equation on triangular grids

Cells	FVM(Superbee)			MCV			MCV-MLP-BVD		
	L_1 error	order	time(s)	L_1 error	order	time(s)	L_1 error	order	time(s)
226	1.027×10^{-1}		0.15	9.292×10^{-2}		0.61	9.292×10^{-2}		0.70
849	7.228×10^{-2}	0.51	0.53	1.177×10^{-2}	3.00	1.65	1.177×10^{-2}	3.00	2.01
3588	3.327×10^{-2}	1.12	1.69	1.445×10^{-3}	3.02	5.54	1.445×10^{-3}	3.02	6.74
14412	1.162×10^{-2}	1.51	6.46	1.783×10^{-4}	3.01	52.30	1.783×10^{-4}	3.01	63.96
57518	3.458×10^{-3}	1.75	46.08	2.244×10^{-5}	3.00	562.26	2.244×10^{-5}	3.00	692.70

TABLE 6.4: Numerical errors and convergence orders of the advection equation on quadrilateral and triangular grids.

Grid	Cell	CFL=0.2			CFL=0.9			
		L_1 error	order	L_∞ error	order	L_1 error	L_∞ error	order
Triangular	226	9.292×10^{-2}		9.452×10^{-2}		1.002×10^{-1}		1.203×10^{-1}
	894	1.177×10^{-2}	3.00	1.194×10^{-2}	3.01	1.279×10^{-2}	2.99	1.763×10^{-2}
	3588	1.445×10^{-3}	3.02	1.467×10^{-3}	3.02	1.576×10^{-3}	3.03	3.377×10^{-3}
	14412	1.783×10^{-4}	3.01	1.841×10^{-4}	2.99	1.944×10^{-4}	3.01	5.060×10^{-4}
	57518	2.244×10^{-5}	3.00	2.492×10^{-5}	2.89	2.439×10^{-5}	3.00	7.758×10^{-5}

TABLE 6.5: Comparisons with WENO schemes about numerical errors and convergence rates of the advection equation on uniform triangular grids.

Grid	Cell size	3rd WENO [4]		VPM-MLP-BVD					
		L_1 error	L_∞ error	order	order	L_1 error	L_∞ error	order	order
Triangular	1/5	8.11×10^{-2}	1.93×10^{-1}			3.43×10^{-3}	3.45×10^{-3}		
	1/10	2.65×10^{-2}	6.16×10^{-2}	1.62	1.65	4.35×10^{-4}	4.36×10^{-4}	2.98	2.98
	1/20	2.68×10^{-3}	8.77×10^{-3}	3.31	2.81	5.45×10^{-5}	5.46×10^{-5}	3.00	3.00
	1/40	1.44×10^{-4}	4.88×10^{-4}	4.22	4.17	6.83×10^{-6}	6.83×10^{-6}	3.00	3.00

TABLE 6.6: Element statistics of different types unstructured grids used for advection test.

Element	N_{edge}	N_{hexa}	N_{tetra}	N_{prism}	N_{pyra}	N_{total}
Hexahedral	10	1,000	0	0	0	1,000
	20	8,000	0	0	0	8,000
	40	64,000	0	0	0	64,000
	80	512,000	0	0	0	512,000
Tetrahedral	10	0	8,097	0	0	8,097
	20	0	58,880	0	0	58,880
	40	0	411,104	0	0	411,104
	80	0	3,278,297	0	0	3,278,297
Prismatic	10	0	0	2,260	0	2,260
	20	0	0	17,960	0	17,960
	40	0	0	143,520	0	143,520
	80	0	0	1,152,480	0	1,152,480
Hybrid	10	1,644	535	0	96	2,295
	20	7,784	1,926	0	216	9,926
	40	62,272	19,311	0	864	82,447
	80	498,176	183,839	0	3,456	685,471

To illustrate the superiority of the present scheme against the high order finite volume method, we solve two-dimensional linear equation on uniform triangular meshes and make a comparison with the 3rd order WENO scheme [4] in regard to numerical accuracy and computational cost. To facilitate comparison, we use the same condition as [4], where the initial profile $\phi_0(x, y) = \sin(0.5\pi(x + y))$ is set on the domain of $[-2, 2]^2$. Uniform triangular meshes are obtained by adding one diagonal line in each rectangle and are employed in this test. The comparison between the 3rd order WENO scheme with the VPM-MLP-BVD scheme is shown in the Table .6.5. It can be seen that the numerical errors of VPM-MLP-BVD scheme is much less than 3rd order WENO scheme. Also, the convergence rate of VPM-MLP-BVD is uniform 3rd order while the order of WENO scheme is distinctly influenced by nonlinear switching between different stencils.

As for computational cost, for each time stage and each triangle, the number of reconstruction is upto 18 for the 3rd order WENO scheme since there are 3 reconstruction for each quadrature point, which results in a tremendous calculation counts of 306 multiplications and 234 additions. While for the VPM-MLP-BVD, there are only 3 times of reconstructions which results in 172 multiplications and 156 additions. It is also well known that extension of unstructured WENO scheme to three dimensional case will entail further difficulties in both algorithmic complexity and selection of reconstruction stencils. In contrast, the VPM-MLP-BVD scheme evidently benefits efficiency from compact stencils particular for three dimensional computation. Moreover with less manipulation, the VPM-MLP-BVD can also achieve excellent performance around discontinuity, which will be substantiated in the following sections.

Rotation test of complex profiles

We extend the 1D Jiang and Shu's problem [2] to 2D with the rotational velocity field defined by $(u, v) = (-2\pi x, 2\pi y)$. The computational domain is $[-1, 1] \times [-1, 1]$, and

the initial distribution is defined by

$$\phi_0(x, y) = \begin{cases} \frac{1}{6}(G(r_1 + \delta, \beta) + G(r_1 - \delta, \beta) + 4G(r_1, \beta)), & |r_1| \leq 0.2 \\ 1, & |x| \leq 0.2, -0.7 \leq y \leq -0.3 \\ 1 - |5r_2|, & |r_2| \leq 0.2 \\ \frac{1}{6}(F(r_3 + \delta, \alpha) + F(r_3 - \delta, \alpha) + 4F(r_3, \alpha)), & |r_3| \leq 0.2 \\ 0, & \text{otherwise} \end{cases} \quad (6.47)$$

where

$$r_1 = \sqrt{(x + 0.6)^2 + y^2}, \quad r_2 = \sqrt{(x - 0.6)^2 + y^2}, \quad r_3 = \sqrt{x^2 + (y - 0.6)^2} \quad (6.48)$$

and $G(r, \beta) = \exp(-\beta r^2)$, $F(r, \alpha) = \sqrt{\max(1 - \alpha^2 r^2)}$. The coefficients are set to be $\delta = 0.01$, $\alpha = 5$ and $\beta = \log 2 / (36\delta^2)$. The initial profile which includes four kinds of distributions of different smoothness is depicted in Fig. 6.5. The computation was run up to $t = 1$ (after one revolution) with quadrilateral and triangular meshes respectively. We also made a comparison between the results of the MCV-MLP and MCV-MLP-BVD reconstructions as shown in Fig. 6.6 and Fig. 6.7 on different grids. We can see that there are no visible oscillations around discontinuous regions in both results. Compared to MCV-MLP scheme, MCV-MLP-BVD reconstruction effectively reduces numerical dissipation and resolves all structures with significantly improved solution quality.

Convergence rate for advection equations on 3D hybrid unstructured grids

We first investigate the numerical accuracy and convergence behavior of the proposed model for advection transport. We perform 3D advection test on hybrid unstructured grids including hexahedral, tetrahedral, prismatic and pyramidal elements.

An initial smooth profile $\phi_0(x, y, z) = \sin(2\pi x) \cdot \sin(2\pi y) \cdot \sin(2\pi z)$ is transported by a uniform velocity of $\mathbf{u} = (1, 1, 1)$ in a unit cube $[0, 1]^3$. We used four types unstructured

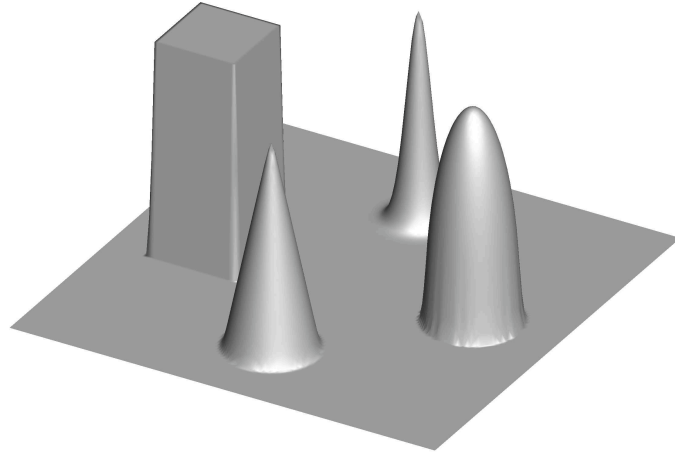


FIGURE 6.5: The bird's eye view of initial complex profile for the solid rotation test.

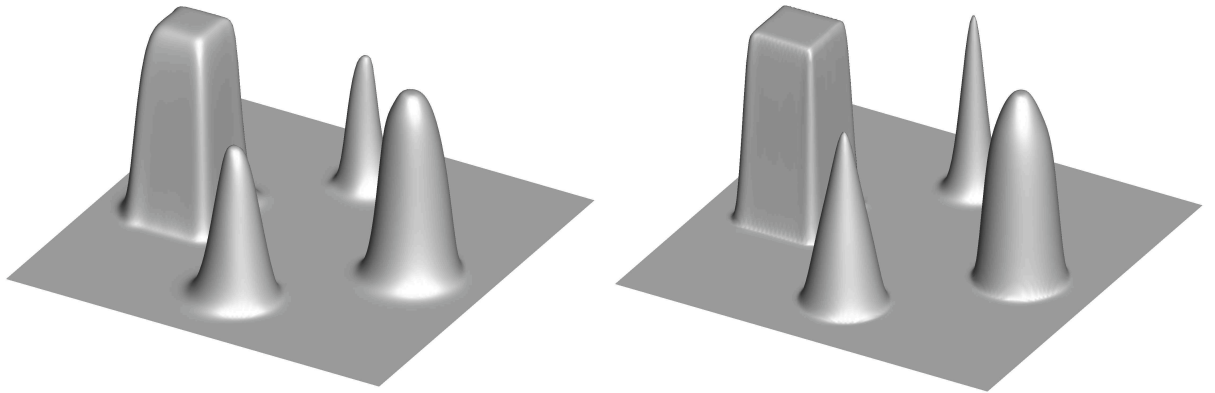


FIGURE 6.6: Same as Fig.6.5, but for the numerical results after one rotation on a grid of 57670 triangular elements with different reconstruction schemes, (a) MCV-MLP; (b) MCV-MLP-BVD.

grids as shown in Fig. 6.8, i.e. three grids with pure hexahedral, tetrahedral or prismatic elements, and a hybrid grid that blends hexahedrons, tetrahedrons and pyramids. The gradually refined grids of different resolutions are generated by specifying 10, 20, 40 and 80 partitions along each boundary edge of the computational domain. The element statistics of different grids are tabulated in Table 6.6. The total number of elements are denoted as N_{total} which varies for different grids. Periodic boundary conditions and a CFL number of 0.25 are used throughout the computations.

The L_1 error and the convergence rate of VPM and VPM-MLP-BVD reconstructions at time $t = 1$ are given in Table 6.7 for different grid resolutions along with the computing time. It is seen that both schemes are verified with over 2nd order accuracy for

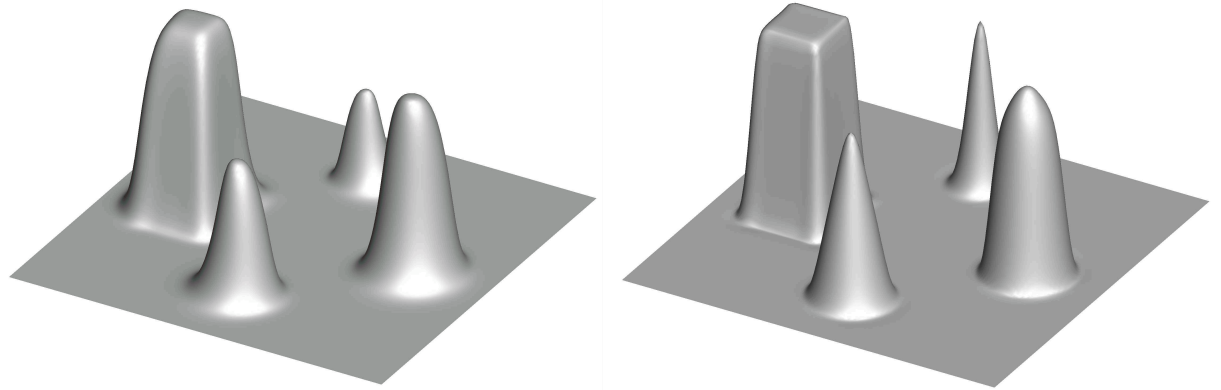


FIGURE 6.7: The same as Fig.6.6 but on 25600 quadrilateral mesh

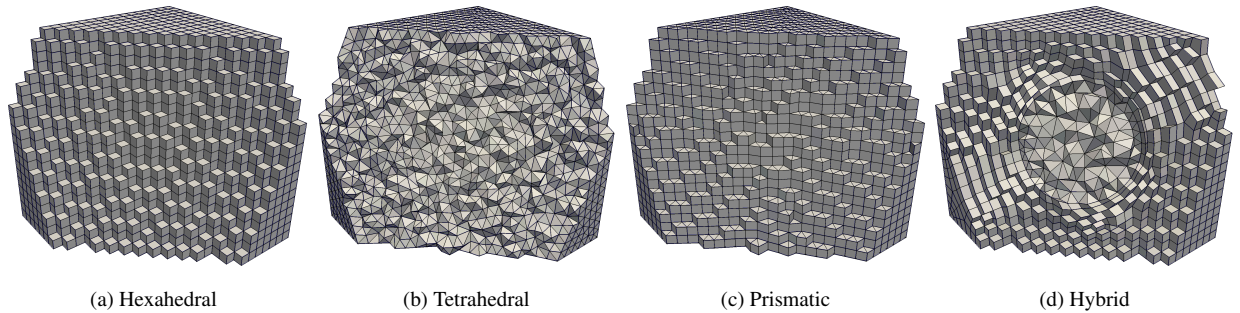


FIGURE 6.8: Cutaway cross-section views of different types unstructured grids for advection test.

TABLE 6.7: Numerical accuracy and convergence rate study for advection test on hybrid unstructured grids.

Element	N_{edge}	FVM			VPM			VPM-MLP-BVD		
		L_1 error	Rate	Time	L_1 error	Rate	Time	L_1 error	Rate	Time
Hexahedral	10	6.84×10^{-1}	—	0.17	3.06×10^{-1}	—	0.51	6.58×10^{-1}	—	0.71
	20	1.91×10^{-1}	1.84	1.58	4.63×10^{-2}	2.72	8.53	4.63×10^{-2}	3.82	9.89
	40	5.48×10^{-2}	1.80	22.80	5.97×10^{-3}	2.96	137.62	5.97×10^{-3}	2.96	158.27
	80	1.50×10^{-2}	1.87	727.35	7.50×10^{-4}	2.99	2768.36	7.50×10^{-4}	2.99	3109.90
Tetrahedral	10	4.33×10^{-1}	—	8.38	2.08×10^{-1}	—	31.37	3.23×10^{-1}	—	35.02
	20	2.47×10^{-1}	0.83	142.75	4.72×10^{-2}	2.24	492.52	6.52×10^{-2}	2.41	605.42
	40	1.36×10^{-1}	0.92	2350.51	1.06×10^{-2}	2.30	6320.79	1.30×10^{-2}	2.49	8274.52
	80	7.08×10^{-2}	0.94	30116.30	2.45×10^{-3}	2.11	86288.01	2.86×10^{-3}	2.18	115858.01
Prismatic	10	4.50×10^{-1}	—	0.56	2.39×10^{-1}	—	2.21	5.18×10^{-1}	—	2.94
	20	1.17×10^{-1}	1.94	6.38	3.70×10^{-2}	2.70	33.06	4.11×10^{-2}	3.66	38.39
	40	3.64×10^{-2}	1.69	118.19	4.81×10^{-3}	2.95	555.97	4.83×10^{-3}	3.10	768.98
	80	9.81×10^{-3}	1.89	2462.32	6.05×10^{-4}	2.98	8950.96	6.08×10^{-4}	2.99	10044.12
Hybrid	10	5.01×10^{-1}	—	2.63	1.92×10^{-1}	—	15.20	5.07×10^{-1}	—	17.86
	20	1.90×10^{-1}	1.99	20.75	4.57×10^{-2}	2.94	158.98	5.15×10^{-2}	4.68	177.42
	40	5.39×10^{-2}	1.78	343.03	6.02×10^{-3}	2.87	2192.58	6.70×10^{-3}	2.89	2424.54
	80	1.51×10^{-2}	1.80	6347.98	8.24×10^{-4}	2.81	26845.80	8.87×10^{-4}	2.86	30967.50

all type grids. Particularly, the results on hexahedral, prismatic and pyramidal elements reach nearly 3rd order, while tetrahedral element degrades to about 2.2th order. This may be partly owe to the fact that reconstruction on tetrahedral element involves fewer DOFs over a compact stencil which only includes adjacent cells sharing the boundary surfaces with the target cell. Although higher order reconstruction can be implemented by broadening stencils, it will considerably increase algorithmic complexity and computational cost. We prefer the present formulation as a good trade-off between accuracy and simplicity. We can also see that the smoothness indicator function can correctly identify smooth solution and switch to the highest possible VPM reconstruction.

For comparison with conventional finite volume method (FVM), we also include the results from the standard MUSCL (Monotonic Upstream-Centered Scheme for Conservation Laws) scheme [25, 39] in Table 6.7 using the templates provided in the OpenFOAM source code [40]. It is observed that VPM and VPM-MLP-BVD reconstructions are much more accurate than the MUSCL scheme in terms of both numerical error and convergence rate. As expected, VPM and VPM-MLP-BVD reconstructions increase the computational cost for the same grid resolution. However, because of the superior convergence property, the present schemes can reach the same error level with much less grid elements and computational time.

A careful comparison between VPM and VPM-MLP-BVD reveals that both the MLP limiting projection and the BVD dissipation-minimizing algorithm do not degrade the numerical accuracy for smooth solutions, while are effective in reproducing discontinuous solutions as shown later in the paper.

3D solid body rotation test

In order to show the capability of the proposed scheme in eliminating both numerical oscillation and dissipation in 3D unstructured grids, the problem of a 3D solid body rotation is performed. The initial condition is the same as in [41]. The computational domain is $[-50, 50] \times [-50, 50] \times [-50, 50]$. The velocity $\mathbf{u} = (u, v, w)$ is set as

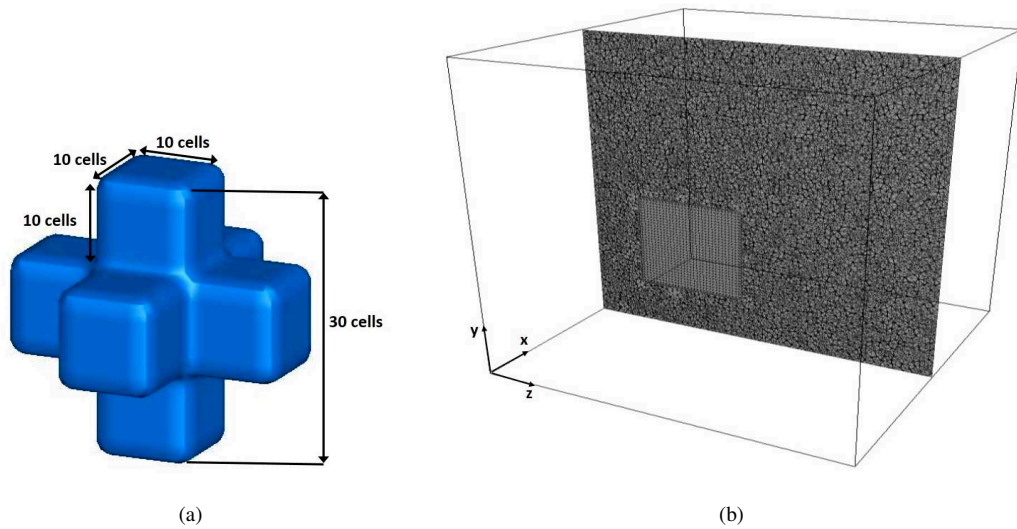


FIGURE 6.9: (a) Initial profile plotted with the 0.5 isosurface. (b) The cross section of the hybrid 3D unstructured grids composed of 27000 hexahedrons, 5400 pyramids and 2545907 tetrahedrons.

$\mathbf{u} = \boldsymbol{\omega} \times \mathbf{r}$, where $\mathbf{r} = (x, y, z)$ is the position vector and $\boldsymbol{\omega} = \sqrt{2}\pi(0, -1, 1)$. As shown in Fig. 6.9 (a), the initial profile is a cubic cross centered at $(x, y, z) = (0, -20, -20)$.

We use two kinds of grids to compute this test: a Cartesian grid with $100 \times 100 \times 100$ elements and a hybrid unstructured grid with 27000 hexahedrons, 5400 pyramids and 2545907 tetrahedrons as shown in Fig. 6.9(b) where a cubic Cartesian subdomain is embedded in the lower-left portion for the convenience to specify the initial profile and compare numerical results. In order to compare our scheme with conventional finite volume method, we compute this problem by the original MLP scheme [34] and the VPM-MLP-BVD scheme. The contour lines of the initial profile after one revolution on the $x - z$ plane cutting through the center of the cubic cross are shown in Fig. 6.10 and Fig. 6.11 respectively. It is observed that the steepness in original profile has been heavily smeared out due to the excessive numerical dissipation in the MLP scheme, while the VPM-MLP-BVD scheme is able to preserve the steepness with a significant improvement in the geometrical faithfulness of the transported object. It is noted that numerical results of the VPM-MLP-BVD scheme on the hybrid unstructured grid have a good quality as well without noticeable degradation in comparison with the Cartesian

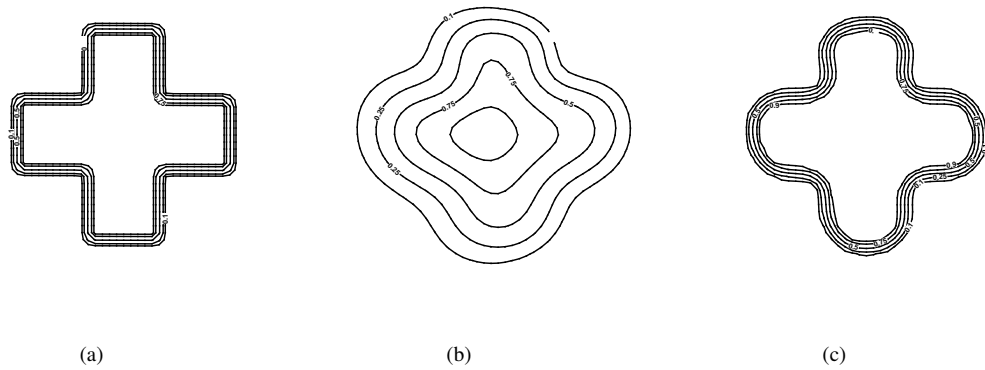


FIGURE 6.10: Contour lines of the results after one revolution on the $x-z$ plane cutting through the center of the cubic cross. The computation is on 100×100 Cartesian grid. Displayed are the initial profile (a), the result computed by the conventional finite volume method with MLP limiting scheme [34] (b) and the result computed by the proposed VPM-MLP-BVD scheme.

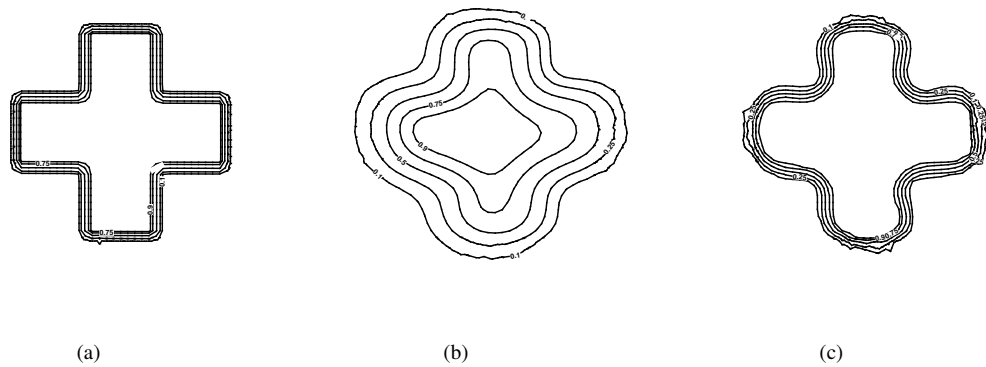


FIGURE 6.11: The same as in Fig. 6.10 but on the hybrid unstructured grids as shown in Fig. 6.9.

grid.

6.6.2 2D Euler equations

Accuracy test of inviscid Burgers' equation

To examine the capability of current scheme to resolve non-linear waves, we examined the convergence rate of the proposed scheme for inviscid Burgers' equation

$$\frac{\partial u}{\partial t} + \frac{\partial u^2/2}{\partial x} = 0.0 \quad (6.49)$$

with initial condition $u(x, 0) = 0.5 + \sin(\pi x)$. The exact solution remains smooth until $t = 1.0/\pi$ before producing a moving shock and a rarefaction wave. We solved this one dimensional test on a two dimensional computational domain $[0, 2] \times [0, 0.2]$ with unstructured grids of uniform triangular cells of different sizes gradually refined as $h = 1/40, 1/80, 1/160, 1/320, 1/640$. The computations were conducted up to $t = 0.5/\pi$. We show L_1 and L_∞ errors, as well as the convergence rates, in Table. 6.8. We also plot the distribution of variable in Fig. 6.12. The proposed MCV-MLP-BVD algorithm can achieve nearly 3rd order accuracy for inviscid Burger's equation.

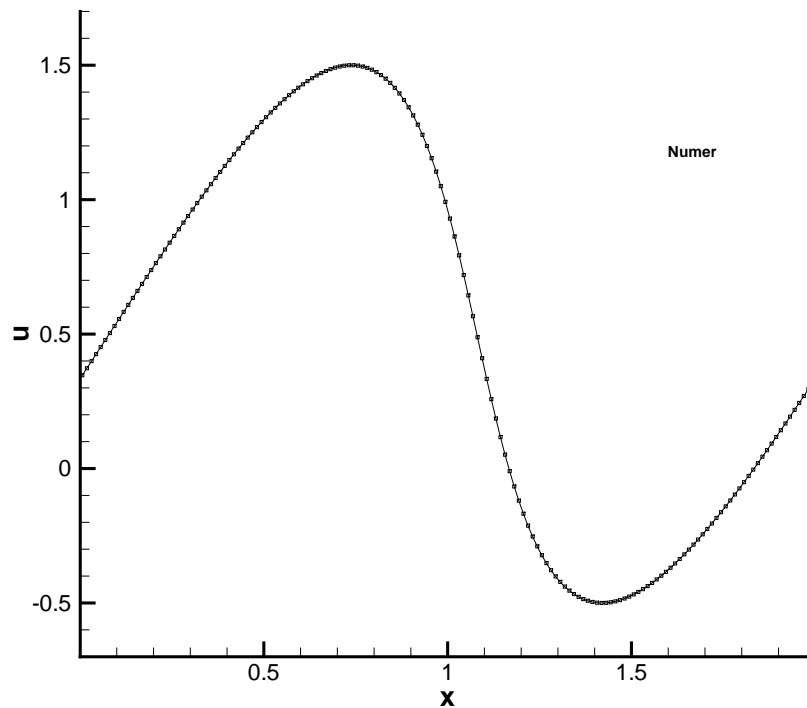


FIGURE 6.12: The distribution of variable along the central line at $t = 0.5/\pi$ with cell sizes of $h = 1/80$.

Convergence studies for 2D Euler equations

TABLE 6.8: Numerical errors and convergence rates of the inviscid Burgers' equation with the MCV-MLP-BVD scheme

Grid Size h	L_1 error	L_1 order	L_∞ error	L_∞ order
1/40	1.011×10^{-4}	-	3.674×10^{-4}	-
1/80	1.424×10^{-5}	2.83	5.200×10^{-5}	2.82
1/160	1.882×10^{-6}	2.92	6.952×10^{-6}	2.90
1/320	2.386×10^{-7}	2.98	8.981×10^{-7}	2.95
1/640	3.005×10^{-8}	2.99	1.135×10^{-7}	2.98

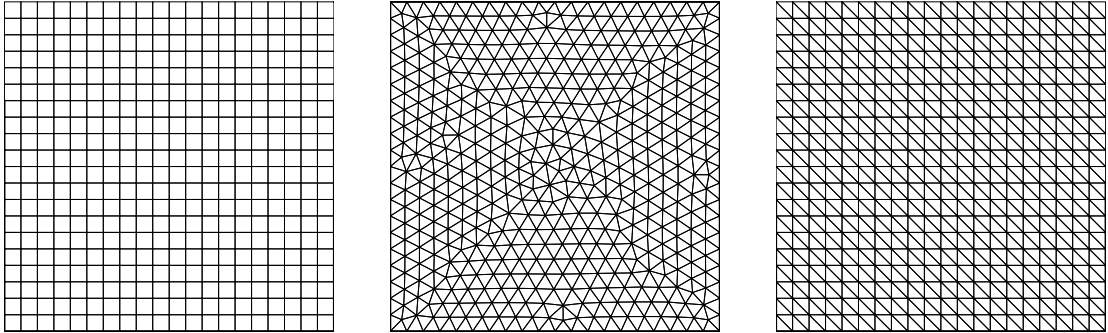


FIGURE 6.13: Computational grids for convergence test of Euler equations. From left to right: grid A, grid B, and grid C.

To show that the present model has 3rd-order accuracy (convergence rate) for Euler equations as well, we solved the propagation of density disturbances with Euler equations. The initial velocity and pressure were specified uniform throughout the whole computational domain, while a sinusoidal perturbation was given to the density field,

$$\begin{cases} \rho(x, y, 0) = 1 + 0.2 \sin(\pi(x + y)), \\ u(x, y, 0) = 0.7, \\ v(x, y, 0) = 0.3, \\ p(x, y, 0) = 1.0. \end{cases}$$

The computational domain is $D = [-1, 1] \times [-1, 1]$ which was divided into uniform quadrilateral, Delaunay and subplitted triangular elements as shown in Fig. 6.13 as grids A, B and C. We used gradually refined grids with periodic boundaries and obtained the numerical results at $t = 2.0$ with a constant CFL number of 0.2. The numerical errors and convergence rates for Euler equations on different grids are summarized in Table 6.9. It is observed that the numerical solutions of Euler equations converged at a

TABLE 6.9: Numerical errors and convergence rates of Euler equations on different grids

	Elements Number	L_1 error	L_1 order	L_∞ error	L_∞ order
grid A	400	1.140×10^{-3}	–	1.602×10^{-3}	–
	1600	1.487×10^{-4}	2.94	2.075×10^{-4}	2.95
	6400	1.898×10^{-5}	2.97	2.687×10^{-5}	2.95
	25600	2.398×10^{-6}	2.98	3.430×10^{-6}	2.97
grid B	902	5.948×10^{-4}	–	1.576×10^{-3}	–
	3604	7.108×10^{-5}	3.07	2.142×10^{-4}	2.88
	14362	9.902×10^{-6}	2.85	3.343×10^{-5}	2.69
	57670	1.300×10^{-6}	2.92	4.642×10^{-6}	2.84
grid C	800	3.100×10^{-4}	–	4.199×10^{-4}	–
	3200	3.978×10^{-5}	2.96	5.458×10^{-5}	2.94
	12800	5.009×10^{-6}	2.99	6.908×10^{-6}	2.98
	51200	6.281×10^{-7}	3.00	8.680×10^{-7}	2.99

rate of nearly third order on all types of grids, which verified the expected accuracy of spatial reconstruction and discretization.

Shock Tube Problems

To examine the capability of current scheme to resolve various non-linear waves, we use two shock tube problems where exact solution can be obtained by solving exact Riemann problem. Computational domain is $[0, 1] \times [0, 0.1]$ filled by uniform triangular grids with grid size of $h = 1/200$. We consider two initial condition here. The first one is Sod problem of which initial profile is

$$(\rho, u, v, p) = \begin{cases} (1, 0, 0, 1) & \text{if } 0 \leq x \leq 0.5, \\ (0.125, 0, 0, 0.1) & \text{otherwise.} \end{cases} \quad (6.50)$$

Another one is Lax problem of which initial profile is

$$(\rho, u, v, p) = \begin{cases} (0.445, 0.698, 0, 3.528) & \text{if } 0 \leq x \leq 0.5, \\ (0.5, 0, 0, 0.571) & \text{otherwise.} \end{cases} \quad (6.51)$$

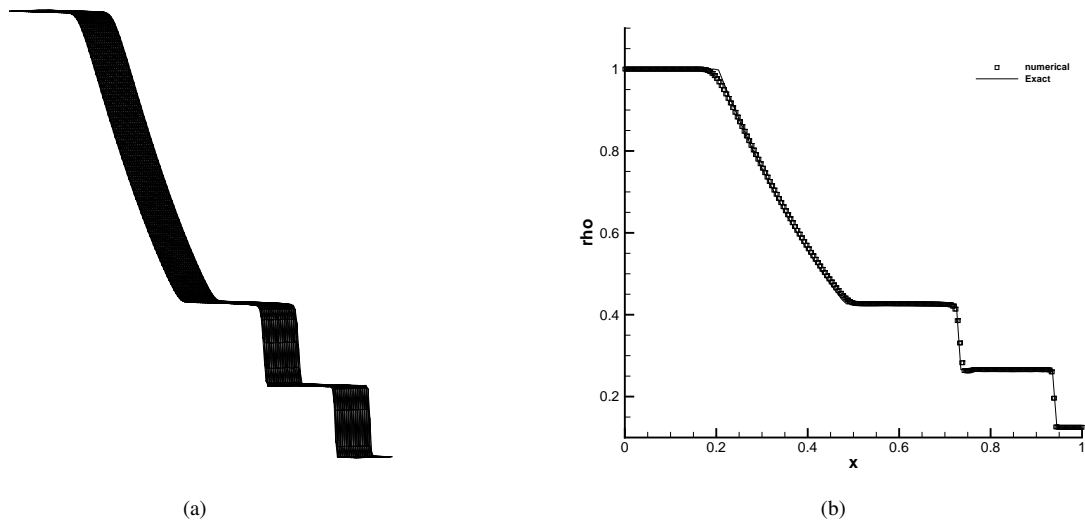


FIGURE 6.14: Numerical results of Sod problem. Bird view of density distribution (a), and the plot along the centerline(b).

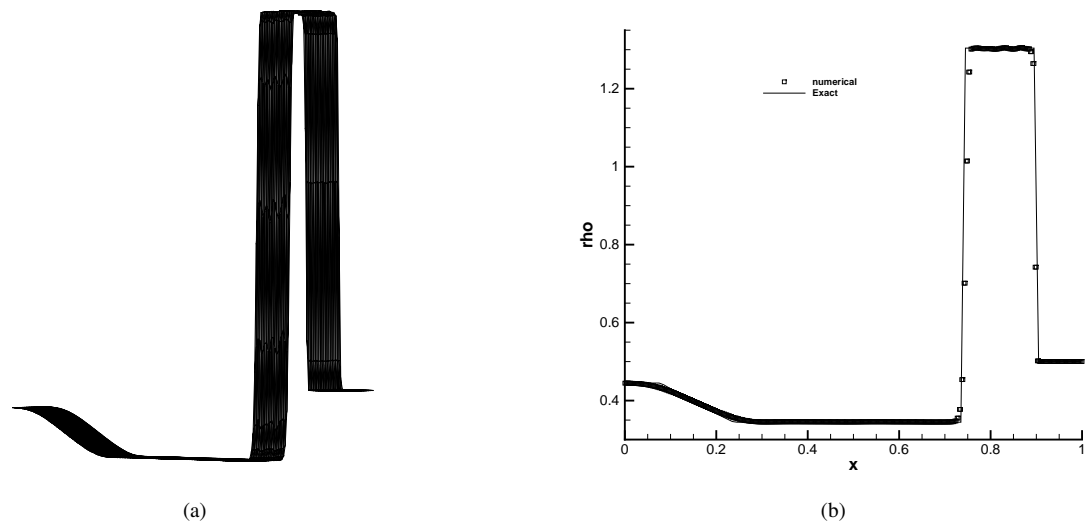


FIGURE 6.15: The same as Fig.6.14 but with Lax problem

The density distributions have been presented in Fig. 6.14 for Sod problem and Fig. 6.15 for Lax problem, respectively. Compared with the results in [210], the present solver demonstrate excellent capability to capture shock waves that the discontinuities are adequately resolved with much less dissipation despite of slight oscillation. For instance, in Sod problem the shock is reproduced within compact thickness of nearly one cell.

A Mach 3 wind tunnel flow with a step

Mach 3 wind tunnel flow with a forward step [42] is widely used to verify the capability of high-resolution schemes in capturing shock-rich flow structures generated from boundary reflections. In this test, a uniform Mach 3 flow is blown into a wind tunnel of $[0, 3] \times [0, 1]$ with a step of 0.2 units high located at 0.6 units away from the left end of the tunnel. The inflow and outflow conditions are prescribed on left and right ends while the reflective condition is imposed at the remaining boundaries. The numerical tests are conducted on unstructured grids with triangular elements of different resolutions. To make a comparison, in Fig. 6.16 we also present the result calculated by the 3rd order WENO scheme [4] with a triangular element size of $1/160$ away from the corner but $1/320$ around the corner. As shown in Figs. 6.17–6.19 which are calculated by our proposed scheme, the contour profiles of the density at $t = 4.0$ on grids of $1/80$, $1/160$ and $1/320$ grid resolutions without fining meshes around the corner are depicted separately. It is seen that the shock waves and strong discontinuities are well resolved without numerical oscillations. We also plot the 3D bird's view of density field on the finest grid in Fig. 6.20 which shows the adequately resolved shock waves and vortices. The numerical dissipation is effectively suppressed so that the vortex structures wave are sufficiently captured, which is quite challenging for conventional FVM schemes with increased numerical dissipation. For example, our scheme can get competitive resolution with nearly half of mesh numbers compared with the 3rd order WENO scheme, see Fig. 6.16 and Fig. 6.17. Moreover, the numerical results converge rapidly on finer mesh and show competitive solution quality compared with other existing high-order schemes in [19, 20, 43]. We also examine the trouble cells identified by the smooth indicator function as plotted in Fig.6.21. It can be seen that the trouble cells, where the limiting projection is triggered, correspond well to the regions containing discontinuous solutions, while the MCV high order reconstruction applies to the regions of smooth solutions.

Double Mach Reflection

The double Mach problem originally proposed in [42] is simulated to further establish

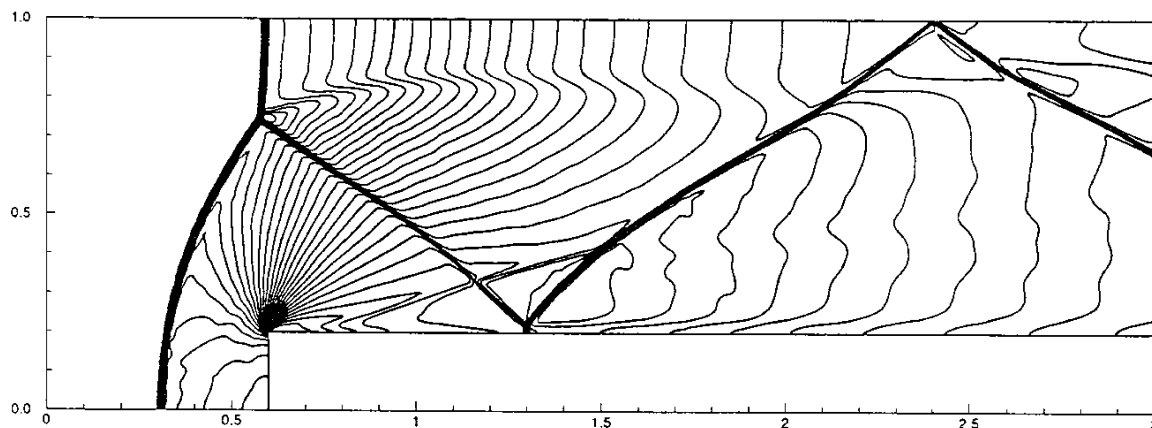


FIGURE 6.16: Numerical solutions calculated by the 3rd order WENO scheme [4] with a triangular element size of $1/160$ away from the corner but $1/320$ around the corner

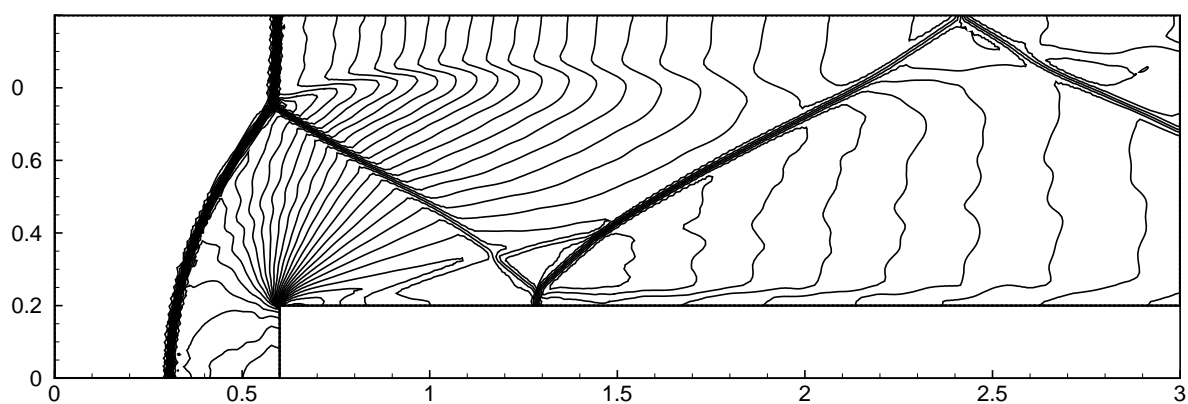


FIGURE 6.17: Density contours for the Mach 3 wind tunnel with a forward step at time of $t = 4$ on a unstructured grid with triangular elements that have $1/80$ edge length along the lower domain boundary.

the accuracy and robustness of the present model. As detailed in [42], a hypersonic flow with a propagating planar shock at $\text{Mach} = 10$ is reflected by a 30 degree ramp. Complex flow structures are generated, which include shock waves and vortices. This example is usually used as a test bed to evaluate capability of numerical schemes in resolving both shock waves and vortex structures. Particularly, the vortex structures are quite challenging to numerical schemes that have excessive numerical dissipations.

In the present work, the computational domain $D = [0, 4] \times [0, 1]$ was divided by triangular elements with different resolutions where the edge length of the grid elements

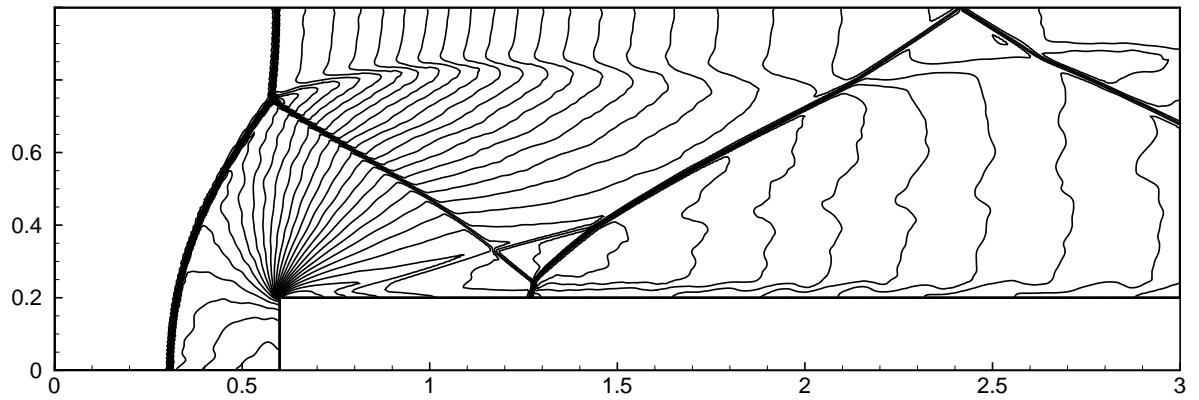


FIGURE 6.18: Same as Fig. 6.17, but with 1/160 triangular grid elements.

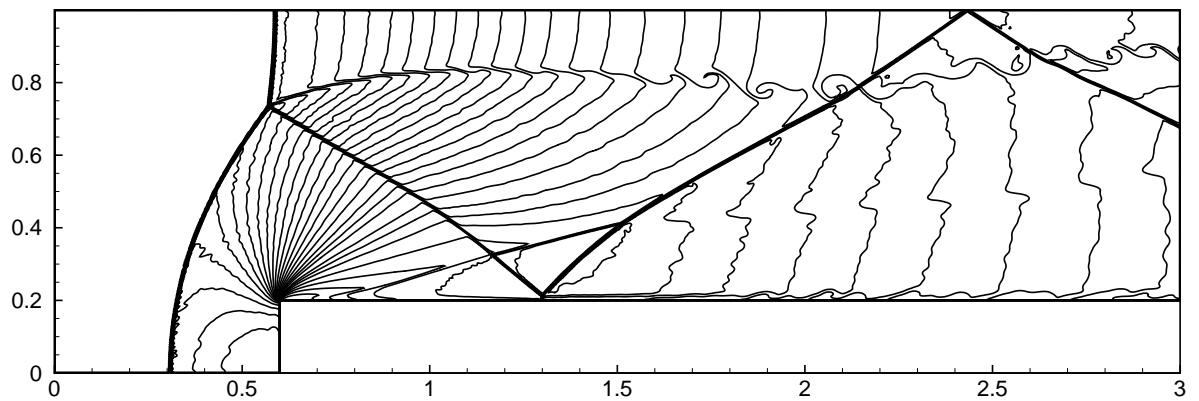


FIGURE 6.19: Same as Fig. 6.17, but with 1/320 triangular grid elements.

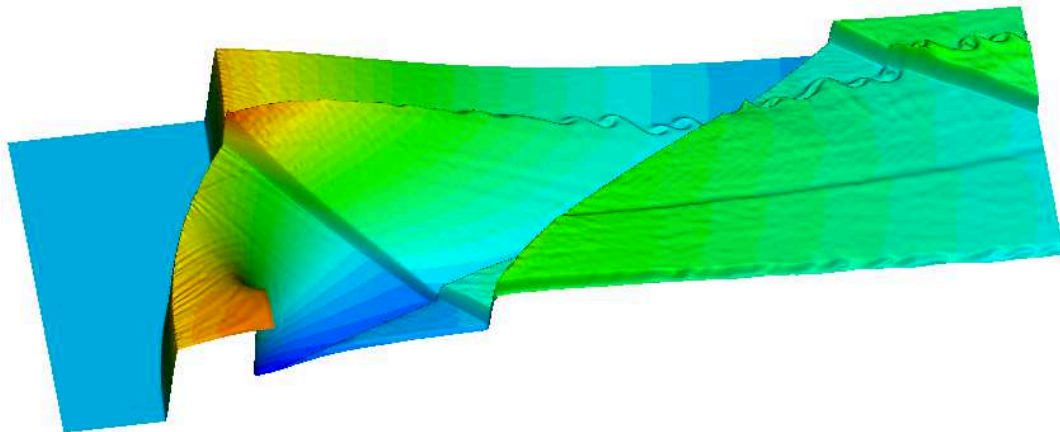


FIGURE 6.20: The bird's eye view of Fig. 6.19.

along the lower domain boundary are 1/120, 1/240 and 1/480 respectively. A right-moving Mach 10 shock is imposed with a 60 angles with respect to the x -axis. The numerical results of density contours at $t = 0.2$ calculated on grids of different resolutions are depicted in Figs. 6.22–6.24 respectively. We also plot in Fig. 6.25 the

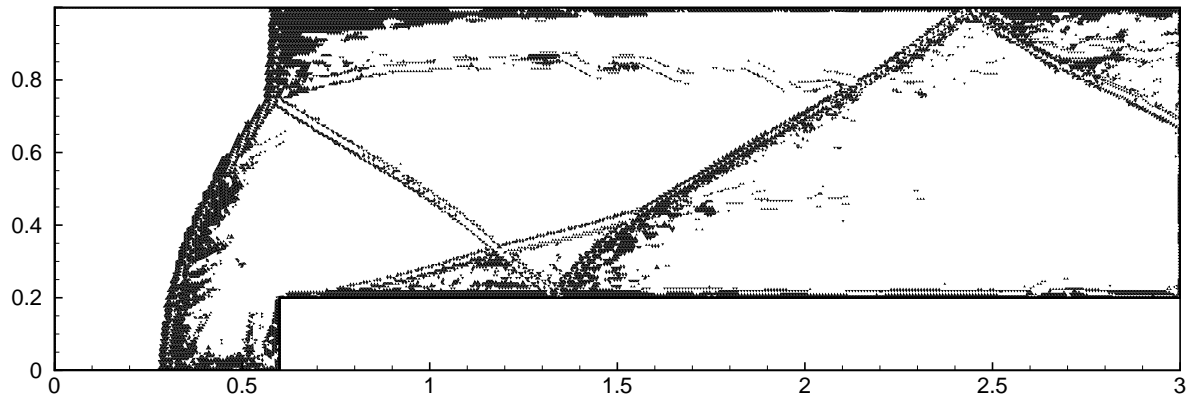


FIGURE 6.21: The cells marked by black color indicate the regions containing discontinuous solutions where the limiter comes into effect in the calculation of Fig.6.18.

enlarged view of the roll-up region. It is observed that the present scheme can capture the shock waves without noticeable numerical oscillations. More importantly, as the grid is refined, the vortical structures are resolved with richer small-scale details as the grid is refined to some extent. Our results are comparable to reference solutions of other high-resolution schemes, e.g. those given in [5].

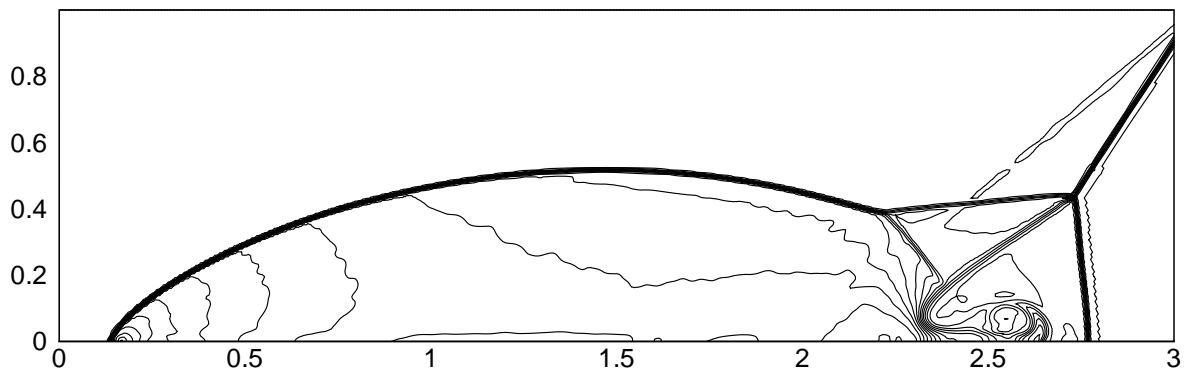


FIGURE 6.22: Density contours of the double Mach reflection test at $t = 0.2$ on the grid of triangular elements of $1/120$ resolutions.

Supersonic inflow passing through a scramjet engine

To verify the performance of present model in complicated geometry, we simulate the benchmark test of a supersonic inflow at Mach 3 passing through a scramjet engine for which the geometrical configuration as well as the computation conditions is described in [211]. The simulation was carried out on a unstructured mesh with 49816 triangular

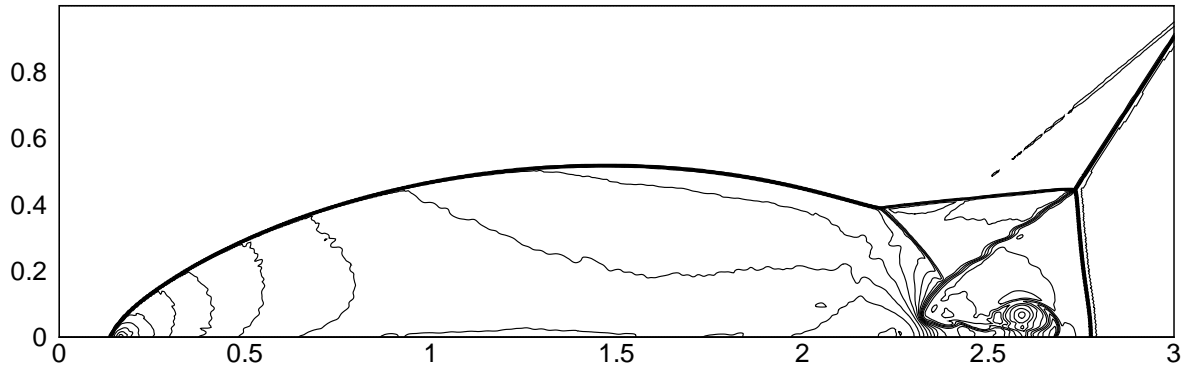


FIGURE 6.23: Same as Fig. 6.22, but on the grid of 1/240 resolution.

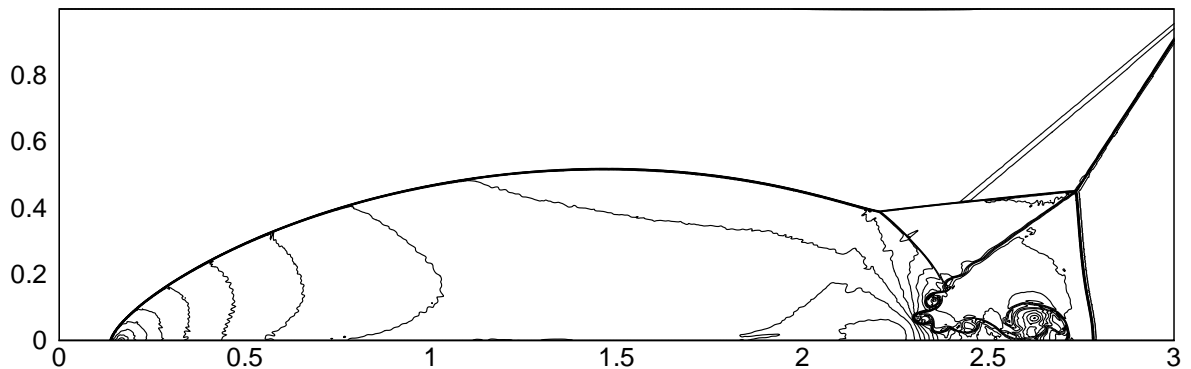


FIGURE 6.24: Same as Fig. 6.22, but on the grid of 1/480 resolution.

cells. A steady state was rapidly reached at the final time $t = 6.0$. The Mach number contours are displayed in Fig. 6.26, which shows the capability of the present model to capture shock waves in complex geometry and the flow structures are in good agreement with the results in [211].

Interaction of a shock wave with a wedge in two dimensions

In this test, we apply the present scheme to the interaction of a shock wave with a wedge. The corresponding experimental data are available in [212]. The computational domain of $[-2, 6] \times [-3, 3]$ is divided into 1.1 million triangular elements which are slightly less than that used in [5]. The initial condition is set according to the Rankine-Hugoniot relations for a shock of Mach 1.3. The image of density field at different time instants are presented in Fig. 6.27. The major features of this case characterized by the reflected shock waves and the vortices shed from the wedge have been sufficiently

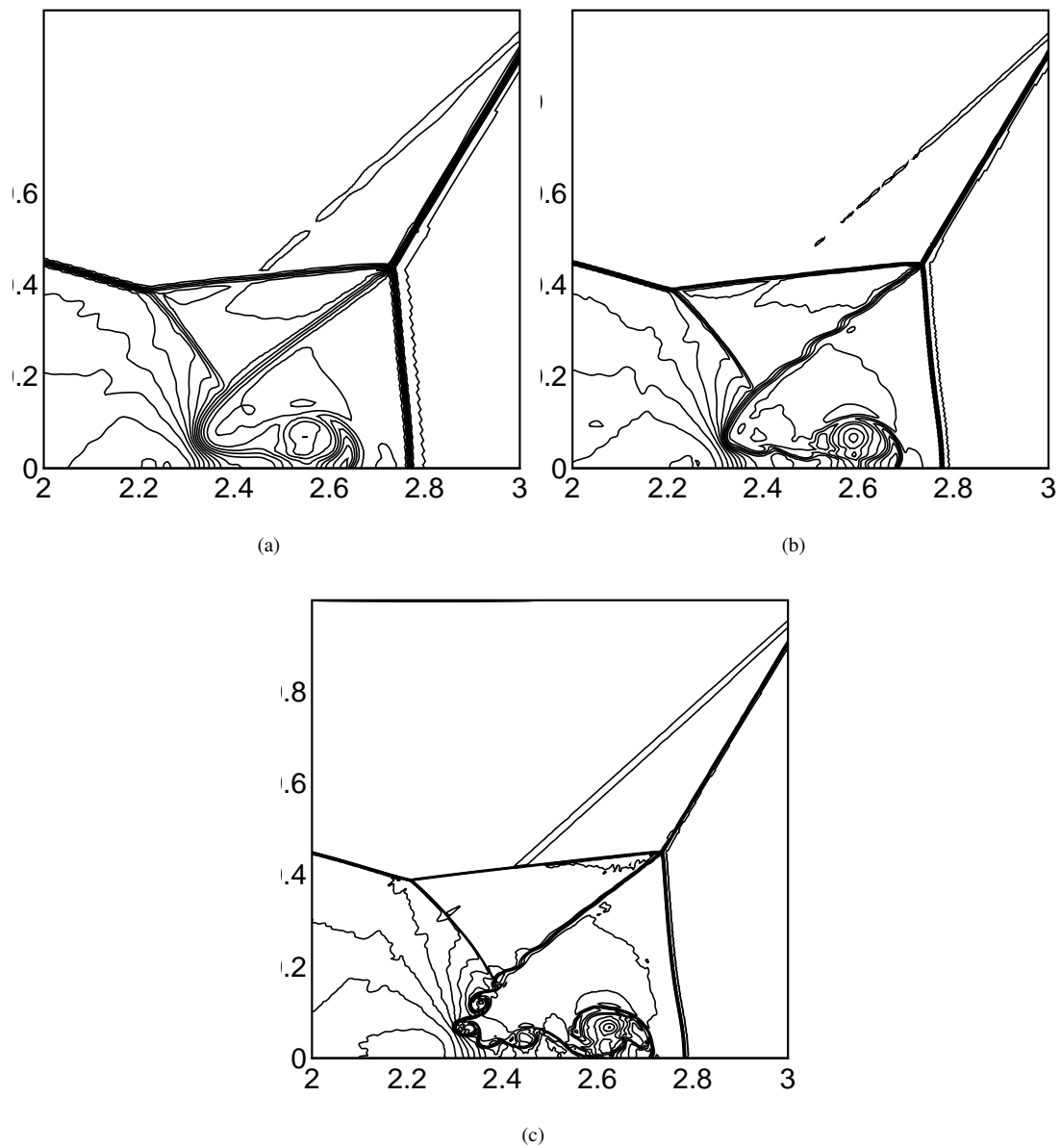


FIGURE 6.25: Closed-up view around the double Mach stem for triangular grids of 1/120(a), 1/240(b) and 1/480(c) resolutions respectively.

resolved with excellent agreement with both the experimental results [212] (Fig. 6.28) and the numerical solutions [5].

Flow past a circular Arc bump in a channel

In this test case, we investigated the simulation of subsonic, transonic and supersonic flows passing through a circular bump which is widely used to test the accuracy and robustness of numerical schemes to solve compressible flows of different Mach numbers[213,

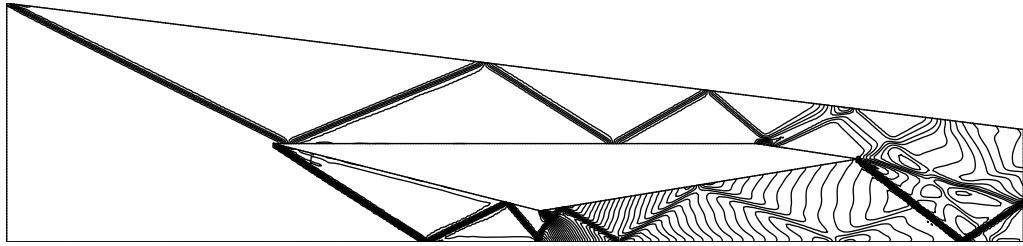


FIGURE 6.26: Mach number contours for supersonic inlet flow in a steady state on 49816 triangular grid elements.

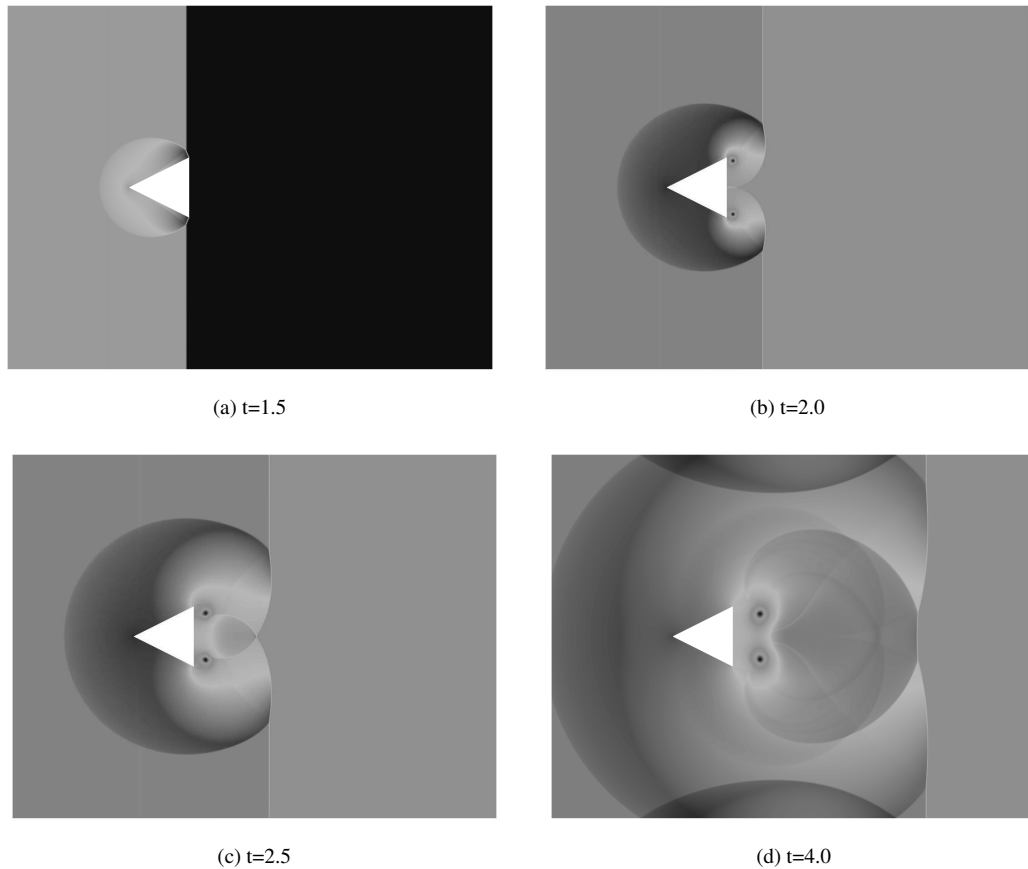


FIGURE 6.27: The images of density field of interaction of a shock wave with a wedge at different instants.

214]. The computational domain consists a channel with $3L$ in length and L in height where a circular arc of length L is placed at the central of the lower boundary. The thickness of bump is $0.1L$ for the subsonic and transonic flows, while $0.04L$ for the supersonic case. The computational domain is divided into 200×40 and 156×78 non-uniform quadrilateral elements respectively. We evaluate the solution quality by making comparison with the reference results in [215] which were obtained on a finer

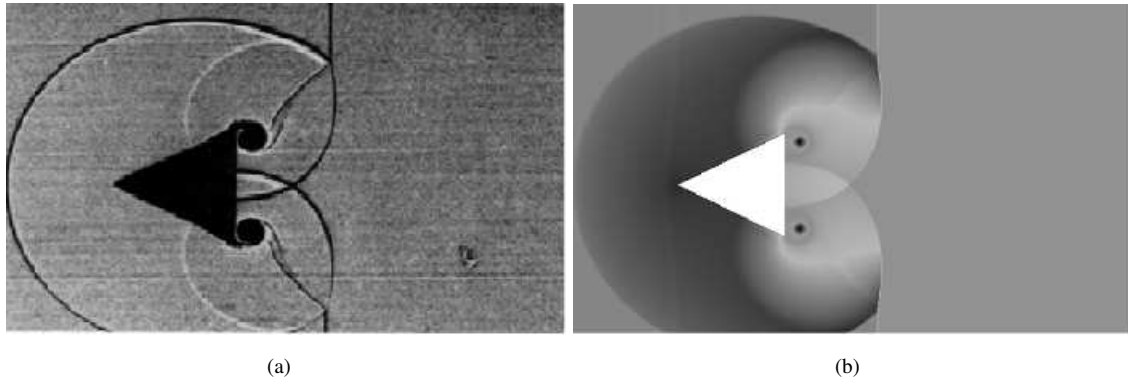


FIGURE 6.28: A comparison between the experimental result (a) and computational one (b) at $t=2.2$.

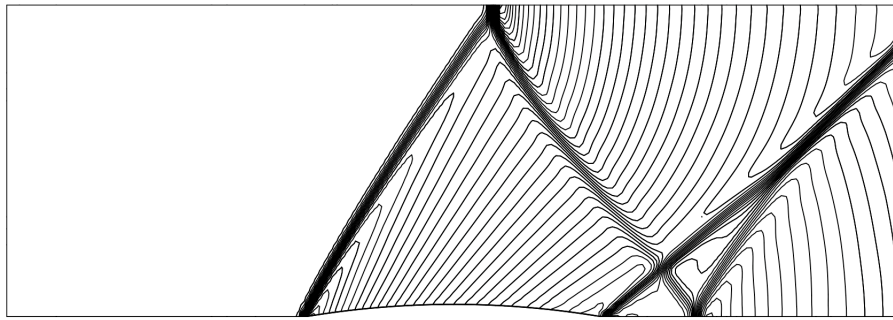
grid.

For the supersonic case, inlet Mach number is 1.4. Mach contours at steady state are shown in Fig. 6.29 where the intersection and reflection of shock waves are well resolved without unphysical oscillations. Fig. 6.29 also presents the quantitative comparison with the reference solution of Mach number distribution along the lower wall, which exhibits good agreement.

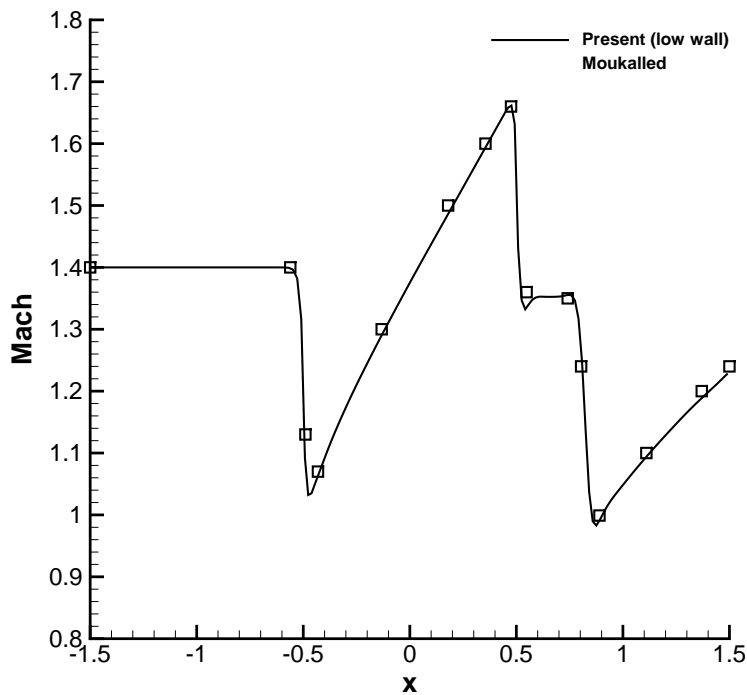
For a transonic regime, the flow at inlet remains subsonic with Mach number 0.675 and a shock wave is created around the top of bump due to the increase of velocity. In Fig. 6.30, Mach number contours as well as its distribution along the lower wall at steady state are presented. A comparison with the reference solution on a denser grid (252×54) is also included. The results show that our numerical model accurately captures transonic flow features and agrees well with previous studies.

With the same geometry and grid configuration of transonic case, we conduct the subsonic flow test with an inlet Mach number of 0.5. As a result, the inviscid flow in the channel should be subsonic and symmetric with respect to the throat cross-section. Shown in Fig. 6.31, symmetric distribution of the Mach number is reproduced by our numerical model which agrees well with the reference solution.

Low Mach explosion



(a)

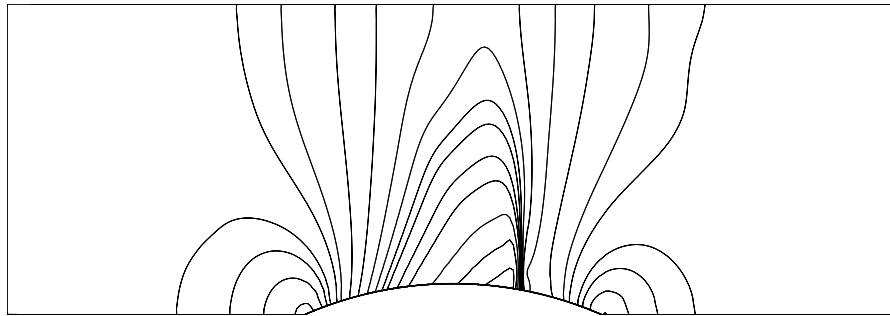


(b)

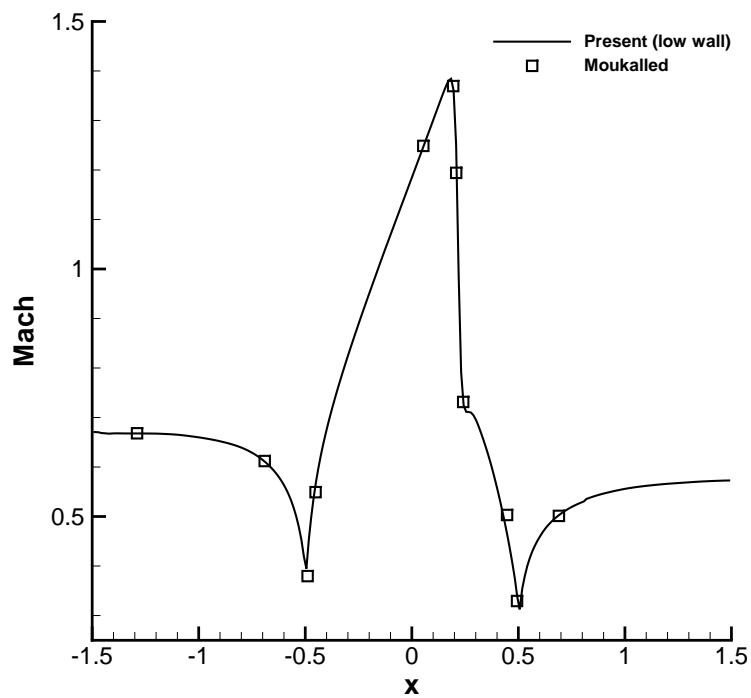
FIGURE 6.29: The Mach number contours for supersonic bump flow at steady state on 158×78 quadrilateral elements (a), and the plot of the Mach number along the lower wall in comparison with the results from [215] (b).

A two-dimensional axi-symmetric explosion was also simulated by present model to verify the calculation of low Mach number flows ($\text{Mach} < 0.01$) [216, 217]. The computational domain $[-1, 1] \times [-1, 1]$ is divided into 57670 triangular elements. The initial condition is defined by

$$(\rho, m_x, m_y, p) = \begin{cases} (10^{-3}, 0, 0, 10^4) & \text{for } r \leq 0.4 \\ (10^{-3}, 0, 0, 10^{-1}) & \text{for } r > 0.4 \end{cases}$$



(a)

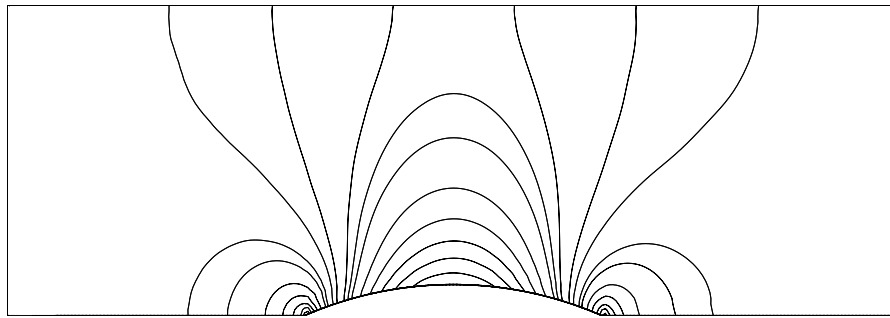


(b)

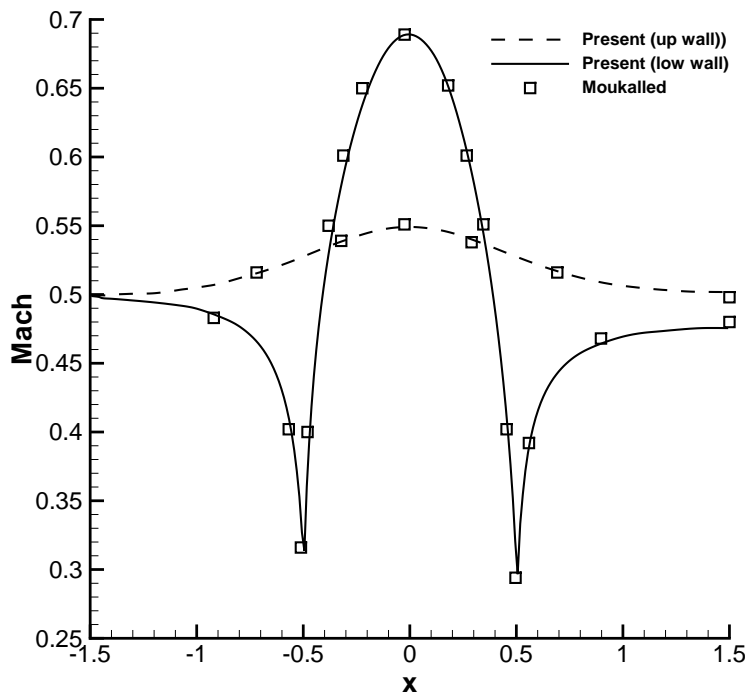
FIGURE 6.30: Same as Fig. 6.29, but for transonic flow regime.

where $r = \sqrt{x^2 + y^2}$ is the radius. As shown in Fig. 6.32 and 6.33, our scheme is of great robustness to work for low-speed flow and captures both discontinuous and smooth structures of axis-symmetrical distributions with good solution quality.

Two-dimensional viscous shock tube problem



(a)



(b)

FIGURE 6.31: Same as Fig. 6.29, but for subsonic flow regime.

The interaction between shock wave and boundary layer will be shown in this test case.

The initial condition is

$$(\rho, u, v, p) = \begin{cases} \left(120, 0, 0, \frac{120}{\gamma} \right) & \text{if } 0 \leq x \leq 0.5, \\ \left(1.2, 0, 0, \frac{1.2}{\gamma} \right) & \text{otherwise.} \end{cases} \quad (6.52)$$

From this initial condition, an incident shock wave and contact discontinuity will propagate from left to right causing a boundary layer along horizontal wall. After the shock wave reflects at the right wall, strong interaction between shock and boundary layer will

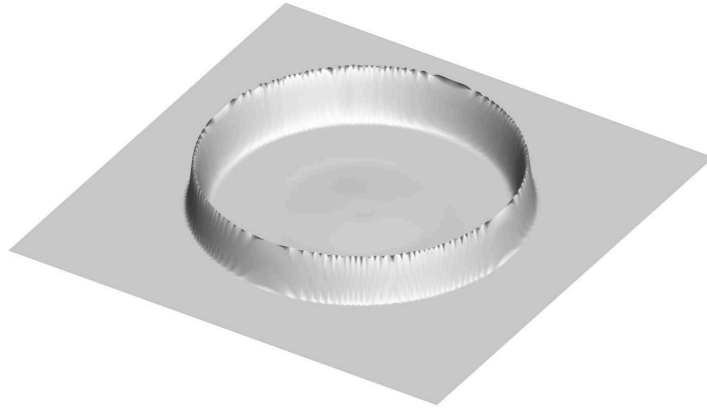


FIGURE 6.32: Bird's eye view of the density of the circular explosion test at $t = 0.00012$

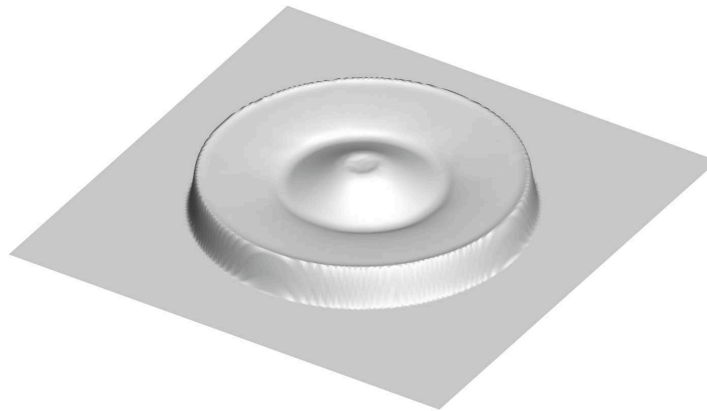


FIGURE 6.33: Same as Fig.6.32, but for pressure.

develop. The computation domain is $[0, 1] \times [0, 1]$. We assume that the viscosity is constant. The Reynolds number is 200 and the Prandtl number is 0.73. The viscous flux for PVs at cell center is discretized as in [218] while the TEC(Time-evolution Converting) formula [217] is applied to update viscous term for PVs at cell vertices. We conduct our computation on an unstructured grid of approximately three hundreds thousand triangular elements. The computational result is plotted in Fig.6.34. The height of the primary vortex is 0.168, which agrees well with the result in [219].

6.6.3 2D reacting Euler equations

Resolution studies for unstable oblique detonation waves

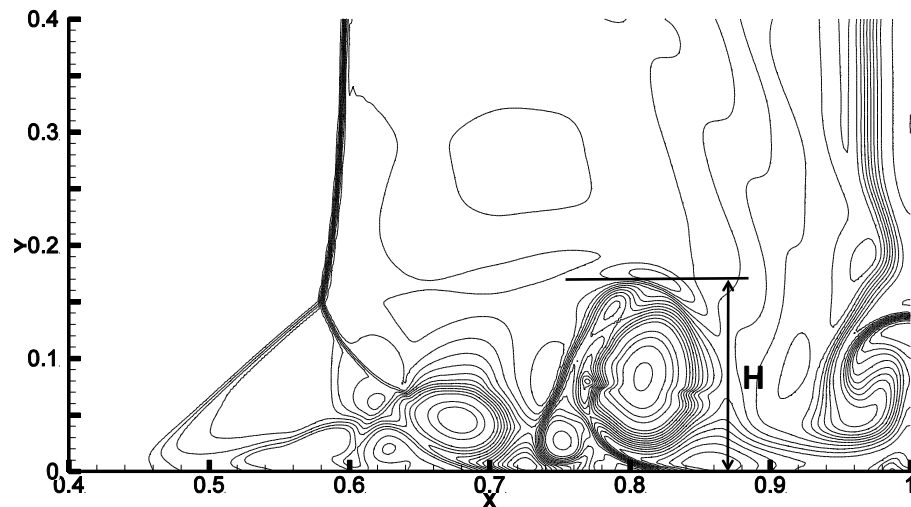


FIGURE 6.34: Density field of numerical solution to the interaction between a shock wave and boundary layer at $t = 1.0$.

To demonstrate the high resolution property of our numerical model, oblique detonation waves (ODWs) is studied in this case. As one of promising combustion ways for hypersonic propulsion, ODW has been studied numerically by a number of work [176–178]. However, as indicated in [178], the grids number to resolve the ODW front structures is stringent since excessive numerical diffusion will smooth out cell structures which can only be captured by extreme high grids density. For example, as reported in [176], insufficient resolution may lead to wrong estimation of the critical value defining the instability boundary of ODW. Here we apply our numerical model to simulate the case of which computation condition is the same as [177], where inflow Mach number is 12.0, activation energy $E_a = 31.0$, heat release $q = 50$ and wedge angle $\theta = 26^\circ$. To make a comparison between conventional finite volume method and current numerical model, we conduct the resolution study by using MLP and VPM-BVD respectively.

The results of resolution study by MLP scheme are presented in Fig. 6.35, where increasingly grids resolution 750×200 , 1500×400 and 1750×600 is applied. It can be seen obviously that low grids resolution can not resolve the cell structure since excessive numerical diffusion will smooth out the disturbance in shock front. In contrast to this, the results got from VPM-BVD produce cell structure even with low grids resolution

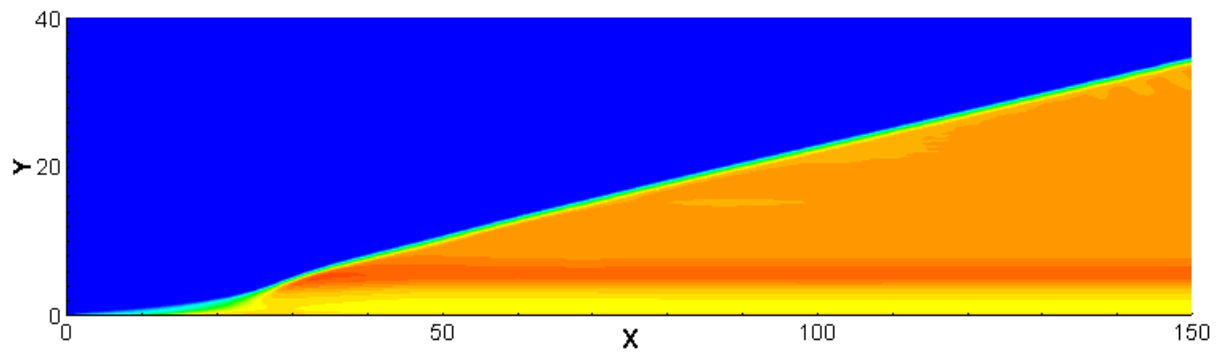
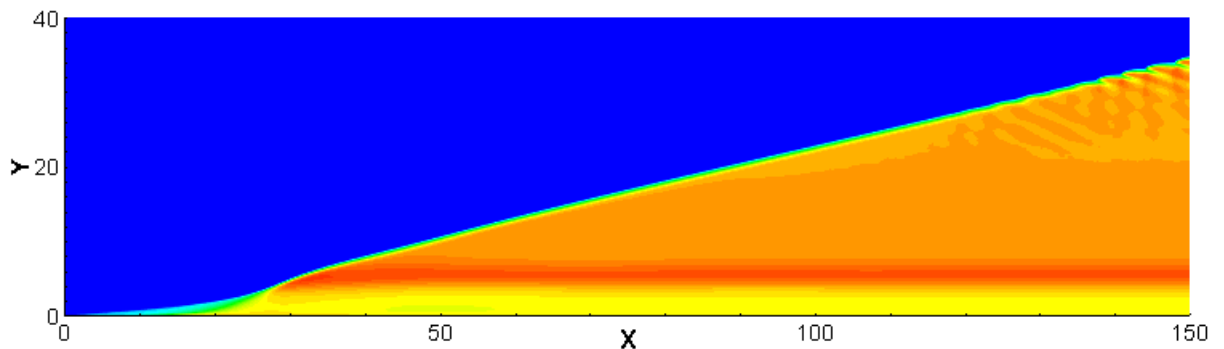
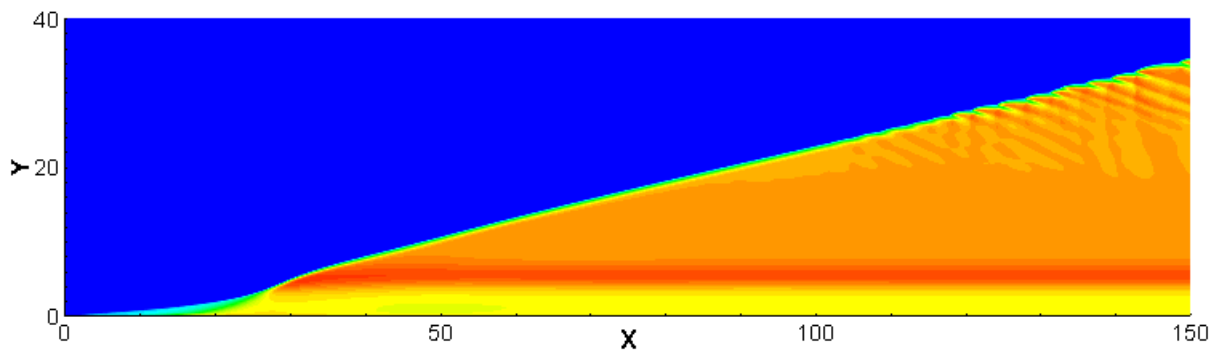
(a) Grids resolution with 750×200 . The number of DOF is 1.5×10^5 (b) Grids resolution with 1500×400 . The number of DOF is 6.0×10^5 (c) Grids resolution with 1750×600 . The number of DOF is 1.0×10^6

FIGURE 6.35: Temperature fields of unstable oblique detonation waves with the MLP scheme on different grids resolution

due to small numerical diffusion of VPM-BVD reported in [29]. The cell like structures resolved by high resolution scheme is reported in [178]. The proposed scheme resolves the typical cell like structures formed by slip surface and transverse wave.

Shock focusing detonation problem

To apply our numerical model to irregular boundaries, the shock focusing problem,

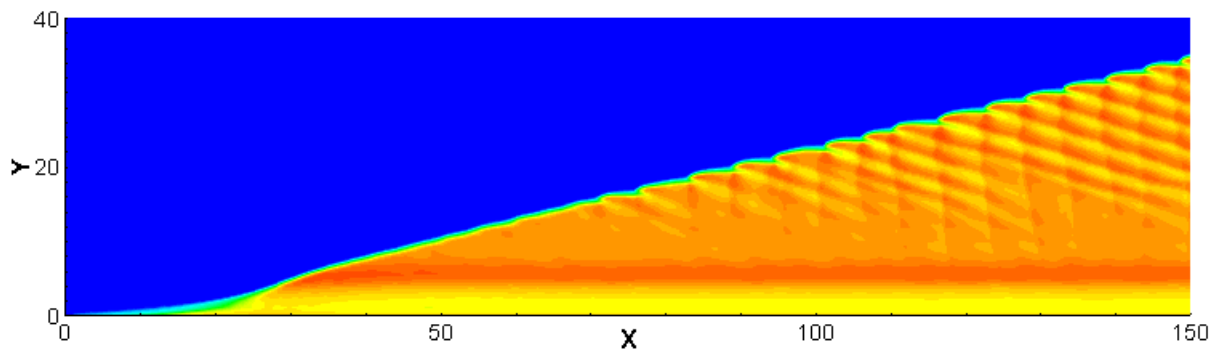
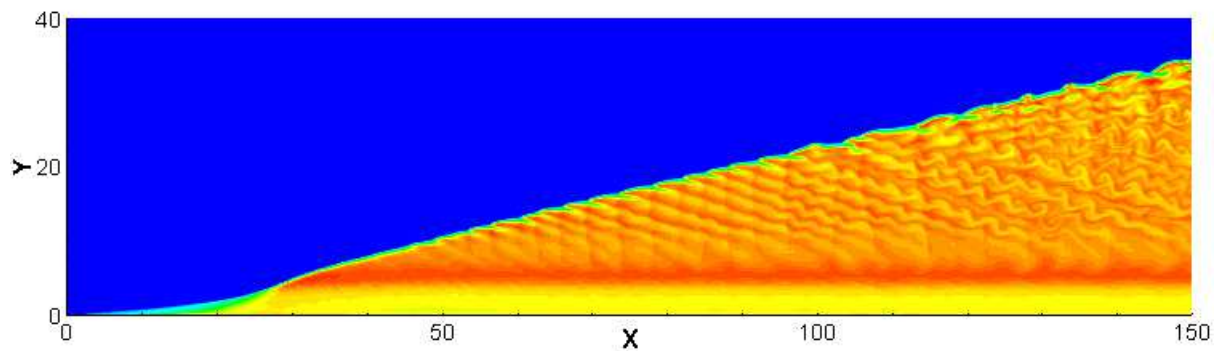
(a) Grids resolution with 750×200 . The number of DOF is 3.0×10^5 (b) Grids resolution with 1500×400 . The number of DOF is 9.0×10^5

FIGURE 6.36: The same as Fig.6.35 but with the high resolution scheme VPM-BVD

which has been studied experimentally and numerically in [179, 180], is considered here. The computation domain is the same as [169], where a parabola $y^2 = -2.7x$ is set as right boundary profile. Due to symmetry of this case, only half of domain is considered in our simulation and the symmetric boundary condition is used at $y = 0.0$. The activation energy $Ea = 20$ and $Q = 50$. We use triangular mesh here, of which size $h = 1/160$. A right moving shock is initially positioned. The high pressure and temperature local zones will form as incident shock entering the cavity of the domain, which will cause self-ignition. At certain conditions, detonation waves will form.

Here we consider two initial condition, $Ma = 2.2$ and $Ma = 2.5$ respectively. The results have been shown in Fig. 6.37 and Fig. 6.38. Our numerical model resolves main structures of combustion and get competitive results with published work [169].

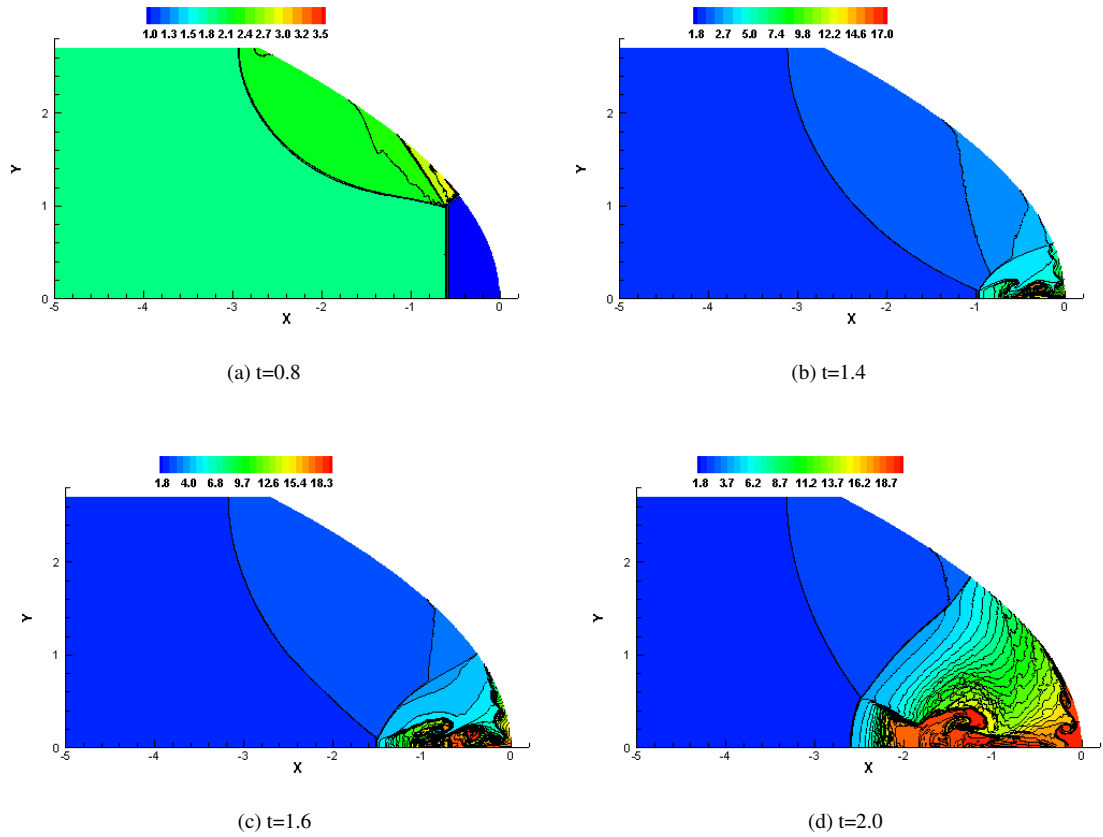


FIGURE 6.37: Temperature contours of the shock focusing problem with right-moving Mach 2.2 at different time

6.6.4 3D numerical experiments

3D explosion problem

A three-dimensional spherical explosion is computed within a cube of $[-1, -1, -1] \times [1, 1, 1]$, which can be viewed as the three dimensional version of the Sod shock problem. The initial conditions are set as follows,

$$(\rho, u, v, w, p) = \begin{cases} (1.0, 0, 0, 0, 1.0) & \text{if } r \leq 0.4 \\ (0.125, 0, 0, 0, 0.1) & \text{if } r > 0.4 \end{cases}$$

where $r = \sqrt{x^2 + y^2 + z^2}$ is the radius.

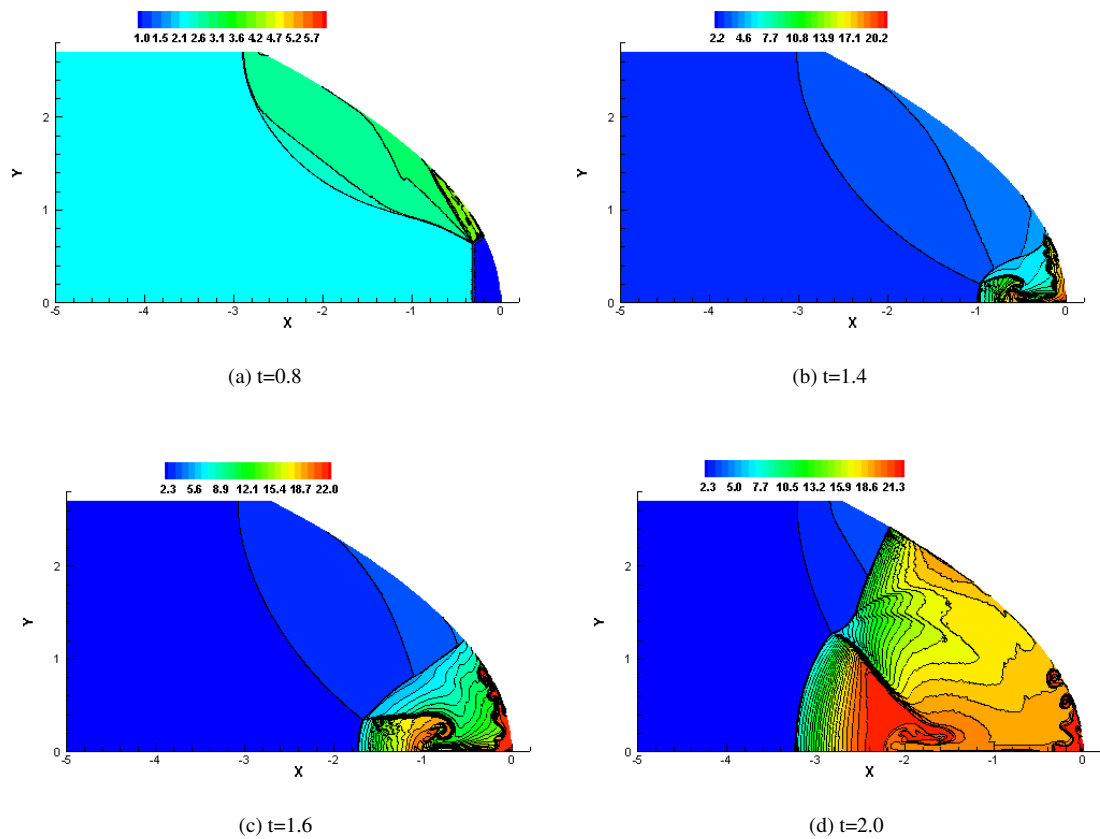


FIGURE 6.38: Temperature contours of the shock focusing problem with right-moving Mach 2.5 at different time

Two unstructured grids were used in this test. They are constructed separately with uniform prismatic and hexahedral elements with 80 partitions along each edge, which result in two grids of about 1.1 million and 5.1 hundred thousands total elements respectively. We show the 3D view density fields on two perpendicular cross-sections of the prismatic grid in Fig. 6.39. Although grid configurations for the two cross-sections are quite different, the distribution of the density field looks almost identical. It proves that our scheme has excellent robustness on different types of unstructured grids. In Fig. 6.40, we also plot the density profiles in the radial-direction computed separately on the prismatic and hexahedral grids in comparison with the reference solution from the one dimensional computation by assuming spherical symmetry [44]. It is seen that all the shock, contact discontinuity and expansion solutions are well resolved without numerical oscillations. A further comparison with the result from [45] which uses much

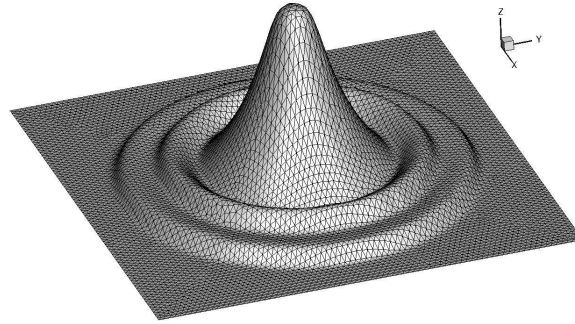


FIGURE 6.39: Numerical results for 3D explosion test on an unstructured grid of 1.1 million prismatic elements. Displayed are the 3D view of density field on two perpendicular cross-sections on the central $x - y$ plane (a) and the central $x - z$ plane.

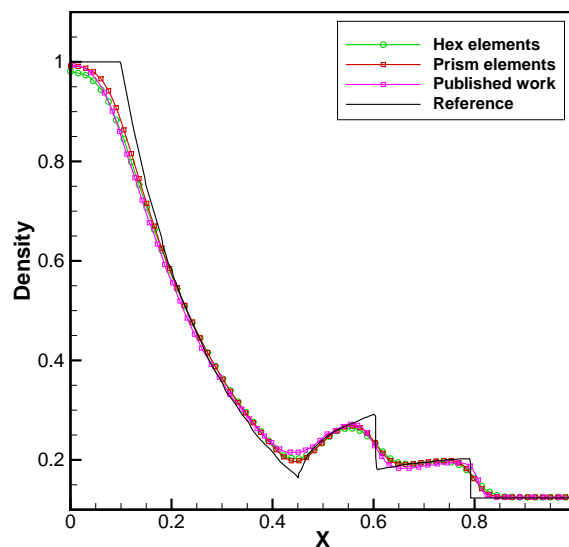


FIGURE 6.40: The density distribution along the radius direction of the results computed separately on the prismatic grid and the hexahedral grid. We also include the result from published work [45] which uses denser hexahedral grid of 400^3 .

denser hexahedral grid of 400^3 shows that our proposed numerical scheme can get competitive resolution with fewer grid elements.

3D interaction of a shock wave with a half cone

Being an example with complex geometrical configuration, in this test case we compute the shock wave passing a half-cone structure. The original setup of this test is detailed in [5] where the computational domain is partitioned with 9.3 million tetrahedrons. In the present study, we use a hybrid unstructured grid of much coarse resolution, which has 1.4 million hybrid elements including 959413 tetrahedral, 153576 hexahedral, 285620

prismatic and 4582 pyramidal elements. The hybrid grid of $1/8$ of the computational domain is displayed in Fig. 6.41, where part of the half-corner is adaptively refined with tetrahedral elements. The 3D view of density iso-surfaces at time of $t = 2.5$ are displayed in Fig. 6.42. It reveals that our 3D model is able to adequately reproduce the reflected waves and the torus-shaped vortex shedding behind the half cone, which is axisymmetric and agrees well with results in [5, 46].

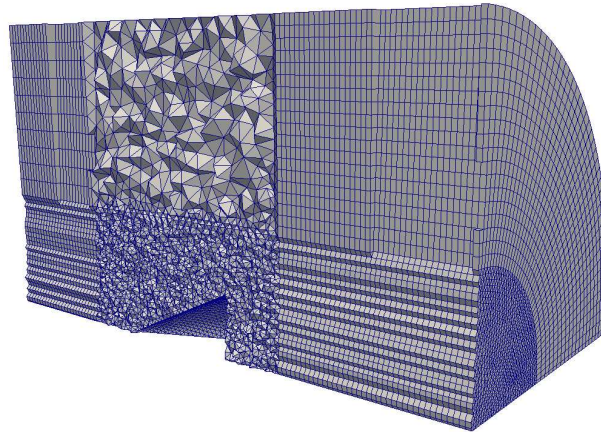


FIGURE 6.41: A view of the hybrid unstructured grid used for the computation of the shock-cone interaction test.

Transonic flow past an ONERA M6 wing

In this example, a transonic flow over the ONERA M6 wing with $Ma_\infty = 0.84$ and angle of attack $\alpha = 3.06^\circ$ was computed. The airfoil has a 10% maximum-thickness / chord ratio cross-section. The mesh in this test is composed of 341797 tetrahedral elements.

The pressure contours on the upper wing surface is shown in Fig. 6.43. In Fig. 6.44, the computed pressure coefficient at four span-wise stations is compared with experimental data [47] and the published work [16], where the DG based on Hierarchical WENO (HWENO) scheme is employed. We can see that the present model can reproduce numerical solution with good accuracy. The results are competitive to the solutions computed by the DG schemes in [16, 19], while from Fig. 6.44 the DG scheme may produce overshoot around critical points. The pressure coefficients are in close agreement with experimental data except near the root stations due to the absence of physical viscosity.

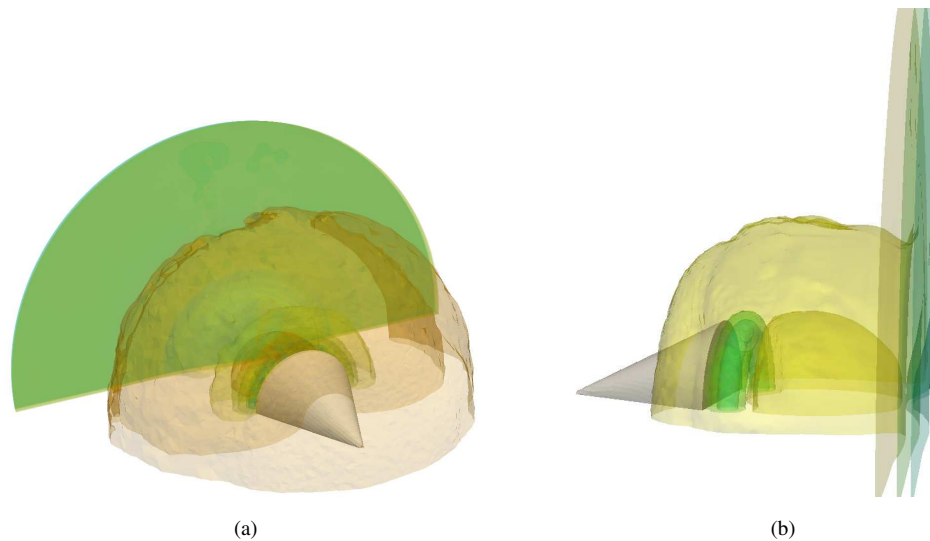


FIGURE 6.42: Density contour surfaces views from different angles. (a): front view where the refracted shock waves can be clearly seen, and (b): a zoomed side view where the vortex half ring shedded behind the half cone is well resolved.

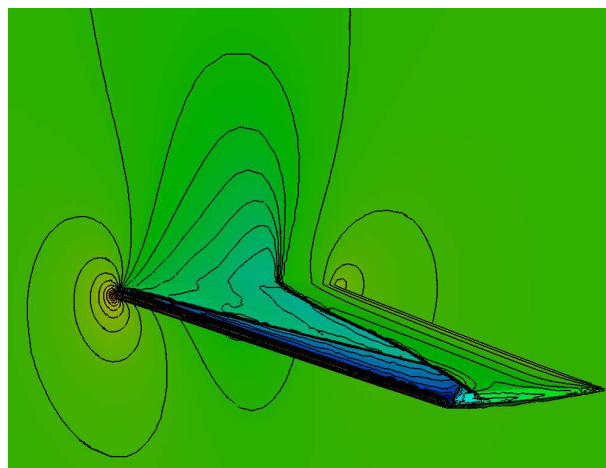


FIGURE 6.43: Pressure contours over the upper wing surface for the transonic flow passing ONERA M6 wing.

Transonic flow past RAE A wing and body

In this last test case, we simulate the transonic flow past a RAE 2822 wing and body with $Ma = 0.9$ and attack angle 3.06° . The geometry and experimental data have been reported in [48]. The background pressure and temperature are $p_\infty = 29765 Pa$ and $T_\infty = 275.38 K$ respectively. The computational grid consists of 459487 tetrahedral elements. The pressure distribution on the wing and body is depicted in Fig. 6.45(a). The pressure coefficient along the body surface on the center cross-section is shown

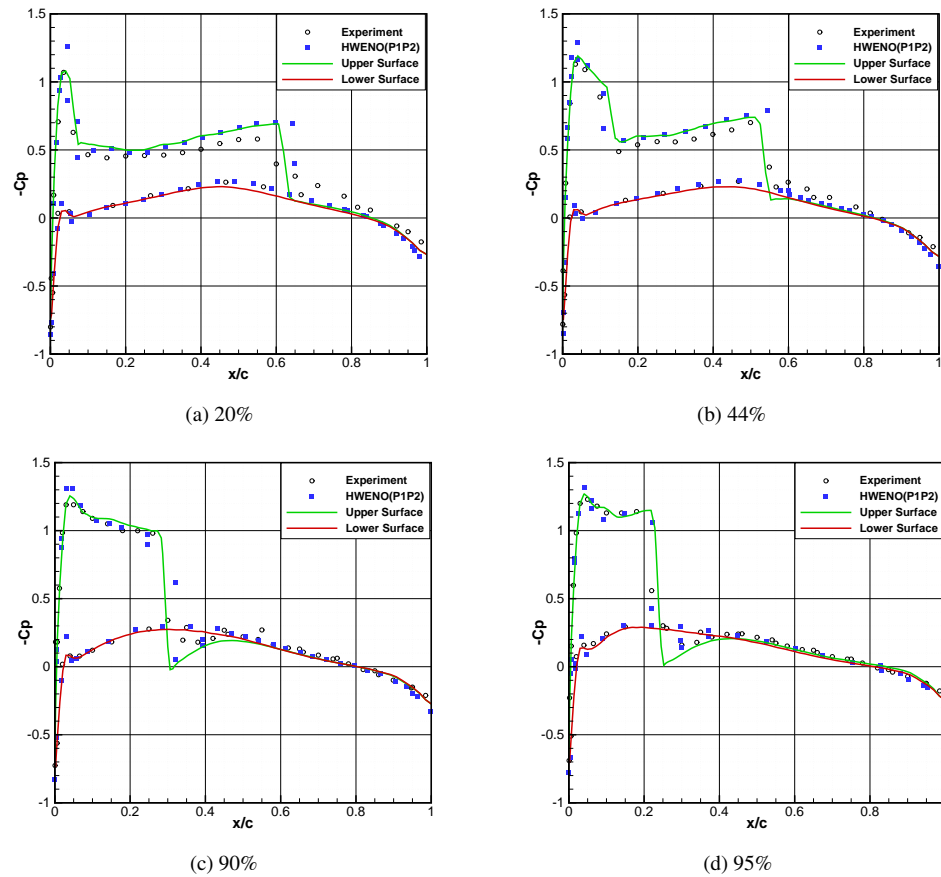


FIGURE 6.44: Comparison of computed pressure coefficient with experimental data and the DG scheme at different semi-span locations denoted by the percentage of the distance from the root to the tip. The results calculated by proposed scheme are shown in green and red lines

in Fig. 6.45(b) against the experiment data. The pressure coefficient is plot along two cutting lines on the fuselage with angular position of 15° and -15° , respectively, relative to the horizontal direction. The result shows very good agreement with experiment data.

6.7 Summary

We have developed an accurate and robust numerical solver for Euler equations on unstructured grids. The present solver has the following three major constituents.

(1) A multi-moment finite volume formulation, MCV/VPM, is used to construct accurate and efficient solver for compressible flows. In the present MCV scheme, we

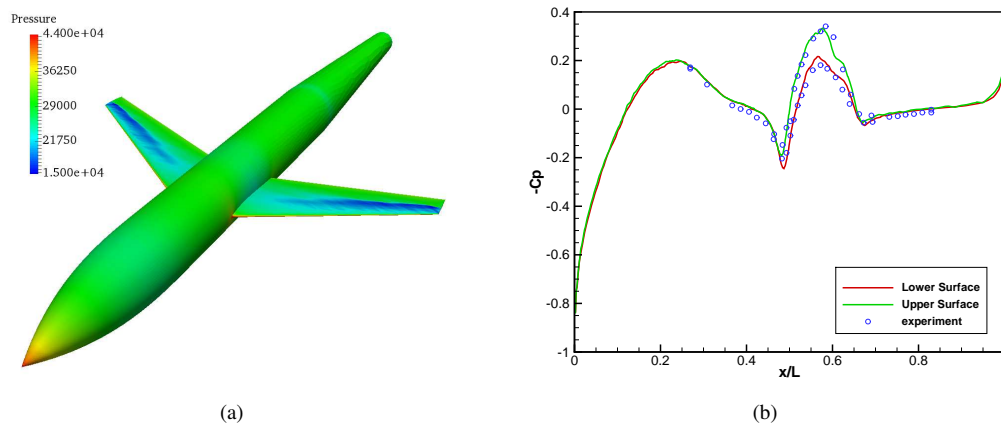


FIGURE 6.45: Numerical results for the transonic flow past RAE 2822 wing and body. (a) Pressure contour on the upper surface of wings and body. (b) Pressure coefficients along upper and lower surfaces of the body.

treat the point values (PVs) at both cell center and cell vertices as the computational variable. We update the centroid PV via a finite volume formulation that ensures the rigorous conservation, and update the PVs at cell vertices using the differential form of the governing equations for computational efficiency.

(2) Different Riemann solvers are used to separately update the point values at centroid and vertices, i.e. the SLAU scheme, a variant of AUSM splitting, is used to update the centroid PV, the Roe's scheme is used for the PVs at vertices. The resultant solver with preconditioner works well for all Mach numbers with robustness.

(3) In order to suppress numerical oscillation and facilitate the MCV reconstruction to compressible flows involving strong discontinuities, MLP limiting projection has been adopted to the cells containing discontinuities which are identified by a criterion based on the jumps (variations) of the reconstructed fields at the cell boundaries. Moreover, the BVD reconstruction has been introduced to control the numerical dissipation of the scheme so as to resolve both smooth and non-smooth solutions with high fidelity. The resultant reconstruction, VPM/MCV-MLP-BVD reconstruction, has been verified to be of 3rd-order accuracy and robust on unstructured grids.

The present solver has been evaluated extensively with various benchmark tests for both

scalar and Euler conservation laws on different unstructured grids, which verified the accuracy, robustness and applicability in simulations with complex geometric configurations.

Showing numerical results with appealing solution quality, the present solver is algorithmically simple and easy to implement. As another advantage for applications on unstructured grids, the present formulation requires compact stencil for spatial discretization that only involves the target cell and its immediate neighbors.

The present solver can be straightforwardly extended to three-dimensions for hybrid unstructured grids. As showcased in the numerical test, the solver can simulate not only inviscid flows but also viscous flows with adequate accuracy, which reveals the great potential and practical significance for real-case applications.

Chapter 7

Conclusions and future work

In this study, I firstly propose several effective variants of BVD algorithm, which serve as new guidelines for reconstruction processes. Different from previous BVD formulation, the proposed versions are simple and effective, which can be extended to unstructured grids directly. The successful implementation of BVD algorithm is verified through combining high order polynomial with non-polynomial based reconstruction function. The proposed scheme can achieve high order accuracy as well as solve sharp discontinuities.

Then, based on proposed BVD algorithm, we construct two practical schemes named MUSCL-THINC-BVD scheme and adaptive THINC-BVD scheme which is a novel limiting-free discontinuity capturing scheme. Different from long-lasting reconstruction processes which employ high order polynomials enforced with some carefully designed limiting projections to seek stable solutions around discontinuities, the current schemes employ low order polynomial or non-polynomial THINC function with adaptive sharpness to solve both smooth and discontinuous solutions. The present methods are able to capture both smooth and discontinuous solutions in Euler equations for compressible gas dynamics with excellent solution quality competitive to other existing schemes. More profoundly, they provide accurate and reliable solvers for a class of

reactive compressible gas flows with stiff source terms, such as the gaseous detonation waves, which are quite challenging to other high-resolution schemes.

Thirdly, the newly proposed schemes are applied to compressible interfacial two phase flow. The present method is able to capture the material interface as a well-defined sharp jump in volume fraction, and obtain numerical solutions of superior quality in comparison to other existing methods. Moreover, the BVD algorithm can realize the consistency among volume fraction and other physical variables, which is not straightforward for other interface capturing schemes.

In order to achieve high order accuracy, we also propose new methods in multi-moment finite volume method to solve compressible flows. We construct new forth-order accuracy schemes with compact stencils. To prevent numerical oscillations caused by high order interpolation, we design a new limiting process based on variation diminishing principle. The designed limiting process can effectively suppress numerical oscillations without decreasing accuracy.

Then we extend our schemes to unstructured grids to solve more practical problems involving complex geometries. Third order accuracy scheme is realized with multi-moment framework, which prevent large stencils in conventional finite volume method. In order to suppress numerical oscillations and reduce numerical dissipations, BVD algorithm is devised on unstructured grids. The proposed schemes are extended to three dimensional problems which are not easy for high order conventional finite volume method.

7.1 Major contributions of present study

The significances of present study are summarized as follows

1. Capturing discontinuity solution in compressible multi-components flow is a long lasting issue for numerical schemes. Most existing numerical schemes either suffer from excessive numerical dissipation or numerical oscillations. The excessive numerical dissipation will smear out fine flow structures and even lead to wrong numerical solutions. The numerical oscillation will influence the robustness of method. The present study solve this problem by devising new schemes based on BVD principle. We get superior results even without relying on high order polynomials. Thus for those problems involving strong discontinuities, our scheme can serve as an efficient tool for numerical simulations due to its simplicity, accuracy and robustness. The present work also indicates that it is not necessary to employ polynomials for reconstruction process. Under the guideline of BVD principle, non-polynomial can be used to minimize numerical dissipation. Thus we find a new way to design more efficient and accurate schemes which are different from conventional methods.

2. To construct high order schemes on unstructured grids is not an easy work. Conventional finite volume method requires large stencils which especially pose difficulties for three dimensional problems. For local high reconstruction schemes, to design limiting processes is more difficult than on structured grids. The present work solve this issue by proposing a practical framework with multi-moment finite volume method. The method can achieve third order accuracy with compact stencils which are using the immediate neighbours of target cells. Also, to design limiting process is straightforward since we introduce first derivative at the cell center. By adding slope limiter, the scheme can effectively suppress numerical oscillations. More importantly, we firstly propose BVD algorithm on unstructured grids. The propose scheme show one of best results within existing numerical schemes.

3. During last decades, several efforts have been made to solve the stiff detonation problems and moving interface compressible flows. These are famous but also extreme difficult issues. The existing methods to solve these issues usually add complexity, which make these methods not practical for engineering applications. The current study

constructs a straight way to solve these problems. With the BVD algorithm, we reduce numerical dissipation fundamentally from numerical schemes. Thus extra assumptions are not needed. Although the designed schemes are simpler than others, the proposed schemes have much better performance, which makes them attractive to be used in numerical simulations.

7.2 Future work

It has to be admitted that there are still many issues in numerical schemes which have not yet be solved or have much space to be improved. In my future work, it's my plan to make following contributions.

1. Higher order shock capturing schemes should be constructed to investigate shock-turbulence interaction. The difficulties of shock turbulence interaction are from the fact that numerical scheme should not only solve discontinuous solution but also resolve wide spectral waves due to turbulence. However, existing spatial discretized schemes have difficulties in obtaining accurate and stable solutions when dealing with high speed turbulence flows especially when involving strong heat release. The co-existence of discontinuities and turbulent features brings challenges to so-called high resolution schemes. Although these schemes achieve high accuracy in smooth regions, they generally suffer from stability or accuracy issues across discontinuities. Our goal is to construct a scheme which is low-dissipative for turbulence flow but is also able to capture sharp discontinuous solutions. A new strategy will be devised to compromise the paradox that central schemes are preferable to calculate non-dissipative flux while upwind-biased flux is demanded to account for hyperbolic system in high speed flow.
2. Numerical model should be able to simulate more complex phenomenon in compressible multi-components flow. For example, phase change such as evaporation, cavitation and boiling should be included. These phenomenon are common in high speed

compressible multiphase flows and play an important role in engineering. The current numerical model is too simple to describe these phenomenon. Thus to simulate practical application problems, advanced model should be constructed with extra terms in control equation to account for phase change. The developed scheme will be expected to be couple with the numerical model to simulate phase change phenomenon.

3. Shock capturing schemes on unstructured grids should be further explored. Although the developed schemes have already achieved certain success, their performance somehow rely on parameters when solving compressible multiphases flows. A simpler and parameter-free numerical scheme on unstructured is preferable for practical simulations. Another issue is how to control numerical oscillations, which is a difficult issue for unstructured grids. For compressible multiphase flow, oscillation-free property is indispensable to guarantee successful computation. Thus in our future work, I will extend the limiter-free schemes to unstructured grids, which will be expected to be an efficient way to control numerical oscillations. With this technique to control numerical oscillations, high order extension can be expected.

Bibliography

- [1] Hollis, B.R. and Borrelli, S., 2012. Aerothermodynamics of blunt body entry vehicles. *Progress in Aerospace Sciences*, 48, pp.42-56.
- [2] Jiang, G.S. and Shu, C.W., 1996. Efficient implementation of Weighted ENO Schemes. *Journal of Computational Physics*, 126(1), pp.202-228.
- [3] Friedrich, O., 1998. Weighted essentially non-oscillatory schemes for the interpolation of mean values on unstructured grids. *Journal of Computational Physics*, 144(1), pp.194-212.
- [4] Hu, C. and Shu, C.W., 1999. Weighted essentially non-oscillatory schemes on triangular meshes. *Journal of Computational Physics*, 150(1), pp.97-127.
- [5] Dumbser, M., Käser, M., Titarev, V.A. and Toro, E.F., 2007. Quadrature-free non-oscillatory finite volume schemes on unstructured meshes for nonlinear hyperbolic systems. *Journal of Computational Physics*, 226(1), pp.204-243.
- [6] Tsoutsanis, P., Titarev, V.A. and Drikakis, D., 2011. WENO schemes on arbitrary mixed-element unstructured meshes in three space dimensions. *Journal of Computational Physics*, 230(4), pp.1585-1601.
- [7] Wang, Q., Ren, Y.X. and Li, W., 2016. Compact high order finite volume method on unstructured grids I: Basic formulations and one-dimensional schemes. *Journal of Computational Physics*, 314, pp.863-882.

- [8] Wang, Q., Ren, Y.X. and Li, W., 2016. Compact high order finite volume method on unstructured grids II: Extension to two-dimensional Euler equations. *Journal of Computational Physics*, 314, pp.883-908.
- [9] Cockburn, B., Hou, S. and Shu, C.W., 1990. The Runge-Kutta local projection discontinuous Galerkin finite element method for conservation laws. IV. The multidimensional case. *Mathematics of Computation*, 54(190), pp.545-581.
- [10] Bassi, F. and Rebay, S., 1997. High-order accurate discontinuous finite element solution of the 2D Euler equations. *Journal of Computational Physics*, 138(2), pp.251-285.
- [11] Bassi, F. and Rebay, S., 1997. A high-order accurate discontinuous finite element method for the numerical solution of the compressible Navier-Stokes equations. *Journal of Computational physics*, 131(2), pp.267-279.
- [12] Godunov, Sergei Konstantinovich. A difference method for numerical calculation of discontinuous solutions of the equations of hydrodynamics. *Matematicheskii Sbornik* 89, no. 3 (1959), pp.271-306.
- [13] Davis, S. F. Simplified second-order Godunov-type methods. *SIAM Journal on Scientific and Statistical Computing* 9.3 (1988), pp.445-473.
- [14] Zhang, L., Liu, W., He, L.X., Deng, X.G., Zhang, H.X., 2012. A class of hybrid DG/FV methods for conservation laws I: Basic formulation and one-dimensional systems. *Journal of Computational Physics*, 231(4), pp.1081-1103.
- [15] Zhang, L., Liu, W., He, L.X., Deng, X.G., Zhang, H.X., 2012. A class of hybrid DG/FV methods for conservation laws II: Two-dimensional cases. *Journal of Computational Physics*, 231(4), pp.1104-1120.
- [16] Luo, H., Xia, Y., Spiegel, S., Nourgaliev, R. and Jiang, Z., 2013. A reconstructed discontinuous Galerkin method based on a hierarchical WENO reconstruction for

- compressible flows on tetrahedral grids. *Journal of Computational Physics*, 236, pp.477-492.
- [17] Huynh, H.T., 2007. A flux reconstruction approach to high-order schemes including discontinuous Galerkin methods. AIAA paper, 4079, p.2007.
- [18] Wang, Z.J. and Gao, H., 2009. A unifying lifting collocation penalty formulation including the discontinuous Galerkin, spectral volume/difference methods for conservation laws on mixed grids. *Journal of Computational Physics*, 228(21), pp.8161-8186.
- [19] Luo, H., Baum, J.D. and Löhner, R., 2007. A Hermite WENO-based limiter for discontinuous Galerkin method on unstructured grids. *Journal of Computational Physics*, 225(1), pp.686-713.
- [20] Zhu, J., Zhong, X., Shu, C.W. and Qiu, J., 2013. Runge-Kutta discontinuous Galerkin method using a new type of WENO limiters on unstructured meshes. *Journal of Computational Physics*, 248, pp.200-220.
- [21] Persson, P.O. and Peraire, J., 2006. Sub-cell shock capturing for discontinuous Galerkin methods. AIAA paper, 112, p.2006.
- [22] Xie, B., Ii, S., Ikebata, A. and Xiao, F., 2014. A multi-moment finite volume method for incompressible Navier-Stokes equations on unstructured grids: Volume-average/point-value formulation. *Journal of Computational Physics*, 277, pp.138-162.
- [23] Xie, B. and Xiao, F., 2014. Two and three dimensional multi-moment finite volume solver for incompressible Navier-Stokes equations on unstructured grids with arbitrary quadrilateral and hexahedral elements. *Computers & Fluids*, 104, pp.40-54.

- [24] Xie, B. and Xiao, F., 2016. A robust PISO algorithm on hybrid unstructured grids for incompressible flow by using multi-moment finite volume method, *Numer. Heat Transfer B*, <http://dx.doi.org/10.1080/10407790.2016.1265325>.
- [25] Van Leer, B., 1977. Towards the ultimate conservative difference scheme. IV. A new approach to numerical convection. *Journal of Computational Physics*, 23(3), pp.276-299.
- [26] Yabe, T., Tanaka, R., Nakamura, T. and Xiao, F., 2001. An exactly conservative semi-Lagrangian scheme (CIP-CSL) in one dimension. *Monthly Weather Review*, 129(2), pp.332-344.
- [27] Eymann, T.A. Active flux schemes, PH.D. thesis, University of Michigan, 2013.
- [28] Xie, B. and Xiao, F., 2016. A multi-moment constrained finite volume method on arbitrary unstructured grids for incompressible flows. *Journal of Computational Physics*, 327, pp.747-778.
- [29] Xie, B., Deng, X., SUN, Z.Y., and Xiao, F., A hybrid pressure-density-based Mach uniform algorithm for Euler equation on unstructured grids by using multi-moment finite volume method, *Journal of Computational Physics*, (in press).
- [30] Deng, X., Xie, B., and Xiao, F., A multi-moment finite volume solver for Euler equations on unstructured grids, *AIAA Journal*
- [31] Shu, C.W. and Osher, S., 1988. Efficient implementation of essentially non-oscillatory shock-capturing schemes. *Journal of Computational Physics*, 77(2), pp.439-471.
- [32] Rohde, A., 2001. Eigenvalues and eigenvectors of the Euler equations in general geometries. *AIAA paper*, 2609, p.2001.
- [33] Li, W., Ren, Y.X., Lei, G. and Luo, H., 2011. The multi-dimensional limiters for solving hyperbolic conservation laws on unstructured grids. *Journal of Computational Physics*, 230(21), pp.7775-7795.

- [34] Park, J.S., Yoon, S.H. and Kim, C., 2010. Multi-dimensional limiting process for hyperbolic conservation laws on unstructured grids. *Journal of Computational Physics*, 229(3), pp.788-812.
- [35] Ivan, L. and Groth, C.P., 2014. High-order solution-adaptive central essentially non-oscillatory (CENO) method for viscous flows. *Journal of Computational Physics*, 257, pp.830-862.
- [36] Sun, Z., Inaba, S. and Xiao, F., 2016. Boundary Variation Diminishing (BVD) reconstruction: a new approach to improve Godunov scheme. *Journal of Computational Physics*, 322, pp.309-325.
- [37] Ii, S., Xie, B. and Xiao, F., 2014. An interface capturing method with a continuous function: The THINC method on unstructured triangular and tetrahedral meshes. *Journal of Computational Physics*, 259, pp.260-269.
- [38] Xie, B., Ii, S. and Xiao, F., 2014. An efficient and accurate algebraic interface capturing method for unstructured grids in 2 and 3 dimensions: The THINC method with quadratic surface representation. *International Journal for Numerical Methods in Fluids*, 76(12), pp.1025-1042.
- [39] Van Leer, B., 1979. Towards the ultimate conservative difference scheme. V. A second-order sequel to Godunov's method. *Journal of Computational Physics*, 32(1), pp.101-136.
- [40] <http://openfoam.org/>
- [41] Nakamura, T., Tanaka, R., Yabe, T. and Takizawa, K., 2001. Exactly conservative semi-Lagrangian scheme for multi-dimensional hyperbolic equations with directional splitting technique. *Journal of Computational Physics*, 174(1), pp.171-207.
- [42] Woodward, P. and Colella, P., 1984. The numerical simulation of two-dimensional fluid flow with strong shocks. *Journal of Computational Physics*, 54(1), pp.115-173.

- [43] Le Touze, C., Murrone, A. and Guillard, H., 2015. Multislope MUSCL method for general unstructured meshes. *Journal of Computational Physics*, 284, pp.389-418.
- [44] Toro, E.F. *Riemann Solvers and Numerical Methods for Fluid Dynamics*, second edition, Springer, 1999.
- [45] Toro, E.F., Castro, C.E. and Lee, B.J., 2015. A novel numerical flux for the 3D Euler equations with general equation of state. *Journal of Computational Physics*, 303, pp.80-94.
- [46] Diot, S., Loubere, R. and Clain, S., 2013. The Multidimensional Optimal Order Detection method in the three-dimensional case: very high-order finite volume method for hyperbolic systems. *International Journal for Numerical Methods in Fluids*, 73(4), pp.362-392.
- [47] Schmitt, V. and Charpin, F., Pressure distributions on the ONERA-M6-wing at transonic Mach numbers, experimental data for computer programme assessment. Report of the Fluid Dynamic Panel Working group, 4.
- [48] Cook, P.H., Firmin, M.C.P. and McDonald, M.A., 1977. Aerofoil RAE 2822: pressure distributions, and boundary layer and wake measurements. RAE.
- [49] Abgrall, R., Shu, C.W. (ed.). *Handbook of Numerical Methods for Hyperbolic Problems: Basic and Fundamental Issues*, Elsevier, 2016.
- [50] Borges, R., Monique C., Bruno C., and Wai S.D. An improved weighted essentially non-oscillatory scheme for hyperbolic conservation laws. *Journal of Computational Physics* 227.6 (2008), pp.3191-3211.
- [51] Xi, D., Bin X. and Feng X. A finite volume multi-moment method with boundary variation diminishing principle for Euler equation on three-dimensional hybrid unstructured grids. *Computers & Fluids*, 153.10 (2017), pp.85-101.

- [52] Liu, X.D., S. Osher and T.F. Chan. Weighted essentially non-oscillatory schemes. *Journal of computational physics* 115(1994), pp.200-212.
- [53] Marquina, A. Local Piecewise Hyperbolic Reconstruction of Numerical Fluxes for Nonlinear Scalar Conservation Laws . *SIAM Journal on Scientific Computing* 15.4 (1994), pp.892-915.
- [54] Xiao, F., Xindong P. A convexity preserving scheme for conservative advection transport. *Journal of Computational Physics* 198.2(2004), pp.389-402.
- [55] Artebrant, R. and H. Joachim Schroll, Limiter-Free Third Order Logarithmic Reconstruction. *SIAM Journal on Scientific Computing* 28.1 (2006), pp. 359-381.
- [56] Xiao, F., Y. Honma, and T. Kono. A simple algebraic interface capturing scheme using hyperbolic tangent function. *International Journal for Numerical Methods in Fluids* 48.9 (2005), pp. 1023-1040.
- [57] Xiao, F., Satoshi I., and Chungang C. Revisit to the THINC scheme: a simple algebraic VOF algorithm. *Journal of Computational Physics* 230.19 (2011), pp. 7086-7092.
- [58] Schulz-Rinne, C.W. Classification of the Riemann problem for two-dimensional gas dynamics, *SIAM J. Math. Anal* 24 (1993), pp.76-88.
- [59] Ma., B., The richtmyer-meshkov instability, *Annu. Rev. Fluid Mech.* 34 (2002), pp. 445-468.
- [60] Henrick, A.K., T.D. Aslam, J.M. Powers, Mapped weighted essentially non-oscillatory schemes: achieving optimal order near critical points, *J. Comput. Phys.* 207 (2005), pp. 542-567.
- [61] Ha, Y., Kim,C.H. Y.J. Lee, J. Yoon, An improved weighted essentially non-oscillatory scheme with a new smoothness indicator, *J. Comput. Phys.* 232 (2013), pp. 68-86.

- [62] Fan, P., Shen, Y., B. Tian, C. Yang, A new smoothness indicator for improving the weighted essentially non-oscillatory scheme, *J. Comput. Phys.* 269 (2014), pp. 329-354.
- [63] Acker, F., R. Borges, B. Costa, An improved WENO-Z scheme, *J. Comput. Phys.* 313 (2016), pp. 726-753.
- [64] Hu, X.Y., Q. Wang, N.A. Adams, An adaptive central-upwind weighted essentially non-oscillatory scheme, *J. Comput. Phys.* 229 (2010), pp. 8952-8965.
- [65] Shen, Y., G. Zha, Improvement of weighted essentially non-oscillatory schemes near discontinuities, *Comput. Fluids* 96 (2014), pp. 1-9.
- [66] Shukla, R.K., C. Pantano, J.B. Freund, An interface capturing method for the simulation of multi-phase compressible flows, *J. Comput. Phys.* 229 (2010), pp. 7411-7439.
- [67] Gerolymos, G.A., D. Sénéchal, I. Vallet, Very-high-order WENO schemes, *J. Comput. Phys.* 228 (2009), pp. 8481-8524.
- [68] Wang, W., C.W. Shu, H.C. Yee, B. Sjögren, High order finite difference methods with subcell resolution for advection equations with stiff source terms, *J. Comput. Phys.* 231 (2012), pp. 190-214.
- [69] Yee, H.C., D.V. Kotov, W. Wang, C.W. Shu, Spurious behavior of shock-capturing methods by the fractional step approach: Problems containing stiff source terms and discontinuities, *J. Comput. Phys.* 241 (2013), pp. 266-291.
- [70] Ketcheson, D.I., M. Parsani, R.J. LeVeque, High-order wave propagation algorithms for hyperbolic systems, *SIAM J. Sci. Comput.* 35 (2013), pp. A351-A377.
- [71] LeVeque, R.J., Wave propagation algorithms for multidimensional hyperbolic systems, *J. Comput. Phys.* 131 (1997), pp. 327-353.

- [72] Toro, E.F. *Riemann solvers and numerical methods for fluid dynamics: a practical introduction*, Springer Science & Business Media, 2013.
- [73] Gottlieb, S., C.W. Shu, E. Tadmor, Strong stability-preserving high-order time discretization methods, *SIAM Rev.* 43 (2001), pp. 89-112.
- [74] Pirozzoli, S. On the spectral properties of shock-capturing schemes, *J. Comput. Phys.* 219 (2006), pp. 489-497.
- [75] Hirsch, C. *Numerical computation of internal and external flows: The fundamentals of computational fluid dynamics*, Butterworth-Heinemann (2007).
- [76] Sod, G.A. A survey of several finite difference methods for systems of nonlinear hyperbolic conservation laws, *J. Comput. Phys.* 27 (1978), pp. 1-31.
- [77] Maire, P.H., R. Loubère, P. Vachal, Staggered Lagrangian discretization based on cell-centered Riemann solver and associated hydro-dynamics scheme, *Comput. Phys. Commun.* 10 (2011), pp. 940-978.
- [78] Zhang, X., C.W. Shu, Positivity-preserving high order finite difference WENO schemes for compressible Euler equations, *J. Comput. Phys.* 231 (2012), pp. 2245-2258.
- [79] Hu, X.Y., N.A. Adams, C.W. Shu, Positivity-preserving method for high-order conservative schemes solving compressible Euler equations, *J. Comput. Phys.* 242 (2013), pp. 169-180.
- [80] Bao, W., S. Jin, The random projection method for hyperbolic conservation laws with stiff reaction terms, *J. Comput. Phys.* 163 (2000), pp. 216-248.
- [81] Tosatto, L., L. Vigeveno, Numerical solution of under-resolved detonations, *J. Comput. Phys.* 227 (2008), pp. 2317-2343.
- [82] Chorin, A.J., Random choice methods with applications to reacting gas flow, *J. Comput. Phys.* 25 (1977), pp. 253-272.

- [83] Courant, R., K.O. Friedrichs, *Supersonic flow and shock waves*, Springer Science & Business Media, 1999.
- [84] Bao, W., S. Jin, The random projection method for stiff detonation capturing, *SIAM J. Sci. Comput.* 23 (2001), pp. 1000-1026.
- [85] Kurganov, A., E. Tadmor, Solution of two-dimensional Riemann problems for gas dynamics without Riemann problem solvers, *Numer. Methods Partial Differential Equations* 18 (2002), pp. 584-608.
- [86] Dumbser, M., O. Zanotti, R. Loubère, S. Diot, A posteriori subcell limiting of the discontinuous Galerkin finite element method for hyperbolic conservation laws, *J. Comput. Phys.* 278 (2014), pp. 47-75.
- [87] Ha, Y., C.H. Kim, Y.J. Lee, J. Yoon, An improved weighted essentially non-oscillatory scheme with a new smoothness indicator, *J. Comput. Phys.* 232 (2013), pp. 68-86.
- [88] Buchmüller, P., C. Helzel, Improved accuracy of high-order WENO finite volume methods on Cartesian grids, *J. Sci. Comput.* 61 (2014), pp. 343-368.
- [89] Abedian, R., H. Adibi, M. Dehghan, A high-order symmetrical weighted hybrid ENO-flux limiter scheme for hyperbolic conservation laws, *Comput. Phys. Comm.* 185 (2014), pp. 106-127.
- [90] Jung, C.Y., T.B. Nguyen, Fine structures for the solutions of the two-dimensional Riemann problems by high-order WENO schemes, *Adv. Comput. Math.* (2017), pp. 1-28.
- [91] Fu, L., X.Y. Hu, N.A. Adams, A family of high-order targeted ENO schemes for compressible-fluid simulations, *J. Comput. Phys.* 305 (2016), pp. 333-359.
- [92] Strehlow, R.A., Nature of transverse waves in detonations, *Astronaut. Acta* 14 (1969), pp. 539.

- [93] Diot, S., R. Loubère, S. Clain, The MOOD method in the three-dimensional case: Very-High-Order Finite Volume Method for Hyperbolic Systems, *Int. J. Numer. Methods Fluids* 73 (2013), pp. 362-392.
- [94] Tryggvason, G., R.Scardovelli, S.Zaleski, *Direct numerical simulations of gas-liquid multiphase flows*, Cambridge University Press, 2011.
- [95] Brouillette, M. The Richtmyer-Meshkov instability, *Annual Review of Fluid Mechanics* 34 (2002), pp. 445-468.
- [96] Hirt, C.W., B.D.Nichols, Volume of fluid (VOF) method for the dynamics of free boundaries, *Journal of computational physics* 39 (1981), pp. 201-225.
- [97] Gueyffier, D., J.Li, A.Nadim, R.Scardovelli, S.Zaleski, Volume-of-fluid interface tracking with smoothed surface stress methods for three-dimensional flows, *Journal of Computational physics* 152 (1999), pp. 423-456.
- [98] Scardovelli, R., S.Zaleski, Direct numerical simulation of free-surface and interfacial flow, *Annual review of fluid mechanics* 31 (1999), pp. 567-603.
- [99] Osher, S., J.A.Sethian, Fronts propagating with curvature-dependent speed: algorithms based on Hamilton-Jacobi formulations, *Journal of computational physics* 79 (1988), pp. 12-49.
- [100] Osher, M., P.Smereka, S.Osher, A level set approach for computing solutions to incompressible two-phase flow, *Journal of Computational physics* 114 (1994), pp. 146-159.
- [101] Sethian, J.A. *Level set methods and fast marching methods: evolving interfaces in computational geometry, fluid mechanics, computer vision, and materials science*. Vol. 3. Cambridge university press, 1999.
- [102] Yabe, T., F.Xiao, Description of complex and sharp interface during shock wave interaction with liquid drop, *Journal of the Physical Society of Japan* 62 (1993), pp. 2537-2540.

- [103] Xiao, F., T.Yabe, A method to trace sharp interface of two fluids in calculations involving shocks, *Shock Waves* 4 (1994), pp. 101-107.
- [104] Yabe, T., F.Xiao, T.Utsumi, The constrained interpolation profile method for multiphase analysis, *Journal of Computational physics* 169 (2001), pp. 556-593.
- [105] Larrouturou, B., How to preserve the mass fractions positivity when computing compressible multi-component flows, *Journal of Computational Physics* 95 (1991), pp. 59-84.
- [106] Karni, S., Multicomponent flow calculations by a consistent primitive algorithm, *Journal of Computational Physics* 112 (1994), pp. 31-43.
- [107] Abgrall, R., How to prevent pressure oscillations in multicomponent flow calculations: a quasi conservative approach, *Journal of Computational Physics* 125 (1996), pp. 150-160.
- [108] Saurel, R., R.Abgrall, A multiphase Godunov method for compressible multi-fluid and multiphase flows, *Journal of Computational Physics* 150 (1999), pp. 425-467.
- [109] Shyue, K.M., An efficient shock-capturing algorithm for compressible multicomponent problems, *Journal of Computational Physics* 142 (1998), pp. 208-242.
- [110] Saurel, R., R.Abgrall, A multiphase Godunov method for compressible multi-fluid and multiphase flows, *Journal of Computational Physics* 150 (1999), pp. 425-467.
- [111] Abgrall, R., S.Karni, Computations of compressible multifluids, *Journal of computational physics* 169 (2001), pp. 594-623.
- [112] Shyue, K.M., A fluid-mixture type algorithm for compressible multicomponent flow with van der Waals equation of state, *Journal of Computational Physics* 156 (1999), pp. 43-88.

- [113] Shyue, K.M., A fluid-mixture type algorithm for compressible multicomponent flow with Mie-Grüneisen equation of state, *Journal of Computational Physics* 171 (2001), pp. 678-707.
- [114] Allaire, G., S.Clerc, S.Kokh, A five-equation model for the simulation of interfaces between compressible fluids, *Journal of Computational Physics* 181 (2002), pp. 577-616.
- [115] Saurel, R., C. Pantano, Diffuse-interface capturing methods for compressible two-phase flows, *Annual Review of Fluid Mechanics* 50 (2018), pp. 105-130.
- [116] Coralic, V., T.Colonius, Finite-volume WENO scheme for viscous compressible multicomponent flows, *Journal of computational physics* 274 (2014), pp. 95-121.
- [117] Johnsen, E., T.Colonius, Implementation of WENO schemes in compressible multicomponent flow problems, *Journal of Computational Physics* 219 (2006), pp. 715-732.
- [118] He, Z., B.Tian, Y.Zhang, F.Gao, Characteristic-based and interface-sharpening algorithm for high-order simulations of immiscible compressible multi-material flows, *Journal of Computational Physics* 333 (2017), pp. 247-268.
- [119] He, Z., Y.Zhang, F.Gao, X.Li, B.Tian, An improved accurate monotonicity-preserving scheme for the Euler equations, *Computers & Fluids* 140 (2016), pp. 1-10.
- [120] Luo, H., J.D.Baum, R.Löner, On the computation of multi-material flows using ALE formulation, *Journal of Computational Physics* 194 (2004), pp. 304-328.
- [121] Daude, F., P.Galon, Z.Gao, E. Blaud, Numerical experiments using a HLLC-type scheme with ALE formulation for compressible two-phase flows five-equation models with phase transition, *Computers & Fluids* 94 (2014), pp. 112-138.

- [122] Ball, G.J., B.P.Howell, T.G.Leighton, M.J.Schofield, Shock-induced collapse of a cylindrical air cavity in water: a free-Lagrange simulation, *Shock Waves* 10 (2000), pp. 265-276.
- [123] Terashima, H., G.Tryggvason, A front-tracking/ghost-fluid method for fluid interfaces in compressible flows, *Journal of Computational Physics* 228 (2009), pp. 4012-4037.
- [124] Hu, X.Y., B.C.Khoo, An interface interaction method for compressible multifluids, *Journal of Computational Physics* 198 (2004), pp. 35-64.
- [125] Hu, X.Y., B.C.Khoo, N.A.Adams, F.L.Huang, A conservative interface method for compressible flows, *Journal of Computational Physics* 219 (2006), pp. 553-578.
- [126] Liu, T.G., B.C.Khoo, C.W.Wang, The ghost fluid method for compressible gas-water simulation, *Journal of Computational Physics* 204 (2005), pp. 193-221.
- [127] Nourgaliev, R.R., T.G.Theofanous, High-fidelity interface tracking in compressible flows: Unlimited anchored adaptive level set, *Journal of Computational Physics* 224 (2007), pp. 836-866.
- [128] Garrick, D.P., M.Owkes, J.D. Regele, A finite-volume HLLC-based scheme for compressible interfacial flows with surface tension, *Journal of Computational Physics* 339 (2017), pp. 46-67.
- [129] Shukla, R.K., Nonlinear preconditioning for efficient and accurate interface capturing in simulation of multicomponent compressible flows, *Journal of Computational Physics* 276 (2014), pp. 508-540.
- [130] Kokh, S., F.Lagoutiere, An anti-diffusive numerical scheme for the simulation of interfaces between compressible fluids by means of a five-equation model, *Journal of Computational Physics* 229 (2010), pp. 2773-2809.

- [131] So, K.K., X.Y.Hu, N.A.Adams, Anti-diffusion interface sharpening technique for two-phase compressible flow simulations, *Journal of Computational Physics* 231 (2012), pp. 4304-4323.
- [132] Shyue, K.M., F. Xiao, An Eulerian interface sharpening algorithm for compressible two-phase flow: The algebraic THINC approach, *Journal of Computational Physics* 268 (2014), pp. 326-354.
- [133] Tiwari, A., J.B.Freund, C.Pantano, A diffuse interface model with immiscibility preservation, *Journal of computational physics* 252 (2013), pp. 290-309.
- [134] Marsh, S.P., *LASL shock Hugoniot data*, Vol. 5. Univ of California Press, 1980.
- [135] LeVeque, R.J., Wave propagation algorithms for multidimensional hyperbolic systems, *Journal of Computational Physics* 131 (1997), pp. 327-353.
- [136] LeVeque, R.J., *Finite volume methods for hyperbolic problems*, Vol. 31. Cambridge university press, 2002.
- [137] Pilliod, J.E., E.G.Puckett, Second-order accurate volume-of-fluid algorithms for tracking material interfaces, *Journal of Computational Physics* 199 (2004), pp. 465-502.
- [138] Johnsen, E., On the treatment of contact discontinuities using WENO schemes, *Journal of Computational Physics* 230 (2012), pp. 8665-8668.
- [139] Johnsen, E., F. Ham, Preventing numerical errors generated by interface-capturing schemes in compressible multi-material flows, *Journal of Computational Physics* 231 (2012), pp. 5705-5717.
- [140] Saurel, R., R.Abgrall, A multiphase Godunov method for compressible multi-fluid and multiphase flows, *Journal of Computational Physics* 150 (1999), pp. 425-467.

- [141] Liu, T.G., B.C.Khoo, K.S.Yeo, Ghost fluid method for strong shock impacting on material interface, *Journal of Computational Physics* 190 (2003), pp. 651-681.
- [142] Marquina, A., P.Mulet, A flux-split algorithm applied to conservative models for multicomponent compressible flows, *Journal of Computational Physics* 185 (2003), pp. 120-138.
- [143] Shyue, K.M., A wave-propagation based volume tracking method for compressible multicomponent flow in two space dimensions, *Journal of Computational Physics* 215 (2006), pp. 219-244.
- [144] Han, L.H., X.Y.Hu, N.A.Adams, Adaptive multi-resolution method for compressible multi-phase flows with sharp interface model and pyramid data structure, *Journal of Computational Physics* 262 (2014), pp. 131-152.
- [145] Luo, J., X.Y.Hu, N.A.Adams, Efficient formulation of scale separation for multi-scale modeling of interfacial flows, *Journal of Computational Physics* 308 (2016), pp. 411-420.
- [146] Haas, J.F., B.Sturtevant, Interaction of weak shock waves with cylindrical and spherical gas inhomogeneities, *Journal of Fluid Mechanics* 181 (1987), pp. 41-76.
- [147] Lax, P.D., X.D. Liu, Solution of 2-D Riemann problems of gas dynamics by positive schemes, *SIAM Journal of Scientific Computing* 19 (1998), pp. 319-340.
- [148] Nourgaliev, R.R., T.N.Dinh, T.G.Theofanous, Adaptive characteristics-based matching for compressible multifluid dynamics, *Journal of Computational Physics* 213 (2006), pp. 500-529.
- [149] Chang, C.H., M.S.Liou, A robust and accurate approach to computing compressible multiphase flow: Stratified flow model and AUSM+-up scheme, *Journal of Computational Physics* 225 (2007), pp. 840-873.

- [150] Layes, G., O.Le Métayer, Quantitative numerical and experimental studies of the shock accelerated heterogeneous bubbles motion, *Physics of Fluids* 19 (2007), pp. 042105.
- [151] Kailasanath, K., Review of propulsion applications of detonation waves, *AIAA Journal*, Vol. 38, No. 9, 2000, pp. 1698-1708.
- [152] Roy, G.D., Frolov, S.M., Borisov, A.A. and Netzer, D.W., Pulse detonation propulsion: challenges, current status, and future perspective, *Progress in Energy and Combustion Science*, Vol. 30, 2004, pp. 545-672.
- [153] Wolanski, P., Detonation propulsion, *Proceedings of the Combustion Institute*, Vol. 34, 2013, pp. 125-158.
- [154] Lu, F.K. and Braum, E.M., Rotating detonation wave propulsion: experimental Challenges, modeling, and engine concepts, *Journal of Propulsion and Power*, Vol. 30, No. 5, 2014, pp. 1125-1142.
- [155] Colella, P., Andrew M. and Victor R., Theoretical and numerical structure for reacting shock waves, *SIAM Journal on Scientific and Statistical Computing*, Vol. 7, No. 4, 1986, pp. 1059-1080.
- [156] Jeltsch, R. and Petra K., Error estimators for the position of discontinuities in hyperbolic conservation laws with source terms which are solved using operator splitting, *Computing and Visualization in Science*, Vol. 1, No. 4, 1999, pp. 231-249.
- [157] Zhang, B., Liu, H., Chen, F. and Wang, J.H., The equilibrium state method for hyperbolic conservation laws with stiff reaction terms, *Journal of Computational Physics*, Vol. 263, 2014. pp. 151-176.
- [158] Bihari, B.L. and Donald S., Multiresolution schemes for the reactive Euler equations, *Journal of Computational Physics*, Vol. 154, No. 1, 1999, pp. 197-230.

- [159] Leveque, R.J. and Shyue K.M., One-dimensional front tracking based on high resolution wave propagation methods, *SIAM Journal on Scientific Computing*, Vol. 16, No. 2, 1995, pp. 348-377.
- [160] Nguyen, D., Frédéric G. and Ronald F., A fully conservative ghost fluid method and stiff detonation waves, 12th Int. Detonation Symposium, San Diego, CA. 2002.
- [161] Engquist, B. and Björn S., Robust difference approximations of stiff inviscid detonation waves, Department of Mathematics, University of California, Los Angeles, 1991.
- [162] Bao, W. and Shi J., The random projection method for stiff multispecies detonation capturing, *Journal of Computational Physics*, Vol. 178, No. 1, 2002, pp. 37-57.
- [163] Wang, W., Shu, C.W., Yee, H. C., Kotov, D.V. and Sjögreen, B., High order finite difference methods with subcell resolution for stiff multispecies discontinuity capturing, *Communications in Computational Physics*, Vol. 17, No. 2, 2015, pp. 317-336.
- [164] Gao, Z., Don, W.S. and Li, Z., 2012. High order weighted essentially non-oscillation schemes for two-dimensional detonation wave simulations. *Journal of Scientific Computing*, 53(1), pp.80-101.
- [165] Wang, C., Shu, C.W., Han, W. and Ning, J., 2013. High resolution WENO simulation of 3D detonation waves. *Combustion and Flame*, 160(2), pp.447-462.
- [166] Dou, H.S., Tsai, H.M., Khoo, B.C. and Qiu, J., 2008. Simulations of detonation wave propagation in rectangular ducts using a three-dimensional WENO scheme. *Combustion and Flame*, 154(4), pp.644-659.

- [167] Gao, Z. and Don, W.S., 2013. Mapped hybrid central-WENO finite difference scheme for detonation waves simulations. *Journal of Scientific Computing*, 55(2), pp.351-371.
- [168] Wang, C., Dong, X. and Shu, C.W., 2015. Parallel adaptive mesh refinement method based on WENO finite difference scheme for the simulation of multi-dimensional detonation. *Journal of Computational Physics*, 298, pp.161-175.
- [169] Tan, S., Wang, C., Shu, C.W. and Ning, J., 2012. Efficient implementation of high order inverse Lax-Wendroff boundary treatment for conservation laws. *Journal of Computational Physics*, 231(6), pp.2510-2527.
- [170] Wang, C., Ding, J., Tan, S. and Han, W., 2015. High order numerical simulation of detonation wave propagation through complex obstacles with the inverse Lax-Wendroff treatment. *Communications in Computational Physics*, 18(05), pp.1264-1281.
- [171] Ji, H., Lien, F.S. and Yee, E., 2010. Numerical simulation of detonation using an adaptive Cartesian cut-cell method combined with a cell-merging technique. *Computers & Fluids*, 39(6), pp.1041-1057.
- [172] Togashi, F., Löhner, R. and Tsuboi, N., 2009. Numerical simulation of H₂/air detonation using unstructured mesh. *Shock Waves*, 19(2), pp.151-162.
- [173] Ji, H., Lien, F.S. and Yee, E., 2010. A new adaptive mesh refinement data structure with an application to detonation. *Journal of Computational Physics*, 229(23), pp.8981-8993.
- [174] Friedrich, O., 1998. Weighted essentially non-oscillatory schemes for the interpolation of mean values on unstructured grids. *Journal of computational physics*, 144(1), pp.194-212.

- [175] Lv, Y. and Ihme, M., 2014. Discontinuous Galerkin method for multicomponent chemically reacting flows and combustion. *Journal of Computational Physics*, 270, pp.105-137.
- [176] Teng, H.H., Jiang, Z.L. and Ng, H.D., 2014. Numerical study on unstable surfaces of oblique detonations. *Journal of Fluid Mechanics*, 744, pp.111-128.
- [177] Teng, H., Ng, H.D., Li, K., Luo, C. and Jiang, Z., 2015. Evolution of cellular structures on oblique detonation surfaces. *Combustion and Flame*, 162(2), pp.470-477.
- [178] Choi, J.Y., Kim, D.W., Jeung, I.S., Ma, F. and Yang, V., 2007. Cell-like structure of unstable oblique detonation wave from high-resolution numerical simulation. *Proceedings of the Combustion Institute*, 31(2), pp.2473-2480.
- [179] Gelfand, B.E., Khomik, S.V., Bartenev, A.M., Medvedev, S.P., Grönig, H. and Olivier, H., 2000. Detonation and deflagration initiation at the focusing of shock waves in combustible gaseous mixture. *Shock Waves*, 10(3), pp.197-204.
- [180] Bartenev, A.M., Khomik, S.V., Gelfand, B.E., Grönig, H. and Olivier, H., 2000. Effect of reflection type on detonation initiation at shock-wave focusing. *Shock Waves*, 10(3), pp.205-215.
- [181] Dumbser, M., Käser, M., Titarev, V.A. and Toro, E.F., 2007. Quadrature-free non-oscillatory finite volume schemes on unstructured meshes for nonlinear hyperbolic systems. *Journal of Computational Physics*, 226(1), pp.204-243.
- [182] Jameson, A. and Mavriplis, D., Finite volume solution of the two-dimensional Euler equations on a regular triangular mesh, *AIAA Journal*, Vol. 24, No. 4, 1986, pp. 611-618.
- [183] Batina, J.T., Unsteady Euler algorithm with unstructured dynamic mesh for complex-aircraft aerodynamic analysis, *AIAA Journal*, Vol. 29, No. 3, 1991, pp. 327-333.

- [184] Venkatakrishnan, V., Perspective on unstructured grid flow solvers, *AIAA Journal*, Vol. 34, No. 3, 1996, pp. 533-547.
- [185] Mavriplis, D.J., Unstructured grid techniques, *Annual Review of Fluid Mechanics*, Vol. 29, No. 1, 1997, pp. 473-514
- [186] Nielsen, E.J. and Anderson, W.K., Recent improvements in aerodynamic design optimization on unstructured meshes, *AIAA Journal*, Vol. 40, No. 6, 2002, pp. 1155-1163.
- [187] Barth, T.J. and Frederickson, P.O., High-order solution of the Euler equations on unstructured grids using quadratic reconstruction, *AIAA Paper*, 1990-0013, 1990.
- [188] Cockburn, B., Hou, S. and Shu, C.W., The Runge-Kutta Local Projection Discontinuous Galerkin Finite Element Method for Conservation Laws. 4. The Multidimensional Case, *Mathematics of Computation*, Vol. 54, No. 190, 1990, pp. 545-581.
- [189] Bassi, F. and Rebay, S., A High-Order Accurate Discontinuous Finite Element Method for the Numerical Solution of the Compressible Navier-Stokes Equations, *Journal of Computational Physics*, Vol. 131, No. 2, 1997, pp. 267-279.
- [190] Wang, Z.J., High-order methods for the Euler and Navier-Stokes equations on unstructured grids, *Progress in Aerospace Sciences*, Vol. 43, No. 1, pp. 1-41.
- [191] Xiao, F., Unified formulation for compressible and incompressible flows by using multi integrated moments I: One-dimensional inviscid compressible flow, *Journal of Computational Physics*, Vol. 195, No. 2, 2004, pp. 629-654.
- [192] Ii, S., Shimuta, M. and Xiao, F., A 4th-order and single-cell-based advection scheme on unstructured grids using multi-moments, *Computer physics communications*, Vol. 173, No. 1, 2005, pp. 17-33.

- [193] Chen, C. and Xiao, F., Shallow Water Model on Cubed-Sphere by Multi-moment Finite Volume Method, *Journal of Computational Physics*, Vol. 227, No. 10, 2008, pp. 5019-5044.
- [194] Ii, S. and Xiao, F., High order multi-moment constrained finite volume method. Part I: Basic formulation, *Journal of Computational Physics*, Vol. 228, No. 10, 2009, pp. 3669-3707.
- [195] Ii, S. and Xiao, F., A global shallow water model using high order multi-moment constrained finite volume method and icosahedral grid, *Journal of Computational physics*, Vol. 229, No.5, 2010, pp. 1774-1796.
- [196] Xiao, F., Ii, S., Chen, C. and Li, X., A note on the general multi-moment constrained flux reconstruction formulation for high order schemes, *Applied Mathematical Modelling*, Vol. 37, No. 7, 2013, pp. 5092-5108.
- [197] Yabe, T., Tanaka, R., Nakamura, T. and Xiao, F., An exactly conservative semi-Lagrangian scheme (CIP-CSL) in on dimension, *Monthly Weather Review*, Vol. 129, No. 2, 2001, pp. 332-344.
- [198] Eymann, T.A. , Active flux schemes, PH.D. thesis, University of Michigan, 2013.
- [199] Shima, E. and Kitamura, K., On New Simple Low-Dissipation Scheme of AUSM-Family for All Speeds, *AIAA-Paper*, 2009-136, 2009.
- [200] Shima, E. and Kitamura, K., Parameter-free simple low-dissipation AUSM-family scheme for all speeds, *AIAA Journal*, Vol. 49, No. 8, 2011, pp. 1693-1709.
- [201] Kitamura, K. and Shima, E., Towards shock-stable and accurate hypersonic heating computations: A new pressure flux for AUSM-family schemes, *Journal of Computational Physics*, Vol. 245, 2013, pp.62-83.
- [202] Roe, P.L., Approximate Riemann solvers, parameter vectors, and difference schemes, *Journal of Computational Physics*, Vol. 43, No. 2, 1981, pp. 357-372.

- [203] Weiss, J.M. and Smith, W.A., Preconditioning applied to variable and constant density flows, *AIAA journal*, Vol. 33, No.11, 1995, pp. 2050–2057.
- [204] Shen, C., Sun, F. and Xia, X., Implementation of density-based solver for all speeds in the framework of OpenFOAM, *Computer Physics Communications*, Vol. 185, No. 10, 2014, pp. 2730-2741.
- [205] Turkel, E., Preconditioning technique in computational fluid dynamics, *Annual Review of Fluid Mechanics*, Vol. 31, No. 1, 1999, pp.385-416.
- [206] Liou, M.S. and Steffen, C.J., A new flux splitting scheme, *Journal of Computational Physics*, Vol. 107, No. 1, 1993, pp. 23-39.
- [207] Liou, M.S., A sequel to AUSM: AUSM+, *Journal of Computational Physics*, Vol. 129, No. 2, 1996, pp. 364-382.
- [208] Liou, M.S., A sequel to AUSM, Part II: AUSM+-up for all speeds, *Journal of Computational Physics*, Vol. 214, No. 1, 2006, pp. 137-170.
- [209] Roe,P.L., Some contributions to the modelling of discontinuous flows, *Large-scale computations in fluid mechanics*, Vol. 22, 1985, pp. 163-193.
- [210] Li, W. and Ren, Y.X., Efficient implementation of weighted ENO schemes, *Journal of Computational Physics*, Vol. 231, No. 11, 2012, pp. 4053-4077.
- [211] Tu, S. and Aliabadi, S., A slope limiting procedure in discontinuous Galerkin finite element method for gasdynamics applications, *International Journal of Numerical Analysis and Modeling*, Vol. 2, No. 2, 2005, pp. 163-178
- [212] Van Dyke, M. *An album of fluid motion*, The Parabolic Press, 2005
- [213] Xisto, C.M., Páscoa, J.C., Oliveira, P.J. and Nicolini, D.A., A hybrid pressure–density-based algorithm for the Euler equations at all Mach number regimes, *International Journal for Numerical Methods in Fluids*, Vol. 70, No. 8, 2012, pp. 961-976.

- [214] Lien, F.S. and Leschziner, M.A., A pressure-velocity solution strategy for compressible flow and its application to shock/boundary interaction using second-moment turbulence closure, *Journal of fluids engineering*, Vol. 115, No. 4, 1993, pp. 717-725.
- [215] Moukalled, F. and Darwish, M., A high-resolution pressure-based algorithm for fluid flow at all speeds, *Journal of Computational Physics*, Vol. 168, No. 1, 2001, pp. 101-133.
- [216] Harlow, F.H. and Amsden, A.A., A numerical fluid dynamics calculation method for all flow speeds, *Journal of Computational Physics*, Vol. 8, No. 2, 1971, pp. 197-213.
- [217] Xiao, F., Akoh, R. and Ii, S., "Unified formulation for compressible and incompressible flows by using multi-integrated moments II: multi-dimensional version for compressible and incompressible flows," *Journal of Computational Physics*, Vol. 213, No. 1, 2006, pp. 31-56.
- [218] Frink, N.T., Tetrahedral unstructured Navier-Stokes method for turbulent flows, *AIAA journal*, Vol. 36, No. 11, 1998, pp.1975-1982.
- [219] Kim, K.H. and Kim, C., Accurate, efficient and monotonic numerical methods for multi-dimensional compressible flows: Part I: Spatial discretization, *Journal of computational physics*, Vol.208, No. 2, 2005, pp.527-569.